

UNIVERSITÉ DE LILLE

THÈSE

Présentée en vue de l'obtention du grade de

Docteur

Spécialité MOLÉCULES ET MATIÈRE CONDENSÉE

Ecole Doctorale SMRE, mention CHIMIE DES MATÉRIAUX

Par Sarah CHATENET

An instrumented controlled-atmosphere cone calorimeter to
characterize electrical cable behavior in depleted fires

-

Caractérisation de gaines de câbles électriques en incendie
confiné au moyen d'un cône calorimètre à atmosphère
contrôlée

Soutenue publiquement le 9 Juillet 2019 devant le jury composé de :

Dr. Dhionis DHIMA	Centre Scientifique et Technique du Bâtiment	Rapporteur
Prof. Guillaïn MAUVIEL	Ecole Nationale Supérieure des Industries Chimiques	Rapporteur
Dr. Pascale DESGROUX	Centre National de la Recherche Scientifique	Présidente
Dr. Olivier AUTHIER	EDF R&D	Examineur
Prof. Serge BOURBIGOT	Ecole Nationale Supérieure de Chimie de Lille	Co- directeur
Prof. Gaëlle FONTAINE	Ecole Nationale Supérieure de Chimie de Lille	Directrice

A mon père

A Norah

“ Ce n’est pas parce que les choses sont difficiles que nous n’osons pas,
mais parce que nous n’osons pas qu’elles sont difficiles ”

- Sénèque

Aknowledgments

Je tiens tout d'abord à remercier Gaëlle Fontaine et Serge Bourbigot qui m'ont ouvert la voie de l'incendie en 2015 en m'accueillant pour mon stage de fin d'étude, puis pour avoir dirigé cette thèse. Les échanges que l'on a pu avoir ont été très enrichissants sur le plan scientifique et leur vision m'a aidée à mener à bien ce projet. Leurs qualités humaines ont su instaurer un cadre de travail agréable. Ça a été un réel plaisir de travailler avec vous.

Je remercie vivement Isabelle Flour pour m'avoir accueillie au sein du département MFEE d'EDF R&D durant ces trois années, ainsi que Laurent Gay pour avoir mis en place cette thèse et pour m'avoir fait confiance dans ce projet.

Merci à Olivier Authier pour m'avoir suivie dans le cadre industriel tout au long de ces trois années. Son accessibilité, ses connaissances en génie des procédés et sa rigueur scientifique m'ont beaucoup apporté. Merci pour ta générosité.

Je remercie Pascale Desgroux qui m'a fait l'honneur de présider mon jury de thèse, ainsi que Guillain Mauviel et Dhionis Dhima d'avoir accepté la fonction de rapporteur. Merci pour l'intérêt que vous avez porté à mon travail et pour nos échanges.

Je remercie tout particulièrement les membres de l'équipe incendie à MFEE. En premier lieu Clément Cuperlier avec qui nous avons partagé beaucoup de temps sur l'installation expérimentale et qui, par ses qualités techniques et sa motivation, a permis de finaliser le programme expérimental et de le rendre aussi riche que possible. Merci à Maxime Lemesle pour m'avoir accueillie sur la boucle d'essais en début de thèse. Merci également à Romain Millerot pour avoir été présent pendant une partie des essais et pour avoir accepté de nettoyer l'ELPI un certain nombre de fois. Merci à Rémi Lang pour avoir prêté main forte quand il le fallait, toujours avec une petite blague. Merci à Sylvère Mongruel pour avoir apporté un certain nombre de solutions et s'être montré bien souvent rassurant. Merci à Sébastien Thion pour avoir suivi une partie de la thèse et pour toutes nos discussions. Cette thèse a bien fonctionné grâce à vous tous, un grand merci pour ça. Merci également aux agents que j'ai côtoyés au sein du département et à mes camarades doctorants. J'ai rencontré de belles personnes qui vont me manquer ! Pensée particulière à mon premier co-bureau qui est vite devenu un ami, et qui le restera encore de nombreuses années je l'espère.

Je tiens également à remercier les membres du laboratoire lillois R2F avec qui j'ai travaillé pendant mes visites régulières. Merci à Pierre Bachelet, Johan Sarrazin et Benjamin Dewailly d'avoir toujours été disponibles pour prêter main forte, et ce avec beaucoup de gentillesse. Merci également aux doctorants d'avoir été si accueillants et toujours partants pour partager un petit verre après le labo.

Enfin, je tenais à remercier ma maman d'avoir été l'épaule si solide qui m'a toujours soutenue. Merci à mon papa qui m'a toujours fait croire que tout était à ma portée. Merci à Benjamin, celui qui partage ma vie. Je te suis reconnaissante d'être présent, de m'avoir soutenue et tant rassurée dans les moments de doute. Mes pensées vont enfin à ma fille Norah, qui, en voyant le jour à l'aube de la rédaction de ce manuscrit, a ouvert un nouveau chapitre de ma vie.

Table of contents

Aknowledgments	5
Table of contents	7
Introduction	11
<i>Context.....</i>	<i>11</i>
<i>Aims</i>	<i>12</i>
Chapter I: Bibliography.....	15
1. <i>Introduction.....</i>	<i>15</i>
1.1. Generalities on polymer combustion	16
1.2. Molecular-scale and macro-scale polymer combustion	16
2. <i>Molecular-scale polymer combustion</i>	<i>18</i>
2.1. Condensed phase reaction	18
2.2. Gas phase reactions	23
2.3. Combustion of PMMA.....	27
2.4. Combustion of PVC.....	28
3. <i>Polymer combustion at macro-scale</i>	<i>30</i>
3.1. Combustion efficiency convective and radiative components	30
3.2. Fire stages criteria	32
3.3. Effects of vitiation and equivalence ratio on combustion	34
4. <i>Conclusion</i>	<i>44</i>
Chapter II: Controlled-atmosphere cone calorimeter set-up conception	45
1. <i>Bench-scale apparatus for fire testing</i>	<i>45</i>
1.1. Fire testing.....	45
1.2. Different types of flow-through bench-scale apparatuses for under ventilated conditions	47
1.3. Conclusion on the comparison of the flow-through bench-scale apparatuses for under-ventilated conditions.....	53
2. <i>Development of a new controlled-atmosphere cone calorimeter.....</i>	<i>54</i>
2.1. Context	54
2.2. Design of the apparatus	63
2.3. Controllers and sensors.....	69
2.4. Equipment for smoke analysis	71
3. <i>Conclusion</i>	<i>77</i>
Chapter III: Representative material elaboration	79
1. <i>Introduction.....</i>	<i>80</i>
2. <i>Materials and methods</i>	<i>82</i>
2.1. Materials	82
2.2. Elementary analysis.....	83
2.3. Thermal analysis.....	84
2.4. Optical measurement.....	85
2.5. Thermo-physical analysis	86

3.	<i>Reverse engineering and characterization of electrical cable sheath</i>	87
3.3.	Industrial formulations for electrical cable sheath	87
3.4.	Composition analysis of the cable sheath	89
3.5.	Thermal stability analysis	92
4.	<i>Separate characterization of the main components of the electrical cable sheath</i>	95
4.3.	PVC cable sheath main components thermal stability and interactions.....	95
4.4.	Choice of stabilizing system	98
5.	<i>Elaboration and characterization of representative and simplified materials</i>	99
5.1.	Elaboration of PVC materials.....	99
5.2.	Comparison of the reference material with the electrical cable sheath.....	101
5.3.	Characterization of filled and unfilled PVC properties for numerical simulation inputs.....	102
6.	<i>Conclusion</i>	109
Chapter IV: Study of the under-ventilation effect.....		111
1.	<i>Introduction</i>	111
2.	<i>Data processing</i>	112
2.1.	Data acquisition.....	112
2.2.	Data smoothing	113
2.3.	Data presentation	113
3.	<i>Description of the experiments</i>	114
4.	<i>Well-ventilated experiments in the open configuration cone calorimeter</i>	117
4.1.	Mass loss and heat release rate measured with cone calorimeter in an open configuration	118
4.2.	Evolved gases measured with cone calorimeter in an open configuration	124
4.3.	Evolved aerosols measured with cone calorimeter in an open configuration	126
4.4.	Discussion on the well-ventilated fire parameters and combustion products	129
5.	<i>Under-ventilated experiments in the controlled-atmosphere cone calorimeter</i>	131
5.1.	Characterization of the fire regime	131
5.2.	Influence of the confinement on the fire parameters	132
5.3.	Influence of the confinement on evolved gases	136
5.4.	Influence of the confinement on evolved aerosols.....	138
5.5.	Discussion on the influence of the confinement on fire parameters and combustion products	140
6.	<i>Conclusion</i>	142
Chapter V: Study of the vitiation effect		145
1.	<i>Introduction</i>	145
2.	<i>Effect of vitiation on mass loss and heat release rate</i>	146
2.1.	Effect of vitiation on mass loss and heat release rate for PMMA	146
2.2.	Effect of vitiation on mass loss and heat release rate for unfilled PVC.....	148
2.3.	Effect of vitiation on mass loss and heat release rate for filled PVC.....	151
2.4.	Discussion on the effect of vitiation on the fire parameters	153
3.	<i>Effect of vitiation on the evolved gases</i>	156
3.1.	Effect of vitiation on the evolved gases for PMMA.....	156
3.2.	Effect of vitiation on the evolved gases for unfilled PVC	158
3.3.	Effect of vitiation on the evolved gases for filled PVC	159
4.	<i>Effect of vitiation on the evolved aerosols</i>	160
4.1.	Effect of vitiation on the evolved aerosols for PMMA	160
4.2.	Effect of vitiation on the evolved aerosols for unfilled PVC.....	161

4.3. Effect of vitiation on the evolved aerosols for filled PVC	161
5. Conclusion	163
General conclusion	164
<i>Conclusion</i>	164
<i>Perspectives</i>	165
Appendix	167
Appendix 1: Physical description of soot aggregates and theory of measurement	169
1. <i>Physical description of soot aggregates</i>	169
1.1. Brownian motion	169
1.2. Primary particles diameter D_p	172
1.3. Radius of gyration R_g	172
1.4. Number of primary particles in the aggregate N_p	172
1.5. Expression of the fractal theory	172
2. <i>Physical quantities useful for characterization</i>	174
2.1. Information related to particles weight and volume	175
2.2. The equivalent diameters	176
3. <i>Theory of measurement</i>	178
Appendix 2: Mass spectra of DIDP py-GC/MS	180
Appendix 3: Plaques processing details	181
1. <i>Filled PVC plaques processing details</i>	181
2. <i>Unfilled PVC plaques processing details</i>	183
Appendix 4: Tests performed under air in open and confined configuration	185
1. <i>Open configuration</i>	185
1.1. Mass loss and HRR	185
1.2. Gases	188
1.3. Aerosols	192
2. <i>Confined configuration</i>	194
2.1. Mass loss and heat release rate	194
2.2. Gases	197
2.3. Aerosols	200
Appendix 5: Tests performed in confined configuration under various oxygen contents	203
1. <i>Mass Loss and Heat Release Rate</i>	203
1.1. 18 vol. %O ₂	203
1.2. 16 vol. %O ₂	206
1.3. 13 vol. %O ₂	209
1.4. 9 vol. %O ₂	210
1.5. 6 vol. %O ₂	212
1.6. 2 vol. %O ₂	214
2. <i>Gases</i>	216
2.1. 18 vol. %O ₂	216
2.2. 16 vol. %O ₂	220

2.3.	9 vol. %O ₂	224
2.4.	6 vol. %O ₂	227
2.5.	2 vol. %O ₂	231
3.	<i>Aerosols</i>	235
3.1.	18 vol. %O ₂	235
3.2.	16 vol. %O ₂	236
References		239

Introduction

Context

In the nuclear industry for power generation, fire is the most frequent internal aggression with an occurrence of one fire outbreak per year and per nuclear unit in France. A fire is threatening by two means: the heat it releases that may drive a fire growth and the smoke it yields, composed of potentially toxic and/or corrosive gases and aerosols that may be transported away from the seat of the fire and interact with electrical components in the area. The fire incident in the Nogent-sur-Seine nuclear power plant (NPP) on July 2018 that caused a nuclear reactor to lose its power supply, without impacts to persons and the environment, can be mentioned.

In NPPs, compartments in the buildings are generally sealed from one to another while connected to a ventilation network. This ventilation system provides a suitable pressure cascade to prevent any accidental radioactive leak within the compartment from escaping to the open atmosphere. The compartments where radioactive materials are present are under-pressurized and the outgoing air flows are gathered and filtered thanks to high-efficiency air-cleaning devices [1]. As flaming fires consume the oxygen, this low ventilation level drives confined fires in oxygen depleted conditions (i.e. $[O_2] < 21 \text{ vol. } \%$) at advanced stages. As NPPs can require more than 1 600 km of electrical cable, electrical cable sheaths are the most abundant fire load in these premises [2]. The study of electrical cable sheath material fire behavior is then a first attempt at covering the fire impact in NPPs. In all the running NPPs, i.e. second generation NPPs, electrical cable sheaths are mainly PVC¹-based formulated materials whereas in the next generation NPPs, i.e. third generation, electrical cable sheaths are mainly non-halogenated EVA/ATH² materials.

In 2014, Electricité de France (EDF) was required by the nuclear safety authority (ASN) to study specifically the impacts of NPP fire effluents on the electrical equipment necessary to the nuclear safety [3]. For this reason, a Research and Development (R&D) unit of EDF Lab Chatou³ develops in-depth knowledge on the consequences that might have NPP-type fires by combining an experimental and a numerical approach. The experimental studies are particularly crucial in the fire science field, especially when the burning fuel is as complex as formulated polymeric materials. A bench-scale apparatus allowing to characterize simultaneously the fire parameters, i.e. heat release rate (HRR) and mass loss rate (MLR), and the effluents, i.e. the light gases and the aerosols, by coupling a mass loss

¹ Polyvinyl chloride

² Ethylene-co-vinyl acetate flame retarded with aluminium trihydroxide

³ Fluids Dynamics, Power Generation and Environment department (MFEE)

cone to a Fourier Transformed Infrared spectrometer (FTIR) and to an Electrical Low-pressure Impactor granulometer (ELPI) was developed during a former PhD work [4]. This apparatus permits to study well-ventilated fires in air that can be assimilated to the early fire stages in NPP. This work was focused on the non-halogenated electrical cable sheaths. At the same time, a lack of data concerning the PVC-based electrical cable sheaths fire behavior remains. Moreover, oxygen depleted, i.e. under-ventilated and vitiated fires⁴, have to be considered to study the whole fire scenario.

Aims

In this context, this PhD project is initiated through a collaboration with the *Materials and Transformation Unit* (UMET) of the *Ecole Nationale Supérieure de Chimie de Lille* (ENSCL) to adapt this bench-scale apparatus to oxygen depleted studies and to investigate the fire behavior of electrical cable sheath at different fire stages. The output of this new controlled-atmosphere cone calorimeter is firstly compared with the literature by performing experiments with PMMA⁵, as it is a widely studied material in fire science [5]. Then, an industrial PVC-based electrical cable sheath material is submitted to a reverse engineering to disclose its formulation in the aim at elaborating a representative material of controlled composition and shape. This material, in the form of plaque, is then tested in the controlled-atmosphere cone calorimeter (air/nitrogen mixture) under constant radiative heat flux (50 kW.m⁻²) in well-ventilated, under-ventilated and vitiated conditions. In order to describe more specifically each step of this PhD work, this document is divided into five chapters as follows.

The first chapter gathers a theoretical background on polymer thermal decomposition mechanism and on both gaseous and aerosols formation mechanisms, especially soot particles. Some pieces of fundamental information on the oxygen depleted fire science are approached and, finally, a state of the art on the oxygen depleted fire studies at bench-scale is proposed to position this present work among the literature.

The second chapter presents the conception of the new controlled-atmosphere cone calorimeter. It is compared with the existing benches in the literature that are dedicated to the same studies in confined atmosphere. The technical features are detailed, as well as the analytical equipment aiming at characterizing fire parameters and evolved smoke effluents throughout the material thermal decomposition.

The third chapter is dedicated to the PVC-based electrical cable sheath reverse engineering and to the formulation and characterization of the representative material. Two formulations are developed: the

⁴ Under-ventilated regime corresponds to fuel-to-air equivalence ratio > 1 , and vitiated regime is defined by $[O_2] < 21$ vol. % at the inlet gas stream.

⁵ Polymethylmethacrylate

first one (PVC with mineral filler, i.e. filled PVC) used as the representative material, and the second one (PVC without mineral filler, i.e. unfilled PVC). The unfilled PVC material is developed in order to perform tests in the cone calorimeter with a simpler fuel and thus bridge the gap towards the comprehension of the fire behavior phenomena occurring during the experiments with the representative material. Each main component of the representative material is tested at lab-scale in terms of thermal stability and thermal decomposition mechanism to identify the effect of temperature in controlled and homogeneous conditions. Also, thermo-physical properties of interest in fire science, e.g. thermal conductivity and heat capacity, are characterized for both of filled and unfilled PVC materials.

The fourth chapter deals with the effect of ventilation on the fire parameters and on the smoke effluents. The results of well-ventilated and under-ventilated experiments at 21 vol. % O_2 in the inlet gas stream with PMMA, representative material, i.e. filled PVC and unfilled PVC, are presented and discussed and the differences observed between the two conditions are highlighted.

The fifth chapter relates the study of the effect of vitiation in under-ventilated conditions on the fire parameters and on the smoke effluents for PMMA, filled and unfilled PVC. Varying the oxygen content from 2 vol. % to 21 vol. % allows to investigate its effect in flaming and non-flaming regime. The observed influence of the oxygen content is highlighted for each material and is compared between the materials.

Finally, a conclusion to this PhD work and some perspectives are suggested.

Chapter I: Bibliography

1. Introduction	15
1.1. <i>Generalities on polymer combustion</i>	16
1.2. <i>Molecular-scale and macro-scale polymer combustion</i>	16
2. Molecular-scale polymer combustion	18
2.1. <i>Condensed phase reaction</i>	18
2.1.1. Heating	19
2.1.2. Anaerobic pyrolytic decomposition	19
2.1.3. Thermo-oxidative decomposition	22
2.1.4. Char formation	22
2.2. <i>Gas phase reactions</i>	23
2.2.1. Flame reactions	23
2.2.2. Soot particles formation	24
2.3. <i>Combustion of PMMA</i>	27
2.4. <i>Combustion of PVC</i>	28
3. Polymer combustion at macro-scale	30
3.1. <i>Combustion efficiency convective and radiative components</i>	30
3.2. <i>Fire stages criteria</i>	32
3.3. <i>Effects of vitiation and equivalence ratio on combustion</i>	34
3.3.1. Effect of equivalence ratio on combustion products	34
3.3.2. Effect of vitiation on fuel mass loss rate	36
3.3.3. Oxygen depleted fire studies: a state of the art	38
4. Conclusion	44

1. Introduction

Since the three materials of interest in this work, i.e. PMMA, unfilled PVC and filled PVC, are polymeric materials, it is essential to understand the polymeric materials reaction to fire. For this purpose, the polymer combustion phenomena are first described at a molecular scale, which permits to present the thermal decomposition mechanisms and the evolved gaseous and aerosols species taking part in the combustion in the gas phase. In a second time, since fire is a complex and coupled physical phenomenon, some fundamentals on the combustion phenomena at a macro-scale are presented and the effect of oxygen concentration is specifically detailed.

1.1. Generalities on polymer combustion

When the polymer undergoes a sufficient thermal stress, it heats up and its chemical bonds start to break. This phenomenon is the thermal decomposition or pyrolysis. Pyrolysis leads to different compounds: solids, liquids and volatiles. Among the volatile compounds, some are non-combustible (H_2O , CO_2), but some are combustible (low molecular weight organic compounds such as CH_4 , C_2H_4 ...) with the potential of releasing heat by their combustion reaction. They form with air (the combusting) an inflammable gas phase. Two scenarios may happen: in one case, an external energy source (such a flame, a spark, an incandescent particle...) ignites this combustible/combusting mixture or in the second case, the self-ignition temperature is reached because of the exothermic chemical oxidation reactions and a spontaneous ignition happens. At the ignition, the combustion takes place and the flame produces a heat flux that can be sufficient to sustain the thermal decomposition and, as a result, produce more combustible gases. In this way, fire is a self-sustained phenomenon. The combustion is maintained as long as there is enough energy transferred to the polymer surface to sustain its thermal decomposition.

Polymer thermal decomposition may proceed by heat alone, or by the combined action of heat and oxygen. In many polymers, thermal decomposition processes are accelerated by the action of oxygen, lowering the minimum decomposition temperatures [6]. Prior to ignition, thermo-oxidative decomposition results in aerobic pyrolysis of fuel and other species. After ignition, during flaming, even in well-ventilated conditions, pyrolysis of the condensed phase is essentially anaerobic, with all the oxidation taking place in the gas phase [7]. Thus, the mass loss or the residue formation, resulting from pyrolysis, corresponds to a decomposition of the material in an inert atmosphere [8]. Thermo-oxidative decomposition will then be present during a fire only for non-intense flaming and non-flaming samples or near and after extinction. Furthermore, the observation of bubbles of volatile fuel in decomposing polymers around the time to ignition showed that for many thermoplastics, even prior to ignition, most volatile formation comes from the bulk of the polymer rather than its surface which makes the critical decomposition condition remain anaerobic [9].

1.2. Molecular-scale and macro-scale polymer combustion

When studying fire at a molecular-scale, three stages can be identified and separated: the heating stage, the decomposition stage and the oxidation stage. Each of these three stages are detailed in Table 1. When studying fire at a macro-scale, there are a higher amount of stages to consider. Five stages are listed and described in Table 2: the heating stage, the pyrolysis stage, the ignition stage, the flame spread and the fire development.

The heating stage at the molecular-scale depends on the intrinsic chemical and physical properties of the material whereas at the macro-scale, it takes into account shape factors, e.g. the thickness. The study of the decomposition stage at the molecular-scale is focused on the polymer thermal decomposition mechanisms whereas at the macro-scale, the gaseous compounds diffusion inside the polymer from the bulk to the surface is considered. The oxidation stage at molecular-scale describes the combustion chemical reactions whereas the ignition stage at macro-scale considers the flame radiative feedback to the fuel surface that will furtherly decompose and yields combustible gaseous compounds to the flame. The flame spread stage, resulting from the adjacent materials pyrolysis under the flame increasing heat flux and the fire development stage due to an increase in the materials burning are only considered at the macro-scale.

As illustrated by the confrontation of Table 1 and Table 2, the molecular-scale is necessary to understand the implied mechanisms, but since a lot of physical events are coupled during a fire, the study of the macro-scale is essential.

Table 1: Stages of combustion at a molecular scale [6]

The molecular scale		
Stage 1	Heating	An external heat source supplies heat causing the temperature of the polymer to increase. The extent of temperature change depends on the specific heat of the material. Physical, mechanical, and thermal properties change.
Stage 2	Decomposition	At high temperatures, the majority of the bonds reach failure points, causing the release of gaseous molecules dependent on the nature of the material burning. This can be accelerated by attack of oxygen on the polymer surface.
Stage 3	Oxidation	In the presence of oxygen at high temperatures, oxidation of the gaseous fragments proceeds rapidly, releasing heat and combustion products.

Table 2: Stages of combustion at a macro scale [6]

The macro scale		
Stage 1	Heating	Heat causes a temperature rise which will depend on the thermal inertia of the material.
Stage 2	Pyrolysis	Heat causes decomposition of the fuel, followed by pyrolysis of fuel to the gas phase.
Stage 3	Ignition	Fuel accumulates above the surface, and reacts with oxygen. Once the critical concentration of free radicals is reached, flashing will occur. When the total heat flux to the surface from the fuel oxidation is sufficient to pyrolyze enough fuel to replace it, ignition will occur, the rate of reaction will increase and produce carbon dioxide and water.
Stage 4	Flame spread	As the radiant heat flux increases, it will pyrolyze adjacent materials, leading to a repeated series of ignition, resulting in fire growth.
Stage 5	Fire development	As the flame gets larger, it will no longer be able to entrain sufficient oxygen, and products of incomplete combustion such as carbon monoxide and soot will be produced, increasing the radiative component of heat transfer.

2. Molecular-scale polymer combustion

Considering phenomena at molecular scale allows to decouple the physical phenomena. In this section, the reactions happening in the condensed phase are describe in a first part. In a second part, the reactions happening in the gas phase are presented.

2.1. Condensed phase reaction

There are two categories of polymers: thermoplastics and thermosets. Thermosets have additional covalent bonds forming crosslinkages between the polymer chains resulting in a 3-D network. This network gives the thermosets a particular reaction to thermal stress, preventing the polymer from softening and flowing. Thermosets are not studied in the scope of this literature review. Indeed, PMMA and PVC are thermoplastic polymers. They are constituted of independent polymer chains tangled-up together, which confers the material cohesion. The thermoplastics condensed phase reactions upon heating are described in the following section.

2.1.1. Heating

There are two categories of thermoplastic polymers: amorphous and semi-crystalline. The physical behavior of a thermoplastic under heat depends on its degree of crystallinity. Under heat, thermoplastics soften, melt (only the crystalline parts), then flow. Amorphous polymers stay at the solid state, they transform from glass state ($T < T_g$) to rubber state ($T > T_g$), then to a viscous state ($T < T_d$) by flowing⁶. The crystalline part of semi-crystalline polymers transforms from rubber state to liquid state at $T = T_f$ and their amorphous part undergo the same transformation as amorphous polymers.

2.1.2. Anaerobic pyrolytic decomposition

Thermal decomposition is an endothermic process. An energy higher than the chemical bonds energy is needed to break the chemical bonds present in the macromolecule. The required amount of energy to heat up the polymer to the decomposition temperature is about 1 to 2 kJ.g⁻¹ [10]. There are numerous thermal decomposition mechanisms that depend on the chemical bonds nature, the polymer structure and the presence of oxygen. In the absence of oxygen, thermal decomposition is only due to the action of heat and only anaerobic pyrolytic reactions occur. Anaerobic pyrolytic decomposition of polymers is mainly a free radical process concerning whether the polymer backbone, the pending groups, or both. There are four anaerobic pyrolytic decomposition mechanisms, depending on the polymer structure, that can lead the organic polymer to decompose into volatile products:

- Random chain scission;
- End-chain scission or unzipping;
- Chain stripping;
- Cross-linking.

These four pyrolytic decomposition mechanisms are detailed in the following paragraphs.

2.1.2.1. *Random chain scission*

Random chain scission usually takes place when the bonding energies are similar along the chain. This mechanism is observed for a large amount of thermoplastics (PE⁷, PP⁸, PET⁹, PA66¹⁰...) and leads to a decrease of the polymer molecular weight by the formation of a large range of molecular weight molecules. Some oligomers are small enough to volatilize without any further decomposition. This

⁶ T_g , T_d and T_f are the glass transition temperature, the decomposition temperature and the fusion temperature respectively.

⁷ Polyethylene

⁸ Polypropylene

⁹ Polyethylene terephthalate

¹⁰ Polyamide 6-6

process implies multiple steps free radical reactions: the initiation step (random or end-chain), the propagation step (intra- or inter-molecular hydrogen transfer or depolymerization) and termination (unimolecular termination, recombination, and dismutation) [11].

2.1.2.2. End-chain scission or unzipping

End-chain scission or unzipping corresponds to polymer backbone specific points breaking, generally at the end of the chains. It leads to the formation of monomers by a depolymerization mechanism (the exact reverse mechanism of polymerization). The unzipping reaction pathway then depends on the polymerization technique used to produce the polymer. These reactions are observed for a large range of polymers (PMMA, PTFE¹¹, POM¹²...). The thermal decomposition of polymethylmethacrylate (PMMA) is taken as an example below [12].

PMMA is generally produced by a free radical polymerization method but the anionic method is also used. Figure 1 shows the thermal decomposition mechanism of an anionic polymerized PMMA. In an anionic polymerized PMMA, the C-C bond is the weakest (335 kJ.mol⁻¹) so this is the first covalent bond to undergo a scission. The termination reaction is an intermolecular hydrogen transfer. The major formed product is the MMA (99%).

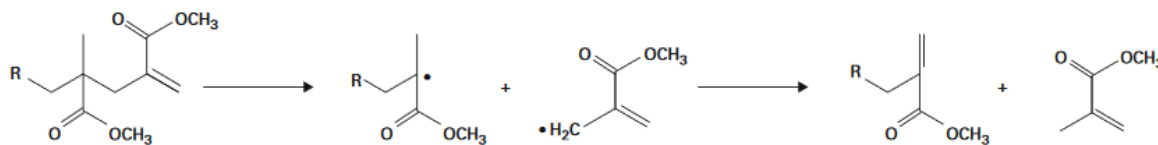


Figure 1: Thermal decomposition of an anionic polymerized PMMA¹³ [12]

Figure 2 shows the thermal decomposition mechanism of a radically polymerized PMMA. In a free radical polymerized PMMA, the presence of structural flaws, particularly head to head bonds [13] are weakest than a regular C-C bond. Their breakage lead to a multiple step decomposition that starts at lower temperatures [14].



Figure 2: Thermal decomposition of a free radical polymerized of PMMA [12]

¹¹ Polytetrafluoroethylene

¹² Polyoxymethylene

¹³ This figure is taken from the literature. Angles between bonds are not respected.

2.1.2.3. Chain stripping

Chain stripping concerns polymers that have pending groups attached to their backbone with weak covalent bonds (PVC, PVAc¹⁴, PS¹⁵, EVA¹⁶...). This weak bond is detached in the first place during thermal decomposition mainly by elimination and cyclization mechanisms. Elimination reactions lead to the formation of volatile products (hydrogen chloride for PVC, acetic acid for EVA, benzene for PS...) and unsaturations on the polymer backbone. These reactions may form an unstable polyene that can in turn form aromatic structures, shorter chain fragments and carbonaceous residues by crosslinking reactions and/or cyclization reactions which is the case for PVC. As regards cyclization reactions, they imply two adjacent pending groups reacting together to form a covalent bond leading to a cyclic structure. The thermal decomposition of PVC is taken as an example below [12].

The weakest bond in the PVC macromolecule is the C-Cl bond (330 kJ.mol^{-1}). Thermal decomposition leads to hydrogen chloride formation and char residue by cyclization reactions (Figure 3).

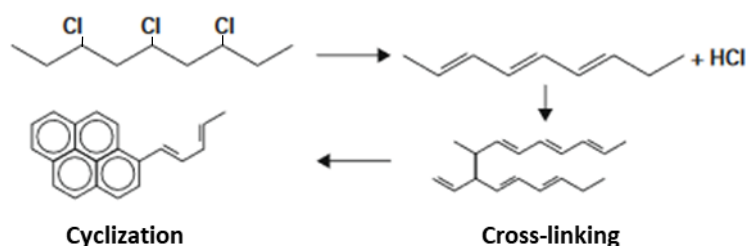


Figure 3: Cross-linking and cyclization reactions during PVC thermal decomposition [12]

2.1.2.4. Cross-linking

Cross-linking reactions, mentioned above, are very important in the formation of char since they generate high molecular weight structures. During this process, the polymer molecules decompose before the chains have acquired sufficient energy to overcome the forces holding them in place [6].

2.1.2.5. Condensed-phase reaction: conclusion

This classification (random chain scission, unzipping, chain stripping and cross-linking) allows a global characterization of polymer behavior. Nevertheless, for a wide range of polymers, thermal decomposition is a combination between different mechanisms that are in competition. The relative importance of competitive processes varies with factors such as the presence of additives, impurities and mostly temperature. Table 3 gathers some common polymers by generalized thermal decomposition mechanisms. For example, in the case of polystyrene (PS), if the main decomposition


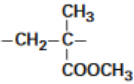
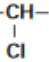
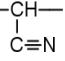
¹⁴ Polyvinyl alcohol

¹⁵ Polystyrene

¹⁶ Ethylene vinyl co-acetate

mechanism is the random chain scission, the polymer usually also undergoes chain stripping decomposition mechanism [15].

Table 3: Generalized mechanisms of polymer decomposition with examples [6]

Mechanism	Typical polymers	Formula	Typical decomposition products
Random chain scission	Polystyrene (PS)	$\text{—CH}_2\text{—CH—}$ 	Styrene monomer, dimer and trimer
	...more generally		Monomers and oligomers
End-chain scission or unzipping	Polymethylmethacrylate (PMMA)	$\text{—CH}_2\text{—C—}$ 	90-100% monomer
	... more generally		Monomer
Chain stripping	Polyvinyl chloride (PVC)	$\text{—CH}_2\text{—CH—}$ 	Hydrogen chloride, aromatic hydrocarbons and char
	... more generally		Small molecules and char
Cross-linking	Polyacrylonitrile (PAN)	$\text{—CH}_2\text{—CH—}$ 	Hydrogen cyanide and char
	... more generally		Volatile products and char

2.1.3. Thermo-oxidative decomposition

Thermo-oxidative decomposition occurs when oxygen is present. Thermo-oxidative decomposition mechanisms are in competition with pyrolytic decomposition mechanisms since they are both initiated with the same mechanism: a weak bond breaking with radicals release. The general thermo-oxidative mechanism is a free radical mechanism that can be summarized by an initiation step, a propagation step, a ramification step and a termination step [12].

2.1.4. Char formation

Solid products issued from thermal decomposition may form a carbonaceous residue, or char. The char is able to isolate the condensed phase from the incident heat flux when it gathers some specific physical properties of cohesion, porosity, density, thickness... Some combustible gases are then constrained in the char instead of being emitted to the gas phase. This carbonaceous residue is issued

from rearrangement reactions present in the condensed phase¹⁷. These reactions are slower than scission reactions. The char enhances thermal stability since it may be thermally stable for hundreds of degrees though it can decompose by chain scission at higher temperatures [16].

The char contains carbon atoms in majority (85 to 98%), traces of aromatic compounds and heteroatoms such as oxygen, nitrogen, phosphorus or sulfur depending of the polymer nature [17]. The char formation is not observed for all polymers. The char yield depends on the polymer nature and its thermal decomposition mechanisms:

- The char yield is negligible for polymers that undergo a chain scission mechanism (both random chain scission and unzipping): polyolefins, PS, PMMA...;
- The char yield is small (5 to 20 wt. %): polyesters, vinyl ester resins, polyepoxides, PVC...;
- The char yield is high for polymers containing an aromatic ring: phenolic resins (40 to 60 wt. % of char yield), aromatic thermosets (polyimides, cyanate esters...) and some thermoplastics (PPS¹⁸, PPO¹⁹, and PEEK²⁰).

2.2. Gas phase reactions

The gas phase above the burning polymer – the smoke – is constituted of combustible gases (mainly hydrocarbonated and oxygenated compounds), non-combustible gases and both solid and liquid particulates (aerosols).

In the flame, combustible compounds are oxidized, producing heat and effluents. The amount of heat produced by the burning of polymers can be partially predict by their structural units [18][19]. Main effluents are carbon dioxide, water vapor, carbon monoxide, methane, aliphatic and aromatic hydrocarbons and other compounds that will be detailed in the following section.

2.2.1. Flame reactions

Combustible gases formed during thermal decomposition react in the flame according to a very exothermic free radical mechanism. The implied radicals are mainly oxygen (O^{\bullet}), hydrogen (H^{\bullet}), and hydroxyl (HO^{\bullet}) radicals. These gas-phase reactions are extremely fast compared to the condensed-phase reactions. The flame reaction of methane is taken as an example [12]. The reaction of methane complete combustion is detailed in Equation 1.

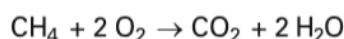
¹⁷ The char formation mechanism is different for intumescent flame retarded materials.

¹⁸ Polyphenylene sulfide

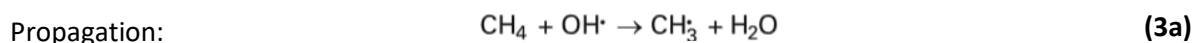
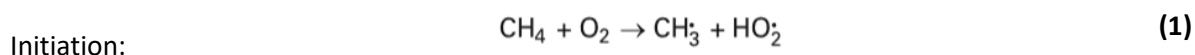
¹⁹ Polyphenylene oxide

²⁰ Polyetheretherketone

Equation 1: Methane complete combustion reaction²¹



The global mechanism of methane complete combustion is detailed as follows²². During the initiation step, methane reacts with oxygen to produce methyl (CH_3^\bullet) and hydroperoxyl (HO_2^\bullet) radicals (1). HO_2^\bullet then dissociates into hydroxyl (OH^\bullet) and oxygen (O^\bullet) radicals that are highly reactive in the flame (2). During the propagation step (3) to (7), methane reacts with the newly formed radicals to finally produce other radicals, carbon monoxide, carbon dioxide and water. The termination step is the recombination of radicals into stable molecules such as water and dihydrogen.



2.2.2. Soot particles formation

Soot formation mechanism is a sequential, complex mechanism with some remaining uncertainties. Two theories are in confrontation as regards the precursors in the soot formation mechanism. The main theory describes the soot formation with PAHs (Polycyclic Aromatic Hydrocarbons) as precursors [20][21]. It is the pathway that will be described in this section. Another theory describes polyynes as

²¹ Reactions implied in methane-air combustion are equilibrium reactions.

²² The detailed mechanism for methane-air combustion is comprised of 325 reactions and 53 species in the case of *GRI-Mech 3.0* mechanism carried out at the University of California at Berkeley.

precursors with a whole mechanism divided in three steps: polymerization, growth and graphitization [22].

Formation of the first aromatic ring

The formation of the first aromatic ring, the benzene ring (C_6H_6), is the first step in the soot particle formation mechanism. In the literature, it can be found that three main routes leading to the benzene formation exist. The first route is the recombination reaction between a 4-carbon alkyl radical (C_4 type radical) with a molecule of acetylene (C_2H_2) [23][24][25][26], the second route is the recombination reaction of C_3 type radicals [27][28] and the third route is the recombination of a C_5 type radical with a methyl (CH_3^\bullet) radical [29][30]. The relative proportion of each route depends on the experimental conditions, especially the nature of the fuel, and the temperature and the pressure of the flame [31].

Polycyclic aromatic hydrocarbons formation

The HACA (Hydrogen-Abstraction/aCetylene-Addition) mechanism (Figure 4), first introduced by Frenklach et al. [32], is considered as the main route leading to the formation of PAHs. This is a repeated sequence of two events, the first one being the hydrogen atom abstraction on an aromatic species by another hydrogen atom, and the second one being the addition of an acetylene molecule on the new radical. This addition leads to an unstable chemical species that stabilizes when cyclizing after the breaking of a C-H bond. This breaking releases a hydrogen atom. After this sequence, a new aromatic ring is formed. Repeating this whole mechanism leads to the apparition of increasing molecular weight aromatic hydrocarbons. Examining, the HACA mechanism, it is easily understood that soot particles are more likely to appear in rich flames, where there is a high concentration of hydrogen atoms compared to the molecular oxygen (O_2).

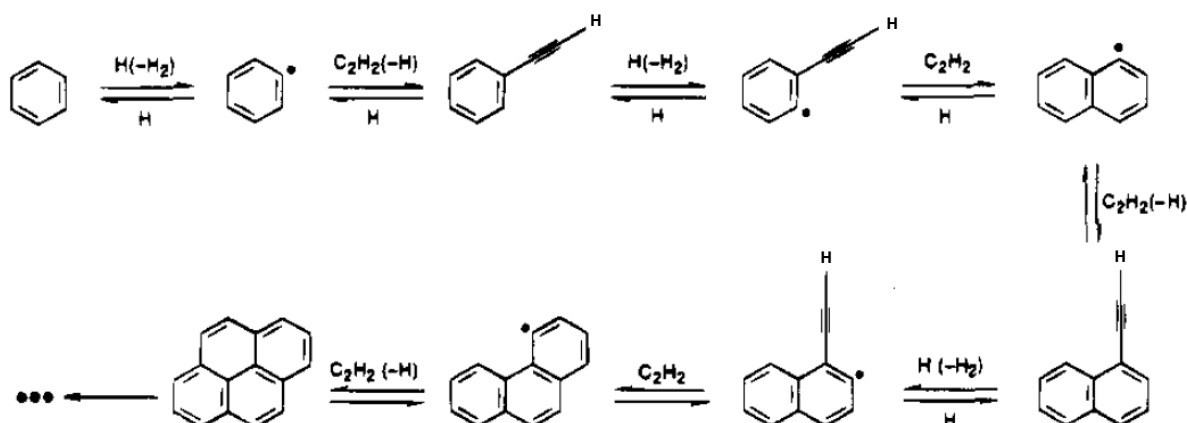


Figure 4: Schematic diagram of the HACA reaction mechanism of PAH formation and growth [26]

Nucleation

Nucleation is the most disputed step as regards the soot particles formation. The first models developed by Frenklach et al. [20] are about a chemical mechanism during which heavy PAHs simply go forward a solid state above a specific size, i.e. a specific amount of aromatic rings.

Other approaches consider that, above a specific size, PAHs bond with each other through Van der Waals interactions and coalesce to form a dimer. Collisions between dimers then form tridimensional clusters composed of layered PAHs [29]. These clusters might have functional groups adsorbed that would give them reactivity towards some molecules such other PAHs or acetylene, allowing their growth by the HACA mechanism (described in Figure 4). The succession of reaction steps through this HACA mechanism explains the pathway from a gaseous to a solid state by the formation of the first soot nuclei.

Surface growth

Nucleation leads to the formation of numerous soot nuclei that represent only a small portion of the total mass of soot particles formed in flames. After the nucleation phase, the number of particles does not increase anymore but the total mass of the particles goes on increasing. The main process responsible of the particle size increasing is the surface growth mechanism. It happens through the reaction between the active sites on the surface particle and the hydrocarbonaceous species present in the gas phase. This process leads to the soot particle diameter increase and, therefore, to an increase in the particle mass and in the soot volume fraction [33].

Coagulation and agglomeration

Soot particles coagulation is a physical process that occurs at the same time as the soot particles growth. During this step, soot particles collide and fusion to form bigger particles while keeping their spherical shape [29]. Coagulation leads to bigger particles while decreasing their number and keeping their total mass stable (the soot particles volume fraction remains the same).

Coagulation happens at the beginning of the combustion when the soot particles are still “young”, coagulation rate decreases rapidly during the soot particles growth. At the end of the soot particles growth process, the number of particles slightly decreases: “mature” particles agglomerate to form kinds of spherule chains. This is the agglomeration step. These chains form soot aggregates that have a fractal-like structure, described firstly in [34].

The conditions that govern the transition between the coagulation step and the agglomeration step remain blur [29]. Two statements are worth considering: the first one suggests that the agglomeration process start when surface reactions are too slow to keep the spherical shape of the particle. The

second one suggests that soot particles are simultaneously produced by surface growth reaction and coagulation and that agglomeration starts only once the growth process of particles is over.

Surface oxidation

The presence of oxidant species can offset the soot particles growth process by oxidizing the particles at their surface and then reducing the quantity of the total formed soot. Soot particles oxidation reactions are heterogeneous surface reactions between active sites at the surface of the particles and oxidative species that lead to a decrease in the soot total mass in favor of carbon dioxide (CO_2) and carbon monoxide (CO) formation. The number of particles yet remains the same. A general review about the soot particles oxidation mechanisms is proposed by Stanmore et al. [35] that listed the potential oxidative species in flames: the molecular oxygen (O_2), the hydroxyl radical (HO^\bullet), water (H_2O), carbon dioxide (CO_2) and nitrogen oxides (NO_x).

Conclusion on soot formation mechanism

The mechanism of soot particle growth is complex and encompasses different processes (surface growth, coagulation, agglomeration, and oxidation) that occur in a simultaneous and/or consecutive way, depending on the experimental conditions. This mechanism finally leads to “mature” soot particles under the shape of fractal-like structured spherule chains. These soot aggregates contain hundreds of spherules, what corresponds to carbonaceous compounds containing billions of carbon atoms.

Influence of the polymer structure

Size range of particles in fire smoke of polymeric materials lies mainly below $1\text{ }\mu\text{m}$ [36]. The chemical structure of a polymer plays a role in its tendency to form soot particulates. Therefore, fundamental knowledge of a polymer pyrolysis chemistry will allow predicting its relative tendency to form soot particles. In diffusion flames, the tendency to form soot among polymers type is in the following order: Aromatics > Alkynes > Alkenes > Alkanes. In other words, the more unsaturated the polymer structure is, the more it will be likely to form soot. The relative tendency of one polymer to form soot compared to another may primarily arise from a difference in the initial rate of formation of aromatic rings. This prior step controls the rate of incipient soot formation, which, in turn, determines the soot volume fraction [37].

2.3. Combustion of PMMA

PMMA ($\text{nC}_5\text{H}_8\text{O}_2$) is probably the polymer with the most widely studied thermal decomposition, and the favorite amongst fire scientists as a model fuel [6]. Chemical reactions of burning PMMA is well documented by Zeng et al. [38]. PMMA is an amorphous polymer that softens on heating to form a viscous liquid. Thermal stability of PMMA is highly related to its tacticity. In spite of decomposing with

the same pathway, syndiotactic PMMA has higher thermal stability than isotactic PMMA due to its lower chain mobility [39]: T_d (syndiotactic PMMA) = 360 – 390 °C whereas T_d (isotactic PMMA) = 241 – 304 °C [6]. However, the majority of industrially produced PMMA is atactic, with an intermediate thermal decomposition temperature around 320 °C [6]. As mentioned before, there are two approaches to synthesize PMMA: the radical polymerization and the anionic polymerization. The PMMA obtained by radical polymerization presents more flaws in the structure such head to head bonds. It also has unsaturated terminal C=C bonds. This has a destabilizing effect and, as a result, radically polymerized PMMA starts decomposing around 220 °C [40][41]. On the other hand, anionic polymerized PMMA has a more regular structure and is, as a result, more thermally stable. Its decomposition begins around 300 °C.

PMMA decomposes by end-chain scission mechanism. It follows a free radical mechanism, stabilized by the four substituents on the α -carbon atom. This allows the unpaired electron to reside on the α -carbon atom long enough for the double bond to reform, releasing methyl methacrylate monomer (MMA). The monomer yield has been quantified as 59-95% depending on the decomposition conditions [42]. In the absence of oxygen, more than 90% of the anaerobic pyrolysis product of PMMA is the methyl methacrylate monomer [38].

When thermally decomposing, PMMA bubbles, which is a consequence of the fact that the polymer is already molten when the thermal decomposition begins [6]. Volatile molecules accumulate within the molten decomposing polymer. Bubbles are then formed and migrate upwards, eventually erupting from the surface. This bubbling phenomenon causes physical swelling, reducing the thermal inertia of the material and, as a result, accelerating the rate of surface heating.

Regarding the gas phase, the main decomposition product of PMMA is monomer MMA which will further decompose to give smaller gaseous products that will undergo combustion. MMA will break down to give mainly carbon dioxide, water, methane, methanol, formaldehyde and acetylene [38].

2.4. Combustion of PVC

PVC ($\text{nC}_2\text{H}_3\text{Cl}$) is ranked third behind PE and PP in terms of worldwide polymer consumption due to its good chemical resistance and its use in many different applications (cables, pipes, furniture...). PVC is not widespread used as the pure polymer as it is rather brittle and difficult to process. The popularity of PVC lied in its unmatched ability to form a stable, dry, flexible and easily processed material when plasticized. However, it involves adding a significant amount of flammable plasticizer (often phthalates) to an otherwise low flammability polymer [6].

PVC is a polymer that undergoes a quite complex thermal decomposition which involves mechanism of 40 species in about 250 reactions [43]. More globally, PVC decomposes in a two-step mechanism.

Between 200 and 300°C, PVC undergoes a dehydrochlorination reaction to release hydrogen chloride by β -elimination to form a conjugated polyene [44] (Figure 5). The dehydrochlorination reaction is an autocatalytic reaction since it is catalyzed by acids such as the hydrogen chloride released from the reaction itself. Between 200 and 300°C, 80-95% of the chlorine content of rigid PVC is released as HCl [45]. As a result, PVC usually contains stabilizers that quench the dehydrochlorination reaction by reacting with hydrogen chloride. The presence of these stabilizers allows the PVC processing around 200°C (extrusion, molding...) without decomposition. During this first step of decomposition, benzene and some naphthalene and phenanthrene are also formed through Diels Alder reactions and successive dealkylation of polyene molecules [43].

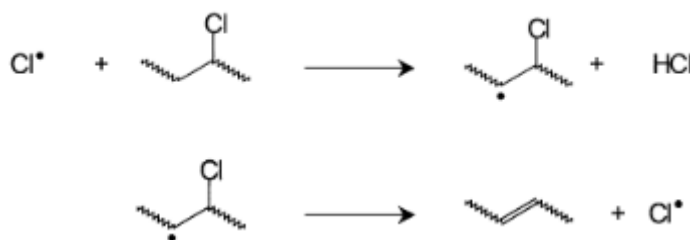


Figure 5: Dehydrochlorination reaction [43]

At higher temperatures, when the chlorine content has been quantitatively released from the melt, the polyene undergoes further rearrangements through cyclization, cross-linking and elimination reactions (Figure 6). These reactions produce a complex pattern of hydrocarbons with aromatic compounds predominating and char residue. The chain either cross-links, as double bonds open and attachments to neighboring chains occur (Figure 6a), eventually leading to char formation, or they break down and cyclize to form volatile aromatic hydrocarbons (Figure 6b).

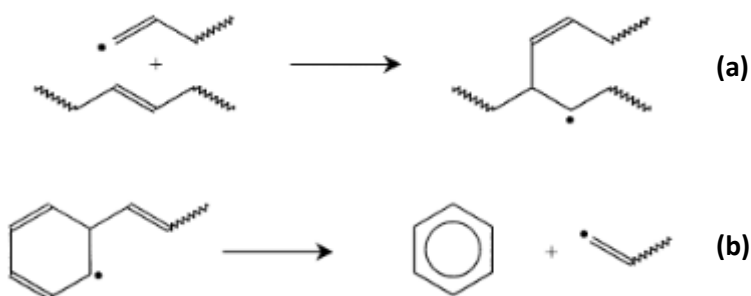
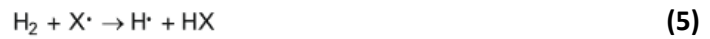


Figure 6: Polyene rearrangement reactions through a) cross-linking reaction; b) elimination reaction [43]

PVC is known as a self-flame retarded material as it generates hydrogen chloride when decomposing that will react with the hot radicals in the flame H^\bullet and HO^\bullet , acting as a quencher. This has the effect

to modify the reaction pathway. The general mechanistic pathway of flame quenching by hydrogen chloride is described as follows [46]. The equation (1) is the generation of reactive species X^\bullet (Cl^\bullet in the case of PVC). From X^\bullet is generated a halogenated hydrogen halide HX (HCl in the case of PVC) by the reaction on the polymer chain (2). Equation (3) and (4) describe the radicals inhibition by the halogenated hydrogen halide and equation (5) describes the regeneration of the reactive species X^\bullet .



3. Polymer combustion at macro-scale

The polymer combustion at a molecular-scale has been described in the previous section. Nevertheless, the knowledge of the molecular-scale phenomena is not sufficient to assess the outcome of a fire. Indeed, during a fire, the phenomena between the condensed phase and the gas phase are highly coupled and gradients due to the thermal thickness of materials are determinant in the way that they react. In the same time, molecular-scale combustion characterization is of great interest as input data for macro-scale fire modeling.

3.1. Combustion efficiency convective and radiative components

In fires, combustion is rarely complete. Thus, the chemical heat release rate is less than the heat release rate for complete combustion. The ratio of the chemical heat release rate to the heat release rate for complete combustion is defined as combustion efficiency (Equation 2).

Equation 2: Definition of combustion efficiency

$$\chi_{ch} = \frac{\dot{q}_{ch}}{\dot{q}_T} = \frac{\dot{m}\Delta H_{ch}}{\dot{m}\Delta H_T} = \frac{\Delta H_{ch}}{\Delta H_T}$$

Where χ_{ch} is the combustion efficiency, \dot{q}_T and ΔH_T are the heat release rate for complete combustion (kW.m^{-2}) and the heat of complete combustion (J.g^{-1}) respectively, and \dot{q}_{ch} and ΔH_{ch} are the chemical heat release rate (kW.m^{-2}) and the heat of combustion (J.g^{-1}) respectively. \dot{m} is the fuel mass loss rate (g.s^{-1}).

The convective and radiative components of the combustion efficiency are defined in a similar fashion (Equation 3 and Equation 4 respectively).

Equation 3: Definition of the convective component of the combustion efficiency

$$\chi_{conv} = \frac{\dot{q}_{conv}}{\dot{q}_T} = \frac{\dot{m}\Delta H_{conv}}{\dot{m}\Delta H_T} = \frac{\Delta H_{conv}}{\Delta H_T}$$

Where χ_{conv} is the convective component of the combustion efficiency χ_{ch} . \dot{q}_{conv} and ΔH_{conv} are the convective heat release rate (kW.m⁻²) and the convective heat of combustion (J.g⁻¹) respectively.

Equation 4: Definition of the radiative component of the combustion efficiency

$$\chi_{rad} = \frac{\dot{q}_{rad}}{\dot{q}_T} = \frac{\dot{m}\Delta H_{rad}}{\dot{m}\Delta H_T} = \frac{\Delta H_{rad}}{\Delta H_T}$$

Where χ_{rad} is the radiative component of the combustion efficiency χ_{ch} . \dot{q}_{rad} and ΔH_{rad} are the radiative heat release rate (kW.m⁻²) and the radiative heat of combustion (J.g⁻¹) respectively.

From Equation 2, Equation 3 and Equation 4, the definition of heat of combustion and combustion efficiency in terms of radiative and convective components can be deduced (Equation 5 and Equation 6).

Equation 5: Heat of combustion in terms of convective and radiative heats of combustion components

$$\Delta H_{ch} = \Delta H_{conv} + \Delta H_{rad}$$

Equation 6: Combustion efficiency in terms of convective and radiative combustion efficiencies

$$\chi_{ch} = \chi_{conv} + \chi_{rad}$$

The chemical, convective and radiative heat release rates, heats of combustion of combustion efficiencies depend on the chemical structures of the materials and fire ventilation. The distribution of the chemical heat into convective and radiative components changes with fire size. The larger the fire size, the larger the fraction of the chemical heat distributed into the radiative component. The chemical, convective, and radiative heats of combustion and the heat release parameter values for well-ventilated fires of PMMA and PVC measured in the FPA (Fire Propagation Apparatus) are listed in Table 4.

Table 4: Heat of combustion components for well-ventilated combustion of PMMA and PVC [47]

Material	ΔH_T (MJ.kg ⁻¹)	ΔH_{ch} (MJ.kg ⁻¹)	ΔH_{conv} (MJ.kg ⁻¹)	ΔH_{rad} (MJ.kg ⁻¹)
PMMA	25.2	24.2	16.6	7.6
PVC	16.4	5.7	3.1	2.6

3.2. Fire stages criteria

The stages of fire growth, in term of heat flux, temperature, oxygen content (to the fire and in the fire effluent), $[\text{CO}_2]/[\text{CO}]$ ratio, equivalence ratio ϕ and combustion efficiency χ_{ch} , have been classified in the standard ISO 19706 [48] (Table 5). Three main stages of fire are described from early to advanced stages. Non-flaming fires, corresponding to very early stages, i.e. before ignition or very advanced stages, i.e. after extinction, are firstly described. Then, well-ventilated flaming fires, covering early to mid-stages, are characterized. Finally, under-ventilated flaming fires, corresponding to mid to advanced stages, are detailed. While some real-life fires may be represented by a single fire stage, most will past through different stages. As they grow, all fires become oxygen depleted. It is of prior importance, in order to assess the fire toxicity at advanced stages to investigate fire behavior in low-ventilated room fires, i.e. stage 3a, and in post flash-over fires, i.e. stage 3b. (Table 5).

Table 5: ISO classification of fire stages, based on ISO 19706 [48]

Fire stage	Heat flux [kW.m ⁻²]	Max temperature [°C]		Oxygen (vol. %)		Equivalence ratio (ϕ)	[CO]/[CO ₂] (vol. /vol.)	Combustion efficiency (χ_{ch})
		Fuel	Smoke	In	Out			
Non-flaming								
1a. Self-sustained smoldering	n.a.	450 - 800	25 - 85	20	0 - 20	/	0.1 - 1	50 - 90
1b. Oxidative, external radiation	/	300 - 600	/	20	20	/	/	/
1c. Anaerobic external radiation	/	100 - 500	/	0	0	/	/	/
Well-ventilated flaming								
2. Well-ventilated flaming	0 - 60	350 - 650	50 - 500	≈ 20	0 - 20	< 1	< 0.05	> 95
Under-ventilated flaming								
3a. Low ventilated room fire	0 - 30	300 - 600	50 - 500	15 - 20	5 - 10	> 1	0.2 – 0.4	70 - 80
3b. Post flashover	50 - 150	350 - 650	> 600	< 15	< 5	> 1	0.1 – 0.4	70 - 90

3.3. Effects of vitiation and equivalence ratio on combustion

In the case of a real enclosure fire, two effects are coupled on fire properties: the vitiation and the under-ventilation. On one hand, a fire is under-ventilated when the air flow rate is less than the amount required for complete combustion (ventilation-controlled combustion, e.g. due to limited ventilation openings). The local equivalence ratio, defined as the fuel-to-air ratio normalized by stoichiometric fuel-to-air ratio, exceeds unity. On the other hand, a fire is vitiated when the oxygen concentration in the inlet gas flow can range from 21 vol. % down to 0 vol. %. It can typically result from the mixing of the fumes within the enclosure, or for particular ventilation conditions²³ where oxygen is gradually consumed and replaced by combustion products.

3.3.1. Effect of equivalence ratio on combustion products

The effect of ventilation on the combustion of polymers is characterized by the equivalence ratio (Equation 7):

Equation 7: Equivalence ratio

$$\phi = \frac{S\dot{m}_f}{\delta\dot{m}_a}$$

Where ϕ is the equivalence ratio, S is the stoichiometric mass air-to-fuel ratio²⁴, \dot{m}_f is the fuel rate ($\text{g}\cdot\text{s}^{-1}$), \dot{m}_a is the air mass flow rate ($\text{g}\cdot\text{s}^{-1}$) and δ is the fraction of entrained air into the flame.

The stoichiometric mass air-to-fuel ratio is calculated according to Equation 8.

Equation 8: Stoichiometric mass air-to-fuel ratio

$$S = \frac{4.76 \times (1 + \frac{b}{4} - \frac{c}{2}) \times M_a}{M}$$

Where M_a is the air molecular weight ($28.98 \text{ g}\cdot\text{mol}^{-1}$), M is the fuel molecular weight ($\text{g}\cdot\text{mol}^{-1}$) calculated for a mole of carbon, b and c are the number of hydrogen and oxygen moles in the fuel respectively.

If the amount of air equals the air requirement of the fuel, then the conditions are said to be stoichiometric and the equivalence ratio equals 1. If the equivalence ratio is higher, then the conditions are defined as the ventilation-controlled combustion, and if the air requirement is exceeded, then the conditions are well-ventilated. The following correlation (Equation 9) has been developed between the product yields and the equivalence ratio [49].

²³ E.g. when ventilation flow rate in the enclosure is lower than flow rate of oxygen consumed by the reactions.

²⁴ E.g. $S = 8.27$ in the case of PMMA and $S = 6.07$ in the case of PVC.

Equation 9: Correlation between the product yields and the equivalence ratio [49]

$$y_i = y_{i\infty} \left(1 + \frac{\alpha}{\exp(\beta\phi^{-\xi})} \right)$$

Where y_i is the product yield (g.g^{-1}), α , β and ξ are the correlation coefficients and ∞ represents infinite amount of air (well-ventilated conditions).

The experiments of Tewarson [49] [50] were performed in the Factory Mutual Research Corporation (FMRC) flammability apparatus. Sample surface was exposed to external heat fluxes in the range of 20 to 60 kW.m^{-2} to vary \dot{m}_f , which was measured by a load cell. Experiments were performed under co-flow conditions in normal air, with air mass flow rate in the range of 1.4 to 4.2 g.s^{-1}

The yields in well-ventilated conditions and correlation coefficients of CO (measured by IR analyzer) and smoke (measured by optical transmission) are listed in Table 6 for both PVC and PMMA. The yields of CO and smoke as a function of equivalence ratio are shown in Figure 7 for PVC and PMMA.

For PVC, the relationships indicate that carbon monoxide yield present a steep increase from 0.06 to 0.47 for $0.80 \leq \phi \leq 1.2$, and smoke yield presents a small increase from 0.17 to 0.23 in the same equivalence ratio range. For PMMA, carbon monoxide yield present also a steep increase from 0.01 to 0.40 for $0.80 \leq \phi \leq 4.0$ whereas smoke yield stays constant when the equivalence ratio increases. These trends suggest that CO and smoke are generated much more readily from PVC than from PMMA, possibly due to the formation of double bonds, as HCl is eliminated at temperatures as low as 100°C from the PVC structure, and formation of various compounds occurs with aromatic/unsaturated bonds whereas for PMMA, an aliphatic carbon-hydrogen-oxygen-atom-containing polymer the strong C-O bond in the structure remains intact as ventilation is reduced [51].

Table 6: Yields and correlation coefficients of CO and smoke for PVC and PMMA [49]

	CO				Smoke			
Material	y_{∞}	α	β	ξ	y_{∞}	α	β	ξ
PVC	0.063	6.5	0.42	8.0	0.172	0.38	0.42	8.0
PMMA	0.010	43.0	1.33	3.2	0.022	1.60	4.61	0.6

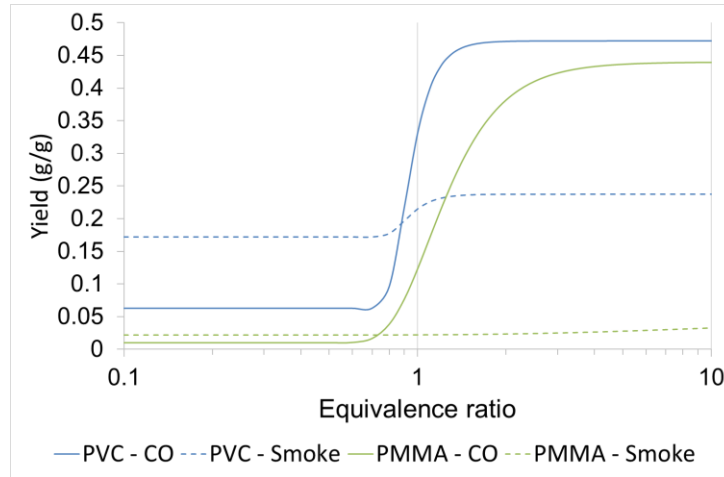


Figure 7: Yields of CO and smoke versus the equivalence ratio for the combustion of PVC and PMMA

3.3.2. Effect of vitiation on fuel mass loss rate

A few correlations have been established to express the mass loss rate (MLR) as a function of the oxygen concentration from experimental results in flaming regime. Tewarson and Pion [52] found a linear correlation between the MLR and the oxygen concentration, particularly for PMMA, PS and POM, between the extinction limit, highly dependent on the fuel²⁵, and 21 vol. % of O₂.

Another general correlation has been determined by Peatross and Beyler [53] to assess the effect of oxygen concentration on decomposition rates, from 14 vol. % (close to the extinction limit of the fire) to 21 vol. % (ambient air). The experimental data obtained from diesel [53], PMMA [54][55] and heptane [54] fires have been represented by a linear correlation. For a given fuel and fuel size, the mass loss rate per unit area is normalized at each oxygen concentration by the corresponding value in normal oxygen concentration, i.e. 21 vol. %:

Equation 10: Correlation determined by Peatross and Beyler to assess the effect of oxygen concentration on decomposition rates [53]

$$\frac{MLR}{MLR_{21}} = 0.1 \times O_2[\%] - 1.1$$

The mass loss rate is directly proportional to the oxygen concentration. Vitiation of air decreases the fuel decomposition rate and the reduced oxygen concentration (14 vol. %) results in decomposition rates that is one third of the value observed in air.

²⁵ PMMA: 16.0 vol. % O₂; PS: 19.5 vol. % O₂; POM: 10.4 vol. % O₂.

In addition, other experimental studies have been reported about the effect of oxygen concentration on decomposition rates, e.g. Santo and Tamanini [55], Mulholland et al. [56], Tewarson et al. [57], Christy et al. [5], Peatross and Beyler [53], Hietaniemi et al. [58], Melis and Audouin [1], Brohez et al. [59], Marquis et al. [60] and Alibert [61]. The results obtained for different materials, e.g. PMMA, heptane and PE, are shown in Figure 8. They are quite consistent with the linear correlation proposed by Peatross and Beyler [53]. The differences observed in the cone calorimeter (Mulholland et al. 1991 [56]) could be explained by the external radiative heat flux, from 15 to 40 kW.m⁻², applied during the entire test duration. Indeed, the external heat flux applied until ignition is generally stopped at the ignition in the other test benches.

The change of normalized mass loss rate is likely influenced by the variation of the radiative heat flux from the flame as well as by the convective heat flux. More precisely, a lower flame temperature and combustion efficiency in the case of oxygen depletion reduce the heat flux due to the flame and received at the material surface (i.e. flame feedback). The radiative heat flux also depends on flame emissivity which is influenced by soot volume fraction, soot absorption coefficient and partial pressure of the gas compounds. The resulting heat transfer between the flame and the material could explain the MLR decrease in agreement with the correlation of Peatross and Beyler [53]. However, advanced theoretical considerations for liquid and solid materials are still necessary to demonstrate the correlation between the normalized mass loss rate per unit area and the oxygen concentration.

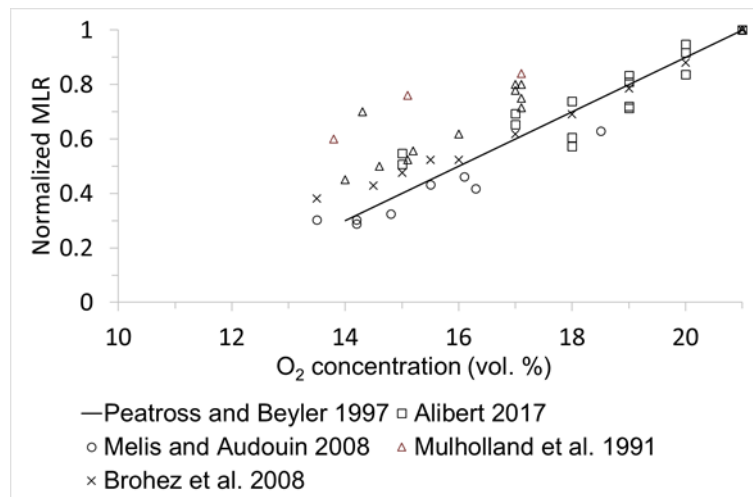


Figure 8 : Effect of oxygen concentration on normalized mass loss rate per unit area for different materials

3.3.3. *Oxygen depleted fire studies: a state of the art*

A number of papers on the effect of oxygen depletion in fire are reported in the literature (Table 7). The varying parameter is specified and whether the tested regime is vitiated or under-ventilated is made explicit.

It stands out that when vitiation increases, the mass loss rate [52][55][56][5], heat release rate and total heat release [56][5] decreases. The carbon monoxide yield [56][59] and the soot yield [59] increase. The total flame radiation and the emittance decreases whereas the flame temperature stays constant [55]. Time to ignition stays constant when vitiation increases [5].

When the equivalence ratio increases (in under-ventilation conditions), the mass loss rate decreases for some authors [53][59][61] and stays constant for others [5][60], the heat release rate decreases [57][5][58], the convective fraction efficiency decreases whereas the radiative fraction efficiency has a gaussian shape [57]. The soot yield increases for most authors [57][61] but stays constant in [58]. The carbon monoxide yield increases and the carbon dioxide yield decreases [57][58][62][61] and gas temperature decreases [61]. Low molecular weight hydrocarbons yield increases [57][62].

Hietaniemi et al. [58] studied the differences between chlorine-containing substances and substances with no chlorine in under-ventilated fires. It turned out that when the equivalence ratio increases, substances with no chlorine have a lower burning efficiency, yield more smoke, carbon monoxide, hydrogen cyanide, nitrogen dioxide and nitrogen oxide. On the contrary, chlorine-containing substances show a constant burning efficiency and a constant gases yield when the equivalence ratio increases. It may be due to the reaction of chlorine in the gas phase that affects the combustion efficiency even in well-ventilated conditions.

This state of the art reveals a lack of data on PVC materials confined fires studies at a bench-scale. For this reason, this work is focused on the characterization of fire parameters and smoke effluents throughout PVC-based materials thermal decomposition with a controlled-atmosphere cone calorimeter of which details are described in the next chapter. Data in Table 5, p. 33 is helpful to choose the heat flux used in this study. As mid to advanced stages are of interest to characterize, the radiative heat flux is set at 50 kW.m⁻².

Chapter I: Bibliography

Table 7: State of the art of oxygen depleted fire studies

Reference	Materials	Apparatus and Conditions	Varying parameter	Observations
Tewarson and Pion (1976) [52]	PMMA, POM, PS, Plywood	- FPA - Heat source: external heat flux (tungsten lamps)	Vitiation: Effect of [O ₂] at fixed inlet flow rate. [O ₂] measured in the inlet flow.	- MLR decreases when [O ₂] decreases in flaming regime and is constant in non-flaming regime
Santo and Tamanini (1981) [55]	PMMA	- Water-cooled cylindrical enclosure. - 30 cm diameter pool fire. - Heat source: flame.	<u>Vitiation</u> : Effect of [O ₂] at fixed inlet flow rate. [O ₂] measured in the inlet flow.	- MLR, flame emittance and total radiation decrease significantly when [O ₂] decreases. - Flame temperature stays constant when [O ₂] decreases.
Mulholland et al. (1991) [56]	6 mm thick black PMMA, Methane, Propane, ABS, PE, Douglas fir	- NIST CACC ²⁶ . - Heat source: external heat flux (conical resistance).	<u>Vitiation</u> : Effect of [O ₂] at fixed inlet flow rate. [O ₂] measured in the inlet flow.	- CO yield increase when [O ₂] decreases - THR ²⁷ , pHRR ²⁸ , MLR (thus the equivalence ratio) decrease when [O ₂] decreases

²⁶ NIST CACC : National Institute of Standard and Technology Controlled Atmosphere Cone Calorimeter [75][72]

²⁷ Total Heat Release

²⁸ Peak of Heat Release Rate

				- Soot yield stays constant when $[O_2]$ decreases
Tewarson et al. (1995) [57]	PE, PP, PS, PMMA, pine wood, Nylon	- FPA ²⁹ . - Heat source: external heat flux (tungsten lamps).	<u>Under-ventilation</u> : Effect of fuel mass loss rate (by varying heat flux from 20 to 60 kW.m ⁻²) and thus equivalence ratio from 0.2 to 4. The inlet air flow rate is kept constant. $[O_2]$ measured in the inlet flow.	- Convective fraction efficiency, chemical efficiency, CO ₂ generation efficiency, O ₂ consumption efficiency decrease when equivalence ratio increases - CO generation efficiency, soot generation efficiency, low molecular weight gaseous hydrocarbon generation efficiency increase when equivalence ratio increases - Radiative fraction efficiency has a Gaussian shape with the variation of equivalence ratio
Christy et al. (1995) [5]	10 mm thick black PMMA	- NIST CACC.	<u>Under-ventilation</u> : Effect of inlet air flow rate.	- pMLR and $[CO]/[CO_2]$ are constant when inlet flow rate decreases - pHRR and average HRR decrease when inlet flow rate decreases

²⁹ FPA : Fire Propagation Apparatus [71]

Chapter I: Bibliography

		- Heat source: external heat flux (conical resistance).	<u>Vitiation</u> : Effect of [O ₂] at fixed inlet flow rate. [O ₂] measured in the inlet flow.	- pMLR, pHRR, average HRR decrease when [O ₂] decreases - TTI ³⁰ stays constant when [O ₂] decreases
Peatross and Beyler (1997) [53]	Diesel fuel, wood cribs, PU slabs	- 34 m ³ compartment. - Heat source: flame.	<u>Under-ventilation</u> : Effect on inlet flow rate. [O ₂] measured at the flame base.	- pMLR decreases when [O ₂] decreases.
Hietaniemi et al. (1999) [58]	Substances with no chlorine: DMMP, TMTM, Nylon, PP	- FTT CACC ³¹ . - Heat source: external heat flux (conical resistance).	<u>Under-ventilation</u> : Effect of inlet flow rate (thus equivalence ratio varying from 0.25 to 1.8).	- pHRR and burning efficiency decrease when ϕ increases - Smoke production stays constant when ϕ increases - CO, HCN, NO ₂ and N ₂ O yields increase when ϕ increases - CO ₂ , SO ₂ and NO yields decrease when ϕ increases
	Chlorine containing substances: Lindane, DCNB, CNBA, CB			- pHRR decreases significantly when ϕ increases - Burning efficiency and smoke production stay constant when ϕ increases

³⁰ Time to ignition

³¹ FTT CACC : Fire Testing Technology Controlled Atmosphere Cone Calorimeter

Chapter I: Bibliography

				- All gases yield stay constant when ϕ increases
Brohez et al. (2008) [59]	Pyridine	<ul style="list-style-type: none"> - FPA. - Heat source: external heat flux (tungsten lamps) of 15 kW.m^{-2} removed after ignition. 	<p><u>Under-ventilation</u>: Increasing diluent concentration while keeping $[\text{O}_2]$ fixed. The inlet flow rate increases. Equivalence ratio varying from 0.25 to 1.</p> <p><u>Vitiation</u>: Effect of inlet flow rate at fixed $[\text{O}_2]$. Equivalence ratio fixed at 1.1.</p>	<ul style="list-style-type: none"> - MLR decreases when ϕ increases - $[\text{CO}]$ increases when $[\text{O}_2]$ decreases - Soot increases when $[\text{O}_2]$ increases
Fourneau et al. (2013) [62]	n-heptane	<ul style="list-style-type: none"> - FTT CACC. - Heat source: external heat flux (conical resistance). 	<u>Under-ventilation</u> : Effect of inlet flow rate at fixed $[\text{O}_2]$.	<ul style="list-style-type: none"> - $[\text{CO}_2]$ decreases when inlet flow rate decreases - $[\text{CO}]$, [total gaseous HC] increase when inlet flow rate decreases
Marquis et al. (2014) [63]	14 mm thick black PMMA	<ul style="list-style-type: none"> - FTT CACC. - Heat source: external heat flux (conical resistance) of 50 kW.m^{-2}. 	<p><u>Under-ventilation</u>: Effect of inlet air flow rate at fixed oxygen concentration.</p> <p><u>Vitiation</u>: Effect of $[\text{O}_2]$ at fixed inlet flow rate. $[\text{O}_2]$ measured in the inlet flow.</p>	<ul style="list-style-type: none"> - $[\text{CO}]/[\text{CO}_2]$ increases and MLR stays constant when inlet air flow rate decreases - MLR and HRR decrease when $[\text{O}_2]$ decreases.

Chapter I: Bibliography

Alibert (2017) [61]	PMMA	CADUCEE (20 m ³ combustion chamber from IRSN) - Heat source: flame.	<u>Under-ventilation</u> : Effect of inlet air flow rate at fixed oxygen concentration.	<ul style="list-style-type: none"> - Radiative and convective fractions of the total heat flux and soot yield are nearly constant when inlet flow rate decreases. - MLR, heat flux, gas temperature, CO₂ yield decrease when inlet flow rate decreases - CO yield increases when inlet flow rate decreases
	heptane			<ul style="list-style-type: none"> - Soot yield increases when inlet flow rate decreases. - Flame feedback decreases when inlet flow rate decreases

4. Conclusion

The principles of polymer combustion at a molecular scale have been reviewed, with an emphasis on the thermal decomposition and on the soot formation mechanisms. The specific case of PMMA and PVC reaction to fire at a molecular-scale have been detailed, as PMMA is used in this PhD work as a reference material and PVC is the polymer present in the electrical cable sheath representative material. PMMA exhibits a one-step thermal decomposition with an onset temperature of about 300°C, yielding no residue and forming a majority of its monomer, i.e. methyl methacrylate, as gaseous compound. PVC is a more complex fuel as it thermally decomposes in two steps with an onset temperature of approximately 200°C, yielding a char residue and forming a large panel of gaseous compounds, including hydrogen chloride, benzene, and heavy polycyclic aromatic hydrocarbons.

Theory of oxygen depleted fires have been described, differentiating the vitiation effect and the under-ventilation effect. Particularly, the effect of the equivalence ratio on the combustion products and the effect of vitiation on the fuel mass loss rate were detailed. Increasing equivalence ratio will increase the formation of unburnt gaseous species and soot particles and increasing vitiation will decrease linearly the fuel mass loss rate.

A state of the art of the effect of oxygen depletion on the fire behavior at a macro-scale showed that, although a lot of results are in accordance, some results are in confrontation since fire behavior is highly dependent on several parameters, e.g. ventilation rate or enclosure materials interaction, and thus on the set-up used for testing. Also, there is a lack of experimental data on the effect of oxygen depletion on the fire behavior of PVC.

For these reasons, the scope of this PhD was led to the study of PVC-based materials thermal decomposition at a bench-scale in confined configurations under a radiative heat flux of 50 kW.m⁻² to reproduce mid to advanced fire stages.

For this purpose, a new bench-scale apparatus – a revisited controlled atmosphere cone calorimeter – allowing to provide trustable data in conceived and presented in the next chapter. PMMA is formerly tested in order to position the new controlled atmosphere cone calorimeter among the ones commonly used in the literature.

Chapter II: Controlled-atmosphere cone calorimeter set-up conception

1. Bench-scale apparatus for fire testing	45
1.1. <i>Fire testing</i>	45
1.2. <i>Different types of flow-through bench-scale apparatuses for under ventilated conditions</i>	47
1.2.1. The Fire Propagation Apparatus	48
1.2.2. The controlled-atmosphere cone calorimeter	49
1.3. <i>Conclusion on the comparison of the flow-through bench-scale apparatuses for under-ventilated conditions</i>	53
2. Development of a new controlled-atmosphere cone calorimeter	54
2.1. <i>Context</i>	54
2.1.1. Temperature rise method for the determination of HRR in under-ventilated fires	54
2.1.2. Oxygen consumption method for the determination of HRR in under-ventilated fire	56
2.1.3. Conclusion	62
2.2. <i>Design of the apparatus</i>	63
2.2.1. Specifications	63
2.2.2. Overview of the apparatus	63
2.2.3. Airtight enclosure	64
2.2.4. The cone calorimeter elements	65
2.2.5. Supply and distribution system for the gases	67
2.3. <i>Controllers and sensors</i>	69
2.4. <i>Equipment for smoke analysis</i>	71
2.4.1. Fourier Transform InfraRed spectrometer	71
2.4.2. Electrical Low-Pressure Impactor	73
2.4.3. Dilution of smoke prior to analysis	76
3. Conclusion	77

1. Bench-scale apparatus for fire testing

1.1. [Fire testing](#)

Investigations in fire science are mainly aimed at assessing fire hazard which is both material composition and fire condition dependent [64]. For that purpose, real-life scenarios have to be reproduced in laboratories to gather data on parameters such as heat release and smoke toxicity throughout a fire. Apparatuses commonly used for fire testing can be divided into three scales: micro-scale (or molecular-scale), bench-scale and full-scale (or macro-scale).

Micro-scale testing involves very small amount of sample reduced in fine powder: from hundreds of micrograms to a few milligrams. This leads to test thermally thin materials with restricted heat transfer inside the sample, which is not representative of a real industrial case. Nevertheless, these tests controlled by chemical kinetics have the advantage of being less expensive to perform while providing a good control of experimental parameters (temperature, atmosphere composition...). Among all the micro-scale tests dedicated to fire science, we can list thermogravimetric analysis (TGA), differential scanning calorimetry (DSC) or pyrolysis combustion flow calorimetry (PCFC) [65]. TGA is used to study thermal stability of materials under a controlled heating rate by measuring its mass at each temperature. DSC is used to study physical changes of the material such as glass transition, melting or crystallization by measuring its enthalpy at each temperature and its heat capacity as a function of temperature. PCFC is used to measure the enthalpy of combustion of gaseous compounds produced from a material heated at a constant temperature rate.

Bench-scale testing involves large samples in the range of grams to kilograms submitted to a constant and calibrated radiative heating source which leads the sample to behave representatively of a real fire at a chosen stage. Indeed, the sample may be raw material such as electrical cable trays and physical processes such as heat and mass transfer inside the material is not neglected. During the test, the condensed phase and the gas phase are not separated so the self-maintained phenomenon of combustion is represented. In this way, bench-scale testing is suitable to study flame spread, heat release rate, time of flaming... Some bench-scale apparatuses of interest are described in more detail in this chapter, section 1.2 p. 47.

Full-scale testing refers to industrial size installations that reproduce the real case in its complexity. They are necessary to perform to gather relevant data when considering a fire scenario in a given configuration. Nevertheless, these tests are highly instrumented and require a lot of space and workers making them more expensive and time consuming. The standard of current full-scale tests was first drafted in 1982 [66]. For instance, in France, the DIVA installation at the IRSN³² is used to study electrical cable fire spread in industrial premises [67]. At the INERIS³³, a gallery is used to study tunnel-type confined configurations [68] and a hall is used to characterize open combustion of various materials.

Bench-scale testing seems to be a compromise because it is quite representative of a real fire scenario at the material scale while allowing a good frequency of experiments at a reasonable cost. That is why

³² Dispositif Incendie Ventilation et Aérocontamination, Institut de Radioprotection et de Sécurité Nucléaire

³³ Institut national de l'environnement industriel et des risques

it is used by most laboratories to investigate flammability parameters and/or smoke composition. Bench-scale fire testing encompasses four general methods [64]:

- **Open tests** that replicate well-ventilated fire conditions;
- **Closed chamber tests** that replicate under-ventilated fire conditions without any control of the oxygen concentration because it encloses the sample in a fixed volume of air;
- **Non-steady flow-through tests** that replicate under-ventilated fire conditions by controlling the oxygen concentration in the flow-through gas mixture and its volume flow rate. The equivalence ratio³⁴ can't be controlled easily in a dynamic way;
- **Steady-state tube furnace tests** that replicate under-ventilated conditions and with which the equivalence ratio can be modulated. These tests have shown good agreement with large-scale product yields.

Steady-state tube furnace tests seem appropriate to study under-ventilated fires because they enable the production of data for specific fire stages by controlling the equivalence ratio. The sample is fed into a furnace at a fixed rate, under a fixed air supply, inside a narrow horizontal tube to ensure adequate mixing of fuel and oxidant. The heat flux is continuously increased to sustain a combustion even at low oxygen concentrations. However, achieving a continuous feeding for solid samples is difficult at lab-scale and the varying parameters of these tests conditions make the comprehension of the phenomena involved in the polymer decomposition and the production of effluent at various oxygen content complicated. Furthermore, the natural dynamic of the combustion of the solid is lost as the combustion is forced.

For these reasons, the preferred configuration for the sake of this study happens to be the non-steady flow-through test. In the following section, three different types of flow-through bench-scale apparatuses for the study of under-ventilated fire are described and compared.

1.2. [Different types of flow-through bench-scale apparatuses for under ventilated conditions](#)

Calorimeters with open configurations are used to study the burning behavior of materials at an atmospheric oxygen content (21 vol.%). The combustion is then considered well-ventilated. Nevertheless, at advanced stages of a confined fire, the combustion becomes under-ventilated with the ambient oxygen content decreasing. It may affect some parameters such as heat release rate, mass loss rate or smoke production [57]. In order to be able to assess the toxic potency of a real fire smoke,

³⁴ Defined in chapter I, p. 30

under-ventilated conditions must be taken into account. That is why various forms of controlled-atmosphere calorimeter have been set up in laboratories.

In this section, the main bench-scale calorimeters used for under-ventilated studies are described synthetically. They are described in a much more detailed way in the chapter “calorimetry” of the handbook of fire protection engineering [69].

1.2.1. The Fire Propagation Apparatus

The Fire Propagation Apparatus (FPA) was designed in the mid-1970s under the direction of A. Tewarson for FMRC. It was standardized as ISO 12136 [70] or as ASTM E2058 [71]. This apparatus is also known as the Tewarson apparatus as it helped him to determine fire hazard indices and material properties in an extensive way [51]. He investigated the effect of environmental conditions such as oxygen concentration on the burning behavior. This is also the apparatus used at the INERIS from the early 2000s.

The apparatus is schematized in Figure 9. Originally, only convective HRR was measured on the basis of enthalpy rise of the exhaust gases with the measurement of the temperature. The sample is located inside a segmented quartz tube of 0.66-m length and 0.17-m diameter. A mixture of oxygen and nitrogen is supplied at the bottom of the tube. A stainless-steel exhaust duct is located above the tube and dilution air is entrained in the area between the tube and the exhaust system. The total flow of gases through the exhaust duct is determined by measuring pressure drop across a precalibrated orifice. A horizontal sample of $0.1 \times 0.1 \text{ m}^2$ is set under four tungsten lamps located coaxially outside the quartz tube. The generated incident heat flux is up to 110 kW.m^{-2} . The ignition is piloted with an ethylene burner. The total gas flow rate supplied to the bottom of the quartz tube is 3.3 L.s^{-1} and oxygen content can be tuned from 0 to 60 vol.%. The apparatus includes instrumentation to measure sample mass loss.

A drawback for this device is the mixing of exhaust gases with ambient air before analysis. Indeed, the exhaust gases may continue to burn as it emerges from the chamber giving ultimately well-ventilated flaming [64].

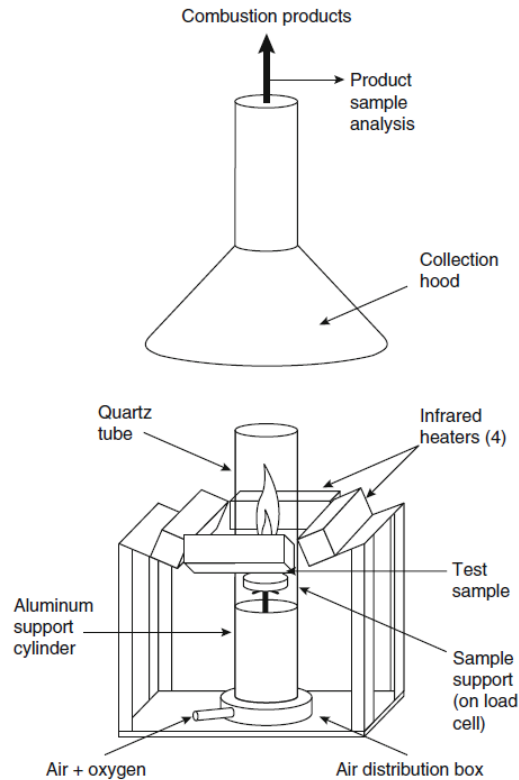


Figure 9: Fire Propagation Apparatus [69]

1.2.2. The controlled-atmosphere cone calorimeter

The cone calorimeter, in its open version, was developed in the early 1980s at the National Bureau of Standards by V. Babrauskas. It is named after the shape of its radiant heater, which is as a truncated cone. It is nowadays the most used bench-scale calorimeter. It is standardized as ASTM E1354 [72] and ISO 5660 [73].

The set-up is schematized in Figure 10. Heat release rate is calculated after measuring oxygen consumption. The standard configuration is open, with free access of air to the combustion zone. The gas flow rate in the exhaust duct is calculated from the pressure drop across and temperature at a precalibrated orifice plate in the duct. Combustion products and dilution air are extracted through the hood and exhaust duct by a high-temperature fan. The initial flow rate can be adjusted between 10 and 32 L.s⁻¹. The heater is a 5 kW electrical heating coil. The 0.1×0.1 m² sample is located horizontally, parallel to the coil, 25 mm underneath the coil's bottom plate. The maximum radiant heat flux is 100 kW.m⁻². The ignition is piloted by an electrical spark over the center of the sample. The sample is set on a load cell in order to record mass loss during the test.

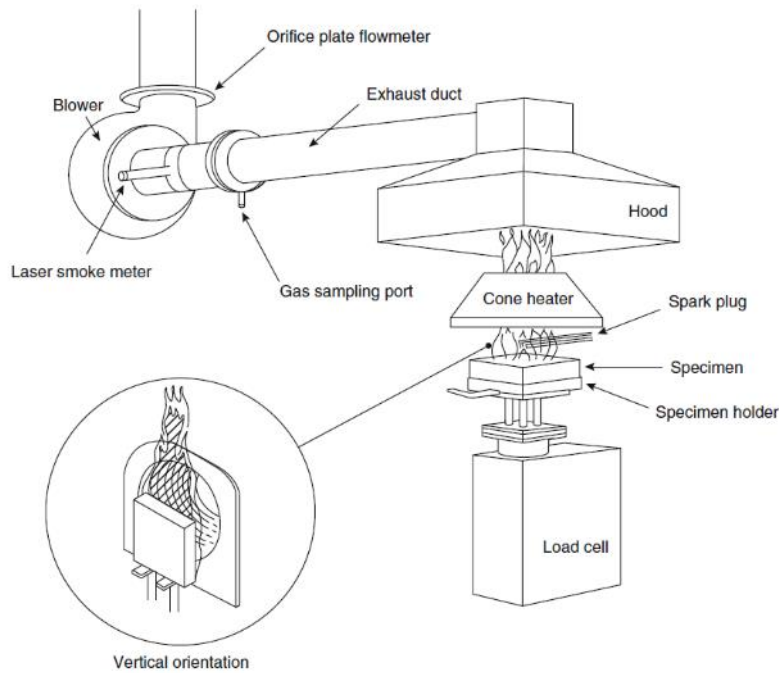


Figure 10: Cone calorimeter [69]

1.2.2.1. The controlled-atmosphere cone calorimeter from Fire Testing Technology

The standard version of the opened cone calorimeter is described in Figure 10 above. With this apparatus as it is, only a narrow range of fire stages can be represented.

The simplest transformation of the opened cone calorimeter into a controlled-atmosphere cone calorimeter is the addition of an airtight box around the sample fitted with a gas injection system. This apparatus is schematized in Figure 11 and it was developed by Fire Testing Technology (FTT). The airtight box is $0.4 \times 0.4 \times 0.4 \text{ m}^3$ and made of stainless steel. The air inflow stream is distributed into the enclosure by two inlet pipes. Above each inlet pipe is a baffle plate intended to dissipate vertical momentum.

The main drawback of the set-up is the mixing between the combustion gases and the ambient air right above the upper part of the truncated cone. This may lead to a partial oxidation of the exhaust gases before the sampling points inside the exhaust duct, especially when the oxygen content in the combustion chamber inlet is low.

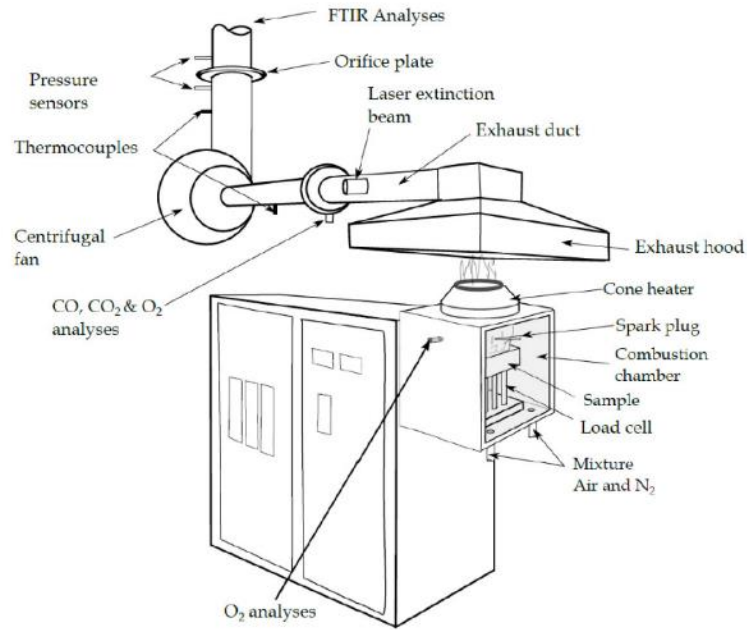


Figure 11: Controlled-atmosphere cone calorimeter developed by FTT without chimney [74]

In order to offset this phenomena, another version of controlled-atmosphere cone calorimeter has been designed by FTT. A 0.6 m high and 0.12 m large metallic exhaust duct is mounted on the top of the cone heater, as shown in Figure 12. This chimney prevents flames to mix with the ambient air. However, when the tested material burns with high intensity, the flames may be drawn near the upper part of the chimney and sometimes go beyond the chimney. This leads to a possible post-oxidation of the gases before their analysis in the exhaust duct. In the case of PMMA plaques burning under 50 kW.m^{-2} , the $[\text{CO}]/[\text{CO}_2]$ [vol.%/vol.%] ratio - representative parameter of the completeness of the combustion - is independent of the inlet flow rate from the threshold of 2.7 L.s^{-1} under which $[\text{CO}]/[\text{CO}_2]$ [vol.%/vol.%] ratio increases when the inlet flow rate decreases [63].

The limitations of the use of the controlled-atmosphere cone calorimeter (CACC) developed by FTT are:

- The material used for the enclosure and the proximity of the wall to the flame may induce a local heating due to the flame radiation reflection;
- The gas in the box may not be homogeneous as the air flow comes through only two inlet pipes;
- The mixing between the combustion gases with the ambient air of the laboratory before the sampling points that may lead to a post-oxidation before the analysis.

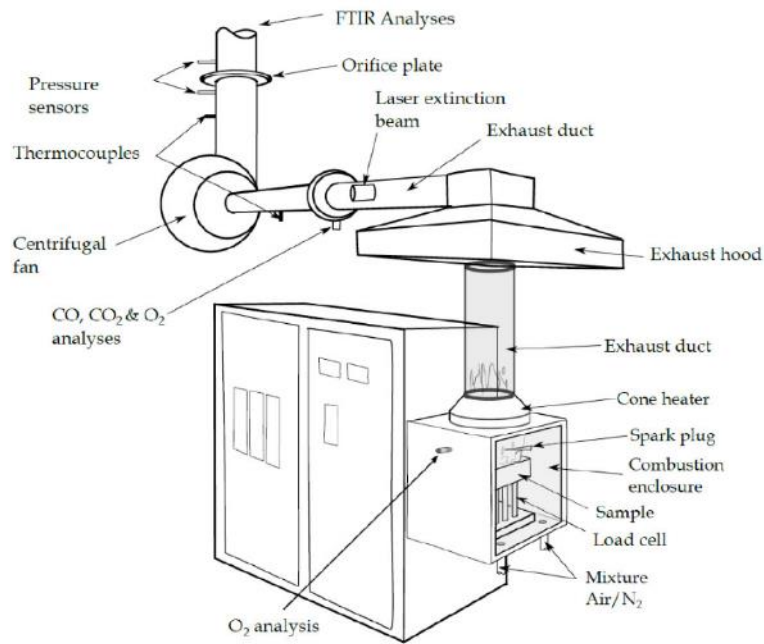


Figure 12: Controlled-atmosphere cone calorimeter developed by FTT with chimney [74]

1.2.2.2. The controlled-atmosphere cone calorimeter from the National Institute of Standard and Technology

The National Institute of Standard and Technology (NIST) developed a CACC in 1992 [75] that is shown in Figure 13. The sample area is enclosed by Pyrex chamber of dimension $0.4(h) \times 0.3(w) \times 0.3(d) \text{ m}^3$ [64]. This glass material has been chosen in order to mitigate heat accumulation while providing an optical access to the sample. The mixed air inflow stream is distributed into four inlet pipes going into the bottom of the enclosure with a baffle plate above to dissipate vertical momentum. Further velocity equilibration is done by passing the streams through a glass bead bed. The flow rate inside the apparatus is roughly 10 L.s^{-1} . It has been determined by the requirement that the exhaust products must flow through and out the enclosure rather than be collected in the combustion chamber and vitiate the inflow mixture.

The main drawbacks of this apparatus are:

- The fact that it is closed until the exhaust orifice plate which induces a possibility of overpressure inside the combustion chamber. Though this safety issue is minimized by the addition of a back door that functions as a blow-out panel, it remains a concern;
- At reduced oxygen concentrations, a lot of unburnt gases are produced. They may condensate in the exhaust duct at cooler points. It induces a laborious work to maintain the apparatus clean between the experiments.

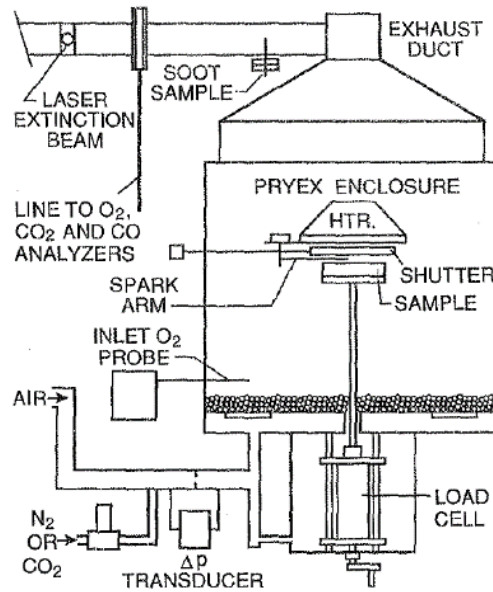


Figure 13: Controlled-atmosphere cone calorimeter developed at the NIST with a direct connection [56]

1.3. Conclusion on the comparison of the flow-through bench-scale apparatuses for under-ventilated conditions

Fire assessment data is highly dependent on the material burning, the fire conditions (temperature, pressure, oxygen available) and the fire environment (enclosure, geometry and ventilation) [64]. It is an important fact to keep in mind when comparing results from different apparatuses. Unfortunately, standardization of the under-ventilated cone calorimeter has not been brought to completion.

However, some important parameters for the three controlled-atmosphere bench-scale apparatuses are compared in Table 8. The three apparatuses give similar operational conditions. It has been demonstrated that the FPA and the cone calorimeter provides similar results when burning PMMA in case in which the heat source of FPA is replaced with that of the cone calorimeter [76].

In order to overcome the drawbacks of these calorimeters and to characterize other materials, a new controlled-atmosphere bench apparatus, inspired from both the FTT CACC and the NIST CACC, has been developed. The development of this bench is described subsequently.

Table 8: Comparison of parameters of importance for three different controlled-atmosphere bench-scale apparatuses

Design and test conditions	FPA	FTT CACC	NIST CACC
Inlet gas flow	Co-flow/natural [69]	Co-flow [69]	Co-flow
Oxygen concentration (vol.%)	0-40 [69]	0-21	0-21
Gas velocity (m.s ⁻¹) at 20°C and 1 atm	0-0.146 [69]	0.016 ²	0.11 ²
External heat flux (kW.m ⁻²)	0-110 [69]	0-100	0-100
Sample dimension (m ²)	0.1x0.1	0.1x0.1	0.1x0.1

²Calculated value by converting L.s⁻¹ into m.s⁻¹ given the gas dispersion area.

2. Development of a new controlled-atmosphere cone calorimeter

2.1. Context

In the scope of a previous PhD work at EDF R&D, a bench-scale test was set up to evaluate the flammability parameters as well as the effluents of a well-ventilated fire: a variation of the cone calorimeter, the Mass Loss Cone (MLC) calorimeter, was coupled to a Fourier Transform InfraRed spectrometer (FTIR) to measure gases concentrations and to an Electrical Low Pressure Impactor (ELPI) granulometer to measure the soot particles concentration in smoke [4].

The MLC standardized by the norm ISO 13927 [77], is a variation of the cone calorimeter that uses a thermopile at the top of the chimney to measure the HRR instead of the oxygen consumption method. A discussion regarding the method to be used to evaluate HRR is proposed in the next sections.

2.1.1. Temperature rise method for the determination of HRR in under-ventilated fires

By measuring the smoke temperature, the thermopile does not measure the total heat released from the flame. Indeed, only a fraction of the heat of combustion contributes to the temperature rise of the gases. This fraction is referred to as the convective fraction of the heat release rate. The remaining fraction of the heat of combustion is mainly lost by thermal radiation to the chimney walls.

The equation (Equation 11) of heat release rate measured by the temperature rise method is developed in [69]:

Equation 11: Measurement of HRR by the temperature rise method

$$\dot{q} - \dot{q}_{f,l} \approx \dot{m}_e C_p (T_e - T_a)$$

With:

- \dot{q} the total heat release rate (W);
- $\dot{q}_{f,l}$ the heat release rate lost from the flame to the apparatus by radiation (W);

- \dot{m}_e the mass flow rate of combustion products (kg.s^{-1});
- C_p the average specific heat capacity of combustion products ($\text{J.kg}^{-1}.\text{K}^{-1}$);
- T_e the temperature of the combustion products measured at the top of the chimney (K);
- T_a the temperature of the incoming air (K).

The heat loss by radiation, $\dot{q}_{f,l}$, may not be negligible. This part can be up to 25% in the case of a PMMA flame [78]. Therefore, it is necessary to measure this term in order to not underestimate the heat release rate. Some calorimeters have water-cooled walls that trap most of the losses. These losses can be estimated by measuring the water temperature rise. Another method consists in installing thermocouples against the chimney walls [78][79].

By other means, a gas burner calibration can be performed to determine $\dot{q}_{f,l}$ in the assumption that the heat loss by radiation is fuel independent. The relation between the fraction of total heat release rate lost by radiation (χ_r) and the heat loss by radiation ($\dot{q}_{f,l}$) is described by Equation 12.

Equation 12: Definition of the loss fraction by radiation

$$\dot{q}_{f,l} \equiv \chi_r \dot{q}$$

Combining Equation 11 and Equation 12 yields to Equation 13.

Equation 13: HRR equation with the temperature rise method considering the heat loss fraction

$$\dot{q} \approx \frac{\dot{m}_e C_p}{1 - \chi_r} (T_e - T_a) \equiv k(T_e - T_a)$$

k is the calibration constant (W.K^{-1}). It is determined from a gas burner calibration with known heat of combustion (\dot{q}). In the case of the MLC, the calibration curve is obtained by feeding the burner with different methane flow rates. Methane has a low heating value (LHV) of 50.0 MJ.kg^{-1} .

This method's first weakness is the assumption that the radiative loss fraction is not dependent on the fuel, which is not true when studying polymeric materials. Indeed, due to their complex chemical structure and formulations, these materials produce a wide range of different flames, more or less radiative, when burning.

Secondly, although this method roughly meets requirements for well-ventilated tests, as soon as the oxygen in the atmosphere is depleted, it becomes less accurate. Indeed, when the oxygen concentration is reduced, the flame temperature decreases and more unburnt species, including soot particles, are produced. Flame radiation is mainly produced by soot particles incandescence, which is dependent on the flame temperature. Highly sooting flames radiate more than low sooting flames and emission gets more important as flame temperature increases. This explains why calibration made

with well-ventilated flames from methane burner can no longer be applied to determine HRR from the temperature measured with the thermopile.

2.1.2. Oxygen consumption method for the determination of HRR in under-ventilated fire

2.1.2.1. Huggett's principle

The concept of measuring heat by oxygen consumption was first proposed by Thornton in 1917 [80]. As part of his work on the ASTM E 84 tunnel test, Parker [81] explored the possibility of using a measurement of the oxygen depletion in fire exhaust gases as an indicator of the amount of heat released by the sample. Parker found that, although the heat released per unit mass of material consumed varied greatly, the amount of oxygen consumed was fairly constant (within 15% of the value for methane, 16.4 MJ.m⁻³ of oxygen consumed).

Later in the decade, Huggett [82] performed a detailed analysis of the critical assumption saying that the oxygen consumption is constantly proportional to the heat release. Instead of expressing results on a unit volume basis, as Parker did, Huggett expressed results in the more convenient unit mass of oxygen consumed. Huggett explained that burning common fuels in a fire would involve breaking similar H-H, H-C, C-C and C-O chemical bounds: the heat generated per unit mass of oxygen consumed appears to be a constant E for complete combustion, roughly equal to 13.1 MJ.kg⁻¹ of oxygen consumed with ±5% accuracy. The heat release rate is then expressed as follow (Equation 14):

Equation 14: Huggett's equation

$$\dot{q} = 10^3 E (\dot{m}_{O_2}^0 - \dot{m}_{O_2})$$

Where:

- \dot{q} the heat release rate (kW);
- E the Huggett constant (MJ.kg⁻¹ of oxygen consumed);
- $\dot{m}_{O_2}^0$ the mass flow rate of oxygen in the incoming air (kg.s⁻¹);
- \dot{m}_{O_2} the mass flow rate of oxygen in the exhaust gas (kg.s⁻¹).

Huggett gathered in Table 9 the heat of combustion of different common polymers (ΔH_c), as well as the heat generated per unit mass of oxygen consumed (E_{O_2}) for complete combustion, i.e. when all the fuel is converted into carbon dioxide and water vapor.

Table 9: Heat of combustion and heat generated per unit mass of oxygen consumed for different common polymers [82]

Fuel	Formula	ΔH_c (MJ.kg ⁻¹)	E_{O_2} (MJ.kg ⁻¹ (O ₂))
Polyethylene (PE)	$(-C_2H_4-)_n$	- 43.28	- 12.65
Polypropylene (PP)	$(-C_3H_6-)_n$	- 43.31	- 12.66
Polyisobutylene (PIB)	$(-C_4H_8-)_n$	- 43.71	- 12.77
Polybutadiene (BR)	$(-C_4H_6-)_n$	- 42.75	- 13.14
Polystyrene (PS)	$(-C_8H_8-)_n$	- 39.85	- 12.97
Polyvinylchloride (PVC)	$(-C_2H_3Cl-)_n$	- 16.43	- 12.84
Polyvinylidene chloride (PVDC)	$(-C_2H_2Cl_2-)_n$	- 8.99	- 13.61
Polyvinylidene fluoride (PVDF)	$(-C_2H_2F_2-)_n$	- 13.32	- 13.32
Polymethylmethacrylate (PMMA)	$(-C_5H_8O_2-)_n$	- 24.89	- 12.98
Polyacrylonitrile (PAN)	$(-C_3H_3N-)_n$	- 30.80	- 14.50 ¹
Polyoxymethylene (POM)	$(-CH_2O-)_n$	- 15.46	- 13.21
Polyethylene terephthalate (PET)	$(-C_{10}H_8O_4-)_n$	- 22.00	- 13.12
Polycarbonate (PC)	$(-C_{16}H_{14}O_3-)_n$	- 29.72	- 13.23
Cellulose triacetate (CTA)	$(-C_{12}H_{16}O_8-)_n$	- 17.62	- 12.67
Polyamide 6-6 (PA 6-6)	$(-C_6H_{11}NO-)_n$	- 29.58	- 12.59
Average value for E_{O_2} (MJ.kg ⁻¹ (O ₂))			-13.02

¹Value omitted by Huggett to determine its constant E_{O_2} .

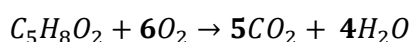
The value of the Huggett constant E is given for a complete combustion. When considering the oxygen consumption method for under-ventilated combustion, it is necessary to integrate the effect of the formation of unburnt species on the heat generated per unit mass of oxygen consumed.

2.1.2.2. Energy released per unit mass of oxygen consumed during incomplete combustion of PMMA

As PMMA is the reference material in cone calorimeter studies, the reaction of PMMA during complete and incomplete combustion is considered for that purpose and the heat of combustion per unit mass of oxygen consumed associated is calculated.

Complete combustion chemical reaction of a PMMA monomer unit is given in Equation 15.

Equation 15: Complete combustion of a PMMA monomer unit



The standard enthalpy of combustion (or low heating value or net caloric value) of PMMA, experimentally determined by calorimetry, is:

$$\Delta H_c(C_5H_8O_2) = -24.89 \text{ MJ.kg}^{-1}$$

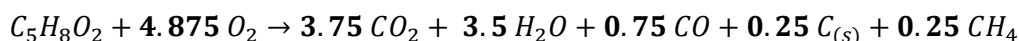
Calculating the corresponding energy released per unit mass of oxygen consumed with the stoichiometry of the reaction yields:

$$\begin{aligned} \Delta H_c(C_5H_8O_2) &= \frac{\Delta H_c(C_5H_8O_2) \times M(C_5H_8O_2)}{M(O_2)} \times \frac{1}{\xi(O_2)} = \frac{-24.89 \times 100.1}{32} \times \frac{1}{6} \\ &= -12.98 \text{ MJ.kg}_{O_2}^{-1} \end{aligned}$$

This value is in agreement with the corresponding value in Table 9.

To describe an incomplete combustion of PMMA, the production of carbon monoxide (CO), soot ($C_{(s)}$) and unburnt hydrocarbons such as methane (CH_4) has to be considered, as described by Equation 16.

Equation 16: Incomplete combustion of PMMA (stoichiometric coefficients are chosen as an example)



The enthalpy of incomplete combustion for PMMA can be recalculated according to the Hess's law. The standard enthalpy of reaction corresponds to the standard enthalpy of formation of products minus the standard enthalpy of formation of reactants (Equation 17).

Equation 17: Calculation of an enthalpy of reaction according to Hess's law

$$\Delta H_{reaction}^0 = \sum \Delta H_{f,products}^0 - \sum \Delta H_{f,reactants}^0$$

In this way, the enthalpy of formation of a monomer unit of PMMA is calculated:

$$\begin{aligned} \Delta H_f(C_5H_8O_2) &= 5\Delta H_f(CO_2) + 4\Delta H_f(H_2O) - \Delta H_c(C_5H_8O_2) \\ \Delta H_f(C_5H_8O_2) &= 5 \times (-393.52) + 4 \times (-241.80) - (-2491.89) = -442.99 \text{ kJ.mol}^{-1} \\ \Delta H_f(C_5H_8O_2) &= -4.42 \text{ MJ.kg}^{-1} \end{aligned}$$

Now, the enthalpy of incomplete combustion of a monomer unit of PMMA can be deduced:

$$\begin{aligned} \Delta H_{c(incomplete\ combustion)}(C_5H_8O_2) &= 3.75\Delta H_f(CO_2) + 3.5\Delta H_f(H_2O) + 0.75\Delta H_f(CO) + 0.25\Delta H_f(CH_4) \\ &\quad - \Delta H_f(C_5H_8O_2) \end{aligned}$$

$$\begin{aligned}
 \Delta H_{c(\text{incomplete combustion})}(C_5H_8O_2) &= 3.75 \times (-393.52) + 3.5 \times (-241.8) + 0.75 \times (-110.53) + 0.25 \times (-74.85) \\
 &\quad - (-442.99) = 1980.62 \text{ kJ.mol}^{-1} \\
 \Delta H_{c(\text{incomplete combustion})}(C_5H_8O_2) &= -19.78 \text{ MJ.kg}^{-1}
 \end{aligned}$$

When calculating the corresponding energy released per unit mass of oxygen consumed with the stoichiometry of the reaction:

$$\Delta H_c(C_5H_8O_2) = -12.70 \text{ MJ.kg}_{O_2}^{-1}$$

The quantity of energy released per unit mass of oxygen consumed decreases when the completeness of the combustion decreases. For the incomplete combustion reaction of PMMA considered in this case, it decreases by 2%.

2.1.2.3. HRR calculation by means of oxygen consumption for incomplete combustion

The works of Parker [83] and Janssens [84] detail the method and equations to calculate the heat release rate by oxygen consumption for various applications. The calculation is expected to be accurate within +/- 10% during complete combustion. The errors are larger in the case of incomplete combustion, e.g. in the case of CO or soot production, or if a large amount of combustion products is other than CO₂ and H₂O, e.g. HCl.

The following assumptions are made:

- The amount of energy released by combustion per unit mass of oxygen consumed is taken as a constant (Huggett's average of 13.1 MJ.kg⁻¹);
- All gases are considered to behave as ideal gases;
- Incoming stream consists of O₂, CO₂, H₂O and N₂;
- O₂ and CO₂ mole fractions are measured on a dry basis, i.e. water is removed from the sample before gas analysis;
- The mass flow rate of N₂ is assumed to be constant, i.e. N₂ is conserved under the assumption of negligible formation of nitrogen oxides and release of nitrogen from the material;
- The molecular weight of exhaust stream is assumed to be equal to the one of incoming stream.

The relation between the mass flow rate of O₂ in the incoming stream ($\dot{m}_{O_2}^0$), the mass flow rate of O₂ in the exhaust stream (\dot{m}_{O_2}) and the mass flow rate of nitrogen (\dot{m}_{N_2}) is given by Equation 18 and Equation 19:

Chapter II: Controlled-atmosphere cone calorimeter set-up conception

Equation 18: Expression of mass flow rate of O_2 in the incoming stream

$$\dot{m}_{O_2}^0 = \frac{X_{O_2}^0}{1 - X_{O_2}^0 - X_{CO_2}^0} \frac{M_{O_2}}{M_{N_2}} \dot{m}_{N_2}$$

Equation 19: Expression of mass flow rate of O_2 in the exhaust gas stream

$$\dot{m}_{O_2} = \frac{X_{O_2}}{1 - X_{O_2} - X_{CO_2}} \frac{M_{O_2}}{M_{N_2}} \dot{m}_{N_2}$$

Where

- $X_{O_2}^0$ the mole fraction of O_2 in the incoming stream;
- $X_{CO_2}^0$ the mole fraction of CO_2 in the incoming stream, assumed to be negligible, e.g. ~ 400 ppm in air;
- M_{O_2} the molecular weight of oxygen (32×10^{-3} kg.mol⁻¹);
- M_{N_2} the molecular weight of nitrogen (28×10^{-3} kg.mol⁻¹);
- X_{O_2} the mole fraction of O_2 in the exhaust stream;
- X_{CO_2} the mole fraction of CO_2 in the exhaust stream.

Rearranging the previous equations leads to Equation 20:

Equation 20: Expression of the consumed mass flow rate of O_2

$$\dot{m}_{O_2}^0 - \dot{m}_{O_2} = \frac{X_{O_2}^0(1 - X_{CO_2}) - X_{O_2}(1 - X_{CO_2}^0)}{(1 - X_{O_2} - X_{CO_2})(1 - X_{O_2}^0 - X_{CO_2}^0)} \frac{M_{O_2}}{M_{N_2}} \dot{m}_{N_2}$$

In the case of incoming stream flow rate measurement, e.g. in controlled-atmosphere system, the heat release rate is given by:

Equation 21: Calculation of HRR in the case of incoming stream flow rate measurement

$$\dot{q} = 10^3 E \frac{X_{O_2}^0(1 - X_{CO_2}) - X_{O_2}(1 - X_{CO_2}^0)}{1 - X_{O_2} - X_{CO_2}} \dot{m}_a \frac{M_{O_2}}{M_a} (1 - X_{H_2O}^0)$$

Where

- \dot{m}_a the mass flow rate of incoming stream (kg.s⁻¹);
- M_a the molecular weight of incoming stream (28.97×10^{-3} kg.mol⁻¹ in the case of air)
- $X_{H_2O}^0$ the mole fraction of H_2O in the incoming stream, assumed to be around 0 as the incoming air is primarily dried.

In the case of exhaust stream flow rate measurement, e.g. in open system where the flow rate into the system cannot be measured, the heat release rate is given by:

Equation 22: Calculation of HRR in the case of exhaust stream flow rate measurement

$$\dot{q} = 10^3 E \frac{\phi}{1 + \phi(\alpha - 1)} \dot{m}_e \frac{M_{O_2}}{M_a} (1 - X_{H_2O}^0) X_{O_2}^0$$

Where

- ϕ the oxygen depletion factor;
- α the expansion factor;
- \dot{m}_e the mass flow rate of exhaust stream (kg.s^{-1}).

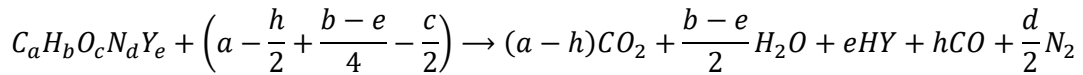
The oxygen depletion factor is defined in Equation 23:

Equation 23: Calculation of oxygen depletion factor

$$\phi = \frac{\dot{m}_{O_2}^0 - \dot{m}_{O_2}}{\dot{m}_{O_2}^0} = \frac{X_{O_2}^0 (1 - X_{CO_2}) - X_{O_2} (1 - X_{CO_2}^0)}{(1 - X_{O_2} - X_{CO_2}) X_{O_2}^0}$$

The expansion factor is given according to the following general reaction and the ratio β between the moles of combustion products formed and the moles of oxygen consumed:

Equation 24: Expansion factor according to the following general reaction (the symbol Y represents any of the halogens)



$$\alpha = 1 + X_{O_2}^0 (\beta - 1)$$

$$\beta = \frac{4a + 2b + 2d + 2e}{4a + b - 2c - e - 2h}$$

Some typical values of β under complete combustion are 1.5 for PMMA ($\text{nC}_5\text{H}_8\text{O}_2$) and 1.6 for PVC ($\text{nC}_2\text{H}_3\text{Cl}$).

The mass flow rate of exhaust stream is assessed by the measurements of temperature and volume flow rate³⁵:

³⁵ Or velocity (ratio of volume flow rate to area of the chimney) at one point, preferentially in turbulent regime where the ratio of the average velocity to the measured velocity is close to 1.

Equation 25: Calculation of oxygen depletion factor

$$\dot{m}_e = \left[\frac{PQM}{RT} \right]_e$$

Where

- P the pressure of exhaust stream (assumed to be 101325 Pa);
- Q the flow rate of exhaust stream ($\text{m}^3 \cdot \text{s}^{-1}$);
- M the molecular weight of exhaust stream ($\text{kg} \cdot \text{mol}^{-1}$);
- T the temperature of exhaust stream (K).

Correction for incomplete combustion is only considered for controlled-atmosphere conditions. For incomplete combustion, the amount of CO released is taken into account³⁶ in order to bring a correction to the heat release rate measured by oxygen consumption calorimetry. A correction has to be made to Equation 21 (heat release rate calculated in enclosed conditions) since E is based on the assumption that combustion is complete. This correction is derived in [84] and the final equation for measuring heat release rate during incomplete combustion in enclosed conditions is given in Equation 26.

Equation 26: Calculation of HRR in the case of incoming stream flow rate measurement with CO taken into account

$$\dot{q} = 10^3 \left[E \frac{X_{O_2}^0 (1 - X_{CO_2} - X_{CO}) - X_{O_2} (1 - X_{CO_2}^0)}{1 - X_{O_2} - X_{CO_2} - X_{CO}} - (E_{CO} - E) \frac{X_{CO} (1 - X_{O_2}^0 - X_{CO_2}^0)}{2(1 - X_{O_2} - X_{CO_2} - X_{CO})} \right] \dot{m}_a \frac{M_{O_2}}{M_a} (1 - X_{H_2O}^0)$$

With E_{CO} the net heat release per unit mass of O_2 consumed for combustion of CO to CO_2 (= 17.6 MJ.kg⁻¹ of O_2).

2.1.3. Conclusion

Both the temperature rise method and the oxygen consumption method lose accuracy when under-ventilated fires are studied and the combustion becomes incomplete. Nevertheless, there is an accessible way of correcting this deviation with the oxygen consumption method. That is the reason why the oxygen consumption method was chosen to determine the HRR during this study. The MLC was then transformed into a controlled-atmosphere cone calorimeter (CACC) as described in 2.2.

³⁶ Other unburnt species such as hydrocarbons or soot particles are not taken into account in the calculation of HRR.

2.2. Design of the apparatus

2.2.1. Specifications

The aim of designing a new controlled atmosphere cone calorimeter at EDF R&D was to fulfill these requirements:

- Controlling confinement and the atmosphere composition between 0 and 21 vol. % as well as the inlet flow rate between 0 and 200 L.min⁻¹.
- Getting a reliable HRR measurement in under-ventilated combustion under an applied heat flux of 50 kW m⁻²;
- Ensuring a dispersion of the gas mixture within the enclosure (horizontally homogeneous flow velocity);
- Allowing a transmission of the infrared emission coming from the flame in order to avoid an additional local heating.
- Allowing a good visibility of the sample burning;
- Facilitating the set up manutention;
- Allowing the instrumentation of mass loss, heat release rate, gas concentration and aerosols concentration to pe performed.

2.2.2. Overview of the apparatus

Figure 14 displays an overview of the apparatus and specific elements are detailed subsequently.

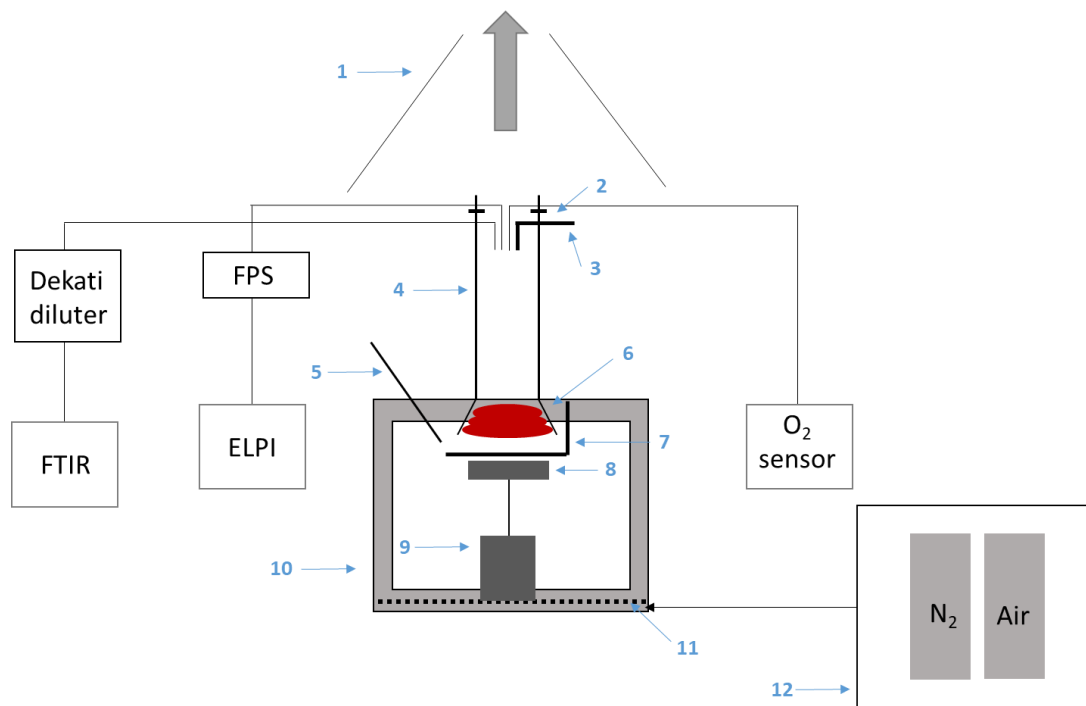


Figure 14: Overview of the apparatus developed at EDF

1: Air extraction	7: Movable shutter
2: Thermocouples	8: Sample holder
3: Flow velocity sensor	9: Load cell
4: Chimney	10: Enclosure
5: Zirconium oxygen sensor	11: Sintered stainless-steel plate
6: Heater	12: Gas mixing board

2.2.3. Airtight enclosure

The airtight enclosure (Figure 15) is composed of a stainless steel 316L framework on which four windows are silicon-sealed. The removable windows are made of a polycarbonate supplied by SABIC under the reference LEXAN™ MR10 sheet. Considering the front, back and two sides' faces of the enclosure, the surface ratio of windows over framework is approximately 80% vs 20%. The bottom and the top of the enclosure are a hundred percent stainless steel.

A stainless-steel framework is necessary to maintain the enclosure and to guarantee its dimensional stability. The polycarbonate was chosen as the windows material because:

- It has a coefficient of thermal expansion similar to the one of stainless steel in the operating temperature range. This is an advantage regarding the structure upkeep when the system is warmed up for a test.
- The transparency towards visible light (%T=88) is interesting to be able to observe the behavior of the sample burning during the test. The transparency towards infrared wavelengths is also of a great interest to transfer the power radiated by the flame during the test and to avoid an extra local heating around the sample.
- The choice of polycarbonate over quartz is for its high impact resistance (windows can be removed and replaced freely without any risk of damage) and its workability (holes can be made to introduce extra sensors if needed).

Moreover, the dimension of the enclosure was chosen to be 60×60×60 cm³ so that the polycarbonate windows would be far enough of the flame to avoid reaching the polymer glass transition temperature, which is approximately 140°C.



Figure 15: Picture of the enclosure

2.2.4. The cone calorimeter elements

Heater

The heater element is wound in the form of a truncated cone rated 4 200 W at 230 V with a heat output of up to 75 kW.m^{-2} . Its temperature is controlled by 3 type K thermocouples inserted inside the spires.

Shutter

A one-piece shutter made of an insulating ceramic fiber element laid on a stainless steel round plate is used to protect the sample from the heat flux of the heater before beginning the experiment (Figure 16) . This shutter is an improvement compared to the two-pieces shutter provided by FTT. Indeed, with thermal expansion of the enclosure after a day of testing, the settings that ensure a good junction between the two half pieces are no longer fitting. Consequently, the sample is no longer fully protected from the heat flux of the heater before the experiment start.



Figure 16: One-piece shutter

Sample holder

The FTT sample holder (Figure 17a) consists in a refractory firebrick on which the aluminum wrapped sample is set. A frame retainer is positioned over the sample and hides a small part of the sample. The exposed area of the sample is recalculated to take into account this hidden part in the HRR calculation. Nevertheless, covering a part of the sample from the heater prevents the sample to be fully decomposed. This hinders the measurement of the integral mass loss.

A new sample holder (Figure 17b) has been designed to avoid recovery of the side-parts of the sample which previously lead to the non-global polymer pyrolysis. The sample is now positioned on a stainless-steel plate which is directly placed on a refractory firebrick. The stainless-steel plate has 1 cm high borders that prevents leakage from the low viscosity polymer brought at high temperature during the test.

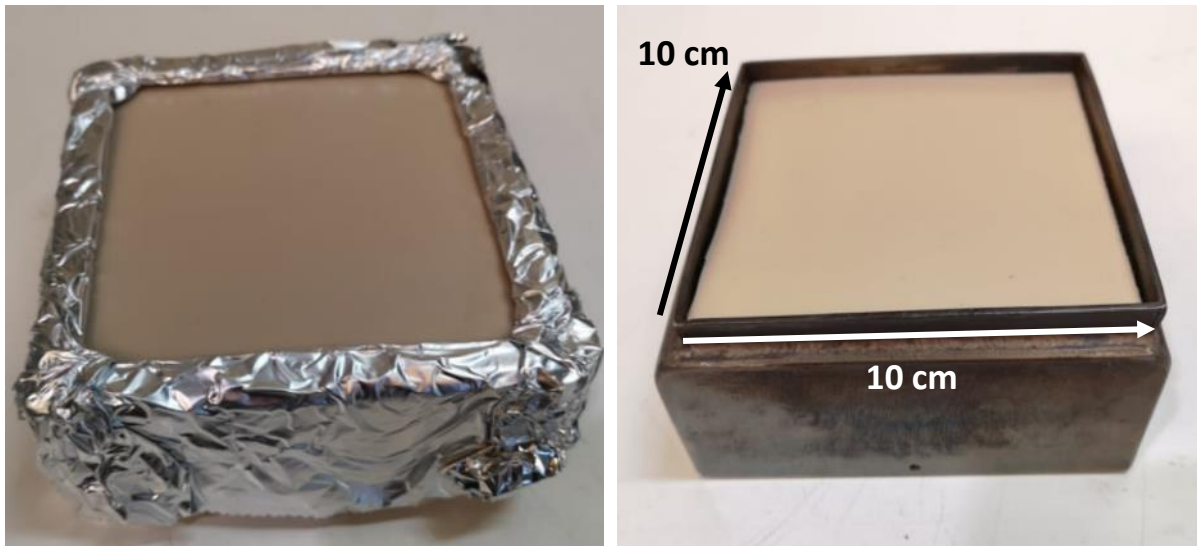


Figure 17: a) Sample placed on the FTT sample holder; b) Sample placed on the new sample holder

Spark igniter

The spark igniter used to pilot the ignition is supplied by FTT and provides a tension of 10 kV between its two electrodes.

Chimney

The chimney is the one provided by FTT. This is a 0.6 m high cylinder of with a 0.12 m diameter. An extra part is mounted on the top of the chimney and is instrumented with three sampling lines, four thermocouples for an average temperature acquisition and a flow velocity sensor. All the captors and sensors details are given in 2.3.

Load cell

The load cell was kept as FTT designed it. It has a sample capacity of over 500 g and an accuracy of 0.01 g. The sampling frequency is 1 Hz.

Exhaust system

An aspiration hood is positioned above the chimney to avoid smoke accumulation in the laboratory. The air extraction flow is set at 3500 m³.h⁻¹.

2.2.5. Supply and distribution system for the gases

Air supply system

Air is provided by a compressor and stored in a 500 L cylinder under 7.5 bar after being cleansed and dried.

Nitrogen supply system

Nitrogen is produced by a generator using a molecular sieve to separate nitrogen and oxygen from the cleansed and dried compressed air. It is stored in a 900 L cylinders under 5 bar. The nitrogen purity varies from 95% to 99.9999%.

Air/Nitrogen delivery system

A regulation system is used to mix and deliver a controlled mixture of air and nitrogen (Figure 18). The volume flow rate of each gas is set with float flow meters. Gases are then mixed in a chamber and the volume flow rate of the mixture is set with a third float flow meter.



Figure 18: Air/Nitrogen regulation plate

The mixture is distributed in a U-shape pipe under the 10 mm-thick sintered stainless-steel plate creating a pressure drop of 0.1 bar (supplier : PORAL), as shown in Figure 19.



Figure 19: U-shape gas distribution system

This system allows to modulate the oxygen concentration in the range between 2 vol. % and 21 vol. % at the working temperatures. The inlet gas flow rate can be varied between 30 L.min⁻¹ and 120 L.min⁻¹ with an accuracy of ± 5 L.min⁻¹ in average.

2.3. Controllers and sensors

Thermocouples

Four type K thermocouples are placed at the top of the chimney to monitor the smoke temperature throughout the test.

Flux meter

A flux meter is needed to daily evaluate the heat flux delivered by the conical resistance (setpoint of 50 kW.m^{-2}). The sensor used is an OP837193 flux meter supplied by Captec. It converts the heat flux received into a tension with a sensitivity of $0.517 \text{ } \mu\text{V.W}^{-1}.\text{m}^{-2}$. It is water-cooled in order to keep it at its proper working temperature.

Zirconium oxygen controller

A zirconium oxygen controller is used to measure the oxygen level inside the enclosure. This is a solid-state oxygen analyzer developed for in-situ applications. The dynamic sensor measures oxygen without using a reference gas and without drying the sampled gas. The sensor consists in two zirconium discs covering both sides of a platinum ring. The measurement chamber is filled with a sample gas. One disc is connected with a reversible oxygen pump. On the opposite disc, the partial pressure of oxygen is determined by measuring the induced Nernst potential. First, the oxygen ions are pumped out of the chamber. The change in electrical charge on the first disc changes in direct linear proportion to the oxygen concentration. This increases the electric potential at the opposite disc. When the electric potential has reached a threshold, the polarity is reversed. Oxygen ions are then pumped back into the chamber and oxygen concentration increases. After reaching a threshold, the polarity changes again. This process is repeated over and over. The time of one period is linearly proportional to the oxygen concentration in the sample gas.

The device used is supplied by Buhler under the reference BA 1000. Its range of measurement is from 0.1 up to 25 vol.% with an accuracy of 0.5% and a response time of 3 seconds.

Paramagnetic Oxygen sensor

This sensor is a Servomex Servopro 4900 that measures the oxygen concentration in smoke from 0 to 25 mol.% with an accuracy of 0.01 mol.% with a gas sampling of 1 L.min^{-1} . Water vapor is removed by a cooling unit and a moisture sorbent. The sensor uses the paramagnetic property of oxygen due to the unpaired electrons in its electronic structure that makes the magnetic dipole of dioxygen molecules shifts towards the external magnetic field direction \vec{H} . As a consequence, the sample has a magnetization \vec{M} dependent on both the magnetic susceptibility χ_m and the external magnetic field (Equation 27). χ_m is a function of temperature, that is why the sample is cooled down to ambient temperature before being analyzed.

Equation 27: Principle of paramagnetic sensor - magnetization

$$\vec{M} = \chi_m(T)\vec{H}$$

Flow velocity sensor

The principle relies on the measurement of a local differential pressure. The conversion of the differential pressure into a velocity is briefly described below [85]:

A flow of velocity V , static pressure p , altitude z and density ρ is considered. If the fluid is incompressible, non-viscous and permanent, the Bernoulli equation (Equation 28) between point A and point B can be applied:

Equation 28: Bernoulli equation

$$p_A + \rho g z_A + \frac{1}{2} \rho V_A^2 = p_B + \rho g z_B + \frac{1}{2} \rho V_B^2$$

If a solid body is placed in the stream, it exists a point O on its surface on which the flow velocity is equal to 0 and the pressure is called stagnation pressure (p_0). This solid body is the Pitot tube and the stagnation pressure can be measured because the point O is drilled and connected to a manometer. The pressure is also measured on a point located on the same flow stream where the velocity V is and the pressure is the static pressure p . These two points have to be sufficiently close for the altitude to be negligible. The Bernoulli equation becomes Equation 29:

Equation 29: Bernoulli equation with two points of same altitude

$$p + \frac{1}{2} \rho V^2 = p_0$$

In order to take into account the slight flow deviation caused by the presence of the tube, a corrective coefficient α is determined after calibration and introduced in Equation 30:

Equation 30: Calculation of flow speed taking into account the deviation caused by the tube

$$V = \alpha \sqrt{\frac{2(p_0 - p)}{\rho}}$$

With

$$\rho = \frac{P_0}{287.1T}$$

α is a corrective coefficient equal to 1.0015 for a L Pitot tube. P_0 is the pressure of the exhaust flow (expressed in Pa). In our application, it is considered at the atmospheric pressure. T is the temperature of the exhaust flow (expressed in K). It is measured by four thermocouples and averaged.

From the measurement of the flow velocity, the volumetric flow rate can be deduced in Equation 31:

Equation 31: Calculation of volumetric flow rate

$$Q = V \times S$$

The velocity of the exhaust flow is measured by a type L Pitot tube CP211 HO R provided by Kimo. It has a measurement range from -100 to 100 Pa with a resolution of 1 Pa and an accuracy of 0.5%. It can be used from 0 to 1000°C.

2.4. Equipment for smoke analysis

In smoke, light gases, i.e. compounds at a gaseous state at 180°C, are measured continuously with a Fourier Transformed InfraRed spectrometer (FTIR) and aerosols, i.e. soot particles and condensed hydrocarbons, are measured continuously with an Electrical Low-Pressure Impactor (ELPI). These two analytical instruments are described in this section.

2.4.1. Fourier Transform InfraRed spectrometer

Infrared spectroscopy is a structural characterization technique that relies on the interaction of electromagnetic waves of wavelength between 0.8 and 100 μm ($1400 - 10 \text{ cm}^{-1}$) and matter. It relies on the fact that some molecules absorb infrared radiations. The frequency of waves absorbed and the degree of absorbance is directly dependent on the structure of the molecule. Indeed, these absorptions are dependent on the resonant frequencies of the vibrational and/or rotational mode of their chemical bonds.

When absorbing these infrared radiations, molecules pass from their ground state to an excited state. The electric field of the incident electromagnetic radiation interacts with the dipole moment of the chemical bond. To be active in infrared spectroscopy, a chemical bond has to have a barycentre of negative charges different to the one of positive charges. Most of chemical species fulfil this requirement, except homonuclear diatomic molecules that share a non-polarized bond such as oxygen (O_2) or nitrogen (N_2). Noble gas such as helium (He) do not have an infrared activity either because they are monoatomic species. Because each molecule has a specific structure, each molecule has a unique absorption of infrared radiations spectrum. This is why FTIR technique can be used to identify a wide range of different species in one sample. Nevertheless, some molecules may be different while possessing same functional groups. They will thus have a different whole spectrum while sharing some absorption areas bringing about an overlapping of their absorbance areas. When considering a

wavenumber range for the quantification of one specie, it is possible that some other species have an infrared activity in this exact same range. This causes an interference. All these unavoidable interferences considered in this work are listed in Table 10. This lack of discretization between molecules entails a limitation to this technique. The real-time FTIR data obtained with OMNIC software is then processed with a calibration method developed with TQAnalyst. The wavenumber ranges considered for the absorption areas of each gas, as well as the range of calibration are listed in Table 10. The core of this calibration method was developed during the previous PhD in EDF [86][4]. It has been slightly modified and completed with benzene and high concentrations of carbon dioxide.

Table 10: Gas calibration parameters used by TQAnalyst

Gas	Wavenumber range for calibration (cm ⁻¹)	Interferences	Maximum measurement range (ppm)
CO ₂ (carbon dioxide)	3700 – 3693	H ₂ O	15 000
CO (carbon monoxide)	2113 – 2092	H ₂ O	3 100
CH ₄ (methane)	3019 – 3015	H ₂ O, C ₂ H ₆ , C ₃ H ₈	100
C ₂ H ₄ (ethene)	951 – 946	/	105
C ₂ H ₄ O ₂ (acetic acid)	1022 – 968	H ₂ O, HF, NO ₂ , C ₃ H ₆ O	381
C ₃ H ₆ O (acetone)	1249 – 1210	C ₂ H ₄ O ₂ , H ₂ O, HF, SO ₂ , NH ₃	500
H ₂ O (water vapor)	3951 – 3921	HF, HCN, C ₃ H ₆ O	61 430
C ₂ H ₆ (ethane)	2957 – 2949	H ₂ O, C ₃ H ₈ , C ₂ H ₂ , SO ₂ , NH ₃ , C ₃ H ₆ O	98
C ₃ H ₈ (propane)	2971 – 2964	CH ₄ , H ₂ O, C ₂ H ₆ , SO ₂ , C ₃ H ₆ O	100
C ₂ H ₂ (ethyne)	3315 – 3307	H ₂ O, HBr, HCN, NH ₃ , C ₃ H ₆ O	100
C ₆ H ₆ (benzene)	3122 – 3076	CH ₄ , C ₂ H ₄ , H ₂ O, HCl	239
HCl (hydrogen chloride)	2823 – 2748	H ₂ O, SO ₂	1 476
HBr (hydrogen bromide)	2527 – 2431	CO, H ₂ O, HCl	508
HF (hydrogen fluoride)	4111 – 3998	H ₂ O, HBr	500
HCN (hydrogen cyanide)	715 – 711	/	250
NO (nitrogen monoxide)	1876 – 1873	C ₂ H ₄ O ₂ , H ₂ O, C ₃ H ₆ O	101
NO ₂ (nitrogen dioxide)	1634 – 1628	H ₂ O, NH ₃ , C ₃ H ₆ O	103
SO ₂ (sulfur dioxide)	1368 – 1352	H ₂ O, C ₃ H ₆ O	98

NH₃ (ammoniac)	935 – 924	H ₂ O, C ₂ H ₆ , C ₃ H ₆ O	50
----------------------------------	-----------	---	----

The apparatus used in this project is a Thermo Nicolet iS10 FTIR spectrometer from Thermofisher Scientific. It is equipped with an Ever-glo™ GLOBAR infrared source able to produce IR radiation over a range from 50 to 7400 cm⁻¹, a 0.2 L volume gas cell with an optical pathlength of 2 m and a MCT (Mercury Cadmium Telluride) detector cooled with liquid nitrogen. The gas sampling from the chimney is made at 10 L.min⁻¹ (0.17 L.s⁻¹) through lines heated at 180°C. The cell is also kept at 180°C under a pressure of 650 Torr (0.85 bar). The gas is filtered in order to eliminate soot particles and condensed gases. The 20-scan background is used to get rid of the influence of the environment such as the ambient air (water vapour, carbon dioxide) or the internal materials of the spectrometer (infrared source, mirrors, windows...) on the gas analysis. The background is made before each acquisition, it thus takes into account the varying atmosphere composition. The acquisition frequency is set at 0.6 Hz and the measurement is accurate within 10% of uncertainty.

2.4.2. Electrical Low-Pressure Impactor

The ELPI is a cascade impactor. It is composed of different impaction stages that collect particles with specific diameter, depending on the stages geometry and the throughput used during the experiment. This impactor (Figure 20) is particularly interesting because it covers a wide range of diameters from 0.006 to 10 µm and permits a fast time-resolution measurement (around one second of residence time).

What makes the ELPI particular is that it is used at low pressure. Indeed, the drag force is dependent on the Cunningham correction factor, which is itself dependent on the pressure. Lowering the pressure then permits to lower the diameter inferior limit [87].

This instrument consists of three main components: a cascade impactor, a unipolar diode charger and a multichannel electrometer. The instrument samples air at a flow rate of 10 L.min⁻¹ inside the ELPI column thanks to a vacuum pump. A flush pump is used to zero the electrometers by passing dried and filtered air through the instrument.

When a sample goes through the instrument, it is first charged at a well-defined level by the charger. The charged particles are then introduced into the cascade impactor. According to their terminal velocity and consequently their aerodynamic diameter, they are classified into 14 size fractions on the impactor. The particles yield their charge to the plate they impact. The multichannel electrometer is used to simultaneously measure the charges carried by the collected particles from each stage. Each

stage is electrically insulated from each other. The measured current signals are then converted to the number concentrations based on the response function of the charger (Equation 32).

Equation 32: Particle concentration determination at each stage of the ELPI

$$C = \frac{I}{PNeQ}$$

Where:

- C is the particle number concentration ($\#.\text{cm}^{-3}$)
- I is the measured electric current due to the flow of charged particles (A)
- P is the fraction of particles penetrating through the charger
- N is the mean number of elementary charges per particle
- e is the elementary charge ($1.6.10^{-19}$ C)
- Q is the flow rate in the impactor (set at $10\text{L}.\text{min}^{-1}$)

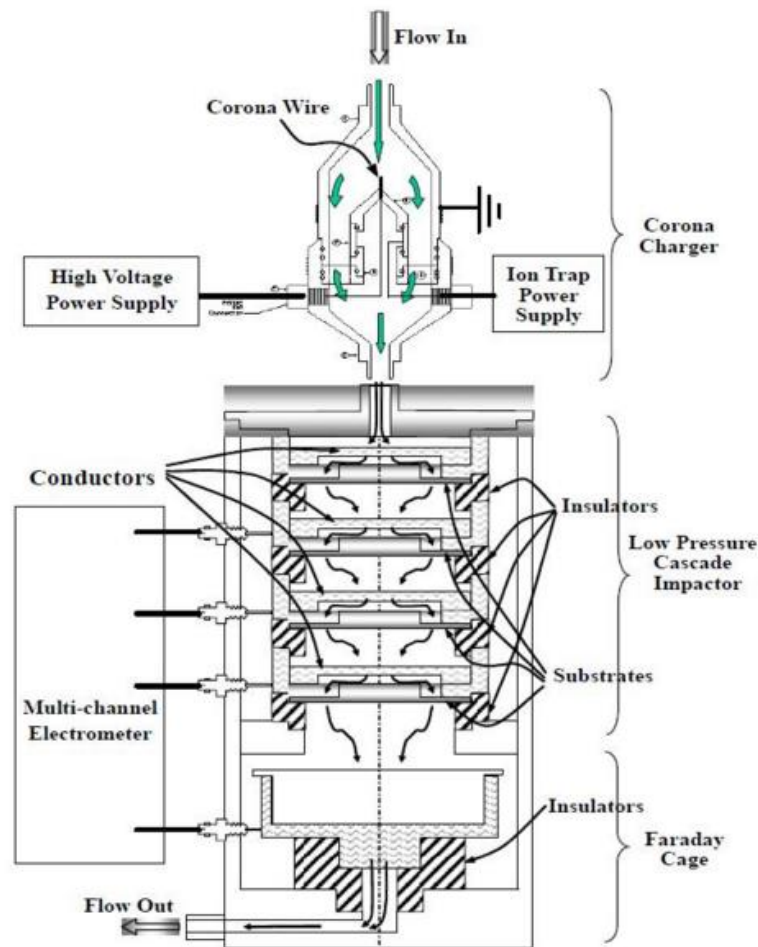


Figure 20: Electrical Low-Pressure Impactor from Dekati

The apparatus used for this study is the ELPI+ from Dekati. The charger delivers a $3.5 \text{ kV} \pm 0.5 \text{ kV}$ voltage and a $1 \text{ }\mu\text{A}$ current. The sampling rate is 10 Hz. The geometric mean particle diameter (D50%) as well as the corresponding range of concentration measurement for each stage are listed in Table 11.

Table 11: Range of measurement for each plate of the ELPI+

Stage	Particle diameter D50% (μm)	Minimal particle concentration ($\#.\text{cm}^{-3}$)	Maximum particle concentration ($\#.\text{cm}^{-3}$)
15	10.000		
14	6.800	0.10	2.4×10^4
13	4.400	0.10	2.4×10^4
12	2.500	0.15	5.4×10^4
11	1.600	0.30	1.1×10^5
10	1.000	0.50	1.9×10^5
9	0.640	1.00	3.5×10^5
8	0.400	2.00	6.4×10^5
7	0.260	3.00	1.2×10^6
6	0.170	5.00	2.1×10^6
5	0.108	10.00	3.7×10^6
4	0.060	20.00	7.3×10^6
3	0.030	50.00	1.7×10^7
2	0.017	100.00	3.4×10^7
1	0.006	250.00	8.3×10^7

Classifying soot particles according to their size is not an easy task because of their nonspherical shape. That is why the ELPI classifies the particles according to their aerodynamic diameter. This physical property is not directly proportional to the particle size. In order to understand what is really measured, an effort was made to understand the soot particles physical properties affecting their aerodynamic diameter³⁷.

³⁷ Soot particles physical description and theory of measurement with the ELPI are detailed in Appendix 1, p.161.

2.4.3. Dilution of smoke prior to analysis

Upstream gas analysis

In the chimney, the sample resulting of the combustion is the smoke mixed with the entrained air. When performing experiments in confined configuration, the amount of entrained air is almost 18 times fewer than well-ventilated tests (30 L.min⁻¹ vs 560 L.min⁻¹ at 20 °C and 1 atm). The quantification method for FTIR is developed in a well-ventilated condition. As a result, the gas concentrations are above the maximum measurement range for FTIR quantification (Table 10).

To enable the measurement of the gases for confined tests, a diluter is placed upstream the FTIR spectrometer. This diluter is a Dekati Diluter. The operation principle of the diluter is based on an ejection type dilution. Clean and dry pressurized dilution air is conducted to the diluter through a critical orifice that controls the airflow. This flow produces pressure drop in the ejector nozzle that draws the sample through the nozzle to the dilution chamber. The dilution air mixes with the sample air in the dilution chamber and further in the diffusion cavity resulting in a homogeneous dilution of gases. To avoid sample condensation, the dilution air is kept at 225 °C thanks to the Dekati Pressurized Air Heater placed around the diluter.

The ratio of dilution air flow to the sample flow determines the dilution ratio. As long as the sample pressure is constant, the dilution ratio stays constant. The initial concentration of the sample is calculated by multiplying the diluted sample concentration with the dilution ratio N . The dilution ratio N is calculated using Equation 33.

Equation 33: Dilution ratio calculation for Dekati Diluter[88]

$$N = \frac{V_{sample} + V_{air}}{V_{sample}}$$

Where V_{sample} is the sample volume flow (L.min⁻¹) and V_{air} is the dilution air volume flow (L.min⁻¹).

In the operating conditions, the dilution ratio upstream the FTIR spectrometer is set at $N= 8$ and the volume flow rate through the diluter is set at $V_{air}= 60$ L.min⁻¹. As a result, the sampling volume flow rate is of approximately $V_{sample}= 8.6$ L.min⁻¹

Upstream aerosol analysis

The dilution of the sample is required for both well-ventilated and confined tests when it comes to aerosol analysis. Indeed, the ELPI+ is commonly used to study small concentrations of soot particles generated by vehicle engines for instance. To extend its use to fire science, a dilution system is needed. The instrument used upstream the ELPI+ analyzer is a FPS-4000 (Fine Particle Sampler) from Dekati [89].

The dilution is carried out in two phases. The first dilution phase is conducted one meter downstream the sampling point in a perforated tube diluter. In our operating conditions, the first dilution stage (i.e. primary dilution) is a hot dilution. The dilution air is warmed up to 180°C. This prevents condensation of volatile species.

The second dilution phase (i.e. secondary dilution) is an ejector type diluter, located downstream the primary dilution. The ejector diluter acts as a pump sucking a known amount of a diluted sample from the primary dilution. Simultaneously, a secondary dilution with cold dilution air is carried out with a dilution air at 20°C.

The dilution ratio is chosen to have, on each ELPI plate, particle concentration inferior to the maximum particle concentration (Table 11). It varies from $N=20$ for well-ventilated burning of the low-sooty material (PMMA) to $N=90$ for confined burning of the high-sooty material (PVC). Chosen dilution ratios for each material and configuration are given throughout the chapter dealing with the results.

3. Conclusion

Developing a new bench-scale apparatus for under-ventilated fires permits to control several parameters such as the air/nitrogen delivery system in the enclosure to minimize flame perturbation and maximize a homogeneous composition, the optical properties of the walls to minimize a local extra heating, and a positioning of the sensors before the mixing between the smoke and the ambient air that avoids skewing the measurements.

A HRR measurement based on oxygen consumption taking into account the amount of carbon monoxide generated is adopted because it is the most adequate method for under-ventilated studies, compared to the sensible temperature rise measurement method. The latter is calibrated for a well-ventilated combustion.

Sample mass loss is measured with a load cell, oxygen measurement for HRR calculation is made with a paramagnetic oxygen sensor, gas concentrations in smoke are analyzed with a FTIR spectrometer and quantified after a method developed on TQAnalyst, and aerosol (soot particles and condensed hydrocarbons) concentration is measured with an ELPI+ granulometer. Dilution of smoke is performed upstream gas and aerosol analysis.

Chapter III: Representative material elaboration

1. Introduction	80
2. Materials and methods	82
2.1. <i>Materials</i>	82
2.1.1 Laboratory-made formulations prior to determining plaques formulations	82
2.1.2 Plaques of PVC formulations	83
2.2. <i>Elementary analysis</i>	83
2.1.1. Ion chromatography	83
2.1.2. Inductively Coupled Plasma – Mass Spectroscopy	83
2.1.3. X-ray fluorescence analysis	84
2.3. <i>Thermal analysis</i>	84
2.3.1. Thermogravimetric analysis coupled to Fourier Transformed Infrared Spectroscopy	84
2.3.2. Thermogravimetric analysis for kinetic modeling	84
2.3.3. Pyrolizer coupled to Gas Chromatography Mass Spectroscopy	85
2.4. <i>Optical measurement</i>	85
2.4.1. Integration sphere	85
2.5. <i>Thermo-physical analysis</i>	86
2.5.1. Hot Disk thermal constant analyzer	86
2.5.2. Differential Scanning Calorimetry	86
2.5.3. Simultaneous Thermal Analysis	86
2.5.4. Pyrolysis-Combustion Flow Calorimetry	87
3. Reverse engineering and characterization of electrical cable sheath	87
3.3. <i>Industrial formulations for electrical cable sheath</i>	87
3.4. <i>Composition analysis of the cable sheath</i>	89
3.4.1. Elementary analysis	89
3.4.2. Organic soluble fraction analysis	91
3.4.3. Conclusion	92
3.5. <i>Thermal stability analysis</i>	92
4. Separate characterization of the main components of the electrical cable sheath	95
4.3. <i>PVC cable sheath main components thermal stability and interactions</i>	95
4.3.1. Thermogravimetry analysis of the individual components	95
4.3.2. Thermogravimetry analysis of the components formulated together	95
4.3.3. Decomposition analysis of DIDP by Py-GC/MS	97
4.4. <i>Choice of stabilizing system</i>	98
5. Elaboration and characterization of representative and simplified materials	99
5.1. <i>Elaboration of PVC materials</i>	99
5.2. <i>Comparison of the reference material with the electrical cable sheath</i>	101

5.3.	<i>Characterization of filled and unfilled PVC properties for numerical simulation inputs</i>	102
5.3.1.	Absorbance	103
5.3.2.	Thermal conductivity	103
5.3.3.	Heat capacity	103
5.3.4.	Heat of decomposition	104
5.3.5.	Heat of combustion	104
5.3.6.	Kinetics of thermal decomposition	105
5.3.7.	Conclusion	108
6.	Conclusion	109

1. Introduction

An electrical cable is an assembly of several layers made of different materials or formulations (Figure 21). Together, they ensure electrical insulation and mechanical resistance. The most important part to be taken into account when considering the fire behavior of an electrical cable is the sheath [90]. Indeed, the sheath is the material that is first submitted to external heat flux. Moreover, it represents 55 wt. % of the combustible parts.³⁸

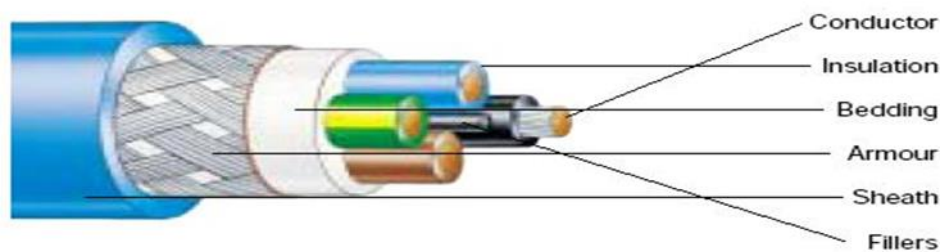


Figure 21: Composition of an electrical cable

In all the currently running French NPPs, electrical cable sheaths are a formulation based on polyvinyl chloride (PVC) for the majority. PVC is the world's third largest plastic in terms of sales volume (after PE and PP) [91] and is often used for electrical cable sheath due to its excellent electrical insulating properties and dielectric constant. Because halogenated polymers are controversial, especially when it comes to the toxic fumes they produce during a fire, new generation of NPPs are equipped with another material based on a non-halogenated polymer for their electrical cable, e.g. ethylene vinyl acetate (EVA), fire retarded with aluminum tri hydroxide (ATH). A comprehensive work on the fire behavior of EVA/ATH material under well-ventilated conditions has been carried out during a previous PhD [4].

³⁸ In the case of the studied PVC cable referenced "PIRELLI 4x1.5 mm²" (grey color).

When performing a test with the cone calorimeter, it is preferable to work with 100×100 mm² plaques of a representative material of electrical cable sheath as sample for two reasons:

- The composition has to be known and controlled to be able to understand the thermal decomposition of the sample;
- Experiments have to be repeated several times to have accurate and trustable data. Thus, the samples have to be identical therefore the repeatability is independent to the sample and is only dependent on the apparatus and operating procedure.

For these reasons, the electrical cable sheath material, obtained from industrial supplier, is submitted to a reverse engineering to disclose its composition and determine the main components. Then, a simplified formulation is established, and plaques of the representative material are manufactured.

The materials and methods implied in this chapter and gathered in Table 12 to address these objectives, are described in a first part. Then, the PVC cable sheath reverse engineering results are disclosed and discussed. The simplified formulation components are then characterized separately in order to investigate their thermal decomposition mechanism and together to study potential interactions during thermal decomposition. Finally, the manufactured PVC plaques, based on the simplified formulations, are characterized in terms of thermal stability, optical and thermo-physical properties.

Table 12: Overview of the properties analyzed and the methods performed in this chapter

Property	Method	Material	Laboratory
Total chlorine	Ion chromatography	Cable sheath	SOCOR
Total calcium	Inductively Coupled Plasma – Mass Spectroscopy	Cable sheath	SOCOR
Elementary analysis	X-ray fluorescence spectroscopy	Cable sheath	SOCOR
Thermal stability & light thermal decomposition products	Thermogravimetric analysis with Fourier Transformed Infrared spectroscopy	Cable sheath	UMET
Thermal stability & kinetic parameters*	Thermogravimetric analysis	PVC DIDP CaCO ₃ PVC/DIDP PVC/DIDP/CaCO ₃ *Filled PVC plaque	UMET

		*Unfilled PVC plaque	
Thermal decomposition products	Pyrolyzer coupled to Gas Chromatography – Mass Spectroscopy	DIDP	UMET
Absorbance	Integration sphere	Filled PVC plaque	UMET
Thermal conductivity	Hot Disk thermal constant analyzer	Filled PVC plaque Unfilled PVC plaque	UMET
Heat capacity	Differential Scanning Calorimetry	Filled PVC plaque Unfilled PVC plaque	UMET
Heat of decomposition	Simultaneous Thermal Analysis	Filled PVC plaque Unfilled PVC plaque	UMET
Heat of combustion	Pyrolysis-Combustion Flow Calorimetry	Filled PVC plaque Unfilled PVC plaque	UMET

2. Materials and methods

2.1. Materials

2.1.1 Laboratory-made formulations prior to determining plaques formulations

Polyvinyl chloride (PVC), diisodecylphthalate (DIDP) and calcium carbonate (CaCO_3) were provided from Sigma Aldrich to characterize thermal stability of pure compounds. The PVC has an average molecular weight of $M_w^{39}=62\,000\text{ g.mol}^{-1}$ and $M_n^{40}=35\,000\text{ g.mol}^{-1}$. The DIDP and the CaCO_3 have a purity $\geq 99.0\%$.

For the first formulation (PVC+DIDP), 1.165 g of PVC (57.6 wt. %) was solubilized in THF (tetrahydrofuran) in a round-bottomed flask under magnetic stirring. Once the polymer was fully solubilized, 0.858 g of DIDP (42.4 wt. %) was added to the solution and the stirring was maintained for approximately five minutes. Then, THF was evaporated with a rotary evaporator. The formulation, in the form of a film stuck to the bottom of the flask, was cut into small pieces and cryoground with liquid nitrogen to get a fine powder. For the second formulation (PVC+DIDP+ CaCO_3), the same protocol was applied with 1.940 g of PVC (38.9 wt. %), 1.432 g of DIDP (28.7. %) and 1.621 g of CaCO_3 (32.4 wt. %). The CaCO_3 was added after the DIDP. The film obtained after the evaporation of THF was white. This

³⁹ Weight-average molecular weight

⁴⁰ Number-average molecular weight

formulation is suspected to be partially inhomogeneous because it was whiter and thicker at the very bottom of the round flask than on the sides. It is suspected CaCO_3 is deposited on the bottom by decantation. As a consequence, the powder obtained after cryogrinding was carefully mixed in order to disperse the mineral filler in the sample.

2.1.2. Plaques of PVC formulations

The PVC, referenced as “PVC Lacovyl S 7015-PCC 016VPT”, is provided by Kem One. Its average molecular weight is $M_n=94\,000\text{ g}\cdot\text{mol}^{-1}$. The DIDP, referenced as “Jayflex” is provided by Caldic. The CaCO_3 , referenced as “EHX1 OM” is provided by OMYA. It contains a tiny percentage of processing aids based on stearate aimed to facilitate the powder dispersion inside the polymer. The mean geometric diameter of the particles ($d_{50\%}$) is $2\text{ }\mu\text{m}$ and the specific area is $4\text{ m}^2\cdot\text{g}^{-1}$. The Ca/Zn stabilizer is a one-pack compound provided by ChemTech.

The formulations were mixed in a CP 200 L high-speed mixer from CACCIA. Neat PVC is first introduced in the mixer and rapidly heats to 80°C . The additives are slowly added before rapid increase of the temperature to 110°C . The formulation is then transferred into a cold tank and the obtained “dry-blend” is conditioned at 25°C in PE bags. The formulations are injection molded in the form of plaques of $100\times100\times3\text{ mm}^3$. Filled PVC is heated up to 200°C in the molding machine and Unfilled PVC is heated up to 170°C . The detailed parameters of dry-blending and injection molding are available in Appendix 3, p.181.

2.2. Elementary analysis⁴¹

2.1.1. Ion chromatography

Ion chromatography, according to the NF EN 14589 standard, separates molecules based on their respective charged groups when passing through a column (stationary phase). The stationary phase surface displays ionic functional groups that interact with analyte ions of opposite charge. The amount of a specific ion is measured by the change in conductivity as the species passes through the detector downstream to the column.

2.1.2. Inductively Coupled Plasma – Mass Spectroscopy

Inductively Coupled Plasma Mass Spectroscopy (ICP-MS) analysis is a technique with which the sample is ionized by inductively coupled plasma and a mass spectrometer is used to separate and quantify the ions.

⁴¹ Elementary analysis were performed by SOCOR. As a consequence, set ups are not detailed.

2.1.3. X-ray fluorescence analysis

X-ray fluorescence spectrometry (XRF) allows the analysis of major, minor and trace elements in various kinds of samples. It can be performed qualitatively as well as quantitatively. The working principle is based on the excitation of the sample atoms by high-energy X-rays, followed by the emission of characteristic photons with a certain energy, well correlated to the atomic number Z of each element (Moseley's law). The determination of the energy (or wavelength) of the emitted photon allows qualitative analysis and the determination of the number of emitted characteristic photons allows quantitative analysis [92].

2.3. Thermal analysis

2.3.1. Thermogravimetric analysis coupled to Fourier Transformed Infrared Spectroscopy

Thermo-Gravimetric Analysis (TGA) coupled with Fourier Transformed InfraRed spectroscopy (TGA-FTIR) were performed on TA instrument Discovery TGA coupled with a ThermoScientific NicoletTM iSTM10 spectrometer. Experiments were carried out using 250 μL open alumina pans. The TGA balance flow was set to 15 $\text{mL}\cdot\text{min}^{-1}$ and the purge flow of nitrogen was set at 50 $\text{mL}\cdot\text{min}^{-1}$. All samples of 10 ± 2 mg underwent a 50°C isotherm for 120 minutes followed by a 10°C $\cdot\text{min}^{-1}$ linear heating ramp from 50°C to 1000°C.

Gases evolved during the TGA experiments are transferred to the FTIR cell continuously through a heated line set at 225°C to avoid condensation. The spectra are recorded using the OMNIC software in a range of 450-4000 cm^{-1} . The number of scans is fixed at 8 and the resolution at 4 cm^{-1} .

Experiments were carried out under both nitrogen and air to study pyrolytic and oxidative conditions respectively. Each part of the cable was cut apart and cryoground with liquid nitrogen in order to get fine powder. This step is of prior importance to make thin layer of powder in the pan and to assume having thermally thin material.

Each TGA experiment was done at least twice. The repeatable curves were almost superposed. Only one curve among the repeatable ones is presented.

2.3.2. Thermogravimetric analysis for kinetic modeling

Thermogravimetric analysis is carried out on a Netzsch TG 209 F1 Libra. The sample purge flow of nitrogen is set at 100 $\text{mL}\cdot\text{min}^{-1}$. Samples of approximately 7 mg are put in open alumina pans (250 μL) and undergo heating from 25°C to 800°C with heating rates of 0.25, 0.5, 1, 2, 5, 10, 20, 50 and 100 °C $\cdot\text{min}^{-1}$. Kinetic analysis and modeling of the decomposition of the sample is made using an advanced thermokinetic software package developed by Netzsch Company (*Thermokinetic3*). The principle is explained in details elsewhere [93].

2.3.3. *Pyrolizer coupled to Gas Chromatography Mass Spectroscopy*

Pyrolysis-gas chromatography-mass spectroscopy (Py-GC/MS) is an identification method by mass spectroscopy. The sample is brought at its decomposition temperature in the pyrolyzer. The evolved gases are introduced inside the GC/MS part where they are separated according to their size and their interaction with the polarized GC column. Consequently, they are introduced inside the MS according to their retention time. The MS spectrometer splits molecules into ionized fragments and, with comparison with a database, the molecule is identified.

The Py-GC/MS analysis is performed on a Shimadzu GC-MS QP2010 SE and a Frontier Lab PZ-20-20iD micro furnace pyrolyzer. The experiment is performed under inert conditions using helium. Sample mass is about 300 µg. The sample is set in a stainless-steel cup and heated from 50°C to 220°C⁴² with a 10°C.min⁻¹ heating ramp. Evolved gases are introduced into the GC/MS system and are separated using a fused silica capillary column of dimension 30 m×0.25 mm with a 10°C.min⁻¹ heating ramp starting once the pyrolyzer program is over.

2.4. *Optical measurement*

2.4.1. *Integration sphere*

The absorbance is determined after the measurement of the reflectance with a VERTEX 80 infrared spectrometer provided by Bruker. This technique relies on an integration sphere that measures the reflectance factor of the sample surface by averaging the signal on every angles of a hemisphere between 2 and 20µm. The experiment is repeated 3 times within less than 1% margin of error. The absorbance is determined after applying the following physical laws.

The reflectance (R) is the ratio of reflected light by a surface out of the incident light on this surface and the emittance (E) is the radiative flux emitted by a surface unit of an extended source. The law of energy conservation involves that the addition of emittance (E), reflectance (R) and transmittance (T) is equal to unity. Samples that are opaque in the infrared region transmit no radiative flux. The emittance is then easily deducted from the reflectance measured (Equation 34).

Equation 34: Deduction of emittance with the measurement of reflectance for samples opaque in the infrared region

$$E = 1 - R$$

The emissivity of a body is the ratio between the integration of its emittance at a given temperature upon a spectral range and the integration of the emittance of the black body at the same temperature upon the same spectral range (Equation 35).

⁴² 220°C is the mid-peak of dTG for DIDP.

Equation 35: Emissivity of a body over a spectral range

$$\varepsilon_T^{\Omega} = \frac{\int [(1 - R_{sample}) * E_{BB}]}{\int E_{BB}}$$

For this experiment, the emissivity of the sample and of the black body is measured at ambient temperature between 8 and 14 μm because it corresponds of the range with the maximum peak of reflectance. According to Kirchhoff's law, at a temperature equilibrium, the emitted radiative flux by a body is equal to the radiative flux that it absorbs. For an opaque sample in the spectral range between 8 and 14 μm , the absorbance is then the result of Equation 35.

2.5. Thermo-physical analysis

2.5.1. Hot Disk thermal constant analyzer

Thermal conductivity measurements are carried out at ambient temperature using a Hot Disk thermal constant analyzer (TPS2500S) from Thermoconcept, which is based on a transient plane source method. The sensor, a 2mm nickel and kapton probe, acts both as a heater and a thermocouple. It is placed between two 3mm-thick plates of the material with a light pressure to ensure a good contact with the sample. The measurements are performed five times within 1% margin of error.

2.5.2. Differential Scanning Calorimetry

Heat capacity is determined with Differential Scanning Calorimetry (DSC) technique. This technique allows to determine the enthalpies of physical transitions and chemical reactions by measuring the differential heat flow necessary to maintain the sample and an inert reference at the same temperature when they are exposed to a temperature change. The rate of the heat flux within a sample is proportional to its heat capacity. The DSC analysis provides this value by comparison with the rate of the heat flux within a reference of a well-known heat capacity. The experiments are run on a discovery provided by TA Instruments. Samples are cryogenically ground into powder and approximately 10 mg are crimped in an alumina pan with lid. The reference is an empty pan with lid. A modulated signal is used with a constant heating rate of $3^{\circ}\text{C}.\text{min}^{-1}$ from -20°C to 150°C with an amplitude of 3°C and a period of 60 seconds.

2.5.3. Simultaneous Thermal Analysis

Heat of decomposition is measured with Simultaneous Thermal Analysis (STA). STA is a technique that allies thermogravimetric analysis (TGA) and differential scanning calorimetry (DSC) in a single instrument. During this test, a sample of approximately 10 mg powder is placed in a crucible and submitted to a heating ramp from 25°C to 800°C with a ramp of $10^{\circ}\text{C}.\text{min}^{-1}$.

2.5.4. Pyrolysis-Combustion Flow Calorimetry

The heat of combustion is measured with a Pyrolysis-Combustion Flow Calorimetry (PCFC) provided by FTT. This technique separately reproduces the solid state and gas phase processes of flaming combustion for milligrams of sample. During this non-flaming test, $5 \text{ mg} \pm 0.5 \text{ mg}$ of material is decomposed under controlled pyrolysis in an inert gas stream (nitrogen) at $60^\circ\text{C}.\text{min}^{-1}$ and its volatiles are then oxidized at 900°C under 20 vol. % of oxygen. Oxygen consumption calorimetry is used to measure the heat of combustion (ΔH_c) of the pyrolysis products.

3. Reverse engineering and characterization of electrical cable sheath

3.3. Industrial formulations for electrical cable sheath

Neat PVC has already excellent fire properties. It is difficult to ignite and stop burning as soon as the heat source is removed. Its neat heat of combustion is $16.9 \text{ MJ}.\text{kg}^{-1}$ whereas most other plastics are in the range of $24\text{--}43 \text{ MJ}.\text{kg}^{-1}$ [94]. However, neat PVC is a very stiff and brittle material. That is why it is always formulated, especially with plasticizers that reduce its brittleness and with stabilizers that avoid the autocatalytic dehydrochlorination that leads to free-radical depolymerization⁴³.

A basic industrial formulation of PVC electrical cable sheath is composed of:

- **PVC**;
- **Plasticizers** – used to increase flexibility and decrease brittleness of the compound;
- **Filler** – used to reduce the price of the compound while improving electrical and physical properties;
- **Pigment** – used to modulate the color of the compound;
- **Stabilizers and co-stabilizers** – used to quench the PVC free-radical decomposition;
- **Lubricants** – used to reduce the sticking of the compound on metal surfaces while processing;
- **Other additives** such as flame retardants, UV-stabilizers...

An example of a PVC electrical cable formulation with specific components and their amount is shown in Table 13. The amount unit used is phr (per hundred resin). A part per hundred resin is a part added for 100 mass unit of resin.

⁴³ PVC thermal decomposition mechanisms are detailed in Chapter I, p. 24.

Table 13: Example of a formulation of PVC electrical cable sheath [95]

Component	phr
PVC	100
ESO ¹ (co-plasticizer and stabilizer)	5
Ca/Zn (stabilizer)	5
DOP ² (plasticizer)	20-50
CaCO ₃ (filler)	40-75
TiO ₂ (color carrier for pigment)	3
Sb ₂ O ₃ (flame retardant)	3
Antioxidant	1

¹Epoxidized soybean oil

²Diocetyl phthalate

The considered electrical cable (Figure 22) is a typical PVC electrical cable from EDF NPP (grey "PIRELLI 4×1.5 mm²"). It is constituted, from the inside to the outside, of the conductors made of copper. These conductors are isolated by the insulation made of an unfilled PVC formulation. The insulated conductors are surrounded by fillers that are a rubber type material. Around the rubber, there is a bedding, made of the same material as the insulation. Around the bedding, there is a metallic armour. Finally, around the armour, there is the sheath made of a filled PVC formulation⁴⁴.

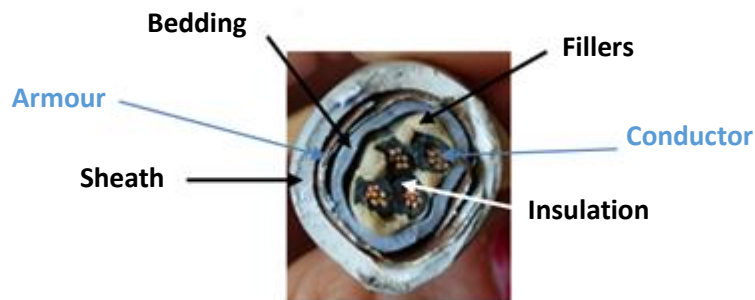


Figure 22: Cut section of the PVC cable "grey PIRELLI 4*1.5mm²"

As the study is focused on the sheath of the cable, the results obtained for the sheath especially are presented hereafter.

⁴⁴ Each organic part of the cable has been analyzed with TGA coupled FTIR.

3.4. Composition analysis of the cable sheath

3.4.1. Elementary analysis

The PVC electrical cable sheath has been analyzed by ion chromatography for determining the total amount of chlorine and by ICP-MS for determining the amount of calcium. The results are gathered in Table 14.

Table 14: Results of elementary analysis on the PVC electrical cable sheath

Analysis	Result	Unit	Method
Total chlorine	177 396	mg.kg ⁻¹	Ion chromatography
Total calcium	10.5	wt. %	ICP-MS

The total chlorine analysis shows that the PVC cable sheath formulation contains 17.7 wt. % of chlorine. Neat PVC contains 56.8 wt. % of chlorine. Thus, it is deduced that the PVC cable sheath formulation contains 31.2 wt. % of PVC.

The most used filler in PVC formulations is, by far, calcium carbonate (CaCO₃). Other fillers such as carbonized clays, talc (Mg₃Si₄O₁₀(OH)₂), dolomites (CaMg(CO₃)₂), barium sulfate (BaSO₄) and metallic oxides are also used [96][97]. The total calcium analysis shows that the PVC cable sheath contains 10.5 wt. % of calcium (Ca). It is deduced that the filler incorporated in the formulation is calcium carbonate (CaCO₃) that is present at 26.2 wt. % .

Besides, a fluorescence X analysis has been performed on the electrical cable sheath. The results obtained are gathered in Table 15. The mass abundance is calculated by the software considering the most likely oxide formed with the analyzed atom (except for chlorine that is measured in its pure form). The oxides are indicated in brackets. These results (mass abundance) are semi-quantitative as the sum of all the analyzed oxides makes approximately 100 wt.%. They are converted into mass percent (wt. %) in the aside column using the weight percent of chlorine determined with ion chromatography as the reference. Still, the results of X-ray fluorescence are only used as a semi-quantitative analysis in the reverse engineering process.

Table 15: Results of the X-ray fluorescence analysis performed on the PVC electrical cable sheath

Atom	Mass abundance (wt. %)	Mass (wt. %)
Al (Al_2O_3)	1.86	0.9
P (P_2O_5)	1.04	0.5
Cl	39.06	17.7
Ca (CaO)	47.08	21.4
Ti (TiO_2)	1.07	0.5
Zn (ZnO)	2.61	1.2
Pb (PbO)	7.04	3.2
Total	99.76	45.4

Presence of chlorine is due to the polymer structure, calcium mainly comes from the filler incorporated in the formulation and titanium certainly comes from the mineral pigments. Indeed, colorants and pigments, incorporated at a low load, comprise organic azo dyes which are soluble in the PVC matrix, mineral pigments (titanium oxide, copper oxides, chromium oxide...), black carbon and metallic pigments [96].

Lead and phosphorus surely are components of the stabilizing system (from the dibasic lead phosphate molecule in Table 16 [98]). Aluminum, zinc and calcium may be also a part of the stabilizing system in the form of metallic soap (their mode of action is explained in section 4.4, p. 98). Phosphorus may act as a co-stabilizing system in the form of organic phosphate. Co-stabilizers are aimed at enhancing stabilizers performance. They are incorporated at a load of 15 to 50 wt. % of the stabilizing system and play a secondary role in stabilization such as antioxidation or HCl absorption [98].

The lead-based stabilizers available in the market are a mixture of several lead salts each comprising more or less amount of lead in their chemical structure (Table 16) [98]. For this reason, a calculation of the amount of the stabilizer incorporated in the formulation given the amount of lead is not possible. A maximum load of 3.2 wt. % is proposed subsequently.

Table 16: Chemical structure of lead-based stabilizers

Name	Chemical structure	Lead concentration (wt. %)
Tribasic lead sulfate	$3 \text{ PbO} \cdot \text{PbSO}_4 \cdot \text{H}_2\text{O}$	83.6
Dibasic lead phosphate	$2 \text{ PbO} \cdot \text{PbSO}_4 \cdot \frac{1}{2} \text{ H}_2\text{O}$	83.7
Dibasic lead phthalate	$2 \text{ PbO} \cdot \text{Pb}(\text{OOC})_2\text{C}_6\text{H}_4$	76.0
Dibasic lead stearate	$2 \text{ PbO} \cdot (\text{C}_{17}\text{H}_{35}\text{COO})_2\text{Pb}$	51.0
Neutral lead stearate	$(\text{C}_{17}\text{H}_{35}\text{COO})_2\text{Pb}$	27.0
Dibasic lead carbonate	$2 \text{ PbO} \cdot \text{PbCO}_3$	80.2

NB: the use of lead in cable formulations is forbidden by the EU since 2015 which is why a different stabilizing system had to be used for the representative material.

3.4.2. *Organic soluble fraction analysis*

An internal internship report [99] on the fire behavior of electrical cables in NPPs relates some characterizations on the PIRELLI grey PVC cable. Especially, the nature and content of plasticizer were analyzed. The cable sheath was put into chloroform that enables solubilization of the plasticizers. The sample was weighted before and after, the mass difference is considered as the amount of plasticizer in the formulation. Then, the chloroform solution was evaporated under vacuum and the residual sample was analyzed by infrared spectrometry. This analysis permits to identify the sample as plasticizer DIDP (diisodecyl phthalate) (Figure 23) that incorporated at an amount of 23.2 wt. %.

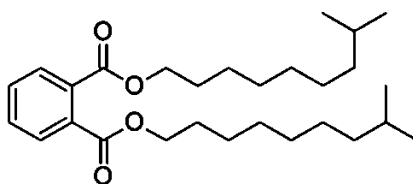


Figure 23: Diisodecyl phthalate (DIDP)

3.4.3. Conclusion

After gathering the data of these analyses, the composition of the electrical cable sheath can be assumed and is described in Table 17.

Table 17: Formulation of PVC cable sheath after structural analysis

Component	Mass fraction (wt. %)	phr
PVC	31.2	100
DIDP (plasticizer)	23.2	74.4
CaCO ₃ (filler)	26.2	84.0
Pb-based stabilizer	≈3	≈10
Unknown	≈16	≈52

3.5. Thermal stability analysis

TGA coupled FTIR is performed on the electrical cable sheath. Thermal stability analysis of a formulation can also insights its composition. The number of decomposition steps along with their respective temperature provides information on the chemical nature of the polymer and the percentage of residue indicates the amount of mineral filler (at least partially if the polymer is not charring). The analysis of the evolved gases during the thermal analysis is a major asset as it allows determining the decomposition step mechanism of the material. The Thermo-Gravimetric (TG) curve and its derivative (dTG) for the PVC electrical cable sheath under nitrogen is shown in Figure 24a. These curves show three apparent steps of decomposition (with a heating ramp of 10°C.min⁻¹). The first step is observed between 215°C and 315°C and corresponds to 41% mass loss, the second step is between 420°C and 500°C and the corresponding mass loss is 7%, the third step appears between 640°C and 760°C with a corresponding mass loss of 5.5%. The amount of residue at 1000°C is 38.2 wt. %.

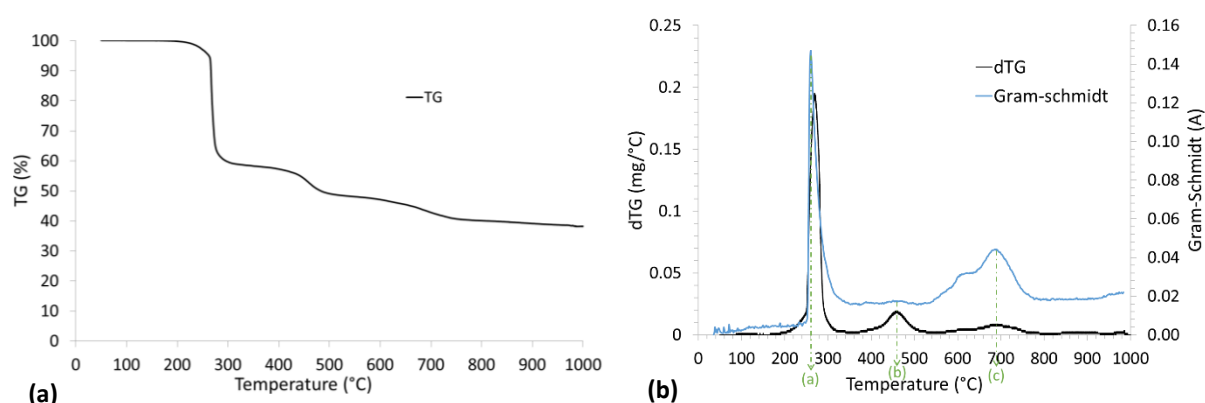


Figure 24: TGA performed under nitrogen at 10°C.min⁻¹ a) TG and dTG curve of PVC electrical cable sheath; b) dTG and Gram-Schmidt curves of electrical cable sheath

The identification of the gases evolved during the decomposition is explained subsequently. The dTG curve of the electrical cable sheath together with the Gram-Schmidt curve from IR spectra are presented on Figure 24b. The Gram-Schmidt signal is the sum of all the absorption intensities. The absorption intensity is related to both the dipolar moment variation and the concentration. In other words, if a specie has a low dipolar moment variation, it will not have a high impact on the Gram-Schmidt curve even if it is present at a high concentration. For this reason, the temperatures of the considered peaks are taken on the dTG curve and the corresponding FTIR spectra are shown in Figure 25. At each temperature, the main species detected by FTIR are determined and their spectra are placed above the obtained experimental FTIR spectra.

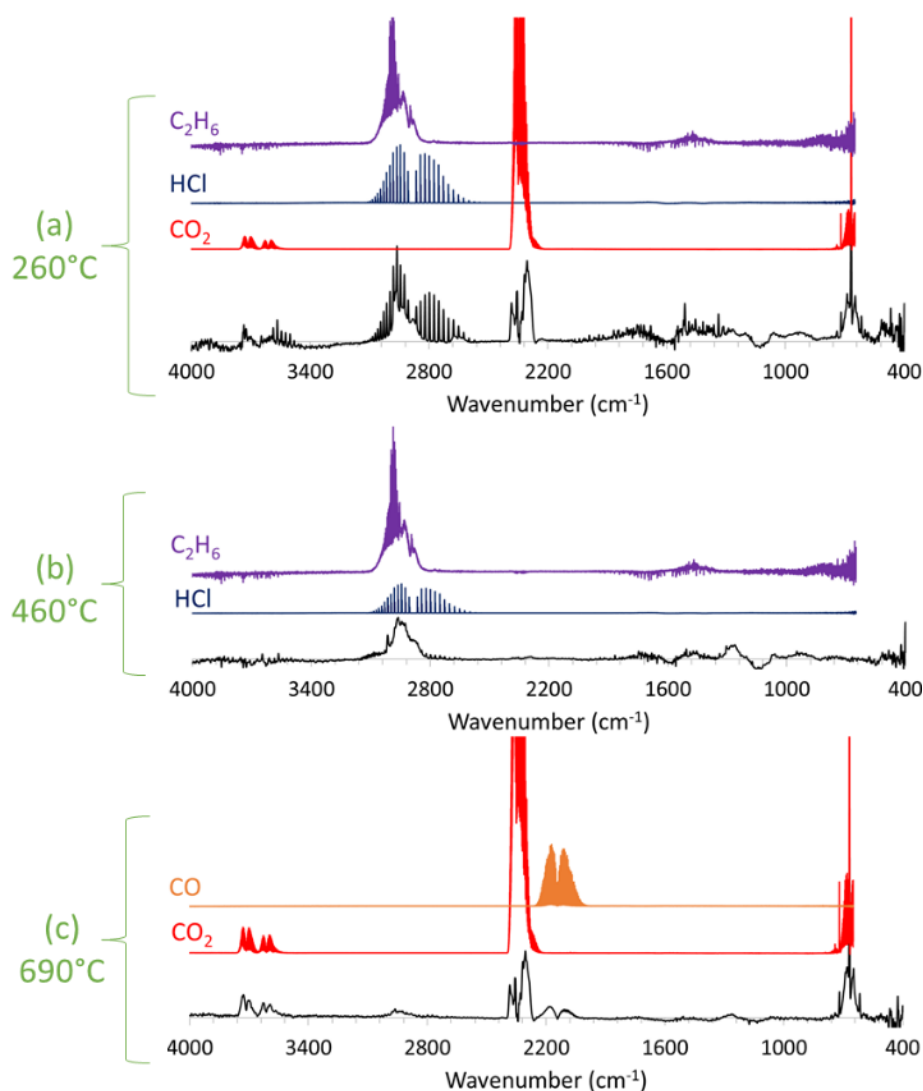


Figure 25: FTIR spectra corresponding to the temperatures of the electrical PVC cable sheath dTG curve peaks

At the maximum of the first step of decomposition 260°C (Figure 25a), the typical vibrations observed are carbon dioxide (CO_2) between 750 and 610 cm^{-1} , between 2230 and 2400 cm^{-1} and between 3540 and 3750 cm^{-1} . The vibrations corresponding to hydrogen chloride (HCl) are observed between 2600

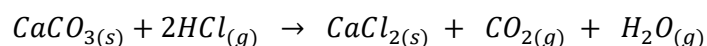
and 3100 cm^{-1} . In the same wavelength range, the $-\text{CH}_2$ bending of aliphatic compound, illustrated with the spectrum of ethane (a large peak at 2850 cm^{-1} and a thin peak at 2925 cm^{-1}) seems to be convoluted to the HCl absorption.

During the second step, at 460°C (Figure 25b), the typical thin peaks of HCl vibrations appears slightly in the range of wavelengths between 2600 and 3100 cm^{-1} while the $-\text{CH}_2$ bending of aliphatic compounds intensity increases.

For the last step, at 690°C (Figure 25c), the vibrations corresponding to CO_2 are observed and these of carbon monoxide (CO) are detected between 2010 and 2250 cm^{-1} .

Since the first decomposition step of PVC is the dehydrochlorination step with hydrogen chloride release, the detection of HCl during this step is relevant. The formation of carbon dioxide during the first step of decomposition is explained by the reaction between calcium carbonate and hydrogen chloride according to Equation 36 [100]. Thus the HCl concentration decreases [101][102].

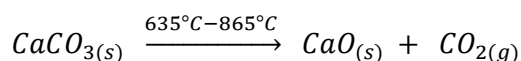
Equation 36: Reaction between calcium carbonate and hydrogen chloride formed during decomposition of PVC cable sheath



The second step of decomposition is the condensation and dehydrogenation reactions along with dealkylation. Dealkylation produces light molecules such as aliphatic hydrocarbons and condensation reactions produce heavy molecules such PAHs (Polycyclic Aromatic Hydrocarbons). Such heavy molecules cannot be seen with FTIR spectroscopy as they are not at a gaseous state at the sampling line and cell temperature of 225°C . Furthermore, aromatic species that passes through the FTIR cell such as benzene are difficult to detect with FTIR spectrometry as they have a very low spectral activity. That is why only aliphatic compounds are detected during this step.

The final step is due to the decomposition of calcium carbonate (CaCO_3) into calcium oxide (CaO) according to Equation 37. The formation of carbon monoxide at this temperature is not fully understood. It may be due to the decomposition a transient char or of an unknown compound in the cable sheath formulation.

Equation 37: Decomposition of calcium carbonate into calcium oxide and carbon dioxide



To sum up, the TGA-FTIR analysis of the electrical PVC cable sheath confirms the conclusions drawn from the elementary analysis regarding the polymer and the filler present in the formulation and gives

some extra information regarding the interactions between PVC and CaCO_3 during thermal decomposition.

4. Separate characterization of the main components of the electrical cable sheath

4.3. PVC cable sheath main components thermal stability and interactions

4.3.1. Thermogravimetry analysis of the individual components

As concluded previously (p.92), three main components were identified and quantified in the cable sheath formulation: namely PVC, DIDP and CaCO_3 . The thermal stability of each component was evaluated (Figure 26).

PVC decomposes in two steps, the first one starts at 240°C and ends at 360°C, leaving an intermediate residue of 38 wt. %, the second one starts at 420°C and ends at 520°C leaving a final residue of 12 wt. %. DIDP starts decomposing at 160°C and is completely volatilized at 315°C. The thermal decomposition mechanism of DIDP is proposed subsequently in section 4.3.3. CaCO_3 decomposes between 610°C and 780°C where it is formed a 56 wt. % stable residue.

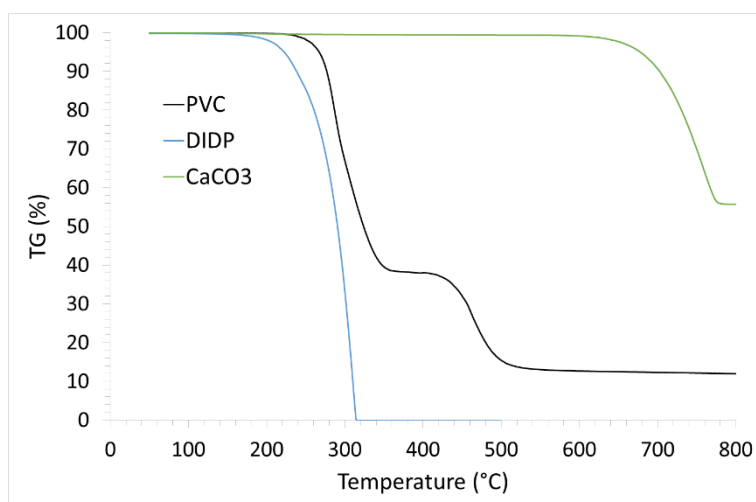


Figure 26: Thermal stability of the cable sheath formulation three main components under nitrogen at 10°C.min⁻¹

4.3.2. Thermogravimetry analysis of the components formulated together

Thereafter, DIDP and CaCO_3 were added to PVC one by one, following the weight ratio determined in Table 17 (p. 92). In order to get a homogeneous mixture, the formulations were made by solubilization.

The thermal stability of PVC with DIDP and PVC with DIDP and CaCO_3 were tested to highlight possible interactions between the components while they are thermally decomposing. The experimental TG curves are compared with their associated calculated TG curves. The calculated TG curve is a linear

combination of the TG experimental curves of each individual component weighted by their content on the formulation. There is an interaction between the components during their thermal decomposition if there is a difference between the experimental TG curve and the calculated TG curve.

For the study of the effect of DIDP on the thermal stability of PVC, the calculated TG curve is based on Equation 38. For the study of the effect of CaCO_3 on the thermal stability of PVC and DIDP, the calculated TG curve is based on Equation 39.

Equation 38: Calculated TG curve of the PVC+DIDP formulation

$$W_{\text{calculated PVC+DIDP}}(T) = \omega_{\text{PVC}} \times W_{\text{PVC}}(T) + \omega_{\text{DIDP}} \times W_{\text{DIDP}}(T)$$

Equation 39: Calculated TG curve of the PVC+DIDP+ CaCO_3 formulation

$$W_{\text{calculated PVC+DIDP+CaCO}_3}(T) = \omega_{\text{PVC+DIDP}} \times W_{\text{PVC+DIDP}}(T) + \omega_{\text{CaCO}_3} \times W_{\text{CaCO}_3}(T)$$

With ω_i the weight fraction of component i in the formulation and $W_i(T)$ the experimental TG curve of component i.

The addition of DIDP to PVC seems to destabilize the PVC matrix as the onset decomposition temperature shifts from 240°C for the neat PVC to 205°C for the PVC+DIDP formulation. Symmetrically, PVC provokes a delay in DIDP decomposition as the onset decomposition temperature of DIDP is 160°C (Figure 27a). The calculated TG curve is plotted in dashed lines. There is no significant interaction between PVC and DIDP during thermal decomposition as the calculated curve is almost superposed on the experimental curve of PVC+DIDP.

The addition of CaCO_3 to PVC+DIDP seems to have no effect on the onset temperature of thermal decomposition as the PVC+DIDP+ CaCO_3 experimental TG curve is superposed on the PVC+DIDP experimental TG curve. The calculated curve has a small delay on the onset of decomposition for the first step which means that the presence of the supposedly inert filler at these temperatures should have retarded the onset decomposition temperature of the formulation. An interaction between CaCO_3 and PVC+DIDP has then been highlighted and it is consistent with the reaction between CaCO_3 and the hydrogen chloride evolved from the dehydrochlorination of PVC during this step. After the first step of decomposition, the calculated curve is under the experimental curve. This may be due to the formation of CaCl_2 during the reaction between CaCO_3 and HCl ($M(\text{CaCl}_2) = 110 \text{ g.mol}^{-1} > M(\text{CaCO}_3) = 100 \text{ g.mol}^{-1}$). Regarding the final step decomposition, the calculated curve is in adequacy with the one of CaCO_3 with a final residue stable at 780°C whereas the experimental curve shows a step that ends much earlier with a final residue stable at 720°C. This suggests that the decomposition of CaCO_3 depends on its environment and seems to be accelerated in presence of PVC+DIDP.

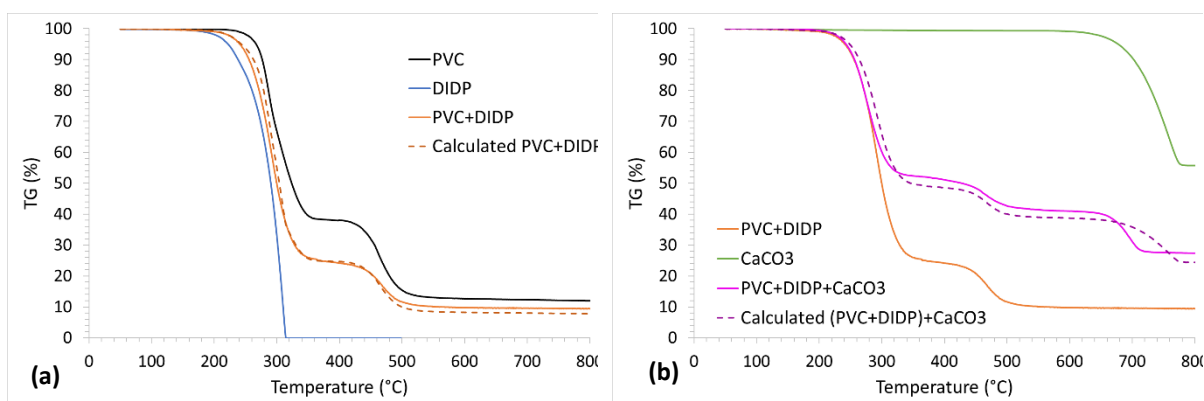


Figure 27: a) The effect of DIDP on PVC thermal stability; b) The effect of CaCO₃ on PVC+DIDP thermal stability under nitrogen at 10°C.min⁻¹

4.3.3. Decomposition analysis of DIDP by Py-GC/MS

A Py-GC/MS analysis is performed on DIDP to disclose its thermal decomposition mechanism. Figure 28 is the obtained desorption spectra. There are five peaks of desorbed molecules. When analyzing the results, the MS spectra were consulted at the beginning, at the middle and at the end of each peak in order to make sure that no convolution occurred. The spectra were the same thus only one spectrum related to one peak is presented. The percentage of confidence for a given molecule according to the obtained MS spectra is calculated by the software and is reported in the bracket aside each molecule. The firsts three peaks are very close to each other, which means that they are similar molecular weight molecules with a similar affinity with the GC column, i.e. similar polarity. The first peak (a) corresponds to 3,7-dimethyl-1-octanol with a 95% confidence. The second peak (b) is an unidentified molecule. The third peak (c) is isodecanol with a 95% confidence. Molecule (a) and molecule (c) being isomers and molecule (b) desorbing between, it can be deduced that molecule (b) is an alcohol with the same molecular formula. The forth peak (d) corresponds to phthalic anhydride with a certainty of 99%. For the fifth and last peak, it is deduced that it corresponds to the remaining DIDP that has not decomposed. Unfortunately, DIDP is not present in the database (which is why an Asterix is put in the bracket aside the molecule instead of the actual percentage of confidence presented by the software) but the software proposed a similar phthalate (didodecyl phthalate, which has two chains of 12 saturated hydrocarbons without any ramification) with a certainty of 86%.

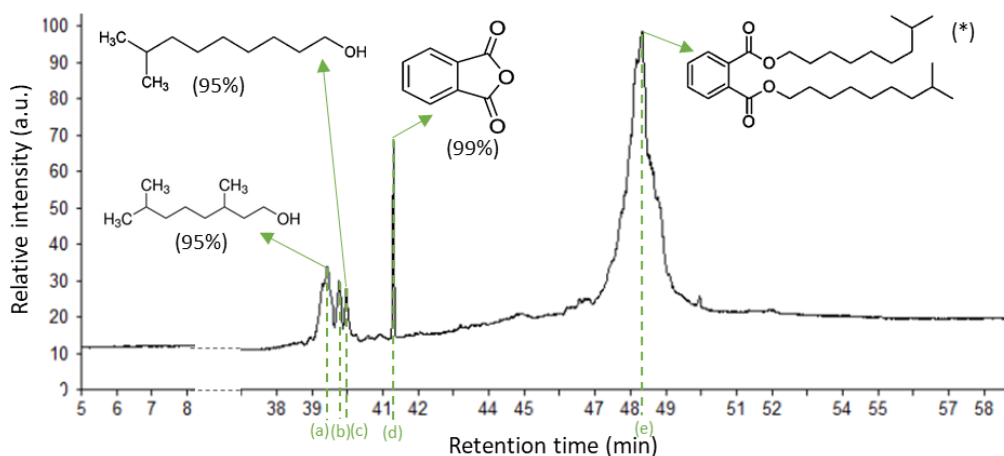


Figure 28: Py-GC/MS spectra for DIDP heated at $10^{\circ}\text{C}.\text{min}^{-1}$ (temperature range : $50\text{--}220^{\circ}\text{C}$)

Regarding the Py-GC/MS results, a DIDP decomposition reaction is proposed in Figure 29.

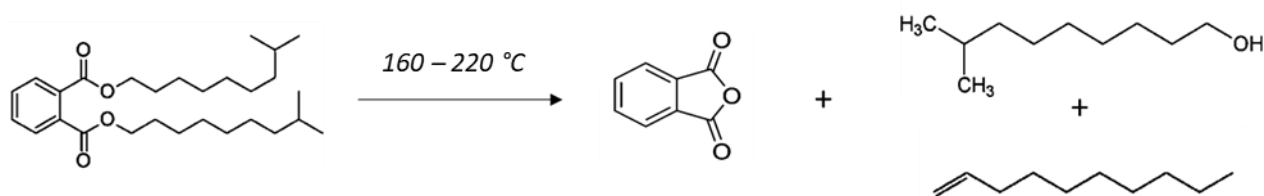


Figure 29: Proposed DIDP decomposition reaction

However, 1-decene has not been identified with the Py-GC/MS experiment. Further investigation would be needed.

Thermal decomposition of phthalates is not well-studied in the literature and even less for DIDP. Even so, some results of thermal decomposition of DOP (didodecyl phthalate) using Py-GC/MS are in accordance with the proposed reaction for DIDP [103].

4.4. Choice of stabilizing system

PVC should be particularly resistant to thermal degradation because of the high bond-dissociation energy between carbon and chlorine ($\Delta H_{298}^0(\text{C-Cl}) = 331 \text{ kJ.mol}^{-1}$ while $\Delta H_{298}^0(\text{C-C}) = 85 \text{ kJ.mol}^{-1}$ for example). Several researchers have highlighted that the destabilization of PVC when heated is due to flaws in its structure that are formed during polymerization. These structural flaws bring about one chlorine atom to be in allylic position (in the alpha position of a double bond), which makes it labile, i.e. very easy to be ripped of the PVC macromolecule. The detached radical chlorine reacts backwards on the PVC macromolecule to rip the proton on the same position as another chlorine atom, leaving the chlorine atom in an allylic position again. This phenomenon is called the autocatalytic

dehydrochlorination and has to be avoided. For this purpose, stabilizers have to be added to the PVC formulation.

A majority of the PVC stabilizers available in the market have a common mode of action described in Figure 30 [104]. This mechanism involves a stabilizer MY, where M must be able to form a stable salt with the chlorine ion and Y is a ligand capable of nucleophilic substitution with the allylic chlorine. MY must also be able to react with HCl to inhibit the autocatalytic dehydrochlorination.

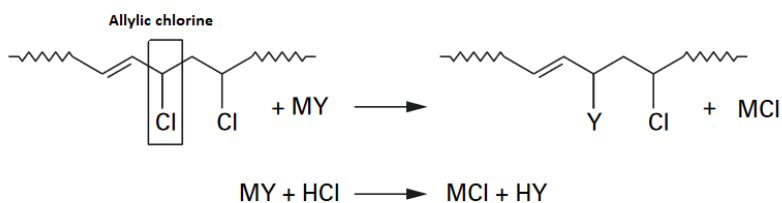


Figure 30: PVC stabilization mechanism

Most of PVC stabilizers are actually mixtures of additives. Stabilizers are mixed with organic and inorganic co-stabilizers that help the primary stabilizer to slow down the PVC degradation. Nowadays, the most used stabilizing system for soft PVC formulation, especially in the cable industry, is Ca/Zn metallic soap. It is a mixture of stearate and oleate salts (C=18), laurate salts (C=12), and benzoate derivatives. The long carboxylate chains play the role of the ligand (Y) and the Ca and Zn atoms play the role of the metallic ion (M) in Figure 30. Likewise lead-based stabilizers, the metallic soaps are sold in a “one-pack” including metallic carboxylate mixture, co-stabilizers and lubricants. The stabilizing system is usually introduced at a 5 phr load in soft PVC formulations.

5. Elaboration and characterization of representative and simplified materials

5.1. Elaboration of PVC materials

The formulation of the electrical PVC cable sheath representative material is given under the name “filled PVC”. The formulation of the simplified material, used to bridge the gap towards the comprehension of the decomposition mechanisms of the representative material is given under the name of “unfilled PVC”. These two formulations are described in Table 18 and pictures of the plaques are displayed in Figure 31.

Table 18: Formulation of the representative (filled PVC) and the reference (unfilled PVC) materials

Filled PVC – representative material			Unfilled PVC – simplified material		
Component	Phr	Mass fraction (wt. %)	Component	phr	Mass fraction (wt. %)
PVC	100	38.3	PVC	100	55.9
DIDP	74	28.4	DIDP	74	41.3
CaCO₃	82	31.4	Ca/Zn	5	2.8
Ca/Zn	5	1.9			

Figure 31: 100×100 mm² Plaques of a) Filled PVC; b) Unfilled PVC

Plaque of filled PVC is opaque with a brownish tint due to the color of the incorporated CaCO₃. In its pure form, CaCO₃ is a white powder but the used grade contains processing aids that gives it a light brown color. Plaque of unfilled PVC is translucent and uncolored.

In Figure 32 are shown the TG and dTG curves obtained when submitting the cryoground powder from a plaque of filled PVC (a) and unfilled PVC (b) to a thermal analysis under nitrogen at 10°C.min⁻¹.

The representative material (filled PVC) decomposes in three steps. The first one occurs from 215°C to 330°C, leaving an intermediate residue of 49 wt. %. The second one occurs between 420°C and 500°C and leaves an intermediate residue of 38 wt. %. The third one, from 640°C and 725°C, leaves a final residue of 29 wt. %. The reference material (unfilled PVC) decomposes in two steps. Similarly to the representative material, the first one occurs between 215°C and 330°C and the second one between 420°C and 500°C. The intermediate residue is 26 wt. % and the final residue is 12 wt. %.

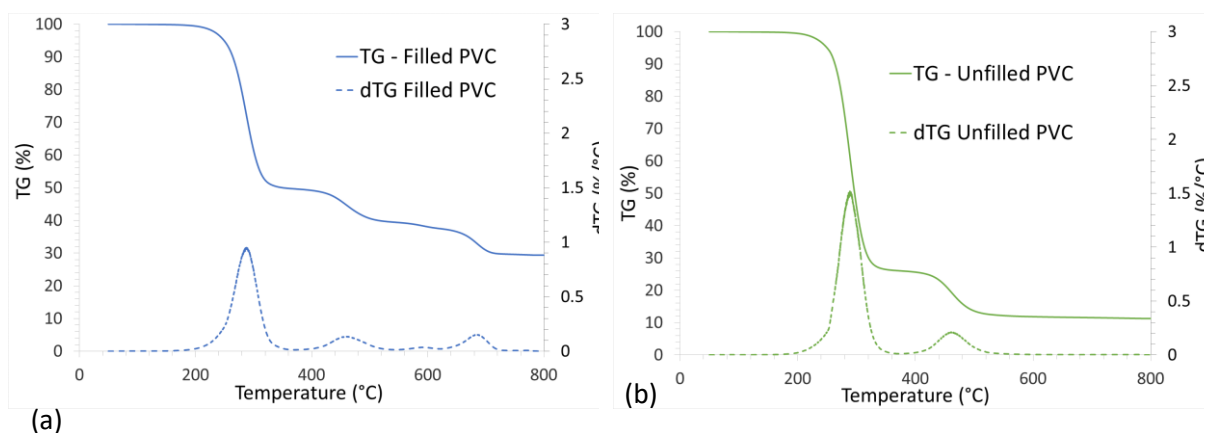


Figure 32: Thermal stability of filled PVC (a) and unfilled PVC (b) under nitrogen at $10^{\circ}\text{C}.\text{min}^{-1}$

5.2. Comparison of the reference material with the electrical cable sheath

A comparison of the thermal stability of the electrical PVC cable sheath material and the representative material (filled PVC) is made in Figure 33 where their respective TG and dTG are plotted together. Decomposition steps are similar. The first step onset temperature is identical even though the step is steeper for the electrical cable sheath material. The compound involved in this accelerated decomposition has not been elucidated. Final residue of electrical cable sheath material at 800°C is 40 wt. % whereas the final residue of representative material at 800°C is 29 wt. %. This is probably due to lead-based, aluminum-based or titanium-based compounds, identified in the cable sheath formulation (cf. section 3.4 p. 89), that have not been incorporated in the representative material in a scope of formulation simplification. The amount of filler incorporated in the formulation was not calculated in order to match the electrical cable sheath residue because the scavenging effect of hydrogen chloride with calcium carbonate (cf. section 3.5 p. 92) would have been overrated.

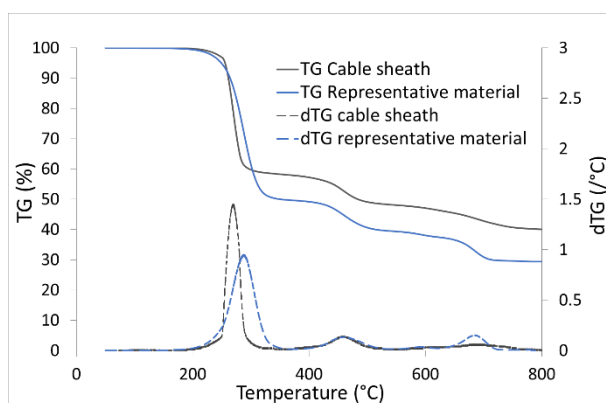


Figure 33: Electrical cable sheath material and representative material thermal stability comparison under nitrogen at $10^{\circ}\text{C}.\text{min}^{-1}$

5.3. Characterization of filled and unfilled PVC properties for numerical simulation inputs

Plaques of filled and unfilled PVC were made to be tested in the controlled-atmosphere cone calorimeter. During these tests, plaques are placed under the conical resistance and are impacted with a radiative heat flux of 50 kW.m^{-2} that induces a thermal decomposition. During thermal decomposition, various phenomena take place inside the material i.e. thermal conduction, chemical reactions, transport of heat and gaseous products, convection, radiation, and heat flux at the exposed face.

As a tool for helping the comprehension of the phenomena occurring during experimental testing, a numerical simulation of the cone calorimeter experiment is done according to a pyrolysis model⁴⁵ [105]. The input data for the numerical simulation are the physical properties listed in Table 19.

Table 19: Properties used as input data for numerical simulation of cone calorimeter experiments

Thermal Properties	Heat capacity – C_p [$\text{J.kg}^{-1}.\text{K}^{-1}$]
	Thermal conductivity – λ [$\text{W.m}^{-1}.\text{K}^{-1}$]
Optical properties	Absorbance – A
	Absorption coefficient – α [m^{-1}]
Chemical properties	Pre-exponential constant – A [s^{-1}]
	Activation energy – E_a [J.mol^{-1}]
	Heat of decomposition – Δh [J.kg^{-1}]
	Heat of combustion – Δh_c [J.kg^{-1}]
Material properties	Permeability – κ [m^2]
	Porosity – ε_g [$\text{kg}_g.\text{kg}_t^{-1}$]
	Viscosity – μ [Pa.s]
	Density – ρ [kg.m^{-3}]

In [105], the properties used as input data for the numerical simulation of PVC behavior in the cone calorimeter are taken from the literature [106] and stand for neat PVC. In the aim at being more precise for the simulation of the experimental study done with the formulated filled and unfilled PVC, the characterization of some of the properties listed in Table 19 was done and the results are given in this section.

⁴⁵ Developed during Luc Murer's master thesis, related to this PhD work.

Physical properties of the materials vary with temperature but are only measured at ambient temperature. They are implemented in the numerical simulation at ambient temperature as a first approximation.

5.3.1. Absorbance

Filled PVC is opaque in the spectral range between 8 and 14 μm . The absorbance in this range can be deduced:

$$A_{\text{filled PVC}} = 0,95$$

Because the unfilled PVC is not opaque in the spectral range between 8 and 14 μm , its emittance is not directly related to its reflectance. A measurement of the transmittance of the material is then needed to know its emissivity and this measurement has not been performed.

5.3.2. Thermal conductivity

The results obtained after performing hot disk testing are the following:

$$\lambda_{\text{filled PVC}} = 0,28 \text{ W} \cdot \text{m}^{-1} \cdot \text{K}^{-1}$$

$$\lambda_{\text{unfilled PVC}} = 0,18 \text{ W} \cdot \text{m}^{-1} \cdot \text{K}^{-1}$$

5.3.3. Heat capacity

The heat capacity (C_p) is the heat (Q) needed from a body of a mass m to vary its temperature of ΔT (Equation 40).

Equation 40: Definition of heat capacity

$$C_p = \frac{Q}{m \times \Delta T}$$

The results obtained after performing DSC testing are shown in Figure 34.

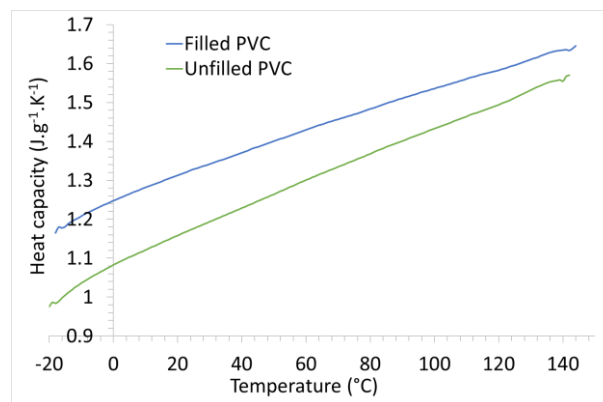


Figure 34: Heat capacity of Filled and Unfilled PVC as a function of temperature

The heat capacity at 20°C (i.e. at ambient temperature) is read on the graph. The values are:

$$Cp_{filled\ PVC} = 1\,310\ J.kg^{-1}.K^{-1}$$

$$Cp_{unfilled\ PVC} = 1\,160\ J.kg^{-1}.K^{-1}$$

5.3.4. Heat of decomposition

Figure 35a shows STA results for filled PVC and Figure 35b shows STA results for unfilled PVC. On each graph, the mass loss obtained with TGA under nitrogen with a $10^{\circ}C.min^{-1}$ heating ramp is also shown. By integrating the areas under the heat flow curve during a decomposition step, it is possible to obtain the enthalpy of the related reaction. The enthalpy related to a mass unit is calculated with the mass at the left boundary of the peak. This may lead to a certain amount of error, especially when a weight loss is consequent during a decomposition step, which is the case for the first step of decomposition. The recalculated enthalpies for each step of decomposition are the one noted in Figure 35. During the first step of decomposition, both filled and unfilled PVC undergo an endothermic reaction that has an enthalpy of $-132.5\ J.g^{-1}$ and $-315.3\ J.g^{-1}$ respectively. Both materials second step of decomposition is also an endothermic reaction that requires much less energy than the first one. The enthalpy of decomposition is of $-82.6\ J.g^{-1}$ for filled PVC and $-50.1\ J.g^{-1}$ for unfilled PVC. Filled PVC third step of decomposition, that corresponds to the transformation of calcium carbonate into calcium oxide, is also an endothermic reaction that has an enthalpy of $-491.5\ J.g^{-1}$.

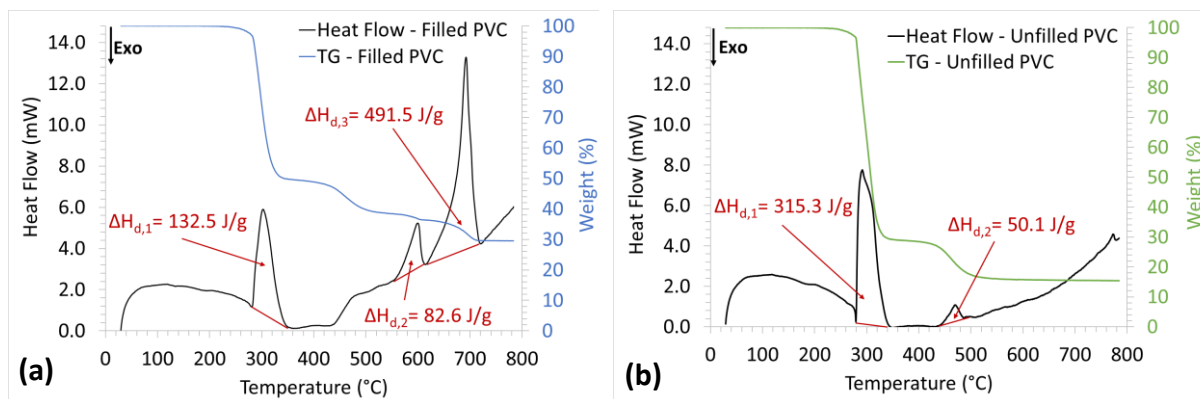


Figure 35: Heat flow (DSC) and weight loss (TG) signals for a) Filled PVC; b) Unfilled PVC

5.3.5. Heat of combustion

The heat of combustion of pyrolysis products as a function of temperature is plotted in Figure 36a for filled PVC and in Figure 36b for unfilled PVC. By integrating the area under each peak, the heat of combustion for each decomposition step is calculated. For both filled and unfilled PVC, the first step of decomposition is the one that releases the most part of heat ($9.2\ MJ.kg^{-1}$ and $14.2\ MJ.kg^{-1}$ respectively). During this step of decomposition, for both of the materials, occurs the release of mainly hydrogen chloride from PVC and the decomposition of DIDP. Hydrogen chloride is incombustible so

the main part of the heat release comes from the combustion of DIDP decomposition products. During the second step of decomposition, for both filled and unfilled PVC, the heat released comes from the combustion of the remaining polyene decomposition products. It is worthy to note that there is not third peak of HRR for filled PVC. This was expected since the filled PVC third step of decomposition, corresponding to calcium carbonate transformation into calcium oxide, releases carbon dioxide which is an incombustible gas.

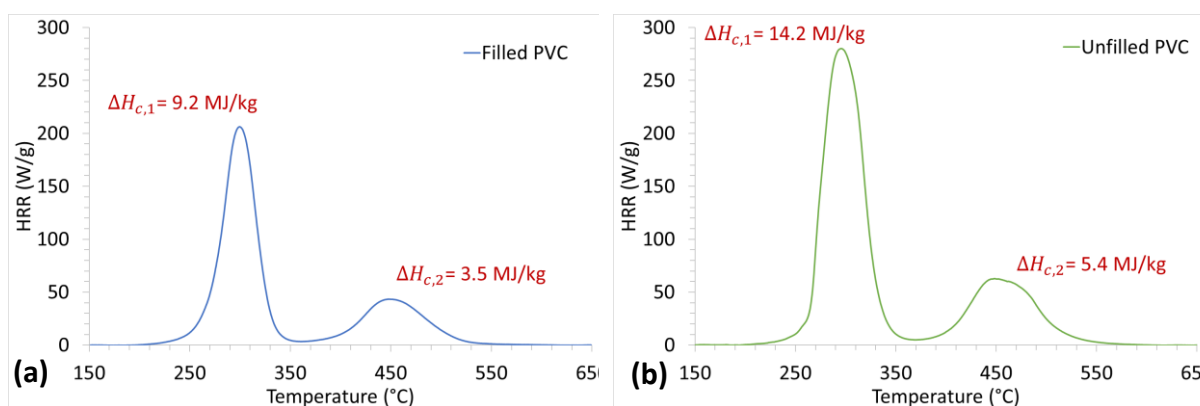


Figure 36: PCFC results for a) Representative material - Filled PVC; b) Reference material - Unfilled PVC

5.3.6. Kinetics of thermal decomposition

Thermal decomposition of the materials was studied under nitrogen at different heating rates, from $0.25^{\circ}\text{C}\cdot\text{min}^{-1}$ to $100^{\circ}\text{C}\cdot\text{min}^{-1}$ in order to seize the overall decomposition of the materials in a wide range of conditions, from slow to high heating rates, simulating different heating rate fire scenarios.

For unfilled PVC, the fit between the modelled kinetic and the experimental data is shown in Figure 37. The mechanistic path chosen is two consecutive step reactions. The first reaction is a n-th order autocatalytic decomposition, and the second reaction is a n-th order Arrhenius decomposition. The fixed parameters are the initial and final weights. The experimental curves are in dotted lines and the simulated curves are in full lines.

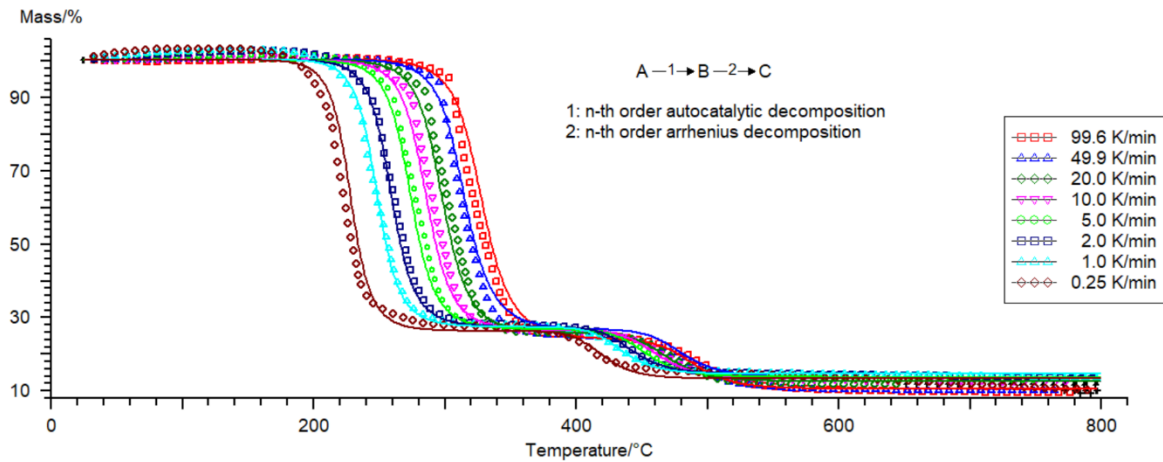


Figure 37: Fit between modelled kinetics (lines) and experimental data (points) for unfilled PVC decomposition under nitrogen

For filled PVC, the fit between the modelled kinetic and the experimental data is shown on Figure 38. The mechanistic path chosen is three consecutive step reactions. As for unfilled PVC, the first reaction is a n-th order autocatalytic decomposition, and the second reaction is a n-th order Arrhenius decomposition. The third reaction is also a n-th order Arrhenius decomposition. The fixed parameters are the initial and final weights. The experimental curves are in dotted lines and the simulated curves are in full lines.

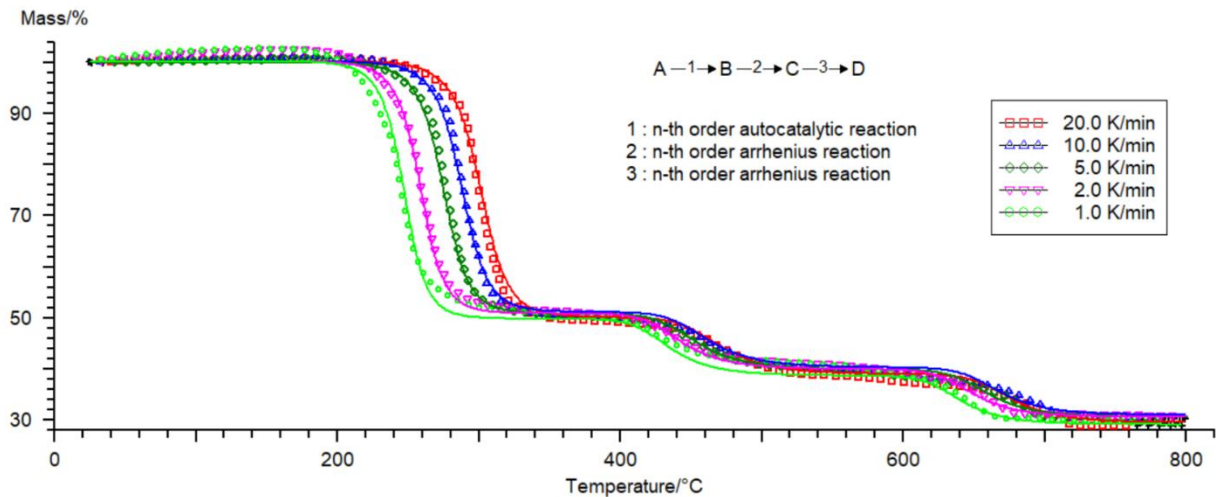


Figure 38: Fit between modelled kinetics (lines) and experimental data (points) for filled PVC decomposition under nitrogen

For unfilled PVC, the kinetic equation of the first step of decomposition is Equation 41 and the one of the second step decomposition is Equation 42. For filled PVC, the kinetic equation of the first step decomposition is Equation 41, the one of the second step decomposition is Equation 42 and the one of the third step decomposition is Equation 43. Values of all the parameters as well as their standard deviation are listed in Table 20 for both materials.

Chapter III: Representative material elaboration

Equation 41: Kinetic equation for the autocatalytic first step of decomposition

$$\frac{dA}{dt} = -A_1 \times e^{-E_1/RT} \times e^{n_1} (1 + Kcat_1 \times B)$$

Equation 42: Kinetic equation for the Arrhenius second step of decomposition

$$\frac{dB}{dt} = -A_2 \times e^{-E_2/RT} \times e^{n_2}$$

Equation 43: Kinetic equation for the Arrhenius third step of decomposition

$$\frac{dC}{dt} = -A_3 \times e^{-E_3/RT} \times e^{n_3}$$

With:

- A the concentration of the virgin component;
- B the concentration of the first intermediate component;
- C the concentration of the second intermediate component (only for filled PVC);
- A_i the pre-exponential factor for reaction i ;
- E_i the activation energy of reaction i ;
- n_i the order of reaction i ;
- $Kcat$ the autocatalytic constant.

Table 20: Kinetic parameters for unfilled PVC and filled PVC decomposition

Material	Parameter	Optimum value	Std Dev.
Unfilled PVC	$\log(A_1/[s^{-1}])$	10.59	0.06
	E_1 (kJ/mol)	140.57	0.63
	n_1	1.95	0.05
	$\log(Kcat_1)$	0.99	0.04
	$\log(A_2/[s^{-1}])$	24.08	0.83
	E_2 (kJ/mol)	363.64	11.79
Filled PVC	$\log(A_1/[s^{-1}])$	9.31	0.11
	E_1 (kJ/mol)	128.34	1.01
	n_1	1.69	0.05
	$\log(Kcat_1)$	1.02	0.05
	$\log(A_2/[s^{-1}])$	23.45	1.06
	E_2 (kJ/mol)	353.94	14.82
	n_2	2.98	0.25
	$\log(A_3/[s^{-1}])$	31.16	2.52

	E₃ (kJ/mol)	592.09	44.18
	n₃	2.90	0.19

5.3.7. Conclusion

All the measured parameters for filled and unfilled PVC, as well as parameters for neat PVC from the literature [106] are gathered in Table 21.

Table 21: Comparison of measured parameters for filled and unfilled PVC with neat PVC from literature [106]

Parameter	PVC (literature)	Filled PVC	Unfilled PVC
Density (kg.m⁻³)	1430	1413 ³	1180 ⁴⁶
Thermal conductivity (W.m⁻¹.K⁻¹)	0.17	0.28	0.18
Heat capacity (J.kg⁻¹.K⁻¹)	1720	1310	1160
Absorbance	0.90	0.95	/
Enthalpy of decomposition (J.kg⁻¹)	1.7 x 10 ⁵	1.3 x 10 ⁵	3.2 x 10 ⁵
	1.2 x 10 ⁶	8.3 x 10 ⁴	5.0 x 10 ⁴
		4.9 x 10 ⁵	
Heat of combustion (J.kg⁻¹)	2.7 x 10 ⁶	9.2 x 10 ⁶	1.4 x 10 ⁷
	3.7 x 10 ⁷	3.5 x 10 ⁶	5.4 x 10 ⁶
Activation energy (kJ.mol⁻¹)	249	128	140
	192	354	360
		592	
Pre-exponential factor (s⁻¹)	9.5x10 ²⁰	4.9x10 ¹⁰	3.8x10 ¹¹
	5.5x10 ¹¹	3.6x10 ²⁴	1.2x10 ²⁴
		6.9x10 ³²	

Density of neat PVC is surprisingly close to the one of filled PVC. In [106], the details of the studied material are not elaborated so it is not known if the material is pure or if it has additives. This high density may be due to some heavy weight additives such as pigments or stabilizers.

⁴⁶ Density has been determined by measuring the mass of a plaque and dividing it by its volume.

Thermal conductivity of unfilled PVC is very close to the one of neat PVC. It is noted that presence of calcium carbonate in the formulation increases thermal conductivity.

The heat capacity of neat PVC from the literature is quite different to the one of unfilled PVC. Presence of calcium carbonate slightly increases heat capacity.

Absorbance of neat PVC is quite similar to the one of filled PVC and enthalpies of decomposition are in the same range for the three materials.

As regards the kinetic study, activation energies and pre-exponential factors are similar for the first two steps of decomposition for filled and unfilled PVC. This was expected since the same reactions are involved and the same mechanistic path were chosen. On the other hand, activation energies and pre-exponential factors for neat PVC in the literature are quite different. It may be explained by the different mechanistic path chosen for the modelling. s

6. Conclusion

A PVC-based electrical cable sheath displayed in French NPPs was analyzed. It contains 31.2 wt. % of PVC, 23.2 wt. % of DIDP, 26.2 wt. % of CaCO_3 , and approximately 3 wt. % of a lead-based stabilizing system and 16 wt. % of unknown compounds.

Thermal stability of each of the three main components (PVC, DIDP and CaCO_3) was studied separately and formulated collectively in order to highlight possible interactions. The only highlighted interaction is the one between PVC and CaCO_3 during thermal decomposition: calcium carbonate adsorbs hydrogen chloride evolved from the PVC decomposition. A reaction occurs to form calcium chloride and carbon dioxide.

A representative material containing 38.3 wt. % of PVC, 28.3 wt. % of DIDP, 31.4 wt. % of CaCO_3 and 1.9 wt. % of a Ca/Zn stabilizing system was manufactured to study the fire behavior of this electrical cable sheath while controlling its composition. Besides, a reference material containing 55.8 wt. % of PVC, 41.3 wt. % of DIDP and 2.8 wt. % of Ca/Zn stabilizing system was also manufactured to study the thermal decomposition of a simplest material and bring key elements for the comprehension of the representative material thermal decomposition.

Finally, thermo-physical, chemical and optical properties of the representative and the reference materials were determined in the aim at predicting their fire behavior through numerical modelling.

Chapter IV: Study of the under-ventilation effect

1. Introduction	111
2. Data processing	112
2.1. Data acquisition	112
2.2. Data smoothing	113
2.3. Data presentation	113
2.3.1. Mass loss, mass loss rate and heat release rate	113
2.3.2. Gases and aerosols	114
3. Description of the experiments	114
4. Well-ventilated experiments in the open configuration cone calorimeter	117
4.1. Mass loss and heat release rate measured with cone calorimeter in an open configuration	118
4.2. Evolved gases measured with cone calorimeter in an open configuration	124
4.3. Evolved aerosols measured with cone calorimeter in an open configuration	126
4.4. Discussion on the well-ventilated fire parameters and combustion products	129
5. Under-ventilated experiments in the controlled-atmosphere cone calorimeter	131
5.1. Characterization of the fire regime	131
5.2. Influence of the confinement on the fire parameters	132
5.3. Influence of the confinement on evolved gases	136
5.4. Influence of the confinement on evolved aerosols	138
5.5. Discussion on the influence of the confinement on fire parameters and combustion products	140
6. Conclusion	142

1. Introduction

In this chapter, a first section is dedicated to the data processing: transfer time correction to match smoke and material dynamic measurements, algorithm applied to smooth raw data, and presentation of the standard deviation in the figures. In a second section, the phenomenology of PMMA⁴⁷ and PVC

⁴⁷ 5 mm-thick transparent PMMA sheets are supplied by Good Fellow and cut into 100×100 mm² plaques. This material has been characterized by TGA/FTIR to control and validate its composition. It thermal decomposes in one step under nitrogen at 10°C.min⁻¹, which means that this is a PMMA polymerized by an anionic pathway [135].

formulations experiments in the cone calorimeter is described and illustrated. In a third section, the results of the tests performed in the cone calorimeter in its open – well-ventilated – configuration with plaques of PMMA, filled and unfilled PVC are exposed according to fire parameters, gases and aerosols measurements. Then, the enclosed – under-ventilated – configuration fire regime is characterized in terms of $[CO]/[CO_2]$ ratio and equivalence ratio as a function of time for the three materials. Finally, in a fourth section, the results in both open and enclosed configurations at 21 vol. % of oxygen are compared to highlight the effect of the confinement, i.e. under-ventilation, on the heat release rate, mass loss rate, and evolved gases and aerosols.

2. Data processing

2.1. Data acquisition

The measurement methods and the transfer times of the acquired and presented data are gathered in Table 22 below. The transfer time – or the mean time of passage – is subtracted to the measurement time before plotting the data on the figures. For example, on the raw smoke oxygen concentration data, the oxygen concentration starts to decrease only 10 seconds after the time to ignition (TTI). The oxygen consumption is a marker of the flame presence. It means that the transfer time for the smoke oxygen concentration measurement is about 10 seconds.

Table 22: Measurement methods and transit times for different types of acquired data

Data	Measurement method	Transfer time
Time to ignition (TTI) and time to extinction (TTE)	Observation	≈ 0 s
Mass	Load cell	≈ 0 s
HRR_{thermo}¹	Thermopile	≈ 0 s
HRR_{O₂}^{2,3}	Paramagnetic oxygen sensor	≈ 10 s
Gases³	FTIR spectrometer	≈ 10 s
Aerosols³	ELPI granulometer	≈ 10 s

¹HRR measured by thermopile

²HRR measured by oxygen consumption calorimetry

³Transfer times were estimated by matching flame markers (CO_2 , H_2O , O_2) with TTI. The sampling flow rate is constant throughout the experiments.

2.2. Data smoothing

Mass loss data has to be smoothed otherwise its time derivate signal (mass loss rate) is too noisy. Raw mass loss data is smoothed with the inverse square algorithm. This algorithm computes the weighted average of the valued at neighboring points, with a sampling portion of 0.05 and using the Cauchy density function. The smoothing algorithm and the sampling portion were chosen in the aim at causing the least modification on the data while getting a derivate signal readable. For example, the superposition of raw and smoothed signals in the case of PMMA decomposition in the open cone calorimeter is displayed on Figure 39a for the mass loss and on Figure 39b for the mass loss rate.

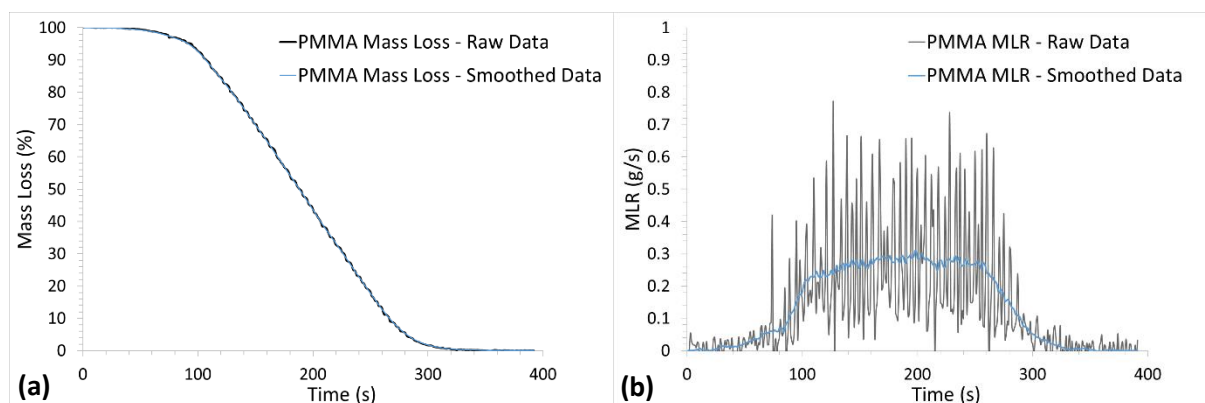


Figure 39: Comparison between the raw and the smooth signals for a) Mass Loss data (both signals are superposed); b) Mass Loss Rate data

2.3. Data presentation

2.3.1. Mass loss, mass loss rate and heat release rate

For each experiment under the same conditions, at least three runs were carried out. The data presented in this chapter is processed in the aim at taking into account the experimental uncertainties and the repeatability. To do so, an average curve for all the runs, as well as the standard deviation associated, are calculated. The run curve that has the minimum difference with the average curve is chosen as the reference. The standard deviation is plotted on the same graph around the average curve which is not displayed to keep the figure clear and readable⁴⁸.

In addition, all the runs are plotted in the same figure in Appendix 4 (p.185), and characteristic values such as time to ignition (TTI), time to extinction (TTE), peak of heat release rate (pHRR) and total heat release (THR) are also gathered in the same table for each experiment.

⁴⁸ The reference curve and the average curve are almost superposed.

2.3.2. *Gases and aerosols*

For each test, gases and aerosols figures are more complex than mass loss or heat release rate figures because of the number of measured parameters, i.e. 19 gaseous compounds and 14 ranges of particle diameter. In order to keep gases and aerosols figures readable, the standard deviation is not plotted on the graphs. Nevertheless, all the data are plotted in Appendix 4 (p. 185) to assess the repeatability of each test and the pages to refer is noted at the beginning of the section.

3. Description of the experiments

Figure 40 is a succession of pictures taken during the PMMA burning experiment in the cone calorimeter in its confined configuration. Though, confined and well-ventilated visual phenomenology being the same, these illustrations are taken generally⁴⁹. The first steps represent the initiation of the chemical reaction and the onset of the nucleation process in depth. Decomposition gases migrate towards the surface because of the induced pressure gradient and buoyancy [107][108], leading to a significant bubbling phenomenon. The flame formed during ignition is a premixed flame as the combustible gases have been accumulated until reaching the lower flammability limit (picture#2 in Figure 40). Then, the bursting of bubbles leads to the formation of cavities that increase the specific area of the PMMA surface [107][108] (picture#4 in Figure 40). The rise of pressure of the gaseous products causes swelling. The thermal feedback induced by the stainless-steel sample holder at the back face of the sample enhances the decomposition rate. Bubbling effect and swelling decrease significantly. At the end of the test, the production of decomposition gases decreases causing the extinction (picture #8 in Figure 40).



(1) $t = 0 \text{ s}$

The sample is suddenly exposed to a 50 kW.m^{-2} heat flux.



(2) $t = 23 \text{ s}$

Ignition occurs and a premixed flame appears above the PMMA surface.

⁴⁹ Time of phenomenon occurrence are different between well-ventilated and confined testing.



(3) $t = 25 \text{ s}$

A diffusion flame is set above the sample surface right after ignition.



(4) $t = 126 \text{ s}$

The bubbling effect can be seen with the small flames popping all across the surface.



(5) $t = 226 \text{ s}$

The bubbling effect is over and the diffusion flame is smoothed.



(6) $t = 253 \text{ s}$

The flame is decreasing.



(7) $t = 272 \text{ s}$

Some small flames remain on the sample holder edges.



(8) $t = 345 \text{ s}$

The extinction occurs because all the combustible is consumed, leaving no residue.

Figure 40: Pictures of PMMA burning in the cone calorimeter at 50 kW.m^{-2}

Figure 41 is a succession of pictures taken during the filled PVC burning experiment in the cone calorimeter. Unfilled PVC has the same behavior in the cone calorimeter. PVC plaques exhibit a surface shrinkage when submitted to the radiative heat flux, which lowers the surface exposed to the radiative heat flux and, as a result, the total energy received by the material. This shrinkage may be due to the rapid cooling during plaque processing that may have induced some stress in the material. Also, the gases generated from the PVC thermal decomposition causes the swelling of the char to form an expanded layer (intumescence) [109] (picture#5 and picture#6 in Figure 41). Comparing with the burning of PMMA, PVC samples does not form any bubbling molten phase.



(1) $t = 0 \text{ s}$

The sample is suddenly exposed to a 50 kW.m^{-2} heat flux.



(2) $t = 24 \text{ s}$

Just before the ignition, the material begins to form a char (the dark bubble).



(3) $t = 25 \text{ s}$

The sample ignites.



(4) $t = 53 \text{ s}$

A diffusion flame is set above the sample surface.



(5) $t = 60 \text{ s}$

The char volume is increasing rapidly.



(6) $t = 173 \text{ s}$

After 173 seconds, the char volume has again increased.



(7) $t = 240 \text{ s}$

The flame surface decreases to be set only around the char.



(8) $t = 329 \text{ s}$

The flame decreases.



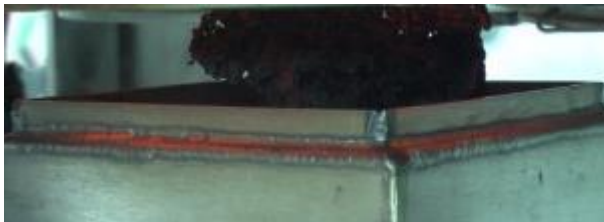
(9) $t = 534 \text{ s}$

Only a small flame remains under the char.



(10) $t = 602 \text{ s}$

The char is smoldering.



(11) $t = 625 \text{ s}$

The test is over. The char residue is concentrated at the center of the sample holder.

Figure 41: Pictures of filled PVC burning in the cone calorimeter at 50 kW.m^{-2}

4. Well-ventilated experiments in the open configuration cone calorimeter

Tests are firstly carried out in the cone calorimeter in its open configuration to obtain results in well-ventilated conditions. The ventilation rate is fixed by modulating the hood draught power in order to have a 0.9 m.s^{-1} air velocity at 20°C and 1 atm at the top of the chimney, which corresponds to a 560 L.min^{-1} volume flow rate through the system⁵⁰.

⁵⁰ The value of 0.9 m.s^{-1} was chosen to study well-ventilated combustion of new-generation electrical cable sheath [4].

4.1. Mass loss and heat release rate measured with cone calorimeter in an open configuration

- PMMA case

Normalized mass and mass loss rate of PMMA versus time are plotted on Figure 42a and Figure 42b respectively, and the heat release rate associated is presented in Figure 43⁵¹. Figure 42a shows that, for this test, the ignition takes place at 94 seconds. Figure 42b shows that the peak of mass loss rate is of 0.27 g.s^{-1} . When burning, PMMA leaves no residue (Figure 42a). This is explained by the fact that PMMA decomposes by a depolymerization mechanism and does not form any char residue. The value of pMLR during well-ventilated burning of PMMA cannot be compared with the values available in the literature because the MLR is highly dependent on the quantity of fuel burnt. In this work, the PMMA plaque thickness is 5 mm, which is considered as a thin plaque. In the literature, under 50 kW.m^{-2} , PMMA medium plaque pMLR is equal to 0.32 g.s^{-1} [110] and PMMA thick plaque pMLR is equal to 0.42 g.s^{-1} [111].

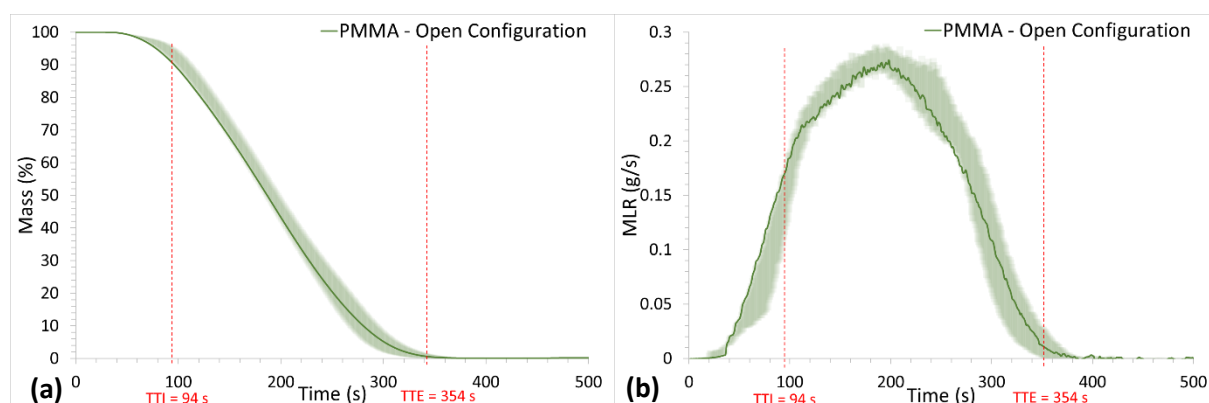


Figure 42: Evolution of mass of PMMA during well-ventilated testing. a) Normalized mass; b) Mass loss rate (cone calorimetry at 50 kW.m^{-2})

Figure 43 shows the comparison of well-ventilated PMMA HRR measurement from thermopile ($\text{HRR}_{\text{thermo}}$) and oxygen consumption (HRR_{O_2}). HRR determined with the sensible enthalpy rise method (thermopile measurement – red curve) shows a peak of 561 kW.m^{-2} and a total heat release of 106 MJ.m^{-2} whereas, with the oxygen consumption calorimetry method (green curve), HRR_{O_2} shows a peak of 696 kW.m^{-2} , which is close to the value of mean HRR_{O_2} for PMMA in the cone calorimeter under 50 kW.m^{-2} found in the literature, equal to 640 kW.m^{-2} in average [111][112]. The measured THR_{O_2} is of 126 MJ.m^{-2} . THR_{O_2} is 19.6% higher than $\text{THR}_{\text{thermo}}$. This difference is explained by the fact that the thermopile measures the heat transported by the fumes, i.e. the sensible enthalpy (temperature rise)

⁵¹ The presented result was obtained among three experiments, all displayed in Appendix 4, p.178.

of the exhaust gas stream [113] and does not take into account the heat losses (e.g. from the flame to the apparatus). These heat losses are mainly due to radiative transfers that is why they are expressed as χ_{rad} ⁵² in Figure 43, with q_{loss} the heat loss to the apparatus and q the total heat released by the flame.

Equation 44: Expression of the heat loss from the flame to the apparatus

$$q_{loss} = \chi_{rad} \times q$$

The cone calorimeter thermopile was calibrated with a methane diffusion flame. Tewarson [47] showed that for a methane diffusion flame, $\chi_{rad} = 0.14$. The HRR measurement with the thermopile formerly calibrated with a methane flame will then be consistent only for materials that have a heat loss fraction of about 0.14 and PMMA has a heat loss fraction of $\chi_{rad} = 0.30$ [47]. For this reason, the thermopile underestimates the amount of heat release rate by PMMA flames by about 25% [78]. In addition, it is noteworthy that the HRR_{O_2} curve is more respectful of the phenomenon dynamics. Indeed, the HRR_{O_2} curve shows a peak right after ignition which is due to the sudden inflammation of the gaseous compounds above the sample.

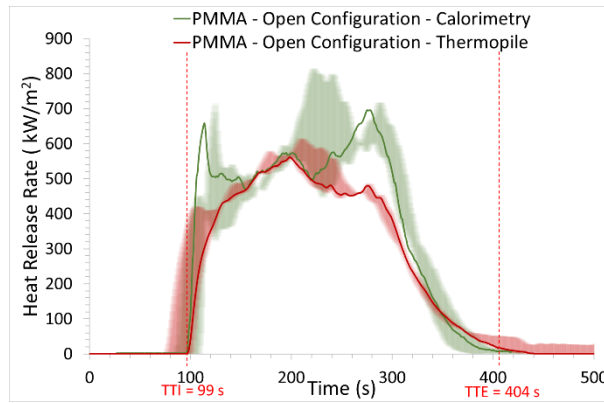


Figure 43: HRR of PMMA combustion during well-ventilated testing (cone calorimetry at 50 kW.m^{-2})⁵³

THR_{O_2} is compared with the maximum value, calculated with Equation 45 and based on the chemical heat of combustion⁵⁴ (ΔH_{ch} – equal to 24.2 MJ.kg^{-1} [47] for PMMA).

Equation 45: Calculation of theoretical maximum value of THR

$$THR_{max} = \frac{\Delta H_{ch} \times m_{plaque}}{S_{plaque}}$$

⁵² Defined in Chapter I, p. 26.

⁵³ The presented HRR result is not from the same experiment than the presented mass loss result, which is why the TTI and TTE are different. The chosen results are detailed in Appendix 4, p. 178.

⁵⁴ Defined in Chapter I, p. 26.

With m_{plaque} the plaque weight (in kg) and S_{plaque} the plaque area (in m^2).

Equation 45 applied to PMMA gives:

$$THR_{\text{max}}(\text{PMMA}) = \frac{24.2 \times 0.0533}{0.01} = 129.0 \text{ MJ} \cdot \text{m}^{-2}$$

The obtained value of THR with the oxygen consumption calorimetry ($126 \text{ MJ} \cdot \text{m}^{-2}$) is very close to the maximum value of THR calculated with Equation 45 (2% lower).

The effective heat of combustion, which corresponds to the heat released by fuel mass unit in average, can be calculated according to Equation 46.

Equation 46: Calculation of effective heat of combustion

$$EHC = \frac{THR \times S_{\text{plaque}}}{m_{\text{plaque}}}$$

In the case of well-ventilated PMMA burning, $EHC_{\text{PMMA}} = 23.6 \text{ MJ} \cdot \text{kg}^{-1}$. In the literature, this value is about $24.1 \text{ MJ} \cdot \text{kg}^{-1}$ for thick black PMMA burning in a cone calorimeter under a heat flux of $50 \text{ kW} \cdot \text{m}^{-2}$ [111][112]. This small difference may be due to the fact that in the literature, authors use black PMMA and the organic pigments may release additional heat.

- Unfilled PVC case

Normalized mass and mass loss rate of unfilled PVC versus time are plotted on Figure 44a and Figure 44b respectively⁵⁵. Figure 44a shows that, for this test the ignition takes place 46 seconds after the start time. Figure 44b shows that the peak of mass loss rate is of $0.20 \text{ g} \cdot \text{s}^{-1}$. When burning, unfilled PVC leaves a residue of 9.6 wt. % (Figure 44a). This is explained by the fact that PVC forms a porous char.

⁵⁵ The presented result was obtained among seven experiments. Seven experiments were performed because it was difficult to manipulate PVC samples, sometimes the ignition spark plug was stuck into the char. Thus, some adjustments have been made. All the results are displayed in Appendix 4, p. 179.

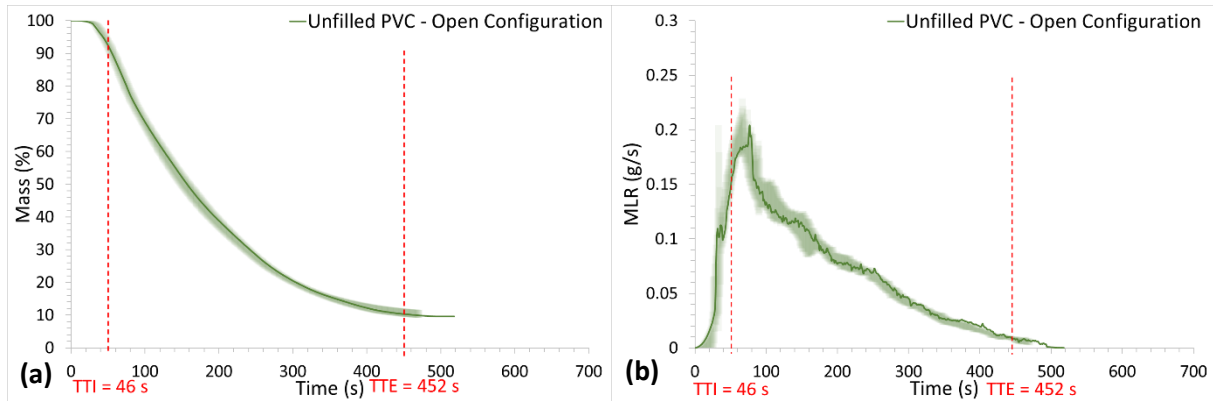


Figure 44: Evolution of mass of unfilled PVC during well-ventilated testing. a) Normalized mass; b) Mass loss rate (cone calorimetry at 50 kW.m^{-2})

Pictures of unfilled PVC before and after testing are shown in Figure 45a and Figure 45b respectively. The char is concentrated at the center of the sample holder. It has some parts of light grey color; these are the parts oxidized by the ambient air.

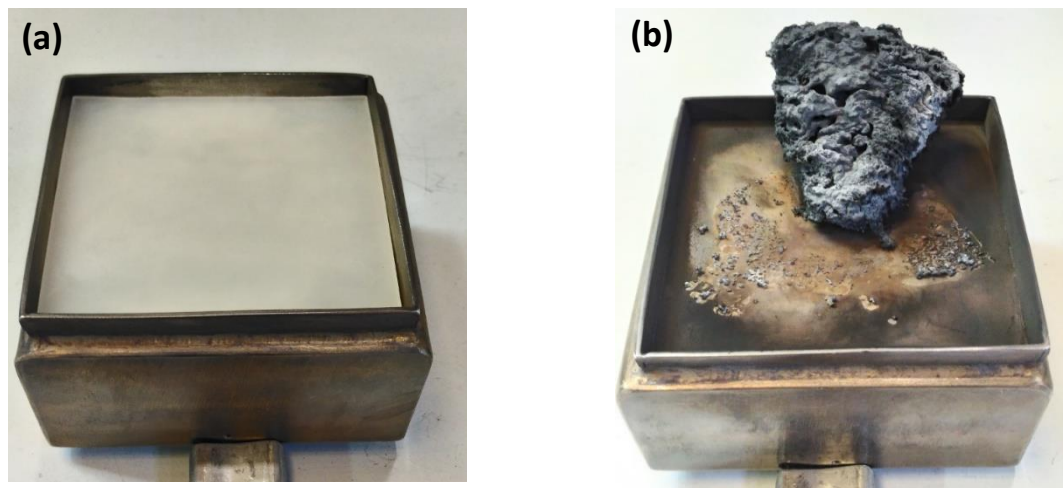


Figure 45: Unfilled PVC a) before testing; b) after testing (cone calorimetry at 50 kW.m^{-2})

Figure 46 shows the comparison of well-ventilated unfilled PVC HRR measurement from thermopile and oxygen consumption. HRR determined with thermopile (red curve) shows a peak of 175.4 kW.m^{-2} and a total heat release of 35.7 MJ.m^{-2} whereas, with the oxygen consumption calorimetry method (green curve), HRR_{O_2} shows a peak of 289.4 kW.m^{-2} and a total heat release of 57.4 MJ.m^{-2} . The THR_{O_2} is 60.8 % higher than $\text{THR}_{\text{thermo}}$. This can be explained by the fact that, for PVC, $\text{HRR}_{\text{thermo}}$ underestimates the actual HRR in a higher extent than for PMMA. Tewarson [47] showed that, for sooty flames such as the ones produced by PVC burning, $\chi_{\text{rad}} = 0.46$. For PVC, heat losses to the apparatus are then of higher importance than for PMMA. The same order of magnitude in the difference of HRR obtained by thermopile and calorimetry is observed for polycarbonate and flame-retarded polycarbonate in the

study of Filipczak et al. [113]. The EHC (calculated with Equation 46, p.120) is equal to 16.2 MJ.kg^{-1} from THR_{O_2} measurement.

THR_{O_2} is compared with the THR_{max} calculated below, according to Equation 45 (p. 119) (ΔH_{ch} is equal to 19.6 MJ.kg^{-1} for unfilled PVC, cf. the heat of combustion results in the characterization of the unfilled and filled PVC materials, cf. Chapter III, p. 104).

$$\text{THR}_{\text{max}}(\text{Unfilled PVC}) = \frac{19.6 \times 0.0355}{0.01} = 69.6 \text{ MJ.m}^{-2}$$

THR_{max} is 21 % higher of THR_{O_2} . This comparison is only indicative as the heat of combustion measurement was performed with a PCFC where the temperature regime is not comparable with the cone calorimeter. Indeed, PCFC deals with thermally thin sample heated under nitrogen up to 800°C at controlled heating rate ($60^\circ\text{C.min}^{-1}$) whereas cone calorimeter deals with thermally thick sample heated under air up to approximately 630°C ⁵⁶. The decomposition regime is then different.

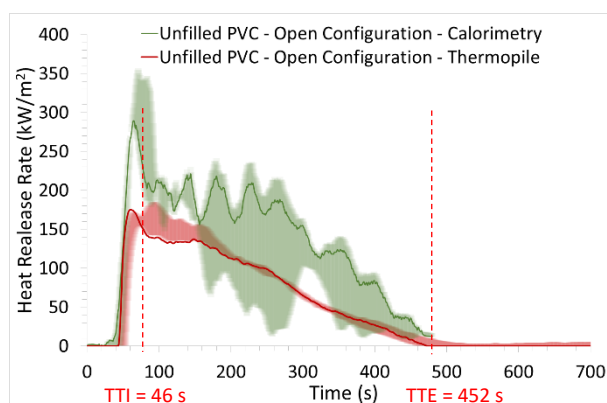


Figure 46: HRR of unfilled PVC combustion during well-ventilated testing (cone calorimetry at 50 kW.m^{-2})

- Filled PVC case

Normalized mass and mass loss rate of filled PVC versus time are plotted on Figure 47a and Figure 47b respectively⁵⁷. Figure 47a shows that, for this test, the ignition takes place 63 seconds after the start time. Figure 47b shows that the peak of mass loss rate is of 0.11 g.s^{-1} . When burning, filled PVC leaves a residue of 36.9 wt. % (Figure 44a) – against 9.6 wt. % for unfilled PVC. This is explained by the fact that PVC forms a char while decomposing and that the filler is present in the condensed phase. Temperatures reached during the test are too low to allow the transformation of calcium carbonate into calcium oxide (this reaction occurs between 635 and 865°C). The mineral filler is then present

⁵⁶ During the test, the theoretical temperature at the surface exposed to the heat flux is around 625°C in steady state [105].

⁵⁷ The presented result was obtained among three experiments, all displayed in Appendix 4, p. 180.

mainly in the residue in the form of calcium carbonate, that may explain an amount of residue as high as 36.9 wt. % for filled PVC.

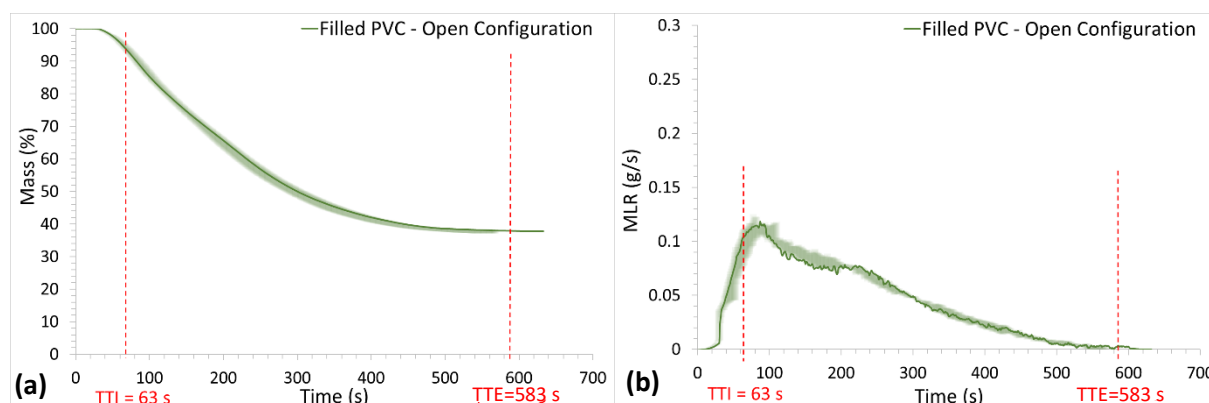


Figure 47: Evolution of mass of filled PVC during well-ventilated testing. a) Normalized mass; b) Mass loss rate (cone calorimetry at 50 kW.m⁻²)

Pictures of filled PVC before and after testing are shown in Figure 48a and Figure 48b respectively. As for unfilled PVC, the char and the filler residue are concentrated at the center of the sample holder.

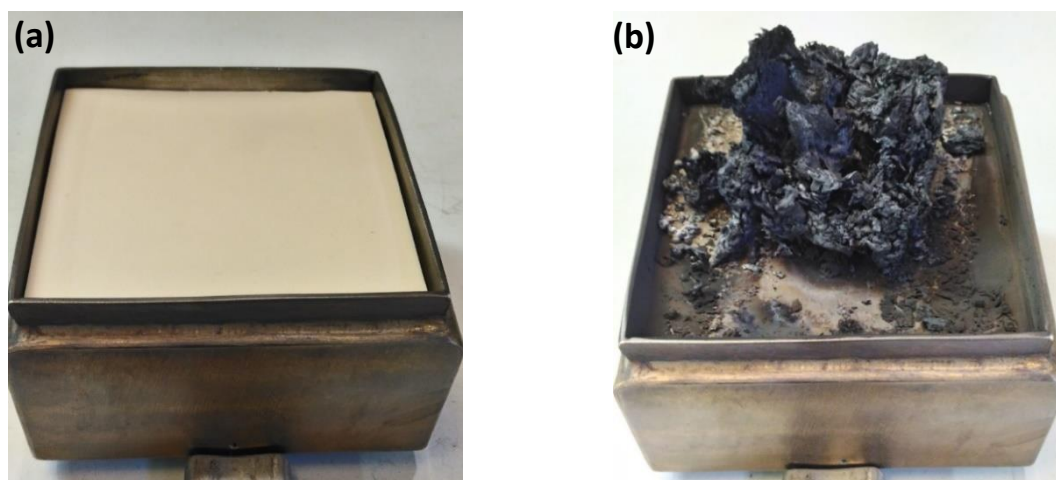


Figure 48: Filled PVC a) before testing; b) after testing (cone calorimetry at 50 kW.m⁻²)

Figure 49 below shows the comparison of well-ventilated filled PVC HRR_{thermo} and HRR_{O₂}. HRR_{thermo} (red curve) shows a peak of 113.6 kW.m⁻² and a THR_{thermo} of 30.9 MJ.m⁻² whereas HRR_{O₂} (green curve) shows a peak of 237.6 kW.m⁻² and a THR_{O₂} of 53.7 MJ.m⁻². The THR_{O₂} is 73.8 % higher than the THR_{thermo}. The EHC (calculated with Equation 46, p.120) is equal to 12.6 MJ.kg⁻¹ from THR_{O₂} measurement.

THR_{O₂} is compared with THR_{max}, calculated below with Equation 45 p.119 and based on the filled PVC chemical heat of combustion (Δ_{Hch} – equal to 13.6 MJ.kg⁻¹ for filled PVC, cf. Chapter III, p. 104).

$$THR_{max}(Filled\ PVC) = \frac{13.6 \times 0.0425}{0.01} = 57.8\ MJ.m^{-2}$$

THR_{max} is 7.6 % higher than THR_{O_2} obtained with oxygen consumption calorimetry.

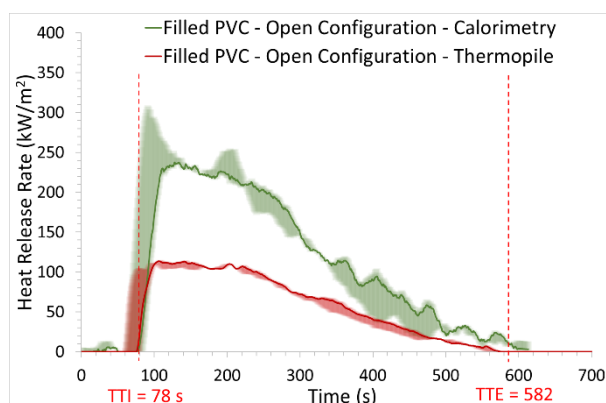


Figure 49: HRR of filled PVC combustion during well-ventilated testing (cone calorimetry at 50 kW.m^{-2})

Fire parameters, i.e. mass loss and heat release rate, of PMMA, unfilled PVC and filled PVC in the open cone calorimeter have been described. Now, the smoke measurements (i.e. gas concentration and aerosols concentration) of the three materials in the open cone calorimeter will be described in the following sections.

4.2. Evolved gases measured with cone calorimeter in an open configuration

When considering gases evolving during a test, three parts can be defined: before ignition, during flaming and after flame out. Before ignition and after flame out, analyzed gases are issued from the material thermal decomposition (i.e. decomposition gases) whereas during flaming, analyzed gases are gases evolving from the combustion (i.e. combustion gases).

The results presented in this section are from the same experiment than the one presented for mass loss and heat release rate⁵⁸.

- PMMA case

For gases evolving during well-ventilated testing of PMMA (Figure 50), before ignition, only hydrocarbons are identified by the FTIR spectrometer with a majority of ethane reaching a peak of approximately 250 ppmv and a small amount of benzene reaching a peak of 50 ppmv both right before time to ignition (TTI). During the flame period, there are no hydrocarbons present in smoke. Carbon dioxide and water vapor are present around 30 000 ppmv and 15 000 ppmv respectively, and carbon monoxide is present around 200 ppmv. After flame out, no gases are evolved.

⁵⁸ The presentation of all the experiments for repeatability issue is presented in Appendix 4 (PMMA: p. 181; Unfilled PVC: p. 183; Filled PVC: p. 184).

These observations are consistent with the observations made in [111] regarding the evolved gases during the burning of PMMA in the cone calorimeter under a heat flux of 45 kW.m^{-2} where the peak of carbon dioxide concentration is recorded around 35 000 ppmv and the peak of water vapor concentration is recorded around 20 000 ppmv.

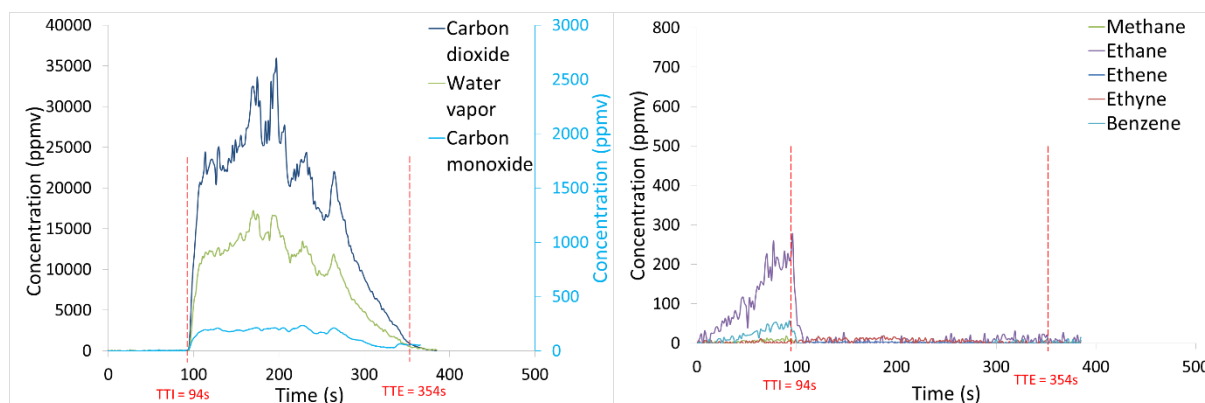


Figure 50: Evolved gases during well-ventilated testing of PMMA (cone calorimetry at 50 kW.m^{-2})⁵⁹

- Unfilled PVC case

For gases evolved during well-ventilated testing of unfilled PVC (Figure 51), before ignition, only hydrogen chloride is identified by the FTIR spectrometer. As shown in [43], gases evolved during PVC thermal decomposition are mainly heavy hydrocarbons, e.g. PAHs (polycyclic aromatic hydrocarbons), that are not visible by the FTIR spectrometer since they are not in a gaseous state at 180°C . At the moment of ignition, the peak of mass loss rate is almost reached (Figure 47b, p. 123), which is consistent with the fact that the release of hydrogen chloride by dehydrochlorination reaction is autocatalytic. During flaming, carbon dioxide, water vapor, carbon monoxide and hydrogen chloride present a peak around 11 000 ppmv, 10 000 ppmv, 1 100 ppmv and 5 500 ppmv respectively just after TTI. Hydrogen chloride is present in smoke throughout the test, during flaming and non-flaming periods, because it is a non-flammable gas. A small amount of methane and ethyne are released right after TTI with a peak around 75 ppmv for both of them.

⁵⁹ Carbon dioxide and water vapor concentrations are read on the left axis whereas carbon monoxide is read on the right axis.

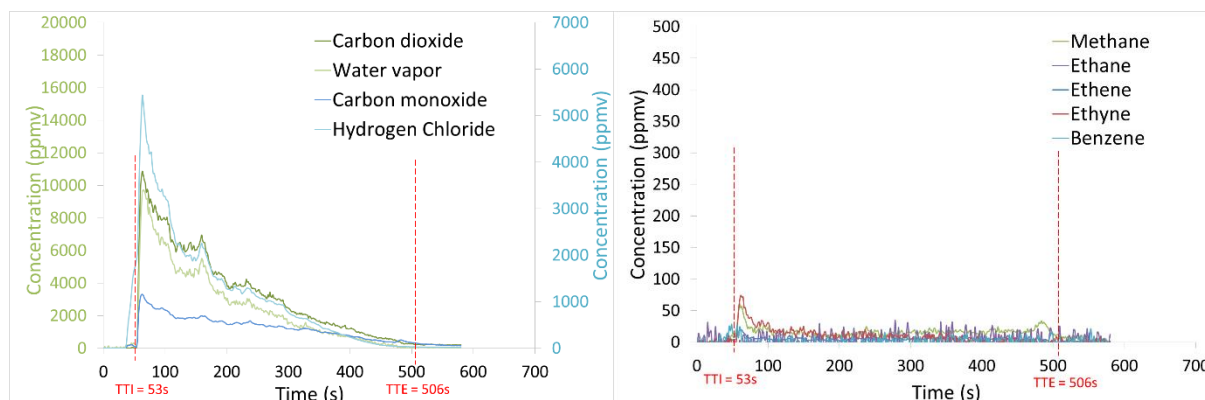


Figure 51: Gases evolved during well-ventilated testing of unfilled PVC (cone calorimetry at 50 kW.m^{-2})⁶⁰

- Filled PVC case

For gases evolved during well-ventilated testing of filled PVC (Figure 52), before ignition, no gases are identified by the FTIR spectrometer in smoke. After ignition, carbon dioxide, water vapor, carbon monoxide and hydrogen chloride present a peak around 11 000 ppmv, 7 000 ppmv, 1 100 ppmv and 4 000 ppmv respectively just after TTI. A small amount of methane and ethyne are released right after TTI with a peak around 60 ppmv for both of them.

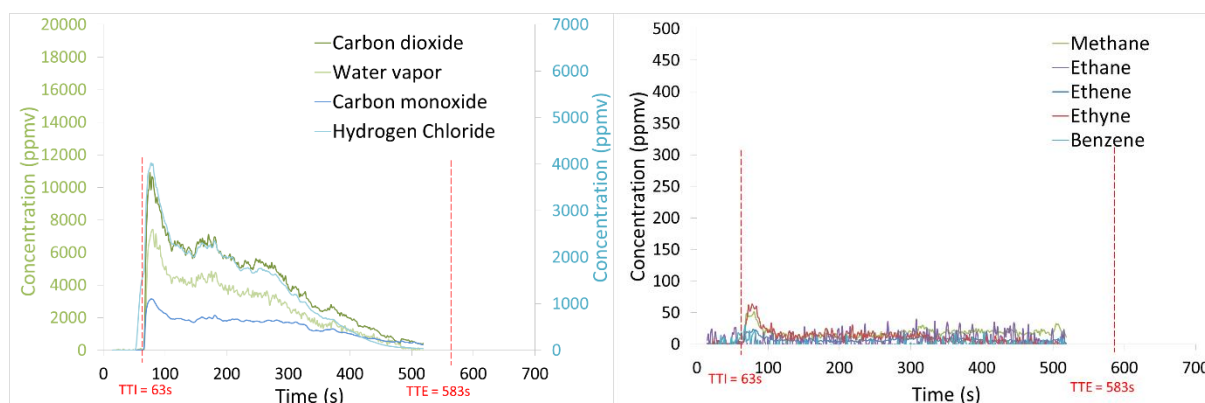


Figure 52: Gases evolved during well-ventilated testing of filled PVC (cone calorimetry at 50 kW.m^{-2})⁶¹

4.3. Evolved aerosols measured with cone calorimeter in an open configuration

Aerosols emitted during a test are composed of soot particles and particulates of condensed hydrocarbons. Deposition of aerosols by thermophoresis effect on the walls between the flame zone and the ELPI cannot be avoided but is supposed to be negligible. The particles concentration in term of number per m^3 is measured and presented in this section. In the ELPI, particles are classified within

⁶⁰ Carbon dioxide and water vapor concentrations (green curves) are read on the left axis whereas carbon monoxide and hydrogen chloride concentrations (blue curves) are read on the right axis.

⁶¹ The FTIR acquisition has been stopped at 500 s whereas the TTE was not reached.

14 size classes, according to their aerodynamic diameter. Size classes are gathered by pair to provide readable data. In order to get data in the measurement range of the ELPI granulometer, the exhaust gas is diluted upstream the ELPI with the FPS (cf. Chapter II, p. 76). The dilution ratio is set at 20 for PMMA and at 40 for both unfilled and filled PVC.

The results presented in this section are also from the same experiment than the one presented for mass loss and heat release rate⁶².

- PMMA case

The profile of aerosols evolved for well-ventilated testing of PMMA is shown in Figure 53. Before ignition, only particles with an aerodynamic diameter (d_a) inferior to $0.03 \mu\text{m}$ are released at a concentration peak of $3.35 \times 10^8 \text{ \#.m}^{-3}$. In the absence of flame, these particles are probably condensed hydrocarbons resulting of PMMA thermal decomposition. During flaming, evolved particles have an aerodynamic diameter comprised between 0.03 and $0.257 \mu\text{m}$ and are released at a concentration of approximately $7.30 \times 10^8 \text{ \#.m}^{-3}$. At 280 seconds of test, the number of evolved particles decreases to reach a minimum between 300 and 310 seconds of test. From 310 seconds, the number of ultra-fine particles ($d_a < 0.03 \mu\text{m}$) drastically increases to reach a maximum of $3.20 \times 10^9 \text{ \#.m}^{-3}$. Visually, between 280 and 310 seconds, there is a transition in the flame regime: the flame, originally centered and localized all across the sample holder, splits into several small flames localized at the sample holder edges. Furthermore, the flame is very luminous and almost white whereas the small flames are less luminous and more yellow. It is deduced that the small flames are at lower temperature than the flame. As a result, the combustion reactions may be different.

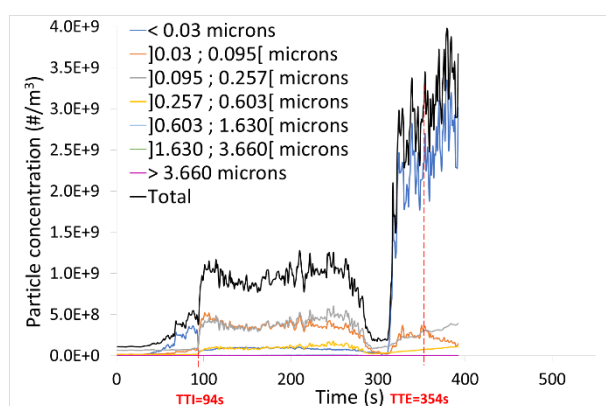


Figure 53: Evolution of aerosols in smoke for well-ventilated testing of PMMA (cone calorimetry at 50 kW.m^{-2})

⁶² The presentation of all the experiments for repeatability issue is presented in Appendix 4 (PMMA: p. 185; Unfilled PVC: p. 186; Filled PVC: p. 186).

- Unfilled PVC case

The profile of aerosols evolved for well-ventilated testing of unfilled PVC is shown in Figure 54. Before ignition, the majority of evolved particles have an aerodynamic diameter (d_a) comprised between 0.095 and 0.257 μm and are released at a peak concentration of $3.35 \times 10^8 \text{ \#} \cdot \text{m}^{-3}$. Bigger and smaller particles are also released at a lower concentration: particles of $d_a =]0.257 ; 0.603[\mu\text{m}$ are released at a concentration peak of $4.60 \times 10^8 \text{ \#} \cdot \text{m}^{-3}$, as well as particles of $d_a =]0.03 ; 0.095[\mu\text{m}$. During flaming, the same profile of evolved particles is observed, at higher concentrations. Particles of $d_a =]0.095 ; 0.257[\mu\text{m}$ are released at a concentration peak right after ignition of $1.40 \times 10^7 \text{ \#} \cdot \text{m}^{-3}$. At the same time, particles of $d_a =]0.257 ; 0.603[\mu\text{m}$ are released at a concentration peak of $4.10 \times 10^7 \text{ \#} \cdot \text{m}^{-3}$ and particles of $d_a =]0.03 ; 0.095[\mu\text{m}$ are released at a concentration peak of $1.20 \times 10^7 \text{ \#} \cdot \text{m}^{-3}$. The concentrations of these three types of particles decrease along the test. A small increase of ultra-fine particles ($d_a < 0.03 \mu\text{m}$) is observed close to the flame out, which is consistent with the observations made with PMMA. Nevertheless, it is not explained by the same phenomenon. Indeed, PVC, as a charring material, does not show a changing behavior as marked as PMMA during the transition towards flame out. In the case of a charring material, the flame becomes softly smaller and smaller, and combustion regime shifts towards smoldering.

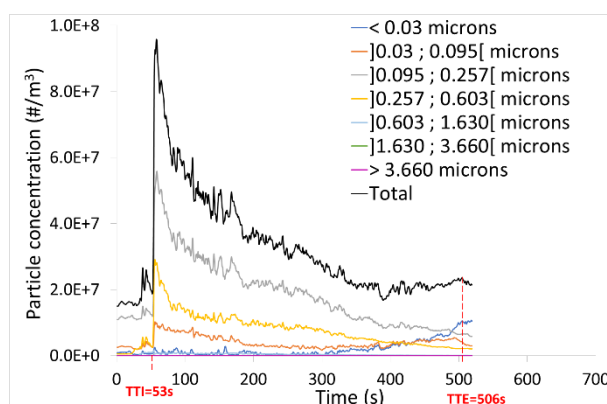


Figure 54: Evolution of aerosols in smoke for well-ventilated testing of unfilled PVC (cone calorimetry at $50 \text{ kW} \cdot \text{m}^{-2}$)

- Filled PVC case

The profile of aerosols evolved for well-ventilated testing of filled PVC is shown in Figure 55. A peak effect happened for this series of tests at the moment of ignition for $d_a < 0.03 \mu\text{m}$ particles, which is why the curve of total amount of particles is out of the figure. Before ignition, the majority of evolved particles have an aerodynamic diameter (d_a) comprised between 0.095 and 0.603 μm and are released at a peak concentration of $3.35 \times 10^8 \text{ \#} \cdot \text{m}^{-3}$. During flaming, particles of $d_a =]0.095 ; 0.257[\mu\text{m}$ are released at a concentration peak right after ignition of $8.10 \times 10^9 \text{ \#} \cdot \text{m}^{-3}$. At the same time, particles of $d_a =]0.257 ; 0.603[\mu\text{m}$ are released at a concentration peak of $1.90 \times 10^9 \text{ \#} \cdot \text{m}^{-3}$ and particles of $d_a =]0.03$

; 0.095[μm are released at a concentration peak of $4.00 \times 10^9 \text{ \#.m}^{-3}$. The concentrations of these three types of particles decrease along the test. From 300 seconds of test, the number of $d_a < 0.03 \text{ \mu m}$ particles increases to reach a maximum of $3.25 \times 10^9 \text{ \#.m}^{-3}$ during flaming regime. As for unfilled PVC, this is due to the fact that flame becomes softly smaller and smaller and the combustion regime shifts towards smoldering. After the flame out, this phenomenon is even more remarkable since the concentration of $d_a < 0.03 \text{ \mu m}$ particles continues to increase to reach a maximum concentration of $8.90 \times 10^9 \text{ \#.m}^{-3}$. The production of this type of aerosol is probably due to smoldering.

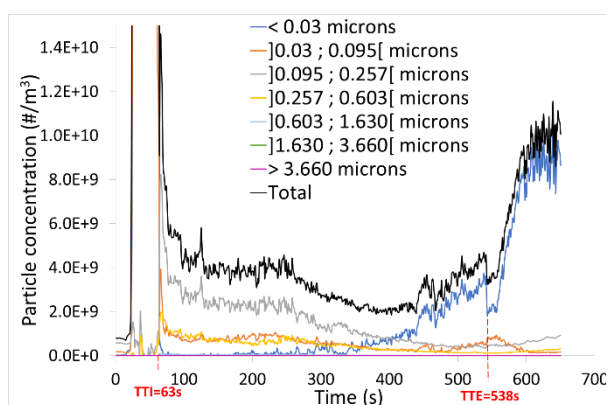


Figure 55: Evolution of aerosols in smoke for well-ventilated testing of filled PVC (cone calorimetry at 50 kW.m^{-2})

4.4. Discussion on the well-ventilated fire parameters and combustion products

Some condensed phase and fire parameters of interest⁶³ for the three materials well-ventilated testing are gathered in Table 23.

Table 23: Condensed phase and fire parameters of interest for well-ventilated testing

Material	m_{sample} (g)	Residue (%)	pMLR (g.s^{-1})	pHRR _{O2} (kW.m^{-2})	THR _{O2} (MJ.m^{-2})	THR _{max} ² (MJ.m^{-2})	EHC (MJ.kg^{-1})
PMMA	53.3	0	0.27	695.9	126.2	129.0	23.6
Unfilled PVC	35.5	10.1	0.20	289.4	57.4	69.5	16.2
Filled PVC	42.5	36.9	0.11	237.6	53.7	57.8	12.6

²Calculated with the chemical heat of combustion of each material

Concentration peaks of evolved gases measured with the FTIR during well-ventilated testing of PMMA, unfilled PVC and filled PVC are gathered in Table 24 below.

⁶³ These parameters are often characterized in the literature for cone calorimeter experiments.

Table 24: Concentration peaks of evolved gases during well-ventilated testing

Material	CO ₂ (ppmv)	CO (ppmv)	H ₂ O (ppmv)	HCl (ppmv)	CH ₄ (ppmv)	C ₂ H ₆ (ppmv)	C ₂ H ₄ (ppmv)	C ₂ H ₂ (ppmv)	C ₆ H ₆ (ppmv)
PMMA	30 000	200	15 000	/	/	250	/	/	50
Unfilled PVC	11 000	1 100	10 000	5 500	75	/	/	75	/
Filled PVC	11 000	1 100	7 000	4 000	60	/	/	60	/

Mean concentrations of total aerosols evolved during well-ventilated of PMMA, unfilled PVC and filled PVC are gathered in Table 25.

Table 25: Mean concentration of total aerosols evolved during well-ventilated testing

Material	Mean concentration of total aerosols (#.m ⁻³)
PMMA	1.3×10^9
Unfilled PVC	5.1×10^7
Filled PVC	4.5×10^9

The peak of MLR, as well as the peak of HRR are higher for unfilled PVC than for filled PVC (Table 23). Unfilled PVC burns more intensely than filled PVC. This is due to the higher amount of fuel (PVC and DIDP) in unfilled PVC (35.5 g) than in filled PVC (29.2 g)⁶⁴. However, the THR_{O₂} of unfilled and filled PVC are equal whereas the THR_{max} of unfilled PVC is higher than the THR_{max} of filled PVC (Table 23). This may be due to the fact that filled PVC produces more aerosols than unfilled PVC when burning (Table 25). The calculation of HRR by the oxygen consumption in our calculation does not take into account the amount of soot particles produced during burning. This may lead to an overestimation of the HRR_{O₂} for the case of filled PVC. The evolved gases concentration peaks of filled and unfilled PVC are comparable and even equal concerning CO₂ and CO (Table 24). However, the gases concentrations decrease faster in the case of unfilled PVC. Indeed, the filled PVC test lasts longer even if the amount of fuel is lower, as if the filler retained the fuel in the condensed phase and slowed down the combustion reaction.

⁶⁴ Filled PVC contains 31.4 wt. % of CaCO₃, which is an inert mineral filler.

5. Under-ventilated experiments in the controlled-atmosphere cone calorimeter

5.1. Characterization of the fire regime

In the case of a real enclosure fire, two effects are coupled on fire properties: the vitiation and the under-ventilation. The controlled-atmosphere cone calorimeter is designed to study the inlet flow rate and the inlet gas composition over a wide range of conditions. The $[CO]/[CO_2]$ ratio is the criteria used in our approach to choose the inlet flow rate to be used in controlled-atmosphere conditions. The ISO 19706 standard [48] gathers some fire characteristics for different development stages. Among them, the $[CO]/[CO_2]$ ratio is defined as a criteria to assess if a fire is under-ventilated, and typical values are given for well-ventilated and under-ventilated fires. The $[CO]/[CO_2]$ (v/v) ratio is inferior to 0.05 for well-ventilated flaming fires. For confined under-ventilated flaming fires, the $[CO]/[CO_2]$ (v/v) ratio is comprised between 0.2 and 0.4. The equivalence ratio is a criterion also used to determine the fire regime. In [48], equivalence ratio of confined under-ventilated flaming fires is larger than 1.

The chosen inlet volume airflow rate of $30 \text{ L}\cdot\text{min}^{-1}$ provides a confined under-ventilated combustion on both the $[CO]/[CO_2]$ (v/v) and the equivalence ratio⁶⁵ criteria basis since the first is between 0.1 and 0.3 for the three materials (Figure 56a) and the second is globally between 1 and 4 for the three materials (Figure 56b). This value of inlet flow rate is close to the inlet flow rates used by Tewarson and Pion (modulated from 25 to $70 \text{ L}\cdot\text{min}^{-1}$) to study the effect of under-ventilation on fire parameters in [52].

⁶⁵ The value of the stoichiometric mass air-to-fuel ratio used to calculate the equivalence ratio is of 8.27 for PMMA and of 8.42 for both unfilled and filled PVC. PVC and DIDP were considered in the combustion reaction and CaCO_3 is considered as an inert.

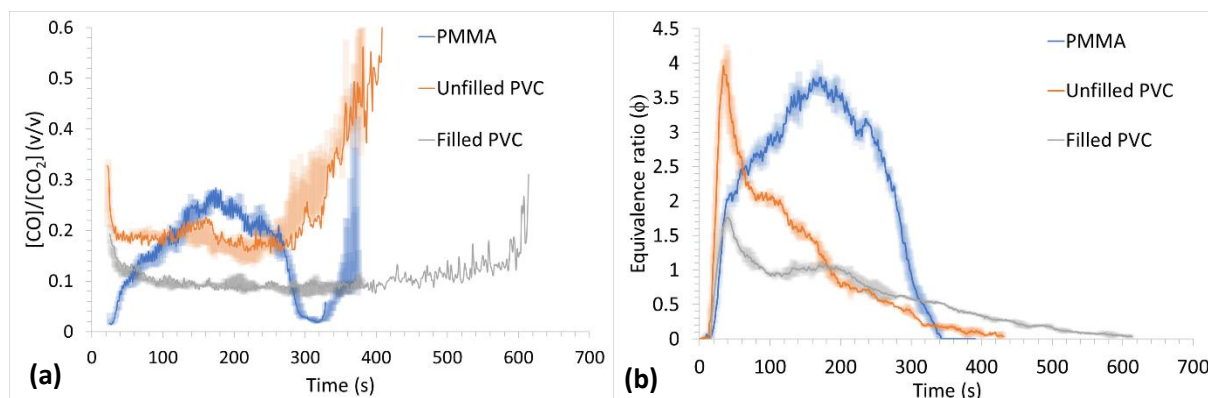


Figure 56: Fire regime of enclosed PMMA, unfilled PVC and filled PVC experiments at 30 L.min⁻¹ of inlet air flow rate a) [CO]/[CO₂] (v/v) ratio vs time; b) Equivalence ratio vs time

5.2. Influence of the confinement on the fire parameters

• PMMA case

The comparison of PMMA⁶⁶ normalized mass and mass loss rate versus time for well-ventilated and under-ventilated, i.e. enclosed, testing at 21 vol% O₂ are plotted in Figure 57a and Figure 57b respectively, and the heat release rates associated are presented in Figure 58. The PMMA normalized mass (Figure 57a) shows that for the enclosed testing (blue curve), the ignition takes place 23 seconds after the start time, against 94 seconds for well-ventilated testing (green curve). The earlier TTI is explained by the fact that for enclosed testing, the ambient air velocity close to the sample is lower (approximately 20 times less than the one of well-ventilated testing). The sample could be less cooled down when enclosed. Furthermore, it could be explained by the fewer amount of ambient air diluting the decomposition gases compared to the case of well-ventilated testing. In other words, the shorter TTI could be explained by less convective transfers in confined configuration, which would lead to a faster combustible gases accumulation. Regarding the mass loss rate (Figure 57b) the peak of mass loss rate for enclosed testing is of 0.28 g.s⁻¹. It is very close of the one of well-ventilated testing (0.27 g.s⁻¹). As for well-ventilated testing, when burning during enclosed testing, PMMA leaves no residue.

⁶⁶The presented result for well-ventilated testing is the same than the one presented in section 2.3.1 and the presented result for enclosed testing was chosen among three experiments, all displayed in Appendix 4, p. 186.

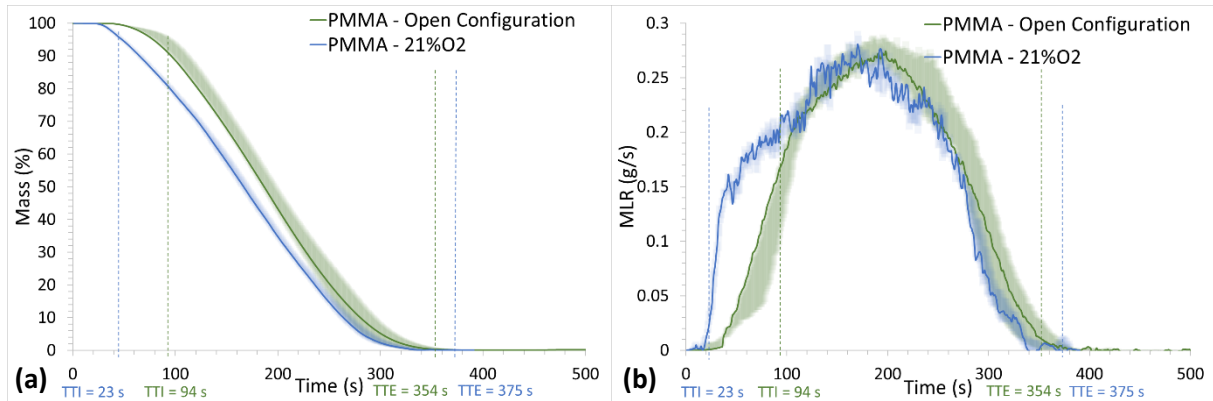


Figure 57: Comparison of evolution of mass of PMMA during well-ventilated and enclosed testing. a) Normalized mass; b) Mass loss rate (cone calorimetry at 50 kW.m^{-2} , 21 vol. % O_2 , 30 L.min^{-1})

The comparison of well-ventilated and enclosed PMMA HRR_{O_2} is presented in Figure 58. HRR_{O_2} measured during enclosed testing (blue curve) shows a peak of 491.5 kW.m^{-2} (against 695.9 kW.m^{-2} during well-ventilated testing) and a THR_{O_2} of 130.1 MJ.m^{-2} (against 126.1 MJ.m^{-2} during well-ventilated testing). This difference is mainly explained by the fact that the initial sample mass was of 57.3 g for enclosed testing instead of 53.3 g for well-ventilated testing⁶⁷. The EHC (calculated with Equation 46, p.120) for enclosed testing is then equal to 22.7 MJ.kg^{-1} (against 23.6 MJ.kg^{-1} for well-ventilated testing).

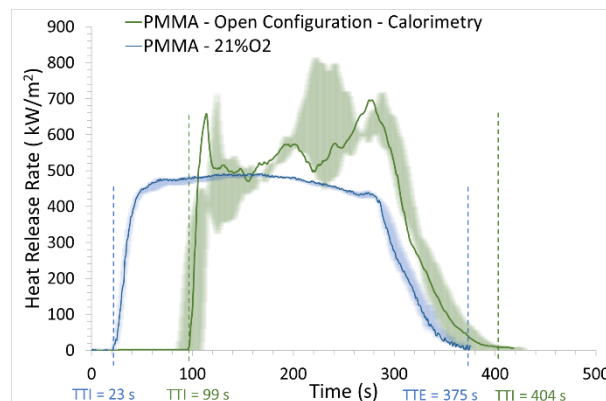


Figure 58: Comparison of HRR of PMMA during well-ventilated and enclosed testing (cone calorimetry at 50 kW.m^{-2} , 21 vol. % O_2 , 30 L.min^{-1})

⁶⁷ The mass difference between plaques is related to the sheet cutting by the mechanical service.

- Unfilled PVC case

The comparison of unfilled PVC⁶⁸ normalized mass and mass loss rate versus time for well-ventilated and enclosed testing are plotted in Figure 59a and Figure 59b respectively, and the heat release rates associated are presented in Figure 60. Figure 59a shows that for the enclosed testing (blue curve), the ignition takes place 20 seconds after the start time, against 53 seconds for well-ventilated testing. As for PMMA, ignition occurs earlier because the sample may be less cooled down by the ambient air when the test is enclosed. Figure 59b shows that the peak of mass loss rate is of 0.29 g.s^{-1} , against 0.20 g.s^{-1} for well-ventilated testing. Also, time to pMLR is shorter in the case of enclosed testing. The earlier ignition in enclosed testing has the effect to add a heat flux earlier to the material and, as a result, increases the MLR compared to the well-ventilated testing. Figure 59a shows that the amount of residue left during enclosed testing is the same than the one left during well-ventilated testing (9.6 wt. %).

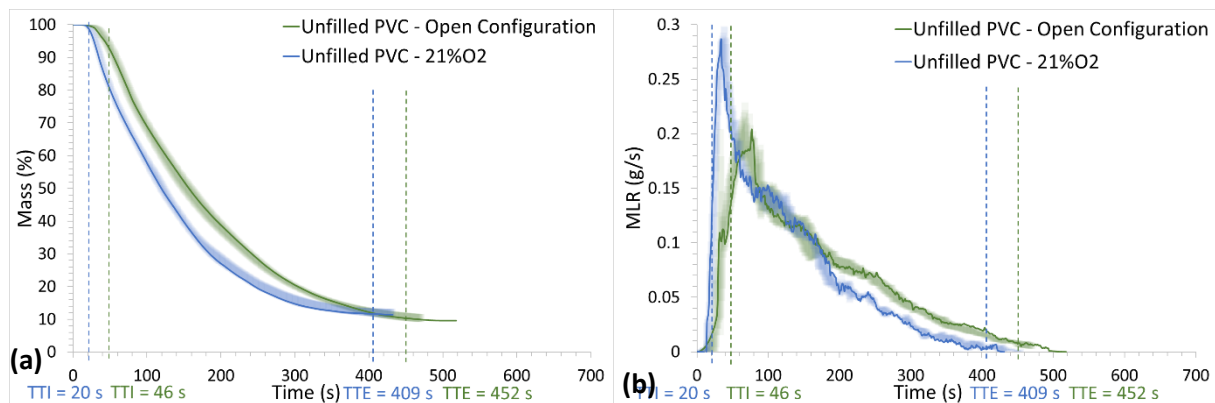


Figure 59: Comparison of evolution of mass of unfilled PVC during well-ventilated and enclosed testing. a) Normalized mass; b) Mass loss rate (cone calorimetry at 50 kW.m^{-2} , 21 vol. % O₂, 30 L.min^{-1})

When HRR_{O_2} for well-ventilated and enclosed unfilled PVC are compared (Figure 60), it is observed that HRR_{O_2} measured during enclosed testing (blue curve) shows a peak of 392 kW.m^{-2} , whereas it is of 289 kW.m^{-2} for well-ventilated testing. A THR_{O_2} of 62 MJ.m^{-2} is measured for enclosed testing against 57 MJ.m^{-2} for well-ventilated testing. The EHC (calculated with Equation 46, p.120) for enclosed testing is then equal to 17.6 MJ.kg^{-1} (against 16.2 MJ.kg^{-1} for well-ventilated testing).

⁶⁸The presented result for well-ventilated testing is the same than the one presented in section 2.3.1 and the presented result for enclosed testing was chosen among three experiments, all displayed in Appendix 4, p. 187.

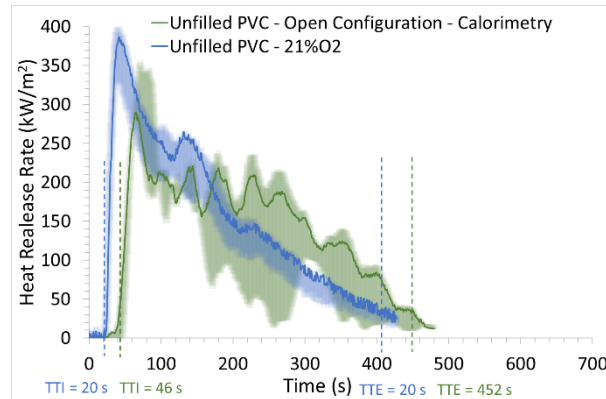


Figure 60: Comparison of HRR of unfilled PVC during well-ventilated and enclosed testing (cone calorimetry at 50 kW.m^{-2} , 21 vol. % O_2 , 30 L.min^{-1})

- Filled PVC case

Figure 61a and Figure 61b show the comparison between well-ventilated and enclosed testing of filled PVC⁶⁹ normalized mass and mass loss rate respectively, and the heat release rates associated are presented in Figure 62. Figure 61a shows that, for the enclosed testing, the ignition takes place 25 seconds after the start time, against 63 seconds for well-ventilated testing. Figure 61b shows that the peak of mass loss rate is of 0.14 g.s^{-1} , against 0.12 g.s^{-1} for well-ventilated testing. Figure 61a shows that the amount of residue left during enclosed testing is of 37.3 % instead of 36.9 % during well-ventilated testing.

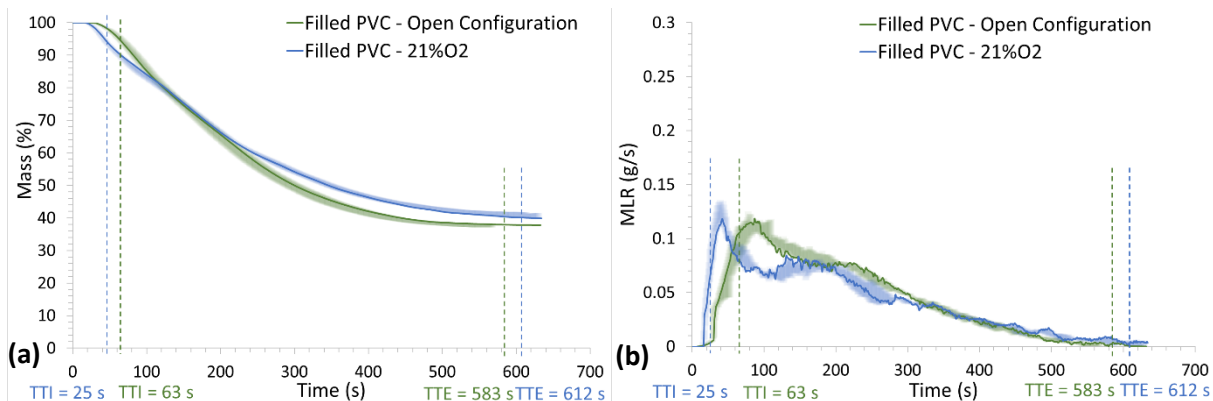


Figure 61: Comparison of evolution of mass of filled PVC during well-ventilated and enclosed testing. a) Normalized mass; b) Mass loss rate (cone calorimetry at 50 kW.m^{-2} , 21 vol. % O_2 , 30 L.min^{-1})

Figure 62 below shows the comparison of well-ventilated and enclosed unfilled PVC HRR_{O_2} . HRR_{O_2} measured during enclosed testing (blue curve) shows a peak of 222.2 kW.m^{-2} , against 237.6 kW.m^{-2}

⁶⁹ The presented result for well-ventilated testing is the same than the one presented in section 2.3.1 and the presented result for enclosed testing was chosen among three experiments, all displayed in Appendix 4, p. 188.

during well-ventilated testing, and a total heat release of 46.9 MJ.m^{-2} , against 53.7 MJ.m^{-2} during well-ventilated testing. The EHC (calculated with Equation 46, p.120) for enclosed testing is then equal to 11.1 MJ.kg^{-1} (against 12.6 MJ.kg^{-1} for well-ventilated testing).

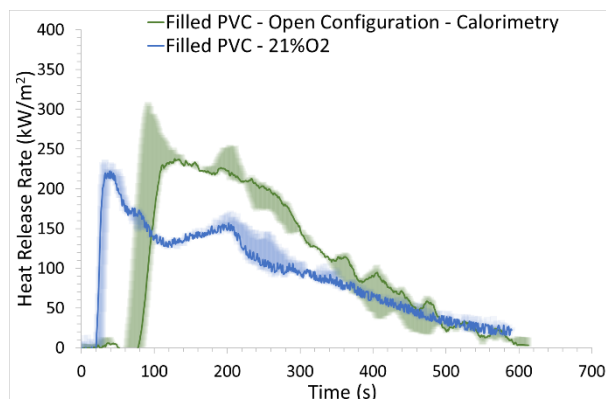


Figure 62: Comparison of HRR of filled PVC during well-ventilated and enclosed testing (cone calorimetry at 50 kW.m^{-2} , 21 vol. % O_2 , 30 L.min^{-1})

5.3. Influence of the confinement on evolved gases

The decomposition and combustion gases⁷⁰ are more concentrated in the exhaust gas during enclosed testing. Indeed, there is less air passing through the system in enclosed configuration than in open configuration. The air velocity⁷¹ at the top of the chimney with the open configuration is at 0.9 m.s^{-1} whereas it is at 0.05 m.s^{-1} with the enclosed configuration at an air feeding rate of 30 L.min^{-1} inside the enclosure. Thus, the concentration of the gases in the fumes are too high to be quantified by the FTIR spectrometer. Therefore, a diluter (cf. Chapter II, p. 76) is required upstream the FTIR spectrometer and apply a hot dilution ratio of 8 to the gases in the aim at injecting gases in the concentration range of quantification.

- PMMA case

For gases evolved during enclosed testing of PMMA (Figure 63), before ignition, no gases are identified in the fumes. During flaming, carbon dioxide and water vapor are present around 65 000 ppmv and 50 000 ppmv respectively, and carbon monoxide is present around 13 000 ppmv. Hydrocarbons evolved during flaming are present at a higher concentration than for well-ventilated testing. Methane,

⁷⁰ The results presented in this section are from the same experiment than the one presented for mass loss and heat release rate. The presentation of all the experiments for repeatability concern is presented in Appendix 4 (PMMA: p.189; Unfilled PVC: p. 190; Filled PVC: p. 191). Air velocities and volume flow rate are given at 20°C and 1 atm.

⁷¹ Air velocities and volume flow rate are given at 20°C and 1 atm.

ethene, ethyne, benzene and ethane are evolved at a concentration peak of 5 000 ppmv, 2 200 ppmv, 2 000 ppmv, 1 200 ppmv and 700 ppmv respectively. After flame out, no gases are evolved.

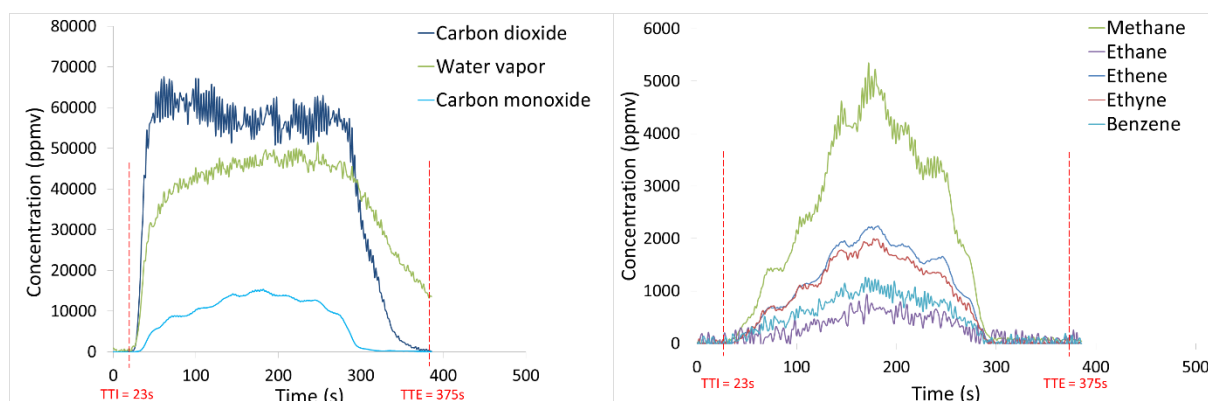


Figure 63: Gases evolved during enclosed testing of PMMA (cone calorimetry at 50 kW.m^{-2} , 21 vol. % O_2 , 30 L.min^{-1})

- Unfilled PVC case

For gases evolved during enclosed testing of unfilled PVC (Figure 64), before ignition, no gases are identified. During flaming, just after TTI, carbon dioxide and water vapor are released at a concentration peak of 40 000 ppmv. At the same time, hydrogen chloride and carbon monoxide present a peak around 19 000 ppmv and 7 000 ppmv respectively. The concentration of these four gases decreases along the test. Hydrocarbons such as methane, ethene, ethyne, benzene and ethane are released just after TTI at a concentration peak of 1 600 ppmv, 800 ppmv, 800 ppmv, 550 ppmv and 500 ppmv respectively. No gases are identified after the flame out.

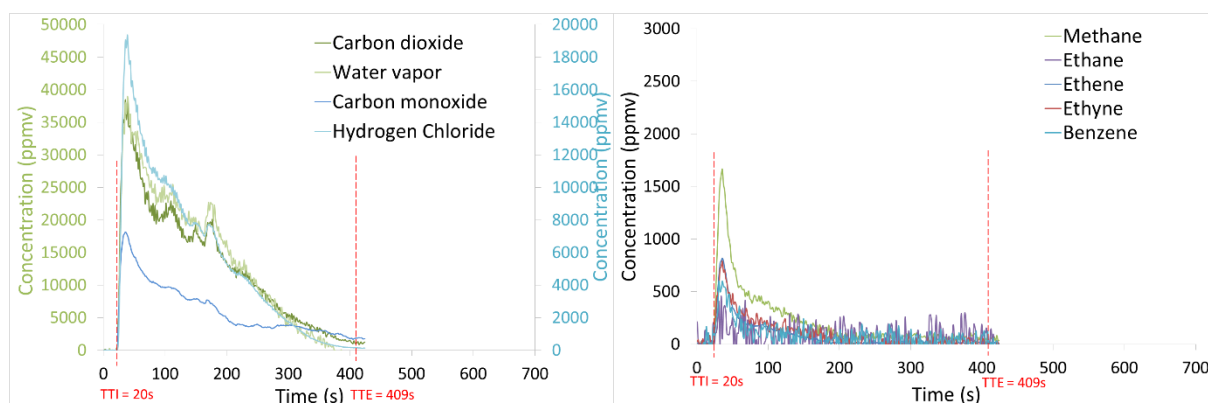


Figure 64: Gases evolved during enclosed testing of unfilled PVC (cone calorimetry at 50 kW.m^{-2} , 21 vol. % O_2 , 30 L.min^{-1})⁷²

⁷² Carbon dioxide and water vapor concentrations (green curves) are read on the left axis whereas carbon monoxide and hydrogen chloride concentrations (blue curves) are read on the right axis.

- Filled PVC case

For gases evolved during enclosed testing of filled PVC (Figure 65), before ignition, no gases are identified. After ignition, just after TTI, carbon dioxide water vapor, carbon monoxide and hydrogen chloride are present at a concentration peak of 32 000 ppmv, 35 000 ppmv, 5 000 ppmv and 5 300 ppmv respectively. At the same time, a small amount of methane is released at a concentration around 400 ppmv and, benzene, ethene and ethyne are released at a concentration around 300 ppmv for the three of them.

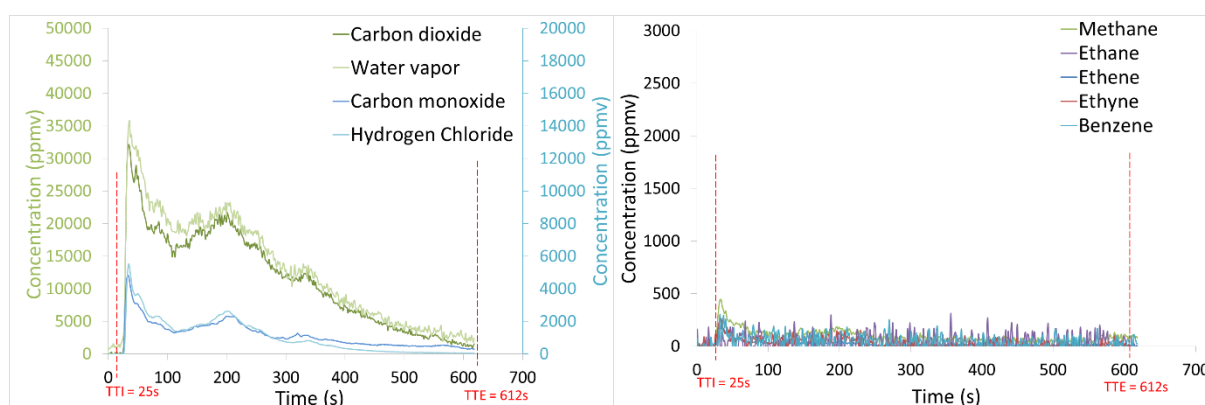


Figure 65: Gases evolved during enclosed testing of filled PVC (cone calorimetry at 50 kW.m^{-2} , 21 vol. % O_2 , 30 L.min^{-1})

5.4. Influence of the confinement on evolved aerosols

As for the gases, the dilution ratio applied by the FPS upstream the ELPI for the aerosols measurement⁷³ is increased during enclosed testing. The dilution ratio during enclosed testing is set at 56 for PMMA, at 69 for unfilled PVC and at 96 for filled PVC.

- PMMA case

The profile of aerosols evolved for enclosed testing of PMMA is shown in Figure 66. Before ignition, no particle is measured, contrary to the case of well-ventilated testing (cf. Figure 53, p.127), because the ignition takes place instantaneously and, as a consequence, condensed hydrocarbons released from thermal decomposition of PMMA undergo oxidation in the flame instead of being transported in the exhaust gas. During flaming, particles of $d_a =]0.095 ; 0.257[\text{ }\mu\text{m}$ are released at a concentration of approximately $1.27 \times 10^8 \text{ \#.m}^{-3}$ and particles of $d_a =]0.257 ; 0.603[\text{ }\mu\text{m}$ are released at a concentration of approximately $1.09 \times 10^8 \text{ \#.m}^{-3}$. Finer particles are also evolved at a lesser amount: particles of $d_a =$

⁷³ The results presented in this section are from the same experiment than the one presented for mass loss and heat release rate. The presentation of all the experiments for repeatability concern is presented in Appendix 4 (PMMA: p. 192; Unfilled PVC: p. 193; Filled PVC: p. 193).

$]0.003 ; 0.095[\mu\text{m}$ are released at a concentration of approximately $6.33 \times 10^7 \text{ \#} \cdot \text{m}^{-3}$ and particles of $d_a < 0.03 \mu\text{m}$ are released at a concentration of approximately $3.14 \times 10^7 \text{ \#} \cdot \text{m}^{-3}$. At 280 seconds, the number of evolved particles decreases to reach a minimum around 325 seconds of test. From 330 seconds, the number of ultra-fine particles ($d_a < 0.03 \mu\text{m}$) drastically increases to reach a maximum of $2.12 \times 10^8 \text{ \#} \cdot \text{m}^{-3}$.

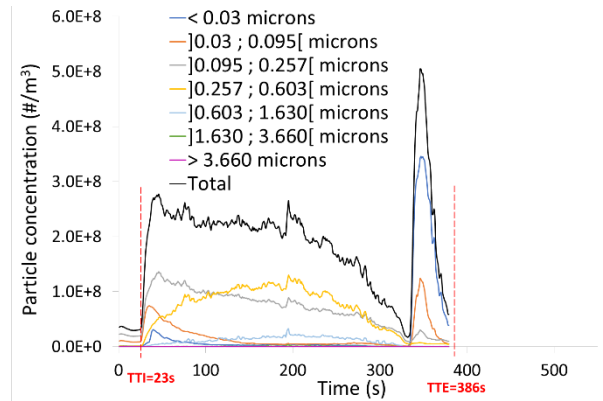


Figure 66: Evolution of aerosols in smoke for enclosed testing of PMMA (cone calorimetry at $50 \text{ kW} \cdot \text{m}^{-2}$, 21 vol. % O_2 , 30 $\text{L} \cdot \text{min}^{-1}$)

- Unfilled PVC case

Aerosols evolved for enclosed testing of unfilled PVC is shown in Figure 67. Before ignition, no particle is released, contrary to the case of well-ventilated testing (cf. Figure 54, p.128), because the ignition takes place instantaneously. At the moment of ignition, at 20 seconds, a peak of $d_a =]0.095 ; 0.257[\mu\text{m}$ particles is observed at a concentration of $5.37 \times 10^7 \text{ \#} \cdot \text{m}^{-3}$. Right after ignition, around 26 seconds, a second peak of $d_a =]0.095 ; 0.257[\mu\text{m}$ particles is observed at a concentration of $2.32 \times 10^8 \text{ \#} \cdot \text{m}^{-3}$. At the exact same time, the concentration of $d_a =]0.257 ; 0.603[\mu\text{m}$ particles reaches a maximum of $1.95 \times 10^8 \text{ \#} \cdot \text{m}^{-3}$. These two particles classes concentration decrease throughout the test.

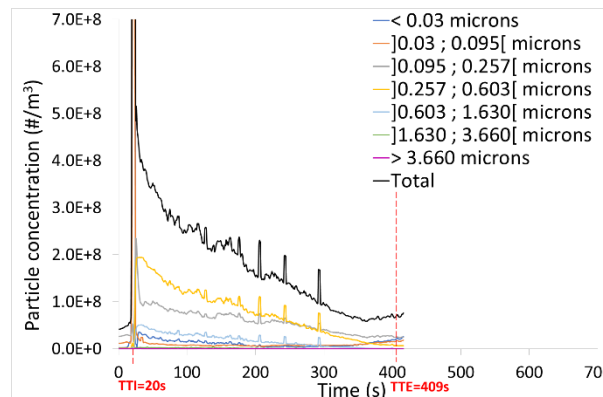


Figure 67: Evolution of aerosols in smoke for enclosed testing of unfilled PVC (cone calorimetry at $50 \text{ kW} \cdot \text{m}^{-2}$, 21 vol. % O_2 , 30 $\text{L} \cdot \text{min}^{-1}$)

- Filled PVC case

Aerosols evolved for enclosed testing of filled PVC is shown in Figure 68. Before ignition, no particle is released, contrary to the case of well-ventilated testing (cf. Figure 55, p.129) due to the earlier TTI in confined conditions. Right after ignition, around 32 seconds, a peak of $d_a =]0.095 ; 0.257[\mu\text{m}$ particles is observed at a concentration of $1.99 \times 10^8 \text{ \#} \cdot \text{m}^{-3}$, also with a peak of $d_a =]0.257 ; 0.603[\mu\text{m}$ particles at a concentration of $1.85 \times 10^8 \text{ \#} \cdot \text{m}^{-3}$, and a peak of $d_a < 0.03 \mu\text{m}$ at a concentration of $1.67 \times 10^8 \text{ \#} \cdot \text{m}^{-3}$. During flaming, the two classes of particles that are released at a significant amount are $d_a =]0.095 ; 0.257[\mu\text{m}$ particles and $d_a =]0.257 ; 0.603[\mu\text{m}$ particles at a concentration of around $7.10 \times 10^7 \text{ \#} \cdot \text{m}^{-3}$ for both. At the end of the test, around 500s, close to the flame out, these particles concentrations decrease and $d_a < 0.03 \mu\text{m}$ particles concentration increases. This is the same observation made with well-ventilated filled PVC testing and it may be due to the char smoldering.

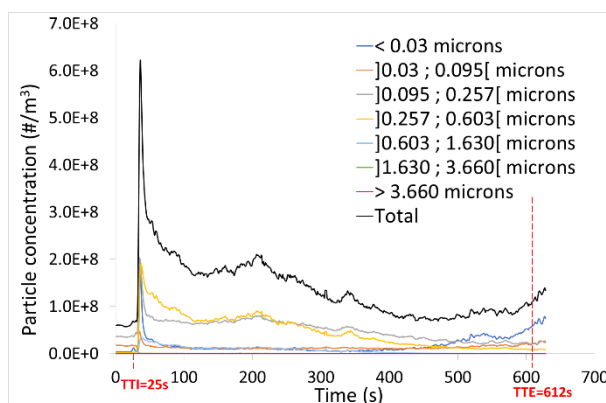


Figure 68: Evolution of aerosols in smoke for enclosed testing of filled PVC (cone calorimetry at $50 \text{ kW} \cdot \text{m}^{-2}$, 21 vol. % O_2 , $30 \text{ L} \cdot \text{min}^{-1}$)

5.5. Discussion on the influence of the confinement on fire parameters and combustion products

Some condensed phase and fire parameters of interest for the three materials during under-ventilated testing are gathered in Table 26. Below each parameter, the correspondent parameter for well-ventilated testing is put in grey for comparison.

Table 26: Condensed phase and fire parameters of interest for under-ventilated testing

Material	m _{sample} (g)	Residue (%)	pMLR (g.s ⁻¹)	pHRR (kW.m ⁻²)	THR (MJ.m ⁻²)	EHC (MJ.kg ⁻¹)
PMMA	57.3	0	0.280	491.5	130.1	22.7
	53.3	0	0.274	761.0	127.8	23.6
Unfilled PVC	35.3	9.6	0.294	392.2	62.0	17.6
	35.5	10.1	0.195	289.4	57.4	16.2
Filled PVC	42.3	37.3	0.136	222.2	45.3	11.1
	42.5	36.9	0.119	237.6	53.7	12.6

In the same way, Table 27 and Table 28 gather evolved gases and evolved aerosols respectively during under-ventilated testing of PMMA, unfilled PVC and filled PVC and the values are compared with well-ventilated testing.

Table 27: Concentration peaks of evolved gases during under-ventilated testing

Material	CO ₂ (ppmv)	CO (ppmv)	H ₂ O (ppmv)	HCl (ppmv)	CH ₄ (ppmv)	C ₂ H ₆ (ppmv)	C ₂ H ₄ (ppmv)	C ₂ H ₂ (ppmv)	C ₆ H ₆ (ppmv)
PMMA	65 000	13 000	50 000	/	5 000	700	2 200	2 000	1 200
	30 000	200	15 000	/	/	250	/	/	50
Unfilled PVC	40 000	7 000	40 000	19 000	1 600	500	800	800	550
	11 000	1 100	10 000	5 500	75	/	/	75	/
Filled PVC	32 000	5 000	35 000	5 300	400	/	300	300	300
	11 000	1 100	7 000	4 000	60	/	/	60	/

Table 28: Mean concentration of total aerosols evolved during under-ventilated testing

Material	Mean concentration of total aerosol (#.m ⁻³)
PMMA	2.3×10^8
	1.3×10^9
Unfilled PVC	1.8×10^8
	5.1×10^7
Filled PVC	2.6×10^8
	4.5×10^9

As during well-ventilated testing, the pMLR, as well as pHRR are higher for unfilled PVC than for filled PVC (Table 26). Unfilled PVC burns more intensely than filled PVC also in under-ventilated fire regime. During enclosed testing, the THR_{O_2} of unfilled PVC is higher than the THR_{O_2} of filled PVC and the aerosols concentrations are similar during unfilled and filled PVC burning (Table 28). The evolved gases concentration peaks of filled and unfilled PVC are comparable but a bit higher for unfilled PVC (Table 27). Gases concentrations peaks are not to take as absolute values when comparing well-ventilated and under-ventilated experiments due to the difference in the smoke dilution with ambient air passing through the cone calorimeter⁷⁴. When thermally decomposing, PMMA yields its monomer, i.e. methyl methacrylate. Among the unburnt hydrocarbons identified by the FTIR spectrometer, methane and ethyne come from the intermediate products of complete combustion of methyl methacrylate [38]. In general, for the three materials, the relative amount of carbon monoxide and hydrocarbons increases and the relative amount of carbon dioxide decreases compared to the well-ventilated experiments. Nevertheless, the relative amount of water and hydrogen chloride does not show any remarkable variation with the ventilation. The EHC of under-ventilated combustion is lower than the EHC of well-ventilated combustion for PMMA and filled PVC, which is consistent with the higher amount of partially oxidized species, i.e. CO, and unburnt hydrocarbons compared with the amount of CO₂ during under-ventilated testing.

6. Conclusion

In this chapter, the combustion in the cone calorimeter under 50 kW.m⁻² of transparent 5-mm thick PMMA plaques and 3-mm thick PVC formulations were described in terms of phenomenology. It appears that PMMA and PVC formulations disclose two very different burning processes. PMMA is entirely consumed and leaves no residue, with a transient bubbling phase that provokes swelling and increases the exposed surface of the plaque, while PVC formulations form carbonaceous residue while burning that concentrates the plaque at the center of the sample holder and increases its thickness.

Tests with PMMA samples were performed in the cone calorimeter in order to compare the test results with the literature, as PMMA is a widely studied material in fire science [5]. The obtained results in terms of mass loss, heat release rate and evolved gases are in agreement with the data available in the literature [111][112]. In well-ventilated conditions, unfilled PVC burns more intensely than filled PVC since it exhibits a higher peak of mass loss rate and peak of heat release rate. However, unfilled PVC and filled PVC have similar total heat release. This is due to the slower combustion of filled PVC. For

⁷⁴ The amount of air passing through the apparatus is ≈ 18 times superior in well-ventilated configuration compared to the under-ventilated, i.e. enclosed configuration: $Q_{\text{well-ventilated}} \approx 560 \text{ L.min}^{-1}$ whereas $Q_{\text{under-ventilated}} = 30 \text{ L.min}^{-1}$.

the same reason, gases evolved during well-ventilated combustion of unfilled PVC and filled PVC exhibit the same concentration peaks but concentration of unfilled PVC evolved gases decrease more rapidly.

After performing well-ventilated tests in the cone calorimeter with the open configuration, the enclosure was sealed around the sample and the fire regime under 50 kW.m^{-2} of radiant heat flux and with an inlet airflow rate of 30 L.min^{-1} is characterized. PMMA, unfilled PVC and filled PVC burn in under-ventilated regime with these conditions, based on the $[\text{CO}]/[\text{CO}_2]$ (v/v) ratio, comprised between 0.1 and 0.3, and the equivalence ratio, comprised between 1 and 4, criteria [48].

Results of the under-ventilated combustion of PMMA, unfilled PVC and filled PVC were disclosed. When the combustion regime shifts from well-ventilated to under-ventilated, the composition of the evolved gases changes. The amount of partially oxidized compounds, i.e. carbon monoxide, and unburnt species increases while the amount of carbon dioxide decreases. The mass loss and heat release rate dynamics are modified with an earlier occurrence since in confined configuration, a lesser amount of air passes through the apparatus and, as a result, the sample may be less cooled down. However, the effect of under-ventilation on the integral values of fire parameters, i.e. total mass loss and total heat release, is not extensive.

Chapter V: Study of the vitiation effect

1. Introduction	145
2. Effect of vitiation on mass loss and heat release rate	146
2.1. <i>Effect of vitiation on mass loss and heat release rate for PMMA</i>	146
2.2. <i>Effect of vitiation on mass loss and heat release rate for unfilled PVC</i>	148
2.3. <i>Effect of vitiation on mass loss and heat release rate for filled PVC</i>	151
2.4. <i>Discussion on the effect of vitiation on the fire parameters</i>	153
3. Effect of vitiation on the evolved gases	156
3.1. <i>Effect of vitiation on the evolved gases for PMMA</i>	156
3.2. <i>Effect of vitiation on the evolved gases for unfilled PVC</i>	158
3.3. <i>Effect of vitiation on the evolved gases for filled PVC</i>	159
4. Effect of vitiation on the evolved aerosols	160
4.1. <i>Effect of vitiation on the evolved aerosols for PMMA</i>	160
4.2. <i>Effect of vitiation on the evolved aerosols for unfilled PVC</i>	161
4.3. <i>Effect of vitiation on the evolved aerosols for filled PVC</i>	161
5. Conclusion	163

1. Introduction

The previous chapter presented the effect of under-ventilation on the fire parameters and the evolved gases and aerosols for PMMA, unfilled and filled PVC. This chapter focuses on the effect of vitiation on these parameters, while keeping the fire regime under-ventilated, i.e. the inlet flow rate is kept at 30 L.min⁻¹. Vitiation effect is investigated by varying the oxygen content in the inlet nitrogen/air mixture from 21 vol. % to 2 vol. %⁷⁵. The effect of oxygen content on the mass loss and heat release rate of the three materials is covered in a first part, on the evolved gases in a second part, and on the evolved aerosols in a third part.

⁷⁵ When injecting 100 % of nitrogen, the oxygen sensor indicates 2 vol. % of oxygen probably due to small air infiltrations when the set-up is brought at high temperatures (thermal dilatation of the stainless steel may decrease the airtightness).

2. Effect of vitiation on mass loss and heat release rate

2.1. Effect of vitiation on mass loss and heat release rate for PMMA

Normalized mass and mass loss rate of PMMA versus time at different oxygen contents in the inlet gas stream (2, 6, 9, 13, 16, 18, 21 vol. %) are plotted in Figure 69a and Figure 69b respectively⁷⁶. It is observed that PMMA leaves no residue after thermal decomposition regardless of the oxygen content in the inlet gas stream (Figure 69a). Also, the onset time of thermal decomposition, as well as the TTI (time to ignition) and the TTE (time to extinction), increase when the oxygen content decreases (Table 29). The increase in the TTI with the decrease of oxygen content was also observed in [5]. Figure 69b that shows that pMLR decreases when the oxygen content decreases in the flaming mode. Between 21 vol. % and 13 vol. % of oxygen, pMLR decreases from 0.284 g.s^{-1} to 0.223 g.s^{-1} (-21%). However, pMLR stays constant, around 0.175 g.s^{-1} , when the oxygen content decreases in the non-flaming mode from 9 vol. % to 2 vol. % of oxygen.

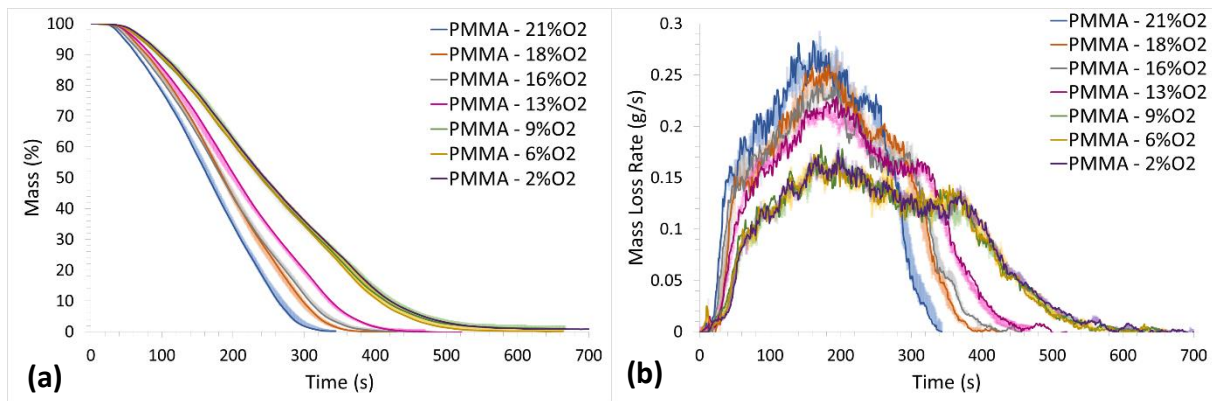


Figure 69: Evolution of mass of PMMA at different oxygen contents in the inlet gas stream. a) Normalized mass; b) Mass loss rate⁷⁷

The equivalence ratio is a function of both the amount of oxygen and the amount of fuel in the flame. It is then dependent on the fuel mass loss rate. The mass loss rate varying with the oxygen content in the inlet gas stream, the equivalence ratio as a function of time for PMMA burning is calculated at each oxygen content and plotted in Figure 70. Around the peak of mass loss rate, i.e. at approximately 180 seconds, the equivalence ratio varies from 3.8 at 21 vol. % O_2 to 2.9 at 13 vol. % O_2 . The fire regime is then still under-ventilated on the equivalence ratio criterion [48] regardless of the oxygen content.

⁷⁶ For each oxygen content, at least three experiments are repeated, the superposition of the data gathered for PMMA evolution of mass and is displayed in APPENDIX4, p. 177 for $[\text{O}_2] = 21 \text{ vol. \%}$. Appendix 5 p. 195 for $[\text{O}_2] = 18 \text{ vol. \%}$. Appendix 5 p. 198 for $[\text{O}_2] = 16 \text{ vol. \%}$. Appendix 5 p. 201 for $[\text{O}_2] = 13 \text{ vol. \%}$. Appendix 5 p. 202 for $[\text{O}_2] = 9 \text{ vol. \%}$. Appendix 5 p. 204 for $[\text{O}_2] = 6 \text{ vol. \%}$. Appendix 5 p. 206 $[\text{O}_2] = 2 \text{ vol. \%}$.

⁷⁷ Signals are read from bottom to top from 2 vol.% to 21 vol.% of O_2 .

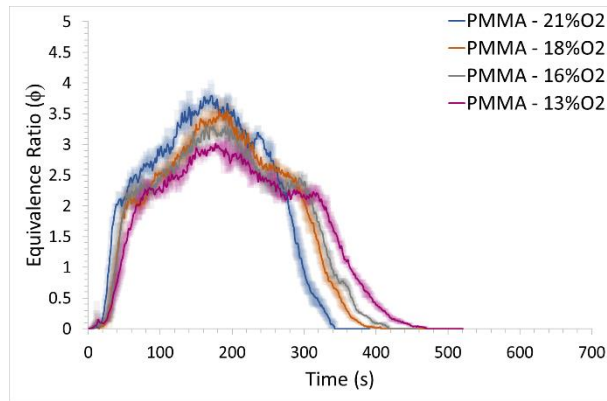


Figure 70: Evolution of equivalence ratio during PMMA burning at different oxygen contents in the inlet gas stream

In Figure 71 are plotted the HRR of PMMA at different oxygen content (from 16 to 21 vol. %). When the oxygen content decreases from 21 vol. % to 16 vol. %, pHRR decreases from 489 kW.m⁻² to 386 kW.m⁻² (-20%) and THR decreases from 130 MJ.m⁻² to 113 MJ.m⁻² (-13%).

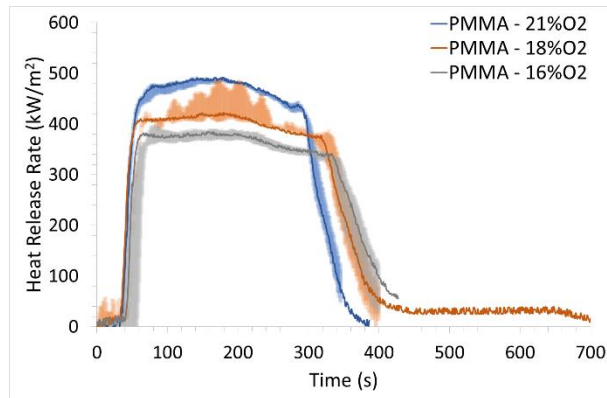


Figure 71: HRR of PMMA combustion at different oxygen contents in the inlet gas stream

13 vol. % of oxygen is the limit between the flaming and non-flaming mode. The flame that is formed above the sample is a premixed flame (Figure 72) that weakens and toughens when the oxygen content slightly varies. It has been shown by Quintiere and Rangwala [114] that the point of extinction is not only defined by a limiting oxygen concentration, but also depends on the local temperature, heat flux and material properties. The presence of a premixed flame during vitiated PMMA burning was also highlighted in the literature where the value of the limiting oxygen concentration depends on the test conditions: 10 vol. % in [63] (FTT CACC – 50 kW.m⁻² – 160 L.min⁻¹ of inlet flow rate) versus 16 vol. % in [52] (FPA – 20 kW.m⁻² – 25 L.min⁻¹ of inlet flow rate).

Because of the transient fire regime, the obtained HRR curves at 13 vol. % of O₂ are not repeatable, which is why the HRR curve at 13 vol. % of O₂ is not plotted in Figure 71.



Figure 72: Premixed flame during PMMA burning at 13 vol. % of oxygen

Table 29 gathers PMMA fire parameters at different oxygen contents. The reported values are average values. Their associated standard deviations are noted in italic grey underneath.

Table 29: Evolution of fire parameters with the oxygen content for PMMA testing

O₂ content (vol. %)	TTI (s)	TTE (s)	Residue (%)	pMLR (g.s⁻¹)	pHRR_{O2} (kW.m⁻²)	THR_{O2} (MJ.m⁻²)
21	22.7	366.7	0	0.284	488.9	129.8
<i>Std Deviation</i>	<i>0.6</i>	<i>24.6</i>	<i>0</i>	<i>0.005</i>	<i>3.9</i>	<i>0.8</i>
18	34.3	393	0	0.264	450.5	126.5
<i>Std Deviation</i>	<i>2.1</i>	<i>7</i>	<i>0</i>	<i>0.009</i>	<i>39.7</i>	<i>1.1</i>
16	40.6	426	0	0.246	385.7	113.2
<i>Std Deviation</i>	<i>16.5</i>	<i>18.4</i>	<i>0</i>	<i>0.003</i>	<i>13.6</i>	<i>3.1</i>
13	43.3	475.5	0	0.223	/*	/*
<i>Std Deviation</i>	<i>18.6</i>	<i>18.6</i>	<i>0</i>	<i>0.005</i>		
9	/	/	0	0.180	/	/
<i>Std Deviation</i>			<i>0</i>	<i>0.004</i>		
6	/	/	0	0.173	/	/
<i>Std Deviation</i>			<i>0</i>	<i>0.002</i>		
2	/	/	0	0.175	/	/
<i>Std Deviation</i>			<i>0</i>	<i>0.009</i>		

*Premixed flame, no repeatable results

2.2. Effect of vitiation on mass loss and heat release rate for unfilled PVC

Normalized mass and mass loss rate of unfilled PVC versus time at different oxygen contents in the inlet gas stream (2, 6, 9, 16, 18, 21 vol. %) are plotted on Figure 73a and Figure 73b respectively. For

each oxygen content, at least three experiments are repeated⁷⁸. Figure 73a shows that the amount of unfilled PVC residue increases when the oxygen content decreases. The onset time of unfilled PVC thermal decomposition, as well as the TTI (≈ 20 s - Table 30), are independent of the oxygen content. Figure 73b shows that the pMLR decreases when the oxygen content decreases in the flaming mode. Between 21 vol. % and 16 vol. % of oxygen, pMLR decreases from 0.284 g.s^{-1} to 0.205 g.s^{-1} (-28%). However, pMLR remains constant around 0.130 g.s^{-1} when the oxygen content decreases in the non-flaming mode from 9 vol. % to 2 vol. % of oxygen.

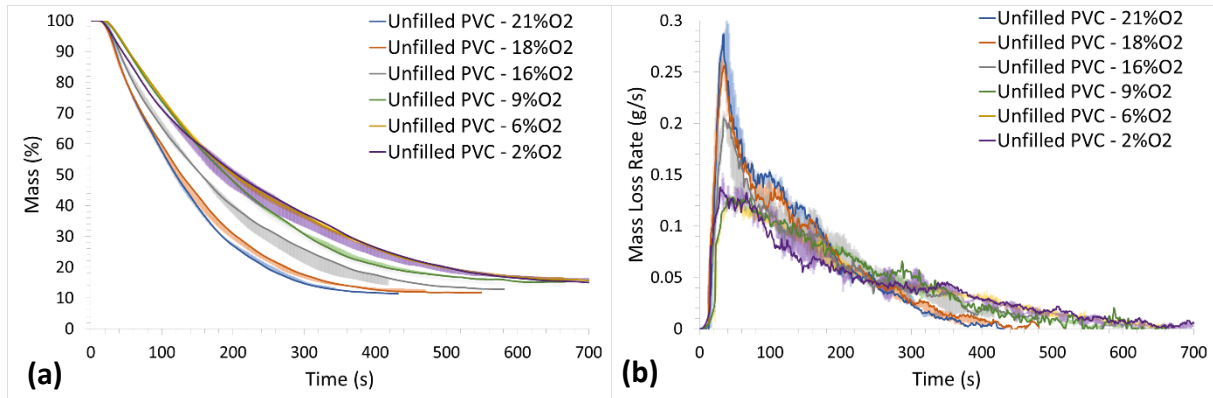


Figure 73: Evolution of mass of unfilled PVC at different oxygen contents in the inlet gas stream. a) Normalized mass; b) Mass loss rate

The equivalence ratio as a function of time for unfilled PVC burning is calculated at each oxygen content and plotted in Figure 74. Around the peak of mass loss rate, i.e. at approximately 50 seconds, the equivalence ratio varies from 3.8 at 21 vol. % O₂ to 2.8 at 16 vol. % O₂ so the fire regime is still under-ventilated on the equivalence ratio criterion [48] at these oxygen contents.

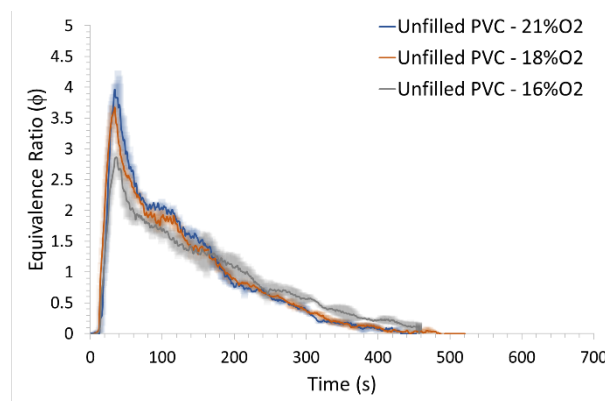


Figure 74: Evolution of equivalence ratio during unfilled PVC burning at different oxygen contents in the inlet gas stream

⁷⁸ The superposition of the data gathered for unfilled PVC evolution of mass and HRR is displayed in Appendix 4, p. 187 for [O₂] = 21 vol. %. Appendix 5 p. 196 for [O₂] = 18 vol. %. Appendix 5, p. 199 for [O₂] = 16 vol. %. Appendix 5, p. 203 for [O₂] = 9 vol. %. Appendix 5, p.205 for [O₂] = 6 vol. %. Appendix 5, p. 207 for [O₂] = 2 vol. %.

In Figure 75 are plotted the HRR of unfilled PVC at different oxygen content (from 16 to 21 vol. %). When the oxygen content decreases from 21 vol. % to 16 vol. %, pHRR and THR do not show any trend variation (in the 10% margin error).

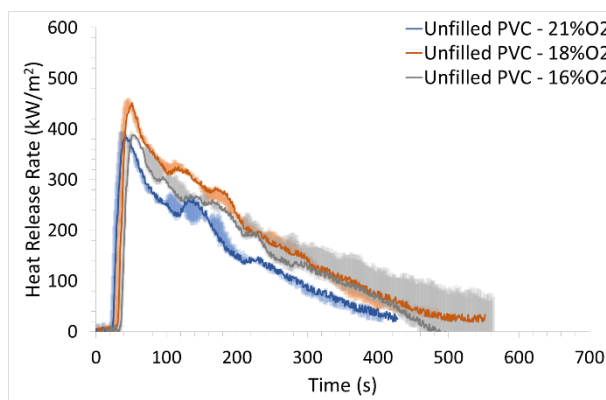


Figure 75: HRR of unfilled PVC combustion at different oxygen contents in the inlet gas stream

Table 30 gathers unfilled PVC fire parameters at different oxygen contents. The reported values are average values. Their associated standard deviations are noted in italic grey underneath.

Table 30: Evolution of fire parameters with the oxygen content for unfilled PVC testing

O ₂ content (vol. %)	TTI (s)	TTE (s)	Residue (%)	pMLR (g.s ⁻¹)	pHRR _{O₂} (kW.m ⁻²)	THR _{O₂} (MJ.m ⁻²)
21	22	430.3	8.4	0.284	389.4	61.7
<i>Std Deviation</i>	<i>2</i>	<i>29.5</i>	<i>1.4</i>	<i>0.012</i>	<i>3.9</i>	<i>0.4</i>
18	18	505.7	9.9	0.261	454.9	81.8
<i>Std Deviation</i>	<i>2.0</i>	<i>33.2</i>	<i>0.4</i>	<i>0.004</i>	<i>3.8</i>	<i>1.4</i>
16	21.3	541.3	10.9	0.205	391.1	75.4
<i>Std Deviation</i>	<i>1.5</i>	<i>42.7</i>	<i>0.2</i>	<i>0.006</i>	<i>4.2</i>	<i>6.6</i>
9	/	/	12.1	0.131	/	/
<i>Std Deviation</i>	<i>/</i>	<i>/</i>	<i>0.4</i>	<i>0.004</i>	<i>/</i>	<i>/</i>
6	/	/	12.9	0.128	/	/
<i>Std Deviation</i>	<i>/</i>	<i>/</i>	<i>0.2</i>	<i>0.001</i>	<i>/</i>	<i>/</i>
2	/	/	13.2	0.145	/	/
<i>Std Deviation</i>	<i>/</i>	<i>/</i>	<i>0.5</i>	<i>0.004</i>	<i>/</i>	<i>/</i>

2.3. Effect of vitiation on mass loss and heat release rate for filled PVC

Normalized mass and mass loss rate of filled PVC versus time at different oxygen contents in the inlet gas stream (2, 6, 9, 16, 18, 21 vol. %) are plotted on Figure 76a and Figure 76b respectively. For each oxygen content, at least three experiments are repeated⁷⁹. Figure 76a shows that the amount of filled PVC residue after thermal decomposition increases when the oxygen content decreases from 36.7 % at 21 vol. % O₂ to 40.4 % at 2 vol. % O₂. The onset time of filled PVC thermal decomposition, as well as the TTI (Table 31), are independent of the oxygen content. Figure 76b shows that the pMLR decreases when the oxygen content decreases in the flaming mode. Between 21 vol. % and 16 vol. % of oxygen, pMLR decreases from (-17%). However, pMLR stays constant around 0.076 g.s⁻¹ when the oxygen content decreases in the non-flaming mode between 9 vol. % and 2 vol. % of oxygen.

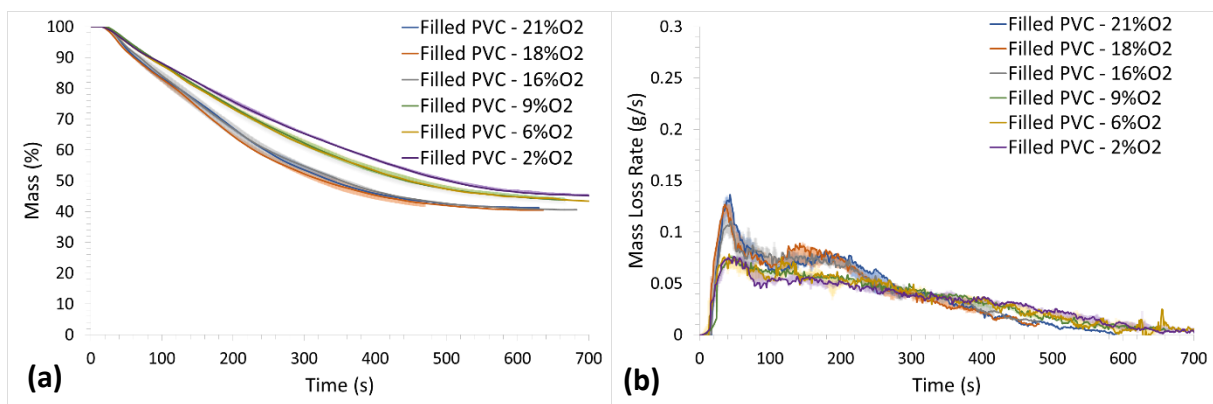


Figure 76: Evolution of mass of filled PVC at different oxygen contents in the inlet gas stream. a) Normalized mass; b) Mass loss rate

The equivalence ratio as a function of time for filled PVC burning is calculated at each oxygen content and plotted in Figure 77. Around the peak of mass loss rate, i.e. at approximately 50 seconds, the equivalence ratio varies from 1.8 at 21 vol. % O₂ to 1.5 at 16 vol. % O₂ so the fire regime is still under-ventilated on the equivalence ratio criterion [48] at these oxygen contents and does not vary much.

⁷⁹ The superposition of the data gathered for filled PVC evolution of mass and HRR is displayed in Appendix 4, p. 188 for [O₂] = 21 vol. %. Appendix 5 p. 197 for [O₂] = 18 vol. %. Appendix 5, p. 200 for [O₂] = 16 vol. %. Appendix 5, p. 203 for [O₂] = 9 vol. %. Appendix 5, p. 205 for [O₂] = 6 vol. %: Appendix 5, p. 207 for [O₂] = 2 vol. %.

Chapter V: Study of the vitiation effect

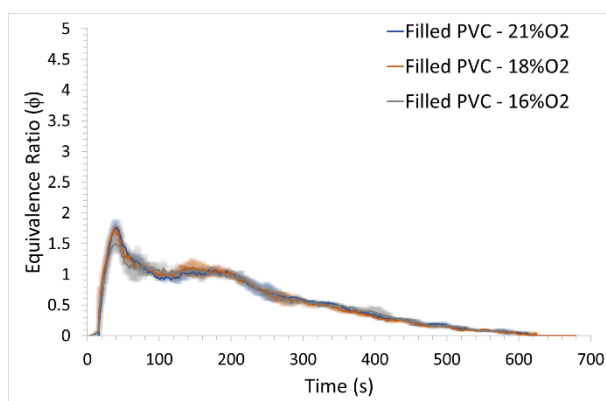


Figure 77: Evolution of equivalence ratio during filled PVC burning at different oxygen contents in the inlet gas stream

In Figure 78 are plotted the HRR of unfilled PVC at different oxygen content (from 16 to 21 vol. %). When the oxygen content decreases from 21 vol. % to 16 vol. %, pHRR and THR do not show any trend variation.

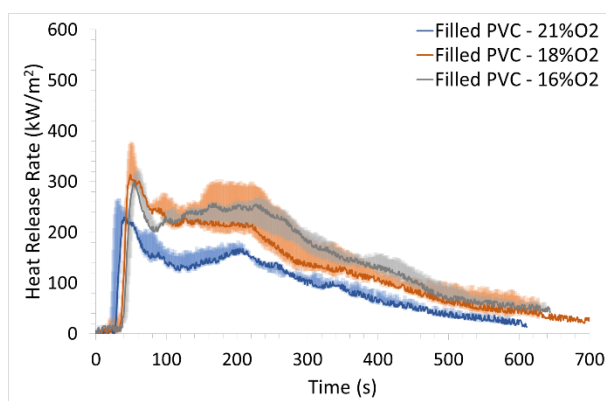


Figure 78: HRR of filled PVC combustion at different oxygen contents in the inlet gas stream

Table 31 gathers filled PVC fire parameters at different oxygen contents. The reported values are average values. Their associated standard deviations are noted in italic grey underneath.

Table 31: Evolution of fire parameters with the oxygen content for filled PVC testing

O ₂ content (vol. %)	TTI (s)	TTE (s)	Residue (%)	pMLR (g.s ⁻¹)	pHRR _{O2} (kW.m ⁻²)	THR _{O2} (MJ.m ⁻²)
21	23.3	621.0	36.7	0.129	226	46.1
<i>Std Deviation</i>	<i>2.1</i>	<i>29.5</i>	<i>0.7</i>	<i>0.009</i>	<i>5.4</i>	<i>1.1</i>
18	22.7	631.6	37.1	0.125	340.3	74.6
<i>Std Deviation</i>	<i>0.6</i>	<i>13.2</i>	<i>0.1</i>	<i>0.006</i>	<i>37.6</i>	<i>11.2</i>
16	23.7	642.7	37.7	0.107	311	73.3
<i>Std Deviation</i>	<i>1.2</i>	<i>22.7</i>	<i>0.5</i>	<i>0.007</i>	<i>12.2</i>	<i>5.1</i>

9 <i>Std Deviation</i>	/	/	38.9 <i>0.3</i>	0.079 <i>0.004</i>	/	/
6 <i>Std Deviation</i>	/	/	40.3 <i>0.4</i>	0.076 <i>0.005</i>	/	/
2 <i>Std Deviation</i>	/	/	40.4 <i>0.5</i>	0.076 <i>0.001</i>	/	/

2.4. Discussion on the effect of vitiation on the fire parameters

Figure 79a, Figure 79b and Figure 79c show the variation of the normalized peak of mass loss rate with the oxygen content for PMMA, unfilled PVC and filled PVC respectively. The dots represent normalized pMLR average values (pMLR values from Table 29, Table 30 and Table 31 are normalized at each oxygen content by the corresponding value in normal oxygen content, i.e. at 21 vol. %) and their respective standard deviations are represented by y - error bars.

In the flaming mode, pMLR decreases linearly when the oxygen content decreases for the three materials whereas in the non-flaming mode, pMLR stays relatively constant when the oxygen content decreases. Once the flame is set, an additional radiative heat flux is applied to the material. The value of this heat flux is estimated around 15 kW.m^{-2} for PMMA well-ventilated fires in the cone calorimeter [115]. This has the effect of increasing the material decomposition rate. As stated in [116], a lower oxygen content strongly decreases the PMMA flame temperature and the combustion efficiency. The additional radiative heat flux received by the PMMA condensed phase is then decreased. On another hand, the effect of oxygen depletion on the condensed phase thermal decomposition has no effect since when a diffusion flame is present, the region above the condensed phase surface is deprived of oxygen as the oxygen is consumed by the flame [107][108].

However, in the non-flaming mode, oxygen may have a direct effect on the condensed phase thermal decomposition since the PMMA surface undergo thermo-oxidative reactions. Though, the experimental results show that oxygen has no significant effect on the thermal decomposition rate of PMMA, unfilled and filled PVC. It may be explained by the fact that at high irradiance exposure such as 50 kW.m^{-2} , the gaseous products emission phenomenon resulting from in-depth thermolysis reactions overcomes the oxygen diffusion phenomenon inside the PMMA material [63]. Then, the oxidative reactions occur only at the surface of the material and as a result are not significant on the decomposition rate.

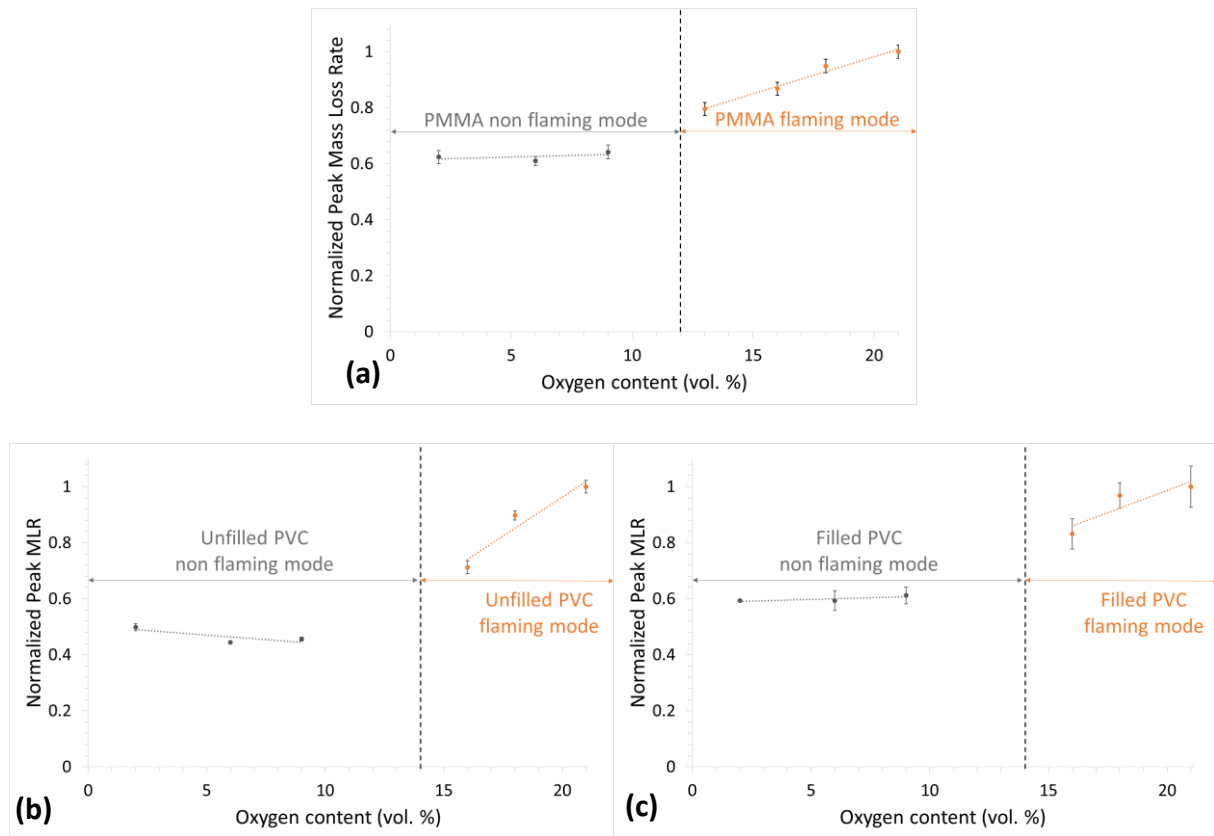


Figure 79: Normalized peak of mass loss rate versus the oxygen content for a) PMMA; b) Unfilled PVC; c) Filled PVC

The decrease of PMMA flame radiation in vitiated atmospheres has been highlighted in [55] and the same observations regarding the dependence of pMLR and pHRR towards the oxygen content with PMMA are found in the literature [63][55][56][5]. A comparison of the present work experimental values of pMLR and pHRR versus oxygen content for PMMA with the mentioned bibliographic references values is made in Figure 80a and Figure 80b respectively. In flaming mode, de PMMA pMLR decreases linearly with the oxygen content. All the studies that experimented the effect of vitiation with PMMA submitted to a 50 kW.m^{-2} radiative heat flux give approximately the same slope in the pMLR decrease. The same study with a radiative heat flux of 30 kW.m^{-2} gives a higher slope in the decrease of pMLR with the oxygen content variation in the flaming mode. All of the data gathered regarding the influence of vitiation in the non-flaming mode indicate that there is no influence of the oxygen content on pMLR. A fewer studies are dedicated to the effect of vitiation on the pHRR. Among the two studies reported in Figure 80b and the present work, all of the three series of data indicate that pHRR decreases also linearly with the oxygen content and the slope seems to be independent on the radiative heat flux from 50 kW.m^{-2} to 30 kW.m^{-2} .

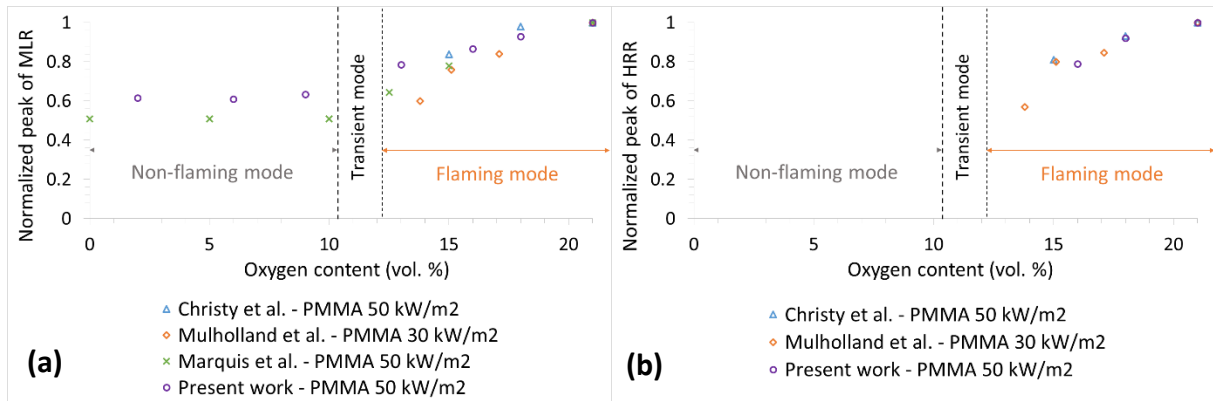


Figure 80: Comparison of the present work experimental values with the literature for a) pMLR vs O_2 content; b) pHRR vs O_2 content

Figure 81 shows the comparison between PMMA, unfilled PVC and filled PVC normalized pMLR values as a function of the oxygen content. It is observed, especially with unfilled PVC, that the slope of the evolution of pMLR is steeper than the one of PMMA. It may be explained by the higher flame radiative feedback in the case of PVC. Indeed, the flame radiative heat flux depends on flame emissivity which is influenced by soot volume fraction, and both PVC materials produce a higher soot volume fraction than PMMA. Furthermore, the soot volume fraction is not influenced by the oxygen content as shown subsequently (section 4 of this chapter, p. 160).

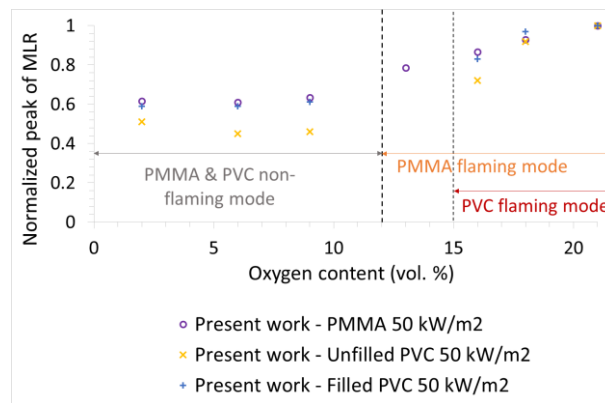


Figure 81: Comparison between PMMA, unfilled PVC and filled PVC normalized pMLR values versus oxygen content

Figure 82 reports the amount of residue for unfilled and filled PVC as a function of the oxygen content. The dots are the average values of residue and the y – error bars correspond to their respective standard deviation (Table 30 and Table 31). A linear trend is seen for the evolution of amount of residue with the decrease of oxygen content for both unfilled and filled PVC and the linear regression lines are plotted in the figure.

The amount of residue of filled PVC is much higher to the one of unfilled PVC because of the mineral filler which is present in the form of calcium carbonate at the end of the test. Furthermore, calcium

carbonate is inert towards oxygen and towards charring mechanisms. The difference of amount of residue is then only due to the char oxidation, which explains the fact that the two linear regression lines have the same slope.

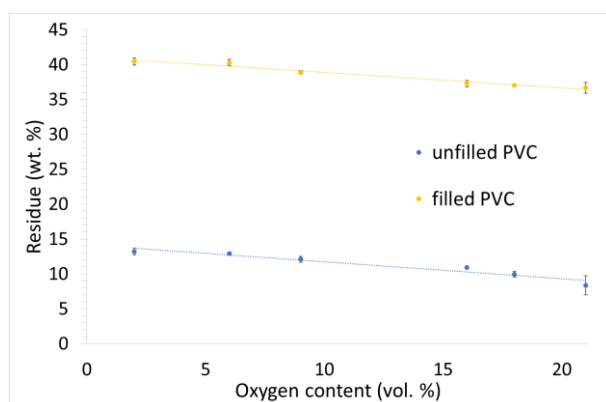


Figure 82: Amount of residue versus oxygen content for unfilled and filled PVC

3. Effect of vitiation on the evolved gases

3.1. Effect of vitiation on the evolved gases for PMMA

Figure 83 shows the evolution of evolved gases during PMMA burning at different oxygen contents⁸⁰. It is seen that, considering the experimental uncertainties, the oxygen content seems to have no effect on the CO₂, CO, H₂O, CH₄, C₂H₄, C₂H₂ and C₆H₆ production, which makes the [CO]/[CO₂] (v/v) ratio remain quite constant regarding the vitiation. CO₂ is released at a concentration of approximately 60 000 ppmv and CO is released at a concentration peak of approximately 13 000 ppmv. H₂O is released at a concentration of approximately 45 000 ppmv and CH₄, C₂H₄, C₂H₂ and C₆H₆ are released at a concentration peak of approximately 5 000, 2 200, 2 000 and 800 ppmv.

In [5], the effect of vitiation when varying oxygen content from 21 vol. % to 15 vol. % in well-ventilated conditions (1 440 L.min⁻¹ of inlet flow rate) increases the [CO]/[CO₂] (v/v) ratio of PMMA from 0.006 to 0.015. This trend is not observed in this present work maybe because the vitiation effect is coupled with under-ventilation effect.

⁸⁰ Data at 18 vol. % O₂ is not presented because the FTIR spectrometer was dysfunctional for this series of test.

Chapter V: Study of the vitiation effect

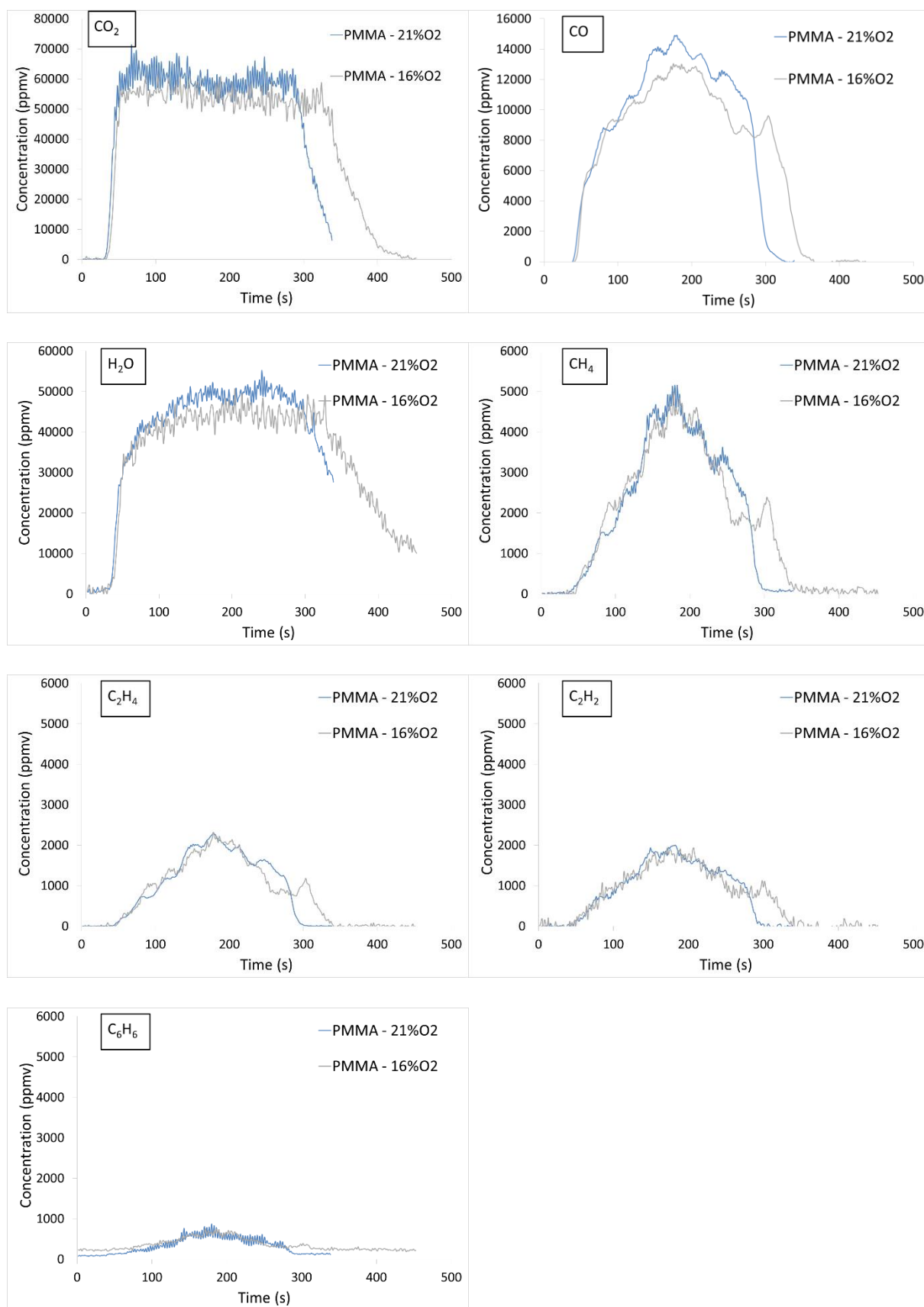
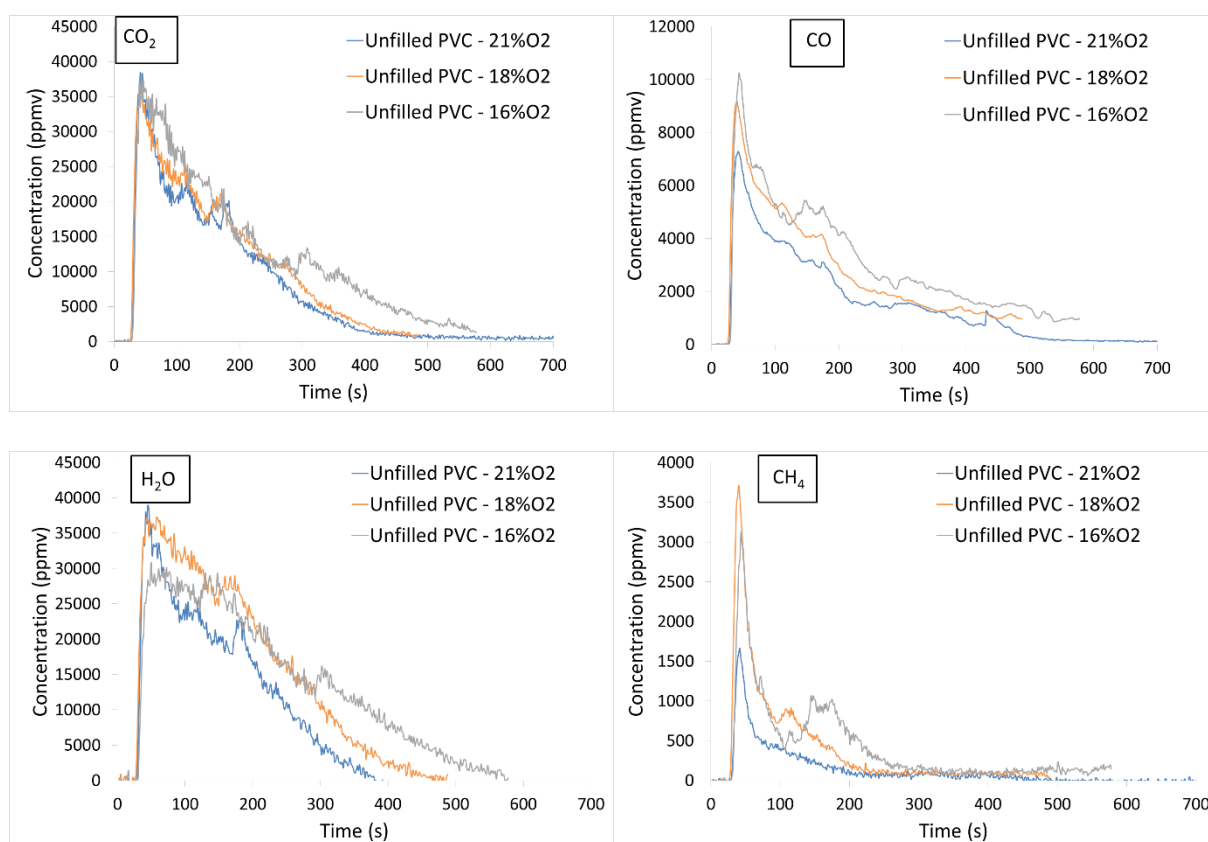


Figure 83: Evolution of evolved gases during PMMA burning at different oxygen contents in the inlet gas stream

3.2. Effect of vitiation on the evolved gases for unfilled PVC

Figure 84 shows the evolution of evolved gases during unfilled PVC burning at different oxygen contents. The oxygen content seems to have no effect on the CO_2 , H_2O , CH_4 , C_2H_4 , C_2H_2 , C_6H_6 and HCl production. However, the CO production seems to increase when the oxygen content decreases⁸¹: it is released at a concentration peak of about 7 200, 9 000 and 10 400 ppmv for oxygen contents of 21, 18 and 16 vol. % respectively. CO_2 is released at a concentration peak of approximately 37 000 ppmv. The $[\text{CO}]/[\text{CO}_2]$ ratio then increases from 0.19 at 21 vol. % O_2 to 0.27 at 16 vol. % O_2 . H_2O is released at a concentration of approximately 35 000 ppmv and CH_4 , C_2H_4 , C_2H_2 , C_6H_6 and HCl are released at a concentration peak of approximately 2 500, 1 200, 1 000, 1 000 and 22 000 ppmv.



⁸¹ The repeatability of the three runs performed allows to draw that conclusion. The superposition of plotted data is available in Appendix 4, p. 194 for 21 vol. % O_2 , Appendix 5, p. 213 for 18 vol. % O_2 and Appendix 5, p. 217 for 16 vol. % O_2 .

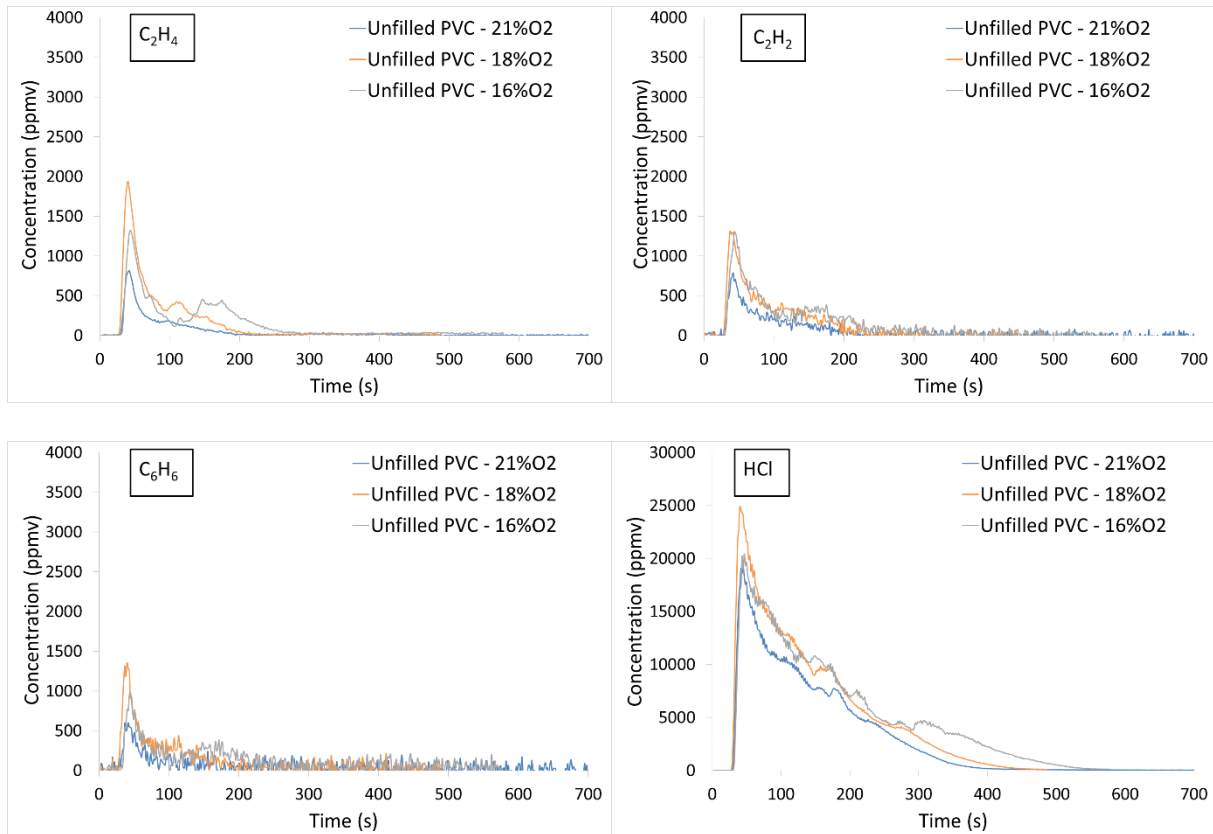
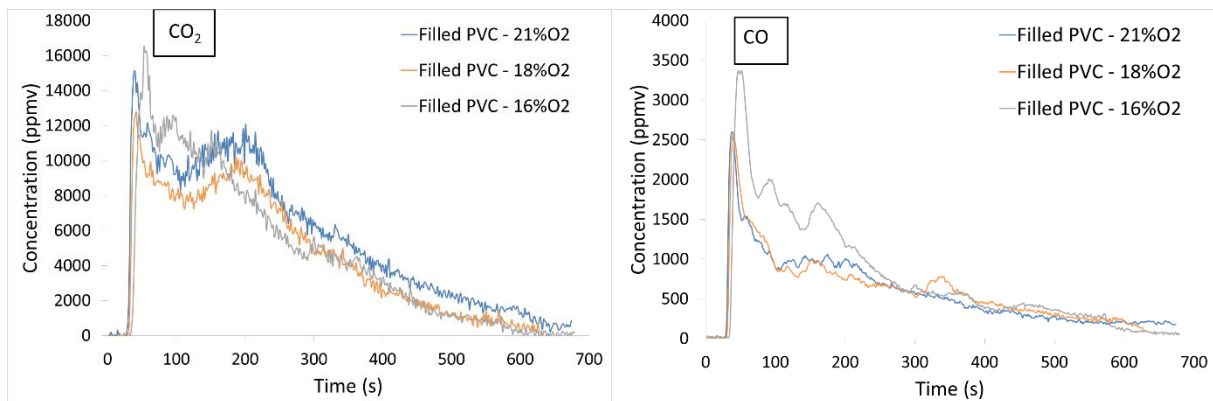


Figure 84: Evolution of evolved gases during unfilled PVC burning at different oxygen contents in the inlet gas stream

3.3. Effect of vitiation on the evolved gases for filled PVC

Figure 85 shows the evolution of evolved gases during filled PVC burning at different oxygen contents. As for unfilled PVC, the oxygen content seems to have no effect on the CO₂, CO, H₂O, CH₄, C₂H₄, C₂H₂, C₆H₆ and HCl production, which makes the [CO]/[CO₂] also independent on the oxygen content. CO₂ is released at a concentration peak of approximately 14 000 ppmv and CO is released at a concentration peak of approximately 2 500 ppmv. H₂O is released at a concentration of approximately 1 500 ppmv and CH₄, C₂H₄, C₂H₂, C₆H₆ and HCl are released at a concentration peak of approximately 300, 150, 200, 150 and 2 500 ppmv.



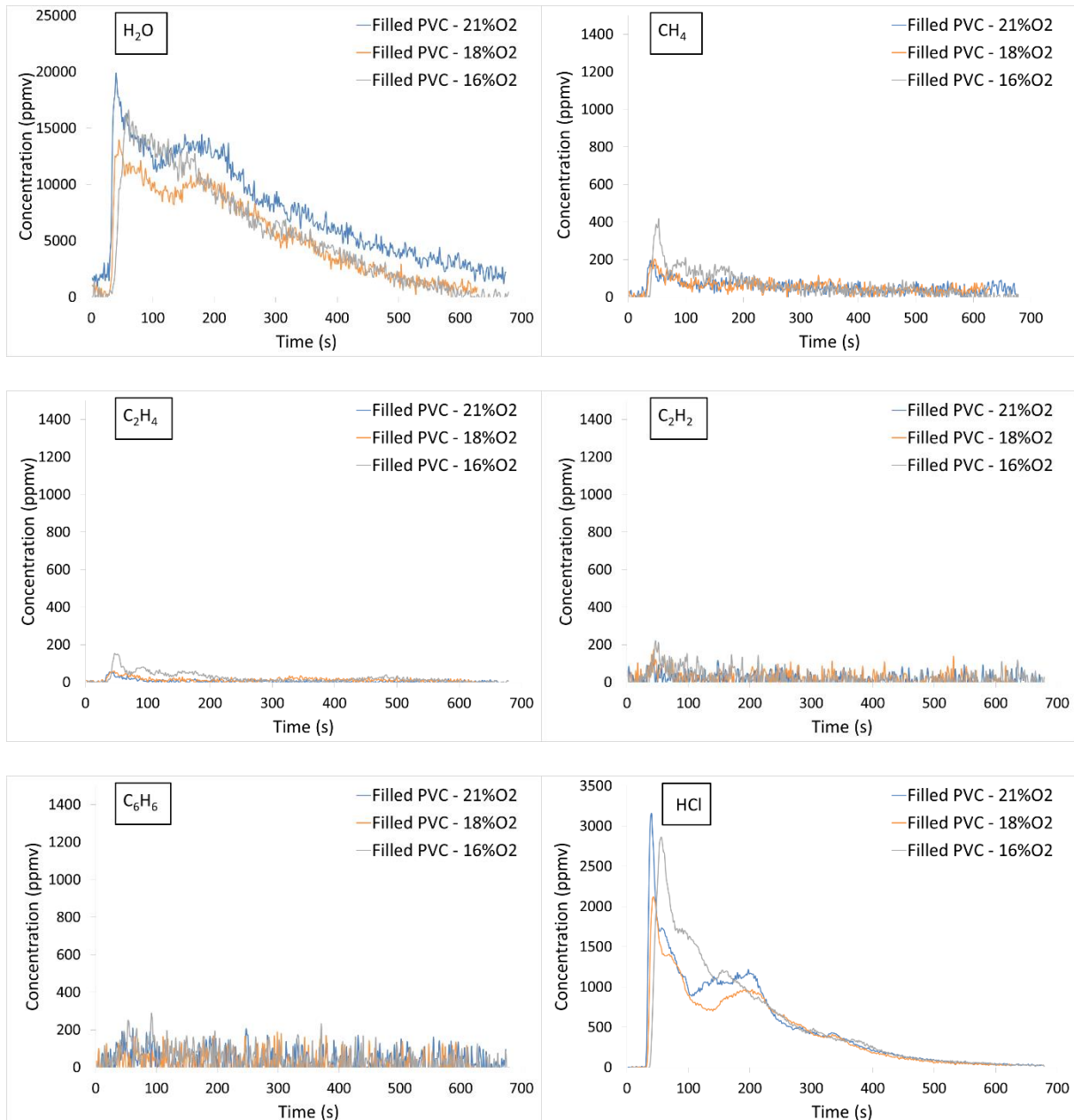


Figure 85: Evolution of evolved gases during filled PVC burning at different oxygen contents in the inlet gas stream

4. Effect of vitiation on the evolved aerosols

4.1. Effect of vitiation on the evolved aerosols for PMMA

Figure 86 shows the evolution of evolved aerosols during PMMA burning at different oxygen contents. The oxygen content seems to have no effect on both the total amount of aerosols released and on their size distribution. The total amount of evolved aerosols during under-ventilated and vitiated burning of PMMA exhibit a stationary phase of around $2.5 \times 10^8 \text{ \#} \cdot \text{m}^{-3}$.

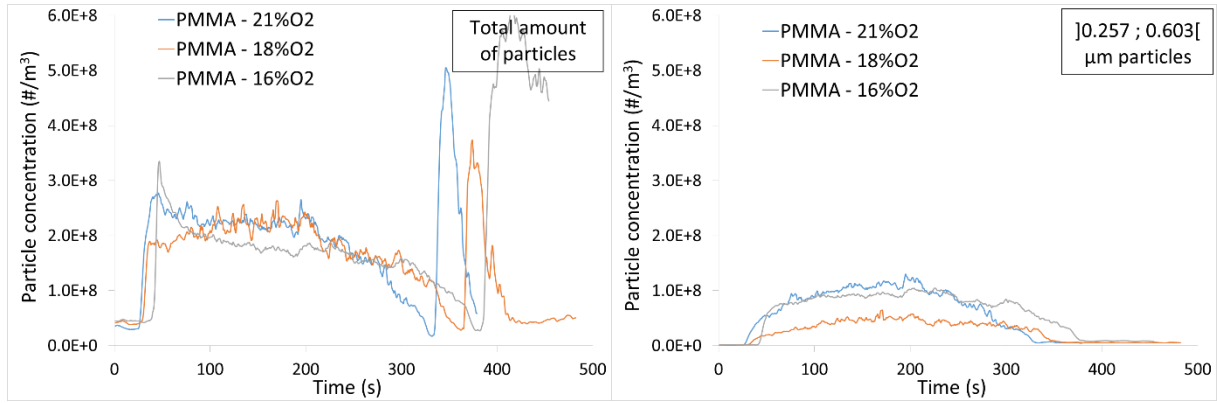


Figure 86: Evolution of evolved aerosols during PMMA burning at different oxygen contents in the inlet gas stream

4.2. Effect of vitiation on the evolved aerosols for unfilled PVC

Figure 87 shows the evolution of evolved aerosols during unfilled PVC burning at different oxygen contents. The oxygen content seems to have no effect on both the total amount of aerosols released and on their size distribution. The total amount of evolved aerosols during under-ventilated and vitiated burning of unfilled PVC is around $2.2 \times 10^8 \# \cdot m^{-3}$.

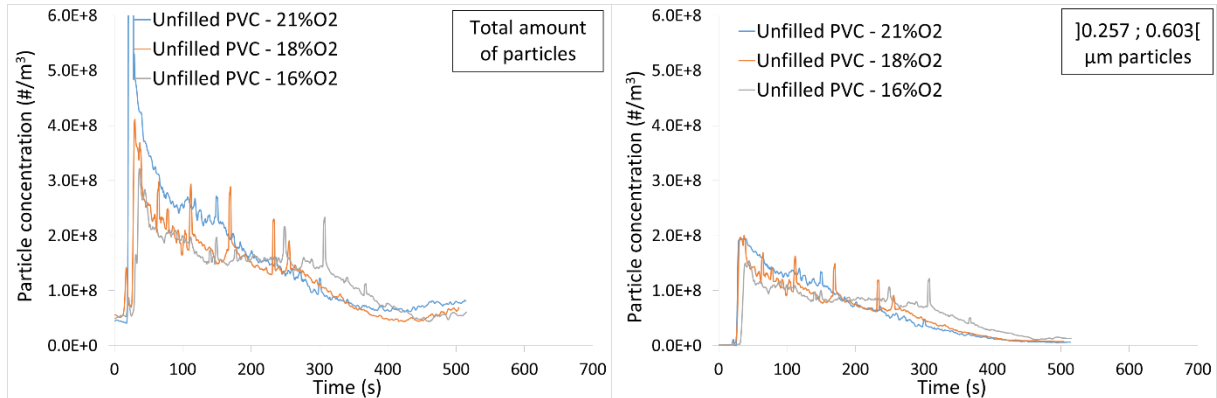


Figure 87: Evolution of evolved aerosols during unfilled PVC burning at different oxygen contents in the inlet gas stream

4.3. Effect of vitiation on the evolved aerosols for filled PVC

Figure 88 shows the evolution of evolved aerosols during unfilled PVC burning at different oxygen contents. The oxygen content seems to have no effect on both the total amount of aerosols released and on their size distribution. The total amount of evolved aerosols during under-ventilated and vitiated burning of unfilled PVC is around $1.8 \times 10^8 \# \cdot m^{-3}$.

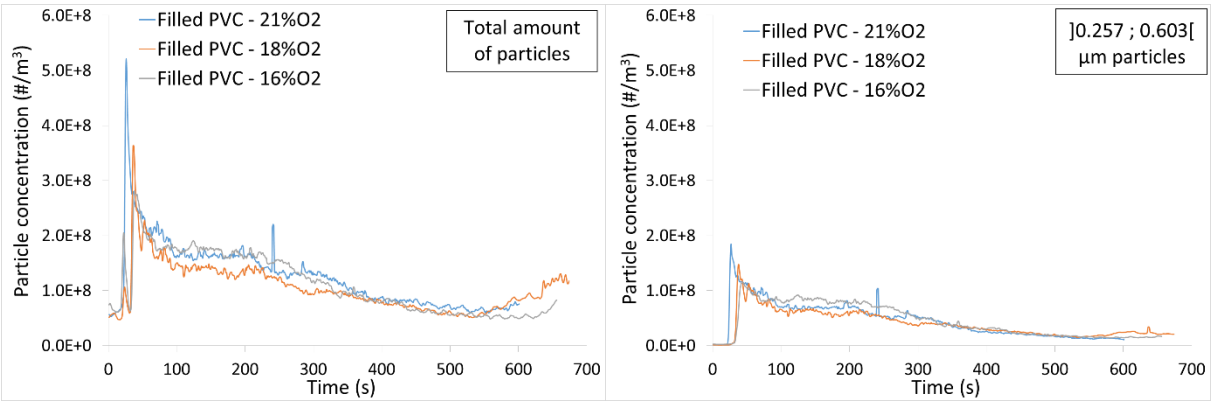


Figure 88: Evolution of evolved aerosols during filled PVC burning at different oxygen contents in the inlet gas stream

5. Conclusion

In this chapter, the studied parameter is the vitiation, i.e. the oxygen concentration in the inlet gas stream, though the experiments were performed in a fire regime both under-ventilated and vitiated.

Under 50 kW.m^{-2} and with an inlet flow rate of 30 L.min^{-1} , PMMA exhibits an extinction limit around 13 vol. % of oxygen whereas both unfilled and filled PVC quench around 15 vol. % of oxygen. For the three materials, i.e. PMMA, unfilled PVC and filled PVC, the pMLR decreases linearly when the oxygen content decreases from 21 vol. % to their respective extinction limits, i.e. in flaming mode. However, in non-flaming mode, pMLR of the three materials are independent on the oxygen content varying from 9 vol. % to 2 vol. %. The pMLR decrease with the decrease of oxygen content may be explained by the decrease in flame radiative feedback when the oxygen content decrease. The PMMA pHRR also decreases linearly when the oxygen content decreases whereas the PVC formulations pHRR does not show any trend variation with the vitiation.

The slope of the PMMA pMLR and pHRR decrease are in agreement with the values available in the literature. Vitiation has also an effect on the amount of residue left during burning of unfilled and filled PVC. Lowering the oxygen content will increase the amount of residue which may be due to the lower char oxidation after flame-out when the oxygen content decreases.

Considering the experimental uncertainties, the oxygen content seems to have no effect on both the evolved gases and aerosols during PMMA and filled PVC burning. As regards unfilled PVC, the decrease in oxygen content seems to increase the CO production, shifting the $[\text{CO}]/[\text{CO}_2]$ (v/v) ratio from 0.19 at 21 vol. % O_2 to 0.27 at 16 vol. % O_2 .

General conclusion

Conclusion

A bench-scale controlled-atmosphere cone calorimeter has been developed for studying oxygen depleted fires. It is a versatile equipment that permits to control several parameters such as the inlet gas composition, its inlet flow rate and distribution into the enclosure, and thus yields repeatable data. A heat release rate measurement adapted to oxygen depleted fires, based on oxygen consumption and taking into account the amount of carbon monoxide, has been implemented to replace the thermopile measurements. Gases and aerosols measurements have been also modified to fit the confined configuration by adding dilution systems upstream the FTIR spectrometer and the EPLPI granulometer respectively.

A representative material of electrical cable sheath – filled PVC – is tested in the cone calorimeter to characterize samples of controlled composition. For this reason, a PVC-based electrical cable sheath material has undergone reverse engineering to disclose its composition. From this, plaques of a representative material containing 38.3 wt. % of PVC, 28.3 wt. % of DIDP, 31.4 wt. % of CaCO_3 and 1.9 wt. % of a Ca/Zn stabilizing system were manufactured and characterized at lab-scale to study their thermal decomposition mechanism. TGA performed under nitrogen showed that the filled PVC material follows a three-step thermal decomposition yielding a 29 wt. % residue and PCFC testing yielded a 11.7 MJ.kg^{-1} heat of combustion. A neat plasticized PVC – unfilled PVC – has also been manufactured in the shape of plaques and characterized at lab-scale.

Well-ventilated tests were performed in the open configuration cone calorimeter under 50 kW.m^{-2} to provide data on mid fire stages. Then, both the under-ventilation and the vitiation effect were studied in the controlled-atmosphere cone calorimeter under 50 kW.m^{-2} . The results obtained for PMMA in well-ventilated conditions are consistent with the literature data in terms of mass loss rate (e.g. $\text{pMLR} = 0.27 \text{ g.s}^{-1}$), heat release rate (e.g. $\text{pHRR} = 696 \text{ kW.m}^{-2}$; $\text{EHC} = 23.6 \text{ MJ.kg}^{-1}$) and evolved gases concentrations (e.g. $\text{p}[\text{CO}_2] = 30\,000 \text{ ppmv}$; $\text{p}[\text{CO}] = 200 \text{ ppmv}$). Furthermore, the trends observed for PMMA behavior in under-ventilated and vitiated conditions are comparable with those reported in the literature [110] [111].

The original results obtained for filled PVC give an insight of the heat released and the species produced simultaneously during an electrical cable fire, from mid to advanced stages. PMMA and PVC-based materials do not exhibit the exact same reaction towards under-ventilation and vitiation. Under-ventilation increases the production of unburnt species, such as carbon monoxide and hydrocarbons, shifting PMMA and filled PVC $[\text{CO}]/[\text{CO}_2]$ (v/v) ratio from 0.007 to 0.20 and from 0.10 to 0.16

respectively whereas vitiation seems to have no effect on the production of gaseous species and aerosols for both of the materials. However, unfilled PVC $[CO]/[CO_2]$ (v/v) ratio shifts from 0.19 to 0.27 when oxygen content decreases from 21 vol. % to 16 vol. %. PMMA exhibits a flame extinction transition around 13 vol. % O_2 whereas PVC-based materials quench around 15 vol. % O_2 . In flaming regime, vitiation decreases the mass loss rate of both PMMA (- 20 % of pMLR between 21 and 13 vol. % O_2) and filled PVC (- 17 % of pMLR between 21 and 16 vol. % O_2) linearly by lowering the flame radiative feedback. Vitiation lowers the heat release rate linearly in the case of PMMA burning (- 20 % of pHRR between 21 and 16 vol.% O_2) whereas it seems to have no significant effect on the heat release rate in the case of PVC-based materials burning.

Perspectives

The new instrumented controlled-atmosphere calorimeter will allow EDF to determine the behavior of several materials used in nuclear power plants throughout a confined fire and, as a result, to be able to assess its impact on the environment such as electrical devices. Especially, now that the set up and procedure yields accurate and repeatable data, the experiments can be reconducted with electrical cables.

To improve the set-up efficiency in the future, the measurement of exhaust flow rate must be improved. This parameter is particularly important to calculate the heat release rate by means of oxygen consumption in the open configuration. The current measurement is performed with a Pitot tube and the obtained signal is noisy. Also, within the scope of the study, the species yields must be determined and the char residue must be analyzed in term of elementary composition in order to achieve an elementary species balance.

In further investigations, the external radiative heat flux is a parameter that may be varied, e.g. from 0 to 150⁸² kW.m⁻². For instance, a lower radiative heat flux may be applied in well-ventilated configuration to study the materials behavior at early fire stages. To extend the evolved smoke characterization during oxygen depleted experiments, heavy hydrocarbons, e.g. PAHs, may be weighted after condensation with a smoke cooling system and the aerosol mass concentration may be measured by coupling an SMPS (scanning mobility particle sizer) to the ELPI [87]. The inlet volume flow rate in the enclosure is a parameter that may be investigate to modulate the under-ventilation, especially because the effect of vitiation in well-ventilated conditions has never been studied to our knowledge in the case of PVC materials. Finally, as the heat conveyed by radiation is the driving force of fire growth, it would be interesting to measure the flame radiative heat flux.

⁸² The heat flux applied by the resistance in the cone calorimeter can be varied from 0 to 75 kW.m⁻². Nevertheless, another set-up allowing to reach radiative heat flux larger than 75 kW.m⁻² may be developed.

Appendix

Appendix 1: Physical description of soot aggregates and theory of measurement

1. Physical description of soot aggregates	169
1.1. <i>Brownian motion</i>	169
1.2. <i>Primary particles diameter D_p</i>	172
1.3. <i>Radius of gyration R_g</i>	172
1.4. <i>Number of primary particles in the aggregate N_p</i>	172
1.5. <i>Expression of the fractal theory</i>	172
2. Physical quantities useful for characterization	174
2.1. <i>Information related to particles weight and volume</i>	175
2.1.1. The equivalent volume diameter D_{ev}	175
2.1.2. The matter volume V_m	175
2.1.3. The material density ρ_m	175
2.1.4. The soot volume fraction f_v	175
2.2. <i>The equivalent diameters</i>	176
2.2.1. The equivalent aerodynamic diameter D_a	176
2.2.2. The electrical mobility diameter D_m	176
2.2.3. Diameters used to characterize a soot aggregate – summary	177
3. Theory of measurement	178

1. Physical description of soot aggregates

1.1. Brownian motion

Particles motion as well as their collision frequency depends on their size and on the carrier gas thermodynamic conditions (mostly pressure and temperature). According to the particles dimension, the carrier gas can be considered whether as a continuous fluid or as a discontinuous corpuscular middle [117].

In the second condition, the Brownian motion, which is directly resulting from the collisions between the particles and the molecules of the surrounding fluid, governs the final morphology of the soot aggregates.

What characterizes the global motion of a particle (λ_p , in nm, expressed in Equation 47) is its mean free path. This is the average distance traveled by a moving particle between successive collisions, which modifies its direction and energy.

Equation 47: Particle mean free path [33]

$$\lambda_p = \frac{8D}{\pi \bar{v}}$$

The mean free path is directly proportional to the diffusion coefficient D , which is inversely proportional to the particle mobility diameter (D_m), as it is expressed in Equation 48.

Equation 48: Particle diffusion coefficient [33]

$$D = \frac{k_B T C_c(D_m)}{3\pi\eta D_m}$$

k_B is the Boltzmann constant [$\text{m}^2 \cdot \text{kg} \cdot \text{s}^{-2} \cdot \text{K}^{-1}$], C_c is the Cunningham correction factor, T is the temperature of the fluid [K], and η is the dynamic viscosity of the fluid [Pa.s].

The motion rate (\bar{v}) is proportional to the temperature and to the particle mass m_p as expressed in Equation 49.

Equation 49: Particle motion rate [33]

$$\bar{v} = \sqrt{\frac{8k_B T}{\pi m_p}}$$

The continuity of the surrounding middle, according to a particle of r_p radius is characterized by the dimensionless Knudsen number (K_n). This number permits to identify the gas flow pattern around a particle.

There are two different flow regimes possible according to the Knudsen number:

- $K_n = \frac{\lambda_g}{r_p} \gg 1$ corresponds to the *free molecular regime*. Particles encounter a small number of molecules on their way. The carrier gas is then described as a series of discrete collision molecules.
- $K_n = \frac{\lambda_g}{r_p} \ll 1$ corresponds to the *continuous regime*. Particles are large compared to the mean free path. Many molecular collisions occur. The carrier gas is defined as a continuous surrounding.

If $0.1 < K_n < 10$, particles are considered in a *transition regime*, as stated by DeCarlo and al. in 2004[118]. It is in this regime that soot particles are formed.

The interaction between the carrier gas and the particles is characterized by the drag force \vec{F} . The Stokes law (1951) describes the resistance force that undergoes a spherical particle in motion with a diameter d_p as expressed in Equation 50.

Equation 50: Drag force according to Stokes (1951)

$$\vec{F} = 3\pi d_p \eta \vec{V}$$

\vec{V} is the relative motion rate of the particle compared to the surrounding fluid. It is worth mentioning that this law is respected in really restricted conditions. The motion rate of the particle must be very small (less than 1 m/s), the superficial layer must be perfectly bonding and the flow must be laminar. When these conditions are not gathered, the resistance of the surrounding fluid towards the particles must be corrected by nonlinear Stokes effects [117].

A corrective factor, called the Cunningham correction factor (C_c) may be applied to the drag force equation (Equation 50) when the surrounding fluid cannot be seen as a continuous fluid (for Knudsen numbers superior to 1). The drag force is then corrected according to Equation 51.

Equation 51: Corrected drag force with the Cunningham factor for transition and free molecular regime

$$\vec{F} = \frac{3\pi d_p \eta \vec{V}}{C_c(d_p)}$$

Cunningham derived the correction factor in 1910 from experimental data. The empirical equation obtained is shown below (Equation 52):

Equation 52: Definition of the Cunningham correction factor

$$C_c = 1 + \frac{2\lambda_p}{d_p} (A_1 + A_2 + e^{-A_3 \times d_p / \lambda_p})$$

Where λ_p is the mean free path of particles [m] as defined in Equation 47 and d_p the particle diameter [m]. For information, Table 32 gathers some Cunningham factor values calculated at $P=101,3$ kPa (pression determines the mean free path), for different particles diameter.

Table 32: Examples of calculated Cunningham factors for given particles diameter [119]

Particle diameter (μm)	Cunningham factor value
0.005	45.21
0.01	22.91
0.05	5.11
0.1	2.92
1	1.15
10	1,02

1.2. Primary particles diameter D_p

It is necessary to know the diameter of the primary particles, also called the monomers, in order to describe the aggregate properly. It is generally accepted to consider the size distribution law of these spherules is of a Gaussian type and that the dispersion is low [120].

Therefore, a simplifying assumption is to recognize that within the aggregate, or more generally for all the aggregates collected in the same location in the flame, we can reduce this parameter D_p to an average value. It is considered as well that all the primary particles have the same size [121]. Many studies have been conducted to determine this parameter and the value of D_p is between 10 and 60 nm [122], and depends on both the type of flame studied and the fuel.

1.3. Radius of gyration R_g

Another important parameter in the description of the soot particles is the radius of gyration R_g . This gives an estimate of the mass distribution of the aggregates. The calculation of this size involves the average of the square of the distance between primary particles (with position vector r_i) and the center of mass of the aggregate (with position vector r_c). The position vector of the center of mass of the aggregate is:

$$r_c = \frac{1}{N_p} \sum_{i=1}^{N_p} r_i$$

The radius of gyration is calculated from the radius of the primary particles R_p ($R_p = \frac{D_p}{2}$), the number of the particles in the aggregate N_p and l_i as expressed in Equation 53.

Equation 53: Expression of the radius of gyration of an aggregate

$$R_g^2 = \frac{1}{N_p} \sum_{i=1}^{N_p} (r_i - r_c)^2$$

1.4. Number of primary particles in the aggregate N_p

The number of primary particles constituting the aggregate is dependent on both the type of combustion involved and the particulate residence time in the flame. Therefore, the values of N_p found in the literature are widely dispersed and can range from just a few to a few hundred particles. For the same fuel and the same flame conditions, the particles observed in the reactive zone of the flame will include a smaller number of monomers than the ones taken from the smoke area [122].

1.5. Expression of the fractal theory

The word “fractal” comes from the latin word “fractus” that means “fragment”. A fractal is a geometrical object “infinitely fragmented” which has eye-visible details at an arbitrary chosen scale.

When zooming on any part of the figure, it is possible to find the whole figure again. A fractal figure is said to be “self-similar”.

In geometry, the Koch slope (or snow flake) is a simple example easy to build and that permits to understand how fractal objects are realized. The transformation operation is built as follows:

- Separating a segment in three parts;
- Constructing an equilateral triangle that lies on the central part;
- Erasing the triangle base.



Figure 89: Prior transformation operations to get a Koch slope [123]

The snow flake is then obtained when the initial figure is an equilateral triangle. The transformation is operated on each side of the triangle and then repeated on each segment of the new figure, as it can be seen on Figure 90.

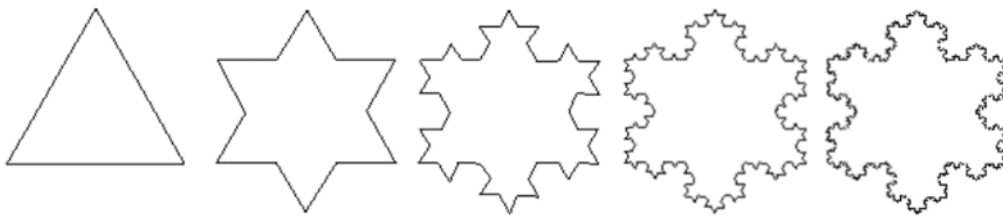


Figure 90: The Koch slope, also known as the snow flake [123]

The concept of fractals was applied by Forrest and al. in 1979 [124] to describe the structure of deposited agglomerate. It was first considered when observing diesel soot and soot-like particles by Samson and al. in 1987 [125], and after by Cai and al. in 1994 [126] and Burtscher in 2000 [127]. The use of the notion of “fractal dimensions” to describe aerosols was introduced by Schmidt-Ott in 1988 [128].

The agglomerates are not true mathematical fractals because they are not infinitely scale invariant [129], but composed of semi-randomly packed primary soot particles of finite size.

The three dimensions $R_p (=D_p/2)$, R_g and N_p are key parameters in the fractal analysis of soot aggregates. A mathematical relation, that is called the fractal law (Equation 54), can be drawn in order to characterize the aggregate. This relation makes two dimension appear: the fractal dimension D_f and the fractal prefactor k_f .

$$N_p = k_f \left(\frac{2R_g}{D_p} \right)^{D_f}$$

The fractal dimension D_f is a term that permits to define the compactness of an object. When $D_f=1$, the object is quite linear. On the other hand, when $D_f=3$, the object is quite compact. The representation of the compactness of an object according to the evolution of its fractal dimension is seen on Figure 91.

As regards soot aggregates, the fractal dimension is typically around 1,6 to 2, as it is seen on the results gathered by Ouf in 2006 [87], which is characteristic of the agglomeration process in flames and corresponds to quite uncompact particulates. In Figure 91, the dependency of a soot aggregate morphology on its fractal dimension D_f is represented.

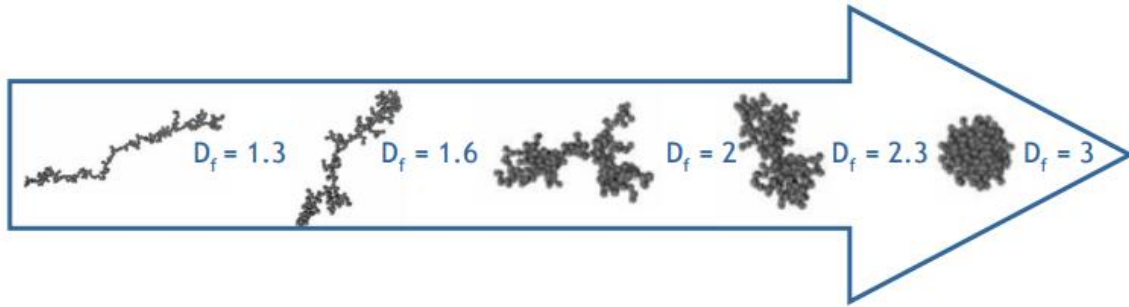


Figure 91: Evolution of soot aggregates morphology according to their fractal dimensions [33]

The fractal prefactor k_f , in a part, describes the morphology of the aggregate. It has been considered of secondary importance for a long time, behind the fractal dimension which acts as a power value. One of the reason why it has been neglected is that it varies a lot according to the experimental conditions. Indeed, the fractal prefactor is highly dependent on the combustive nature and on the combustion system, at the opposite of the fractal dimension that remains in the same range for different types of fuel. Nevertheless, k_f is more and more investigated, by, for instance, Koylu and al. in 1995 [130], Sorensen and al. in 1997 [131], and Ouf and al. in 2008 [132]. In these studies, the importance of the appreciation of k_f lies in the fact that when the number of particles is not known, the uncertainty on the value of N_p is directly linked to the uncertainty on the value of k_f .

2. Physical quantities useful for characterization

The physical quantities used when characterizing an aerosol depend on the technique of measurement. It is important to define these quantities to see how they are related to each other and to get a better understanding of what is actually measured about the particles.

2.1. Information related to particles weight and volume

2.1.1. The equivalent volume diameter D_{ev}

The equivalent volume diameter D_{ev} of a particle corresponds to the diameter that a sphere of a same volume would have. This diameter is a lot smaller than the real non-spherical particulates. This only allows an estimation of the aggregate weight under the condition of appreciating the compound density. No technique permits to characterize this diameter. In the case of soot particles, this diameter is expressed according to the number of primary particles and to their diameter (Equation 55).

Equation 55: Expression of the equivalent volume diameter of a soot particle

$$D_{ev} = N_p^{\frac{1}{3}} D_p$$

Then, the weight of the soot aggregate is expressed according to Equation 56.

Equation 56: Weight of the soot aggregate according to its equivalent volume diameter

$$m_a = \frac{\pi}{6} \rho_{pp} D_{ev}^3$$

2.1.2. The matter volume V_m

The matter volume of the particle is the volume occupied par the whole amount of material, solid or liquid, that composes the particle. It is directly linked to the equivalent volume diameter and is expressed in Equation 57.

Equation 57: Matter volume of the particle according to its equivalent volume diameter

$$V_m = \frac{\pi}{6} D_{ev}^3 = N_p \frac{\pi}{6} D_p^3$$

2.1.3. The material density ρ_m

The material density ρ_m is the mean density of the solid and liquid components that compose the particle. It is expressed from the aggregate weight and the matter volume. In the case of the soot particles, it is equivalent to the primary particles density ρ_{pp} .

$$\rho_m = \frac{m_a}{V_m}$$

2.1.4. The soot volume fraction f_v

In an aerosol, the soot particles volume fraction f_v is defined as being the particles volume by the gas sample volume unit. It is defined from both the soot weight concentration C_s in a well-known volume and the primary particles density ρ_{pp} (Equation 58).

Equation 58: Soot volume fraction according to the soot weight concentration and the primary particles density

$$f_v = \frac{C_s}{\rho_{pp}}$$

2.2. The equivalent diameters

The two diameters the most commonly used to characterize aerosols are the equivalent aerodynamic diameter and the electrical mobility diameter. They are defined below.

2.2.1. The equivalent aerodynamic diameter D_a

The equivalent aerodynamic diameter is generally measured with an impactor. Indeed, in an impactor, particles are classified according to their relaxation time τ (Equation 59).

Equation 59: Relaxation time of a particle according to its weight and its mobility

$$\tau = m_p B$$

- m_p is the particle weight (kg)
- B is the dynamic mobility, directly influencing the diffusion of the particle (Equation 48, paragraph 1.1). It characterizes the forces that the carrier gas applies on the moving particle.

In other words, the equivalent aerodynamic diameter corresponds to the diameter of a sphere with a density of $\rho_0 = 1 \text{ g/cm}^3$ having the same terminal velocity (highest velocity attainable by an object as it falls through air) that the analyzed particle. The expression of the equivalent diameter is then expressed according to Equation 60.

Equation 60: Equivalent aerodynamic diameter equation

$$D_a = \sqrt{\frac{18\eta\tau}{\rho_0 C_c}}$$

With η the dynamic viscosity of the carrier gas (in Pa.s), τ the relaxation time defined in Equation 59 (in s) and C_c is the Cunningham slip correction factor defined in Equation 52.

2.2.2. The electrical mobility diameter D_m

First, it is necessary to introduce the notion of the electrical mobility Z_p . It corresponds to the velocity that gets a particle when it is placed in an electrical field E with a charge of Ne . It is expressed according to Equation 61.

Equation 61: Electrical mobility equation

$$Z_p = \frac{v_{ET}}{E} = NeB = \frac{NeC_c}{3\pi\mu D_m}$$

- v_{ET} is the electrostatic terminal velocity (m/s)
- E is the electric field (V/m)
- e is the elementary charge ($e=1.6 \cdot 10^{-19}$ C)
- N is the number of elementary charges on the particle

The electrical mobility diameter is the diameter of a sphere having the same electrical mobility Z_p that the analyzed particle. It is expressed according to Equation 62.

Equation 62: Electrical mobility diameter equation

$$D_m = \frac{C_c}{3\pi\eta B}$$

2.2.3. Diameters used to characterize a soot aggregate – summary

In Figure 92 are gathered all the diameters commonly used to describe a soot aggregate. From the smallest to the largest, they are listed as follows:

D_p : the primary particles diameter;

D_a : the aerodynamic diameter;

D_{ev} : the equivalent volume diameter;

D_m : the electrical mobility diameter;

D_g : the gyration diameter;

$D_{aggregate}$: the diameter of the smallest sphere enveloping all the aggregate.

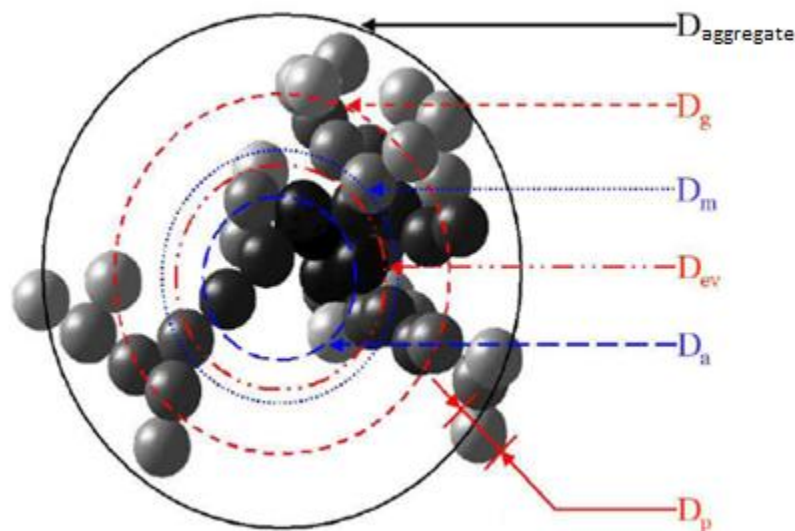


Figure 92: Different diameters commonly used to characterize a soot aggregate [1]

3. Theory of measurement

The mechanical mobility B is defined in Equation 63 below:

Equation 63: Mechanical mobility of a particle in a carrying gas

$$B = \frac{C_c}{3\pi\eta_g d_m}$$

Where C_c is the Cunningham slip correction factor defined in Equation 52.

It is based on the drag force that the carrier gas (with a viscosity η_g) exerts on a moving sphere. In a more figurative way, B is the ease with which a sphere moves through the gas. The mobility diameter d_m follows from the mechanical mobility B . If the aerosol particle is non-spherical, d_m is actually a “mobility equivalent diameter” that indicates the diameter of a sphere on which the gas exerts the same drag force as the actual non-spherical particle.

Another correction beside the Cunningham factor must be introduced into the equation of the drag force (Equation 50) to account for the increased drag on a particle due to nonspherical shape. This correction is called the “dynamic shape factor” (χ). It is defined as the ratio of the resistance force (the drag force) on the nonspherical particle to the resistance force on its volume equivalent sphere [133] (Equation 64):

Equation 64: Definition of the dynamic shape factor

$$\chi = \frac{F_p}{F_{ve}}$$

The dynamic shape factor is almost always greater than one for irregular particles and equal to one for spheres.

The general equation for drag force in any flow regime for nonspherical particles was established by Baron and al. in 2001 [134] (Equation 65):

Equation 65: Drag force corrected with the dynamic shape factor of the particle

$$F = \frac{3\pi\eta V \chi d_{ve}}{C_c(d_{ve})}$$

Aerodynamic diameter is defined as the diameter of a sphere with standard density that settles as the same terminal velocity as the particle of interest. Terminal settling velocity (T_{TS}) is a measure of the aerodynamic properties of the particle. Terminal velocity is obtained when the gravitational force of the particle (F_G) is equal and opposite to its drag force expressed in Equation 66.

Equation 66: Expression of the terminal settling velocity of a nonspherical particle

$$F_G = m_p g = \rho_p \frac{\pi}{6} d_{ve}^3 g = \frac{3\pi\eta V_{TS} d_{ve} \chi}{C_c(d_{ve})} = F$$

With:

- m_p the particle mass (kg)
- g the gravitational constant (m.s⁻²)
- ρ_p the particle density (kg.m⁻³)
- d_{ve} the equivalent volume diameter (m)
- η the dynamic viscosity of the carrier gas (Pa.s)
- χ the dynamic shape factor
- $C_c(d_{ve})$ the Cunningham correction factor

As stated before, the aerodynamic diameter is defined as the diameter of a standard density sphere (ρ_0 ; $\chi=1$) with the same terminal settling velocity (V_{TS}) as the considered particle of density ρ_p . Considering the standard density sphere in *Equation 66*, the *Equation 67* is obtained:

Equation 67: Expression of the terminal settling velocity of a standard density sphere

$$F_G = m_p g = \rho_0 \frac{\pi}{6} d_a^3 g = \frac{3\pi\eta V_{TS} d_a}{C_c(d_a)} = F$$

With:

- d_a the aerodynamic diameter (m)
- $C_c(d_a)$ the Cunningham correction factor

Combining *Equation 66* and *Equation 67*, the expression of the aerodynamic diameter of a nonspherical particle of density ρ_p is obtained in *Equation 68*.

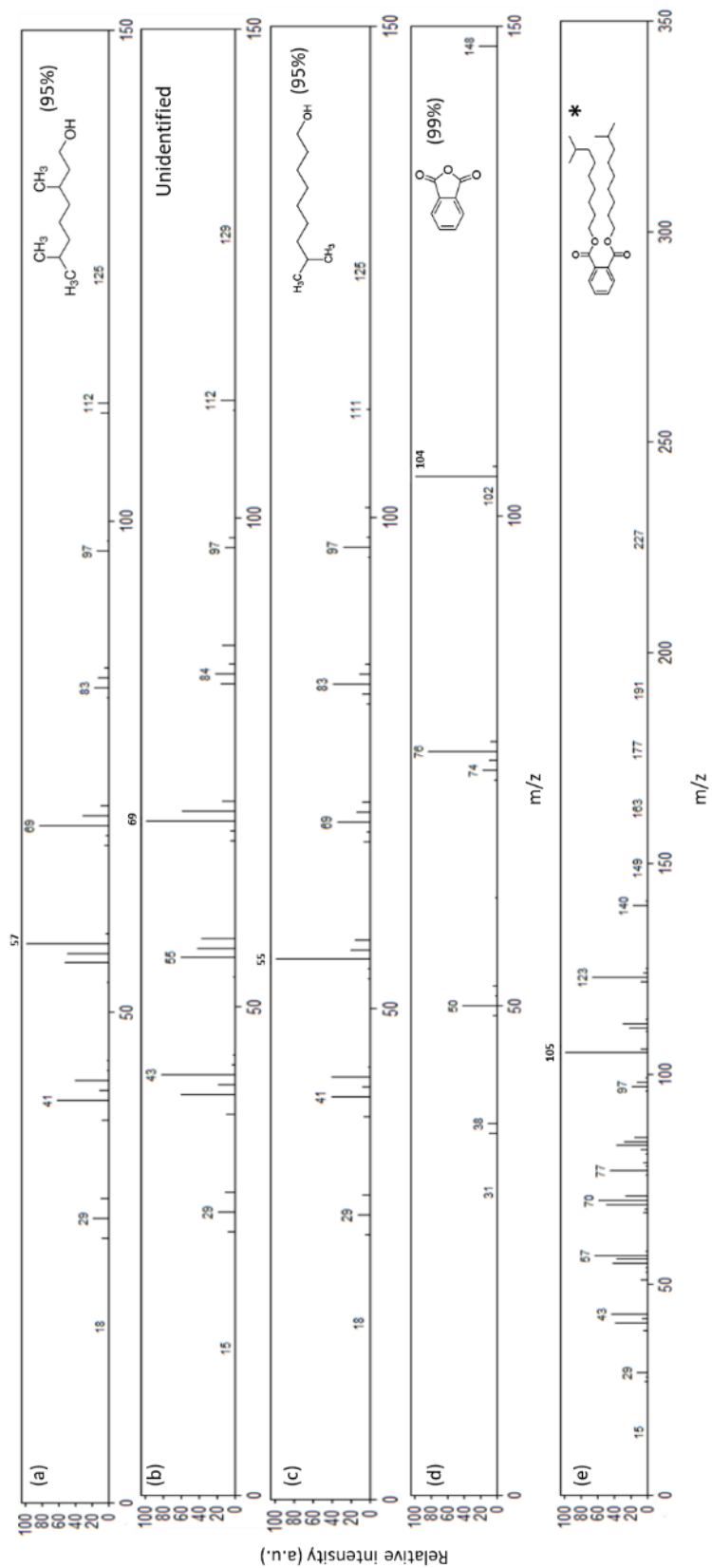
Equation 68: Expression of the aerodynamic diameter of a particle of density ρ_p

$$d_a = d_{ve} \sqrt{\frac{1}{\chi} \frac{\rho_p}{\rho_0} \frac{C_c(d_{ve})}{C_c(d_a)}}$$

As a conclusion, the fact that a particle will impact on an ELPI plate is only dependent on its:

- Dynamic shape factor
- Density
- Volume equivalent diameter.

Appendix 2: Mass spectra of DIDP py-GC/MS



Appendix 3: Plaques processing details

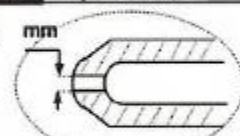
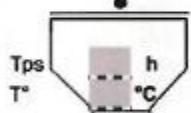
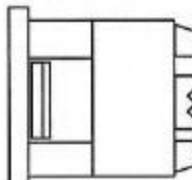
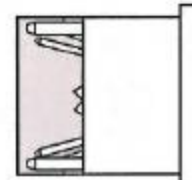
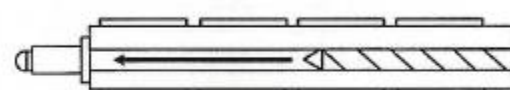
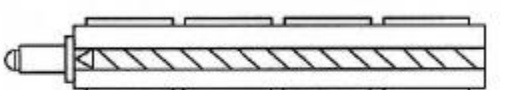
1. Filled PVC plaques processing details 181
2. Unfilled PVC plaques processing details 183

1. Filled PVC plaques processing details

Mélangeage, ISPA-Entreprises		18.05.17
Turbomélangeur	CP 200	Contenance_{max} : 70 kg
CACCIA		
Formulation 1 (avec CaCO₃)		170257
Procédure de fabrication		
Introduction du PVC	Température départ : 24°C	
Mélangeage à vitesse rapide jusqu'à 80 °C	Temps : 8 min	
	Ampérage final : 21 A	
	Température finale : 80°C	
Ajout des additifs à 80 °C et mélangeage à vitesse lente	Temps : 2,0 min	
	Ampérage final : 23,7 A	
	Température finale : 65 °C	
Mélangeage à vitesse rapide jusqu'à 110 °C	Temps : 6,4 min	
	Ampérage final : 37 A	
	Température finale : 110°C	
Transvasement dans la cuve froide et refroidissement :	Température finale : 30°C	



Paramètres INJECTION

N° de devis:	210217D2	N° de rapport:	210827R
Presse :	ENGEL ES330/80	Outillage :	Plaque 100x100xEp.3 mm
Date: 06/06/17	Client: EDF	Nom du Responsable essai :	Anouar Zrita / VA
Type de Matière :	PVC	Référence matière:	Formulation 1
Additifs/Colorants	<input type="checkbox"/> Oui <input checked="" type="checkbox"/> Non	Référence:	Pourcentage:
<div><div><div>T° de masse °C</div><div>3,5 mm</div><div></div></div><div>TEMPÉRATURES CYLINDRE</div><div><div>Dimensions moule : Ø de la rondelle : Type d'éjection :</div><div><div>T° Buse : 200 °C %</div><div><div>Tps T°</div><div></div></div><div><div>Z4 195 °C</div><div>Z3 190 °C</div><div>Z2 185 °C</div><div>Z1 °C</div><div>Bride °C</div></div></div></div></div>			
<div>REGULATION</div> <div><div>Force de fermeture utile : 700 Kn</div><div>Type de fluide : <input checked="" type="checkbox"/> Eau <input type="checkbox"/> Huile</div><div><div><div>Température 15 Nbre de circuit 2</div></div><div><div><div>Température 15 Nbre de circuit 2</div></div></div></div></div>			
<div>INJECTION</div> <div><div><div>Vitesse 3 2 1 Paller 5x1 5x2 7x20 cm³/s Course 24,1 cm³ 513 bars Point Commutation 24,1 cm³ 513 bars Pression limite bars Temps 2,47 sec</div></div></div>		<div>MAINTIEN</div> <div><div><div>Pression 3 2 1 411 x10 bars Temps 6 sec Matelas 8,7 cm³ Temps de refroidissement 15 sec</div></div></div>	
<div>PLASTIFICATION</div> <div><div>Course de dosage : 67,4 cm³ Vitesse de dosage : 30% RPM Contre Pres réelle : 5 bars Tps de retard dosage : 2 sec Temps de dosage : 12 sec</div><div>Recul ponton non <input checked="" type="checkbox"/> oui Décompression non <input checked="" type="checkbox"/> oui Rebroyé <input checked="" type="checkbox"/> non <input type="checkbox"/> oui Temps de cycle : 28 sec</div><div>30 mm. 2,9 cm³ %</div></div>			
Poids pièce :	gr	Poids carotte :	gr
Poids de la moulée :		48,47 gr	

2. Unfilled PVC plaques processing details

Mélangeage, ISPA-Entreprises		18.05.17
Turbomélangeur CACCIA	CP 200	Contenance_{max} : 70 kg
Formulation 2 (sans CaCO₃)		170258
Procédure de fabrication		
Introduction du PVC	Température départ : 24°C	
Mélangeage à vitesse rapide jusqu'à 80 °C	Temps : 7 min	
	Ampérage final : 22 A	
	Température finale : 80°C	
Ajout des additifs à 80 °C et mélangeage à vitesse lente	Temps : 2,0 min	
	Ampérage final : 25 A	
	Température finale : 68 °C	
Mélangeage à vitesse rapide jusqu'à 110 °C	Temps : 7,0 min	
	Ampérage final : 37 A	
	Température finale : 110°C	
Transvasement dans la cuve froide et refroidissement :	Température finale : 30°C	

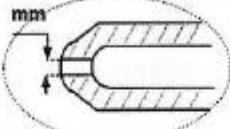


Paramètres INJECTION

N° de devis:	210217D2	N° de rapport:	210827R
Presse :	ENGEL ES330/80	Outillage :	Plaque 100x100xEp.3 mm
Date: 06/06/17	Client: EDF	Nom du Responsable essai :	Anouar Zrita / VA
Type de Matière :	PVC	Référence matière:	Formulation 2
Additifs/Colorants	<input type="checkbox"/> Oui <input checked="" type="checkbox"/> Non	Référence:	Pourcentage:

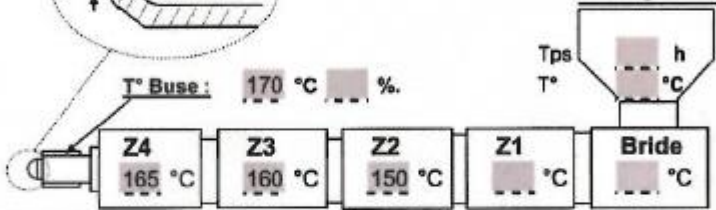
T° de masse
°C

3,5 mm



T° Buse : 170 °C %.

TEMPERATURES CYLINDRE



Z4 165 °C Z3 160 °C Z2 150 °C Z1 °C Bride °C

Dimensions moule :

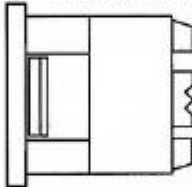
Ø de la rondelle :

Type d'éjection :

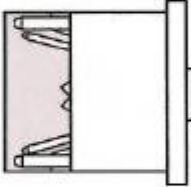
Force de fermeture utile :
700 Kn

Type de fluide :
☒ Eau ☐ Huile

REGULATION



Température 20 Nbre de circuit 2



Température 20 Nbre de circuit 2

INJECTION



Vitesse 3 5x4 2 10 1 20x5 Paller cm³/s

Course 3 5x4 2 10 1 20x5 cm³

Point Commutation 3 21,2 2 mm 1 650 bars

Pression limite 3 21,2 2 bars 1 650 bars

Temps 3 4,13 2 sec 1 4,13 sec

MAINTIEN



Pression 3 411 2 x10 1 bars

Temps 3 411 2 x10 1 4 sec

Matelas 3 411 2 x10 1 18,1 cm³

Temps de refroidissement 3 411 2 x10 1 11 sec

PLASTIFICATION

Course de dosage : 67,4 cm³

Vitesse de dosage : 55% RPM

Contre Pres réelle : 5 bars

Tps de retard dosage : 2 sec

Temps de dosage : 6 sec

Recul ponton : non

Décompression : non

Rebroyé : non

Temps de cycle : 24 sec

non ☒ oui ☐ non ☒ oui ☐ non ☒ oui ☐

30 mm. 2,9 cm³ %.

Poids pièce : gr Poids carotte : gr Poids de la moulée : 40,14 gr

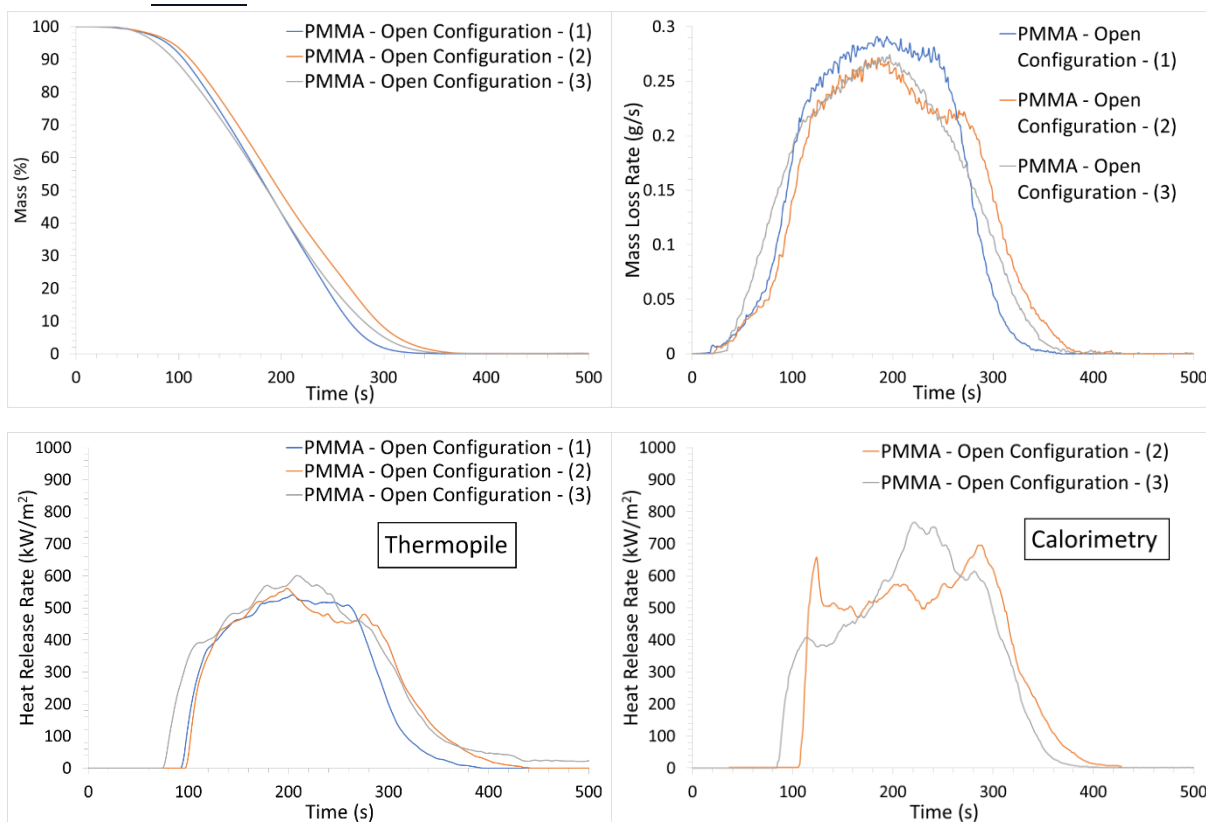
Appendix 4: Tests performed under air in open and confined configuration

1. Open configuration	185
1.1. Mass loss and HRR	185
1.2. Gases	188
1.3. Aerosols	192
2. Confined configuration	194
2.1. Mass loss and heat release rate	194
2.2. Gases	197
2.3. Aerosols	200

1. Open configuration

1.1. Mass loss and HRR

1.1.1. PMMA

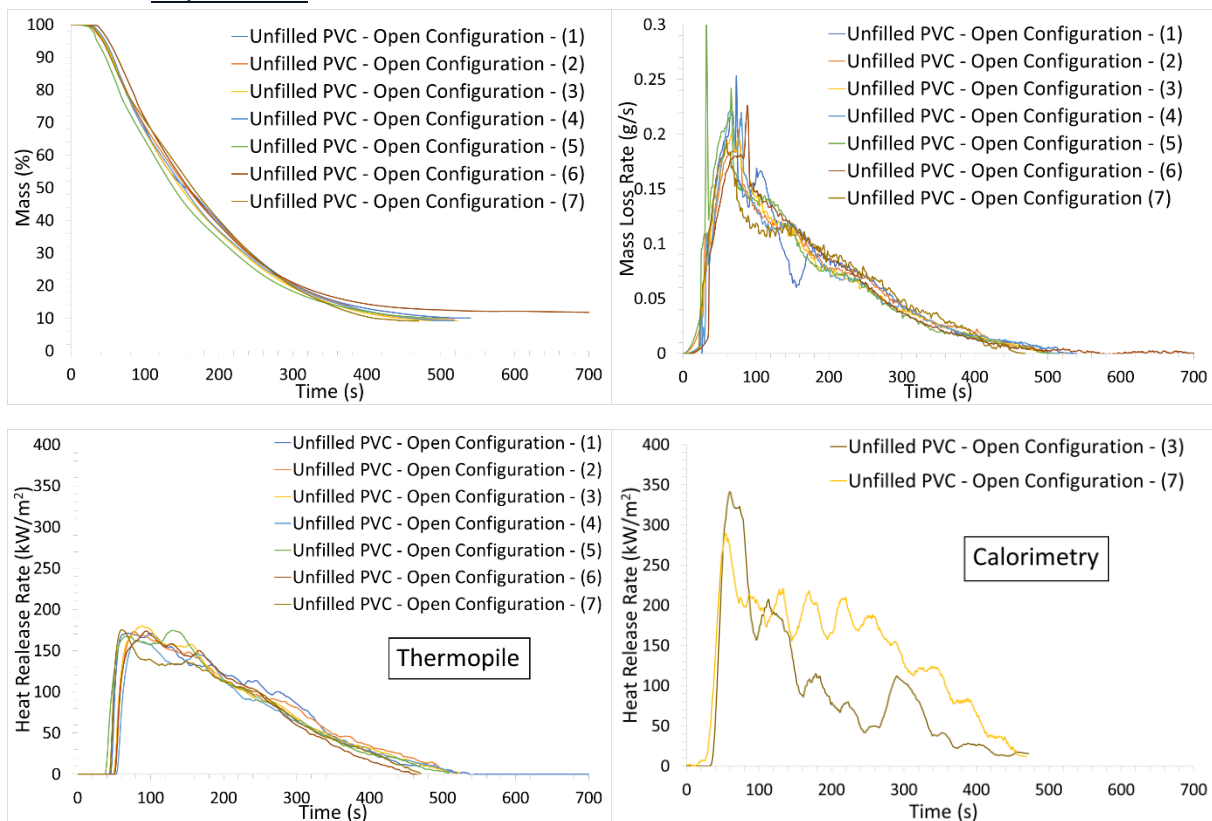


Experiment	TTI (s)	TTE (s)	Residue (%)	pMLR (g/s)	pHRR _{thermo} (kW.m ⁻²)	THR _{thermo} (MJ.m ⁻²)	pHRR _{O2} (kW.m ⁻²)	THR _{O2} (MJ.m ⁻²)
PMMA – Open Configuration – (1)*	94	354	0	0.291	540.8	94.8	/	/
PMMA – Open Configuration – (2)**	99	404	0	0.272	560.8	105.5	695.9	126.1
PMMA – Open Configuration – (3)	76	385	0	0.274	600.7	121.1	761.0	127.8
Average	89.6	381	0	0.279	567.4	107.1	728.5	126.9
Standard deviation	12.1	25.2	0	0.010	30.5	13.1	46.0	1.2

*Experiment presented in the chapter for mass loss and mass loss rate

**Experiment presented in the chapter for HRR

1.1.2. Unfilled PVC

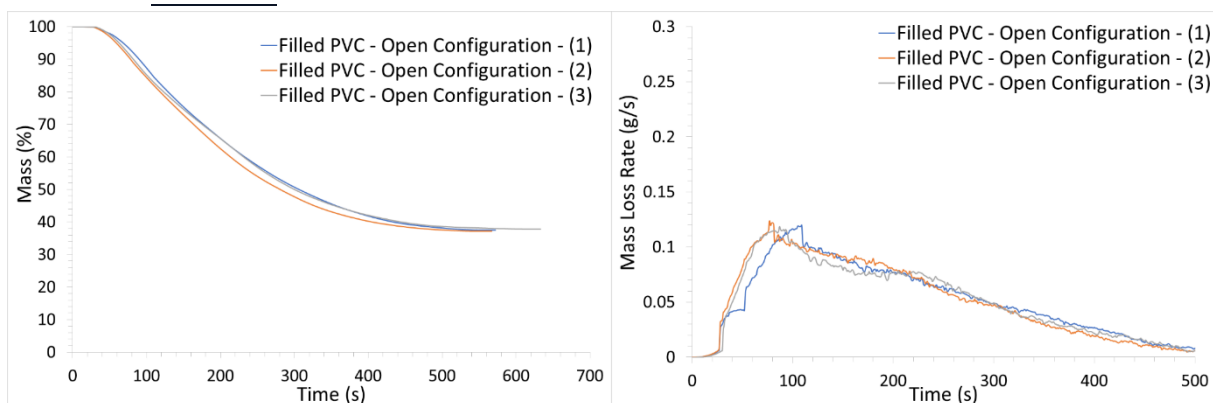


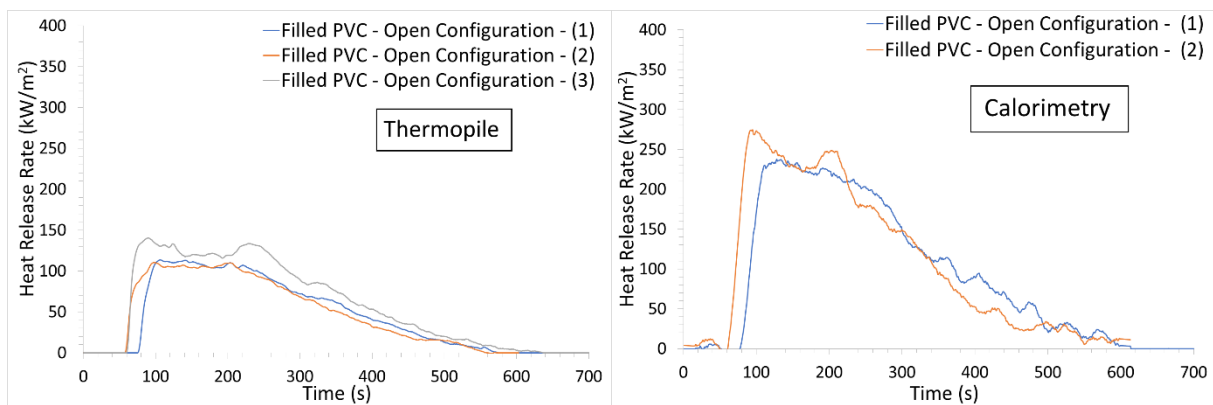
Experiment	TTI (s)	TTE (s)	Residue (%)	pMLR (g/s)	pHRR _{thermo} (kW.m ⁻²)	THR _{thermo} (MJ.m ⁻²)	pHRR _{O2} (kW.m ⁻²)	THR _{O2} (MJ.m ⁻²)
Unfilled PVC – Open	48	512	10.5	0.252	171.3	39.9	/	/

Configuration – (1)								
Unfilled PVC – Open Configuration – (2)	51	483	9.4	0.204	179.9	37.9	/	/
Unfilled PVC – Open Configuration – (3)	53	506	9.6	0.205	175.4	35.7	341.5	34.7
Unfilled PVC – Open Configuration – (4)	55	502	9.2	0.224	162.8	34.9	/	/
Unfilled PVC – Open Configuration – (5)	39	473	6.8	0.314	174.6	38.7	/	/
Unfilled PVC – Open Configuration – (6)	53	480	9.7	0.226	178.8	33.6	/	/
Unfilled PVC – Open Configuration – (7)*	46	452	10.1	0.195	173	38.5	289.4	57.4
Average	49.2	486.2	9.3	0.231	173.6	37.0	315.5	46.1
Standard Deviation	5.4	21.2	1.2	0.041	5.6	2.3	36.8	16.1

*Experiment presented in the chapter

1.1.3. Filled PVC





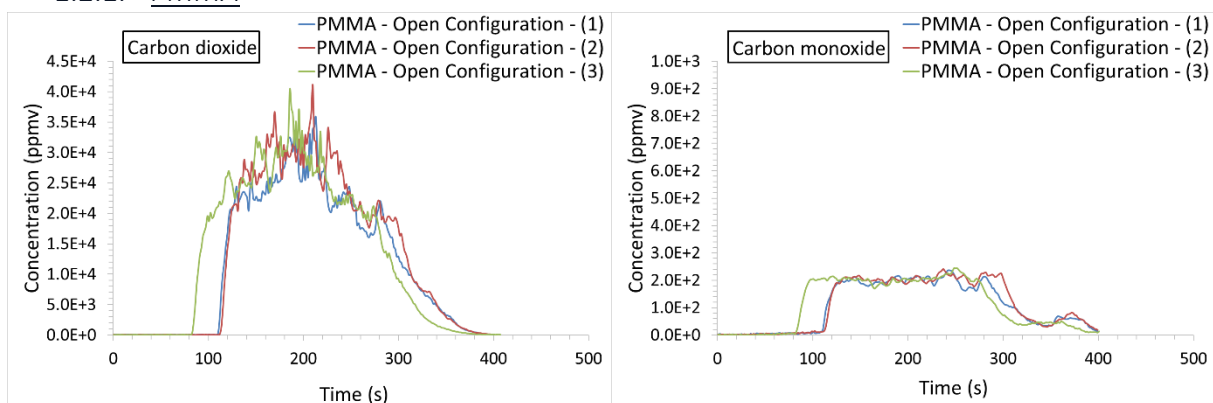
Experiment	TTI (s)	TTE (s)	Residue (%)	pMLR (g/s)	pHRR _{thermo} (kW.m ⁻²)	THR _{thermo} (MJ.m ⁻²)	pHRR _{O2} (kW.m ⁻²)	THR _{O2} (MJ.m ⁻²)
Filled PVC – Open Configuration – (1)**	78	582	36.9	0.119	113.6	30.9	237.6	53.7
Filled PVC – Open Configuration – (2)	60	537	35.7	0.124	110.5	30.6	274.5	58.8
Filled PVC – Open Configuration – (3)*	63	583	42.6	0.119	140.3	40.6	/	/
Average	67	560.6	38.4	0.121	121.4	34.1	256.1	56.3
Standard deviation	9.6	23.1	3.7	0.003	16.3	5.6	26.1	3.6

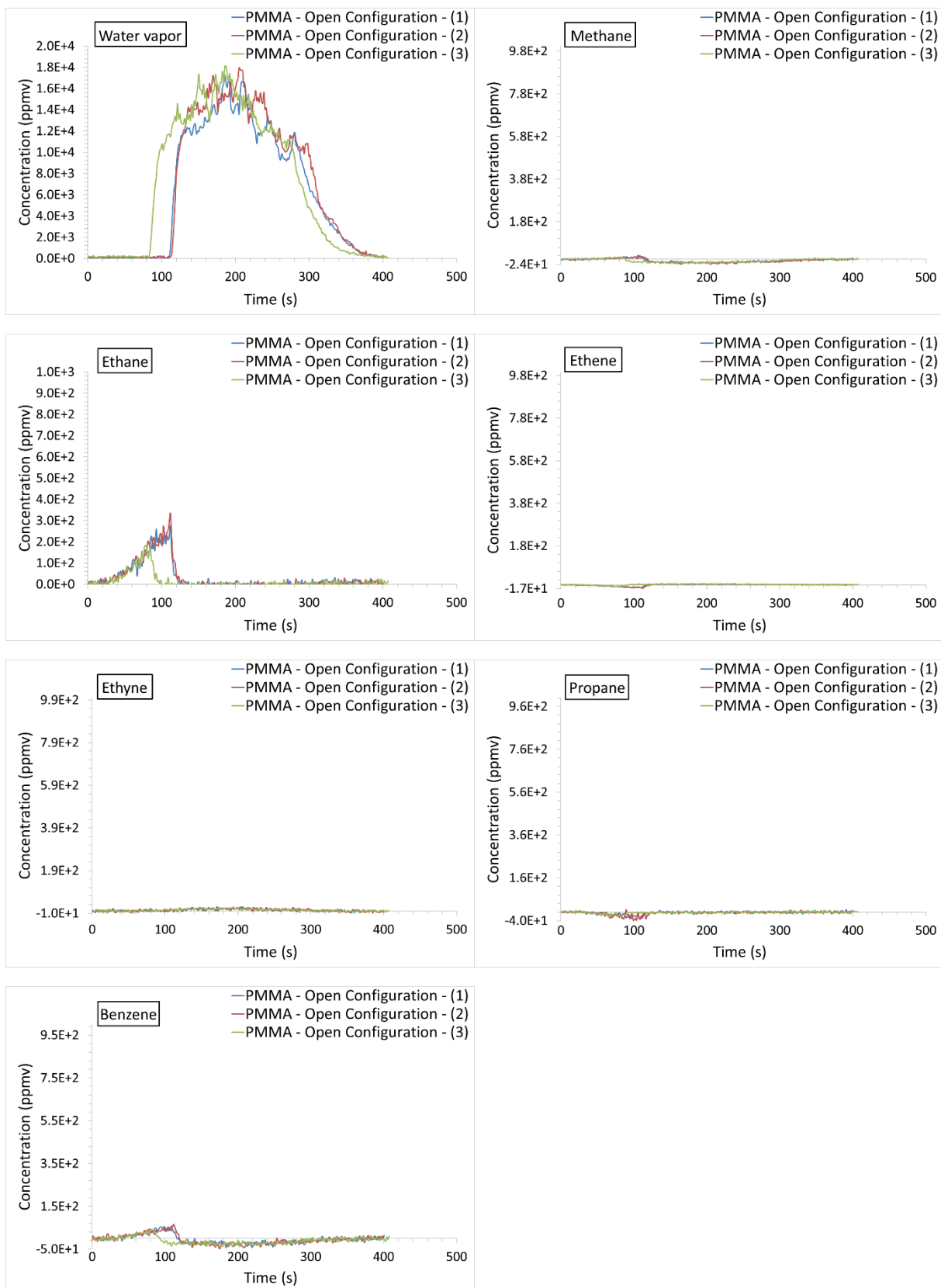
*Experiment presented in the chapter for mass loss and mass loss rate

**Experiment presented in the chapter for HRR

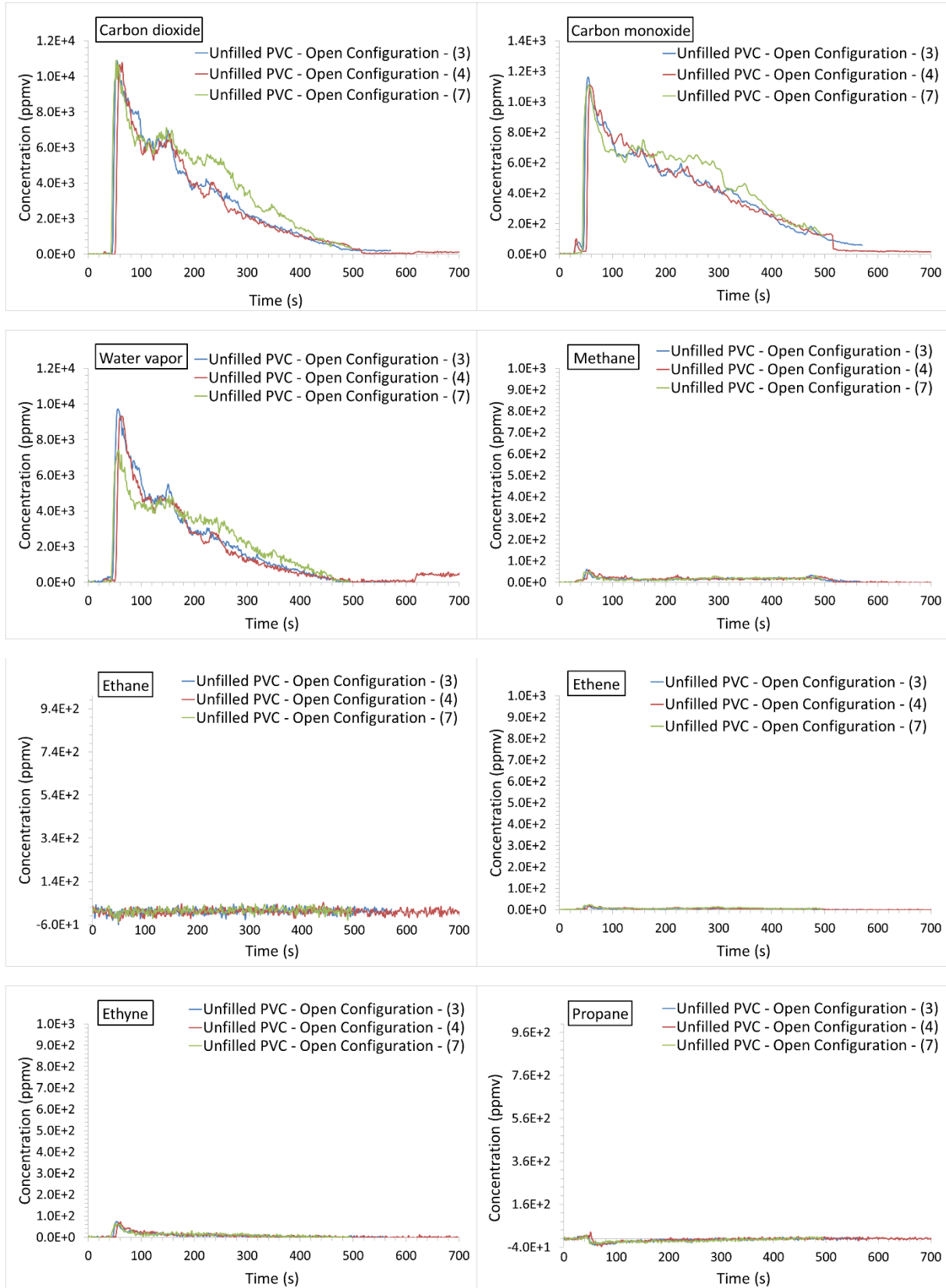
1.2. Gases

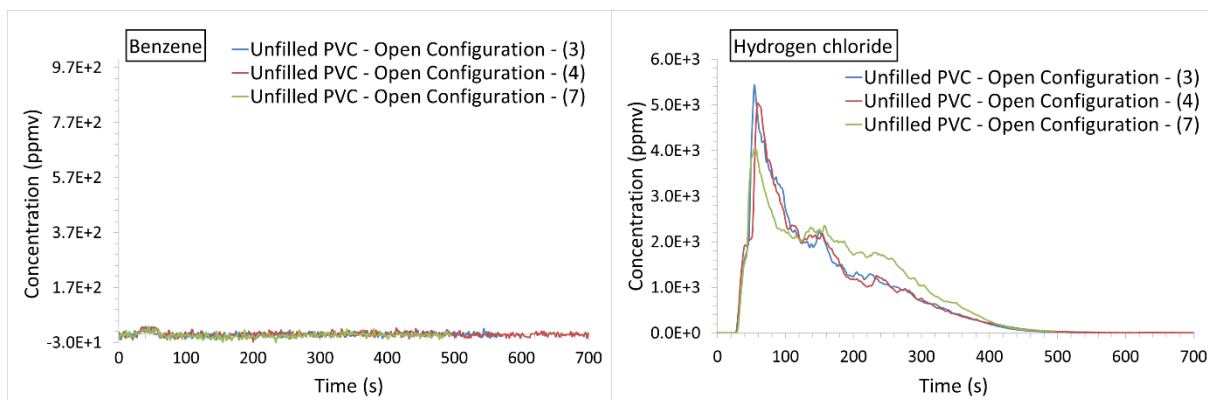
1.2.1. PMMA



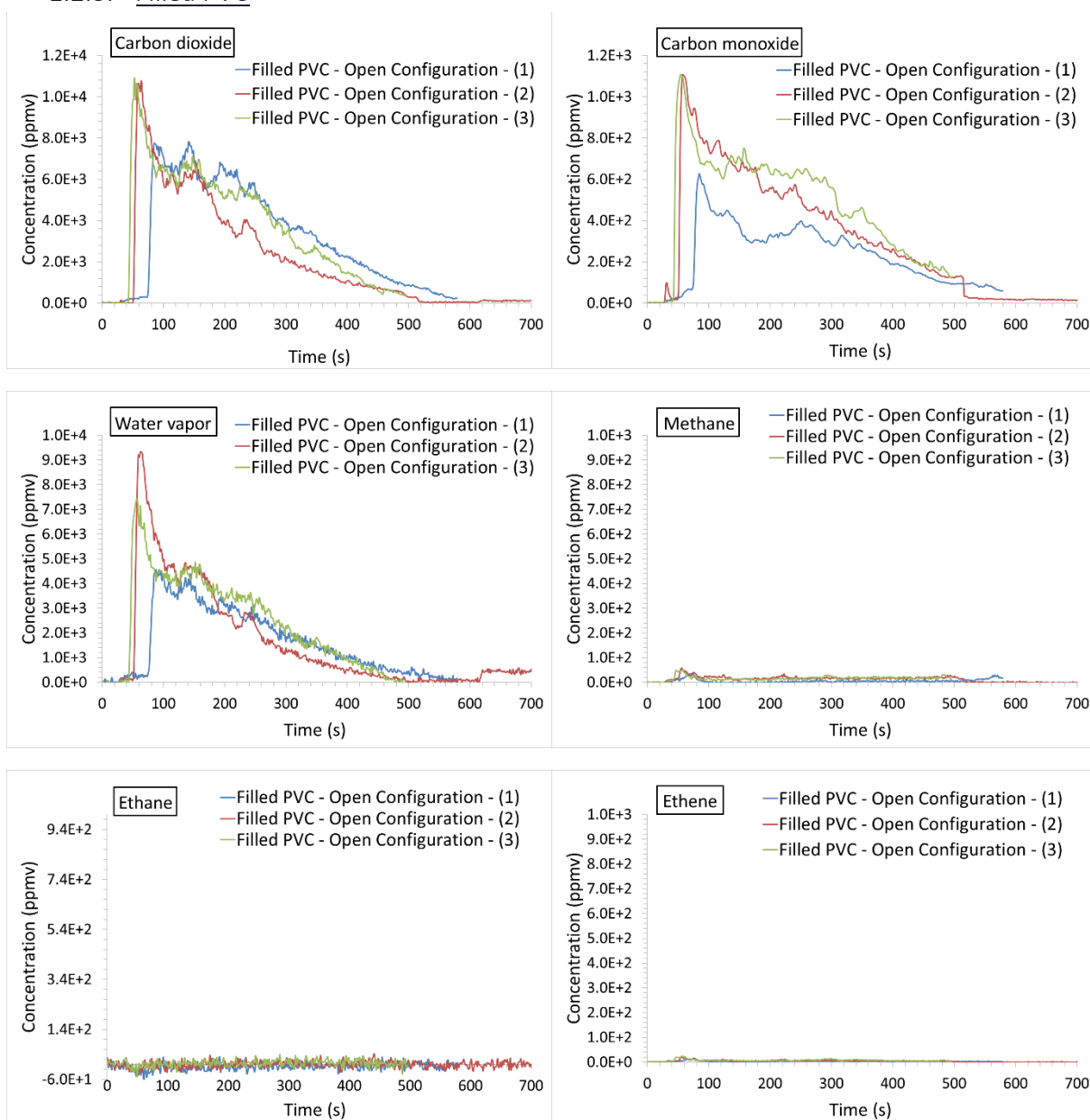


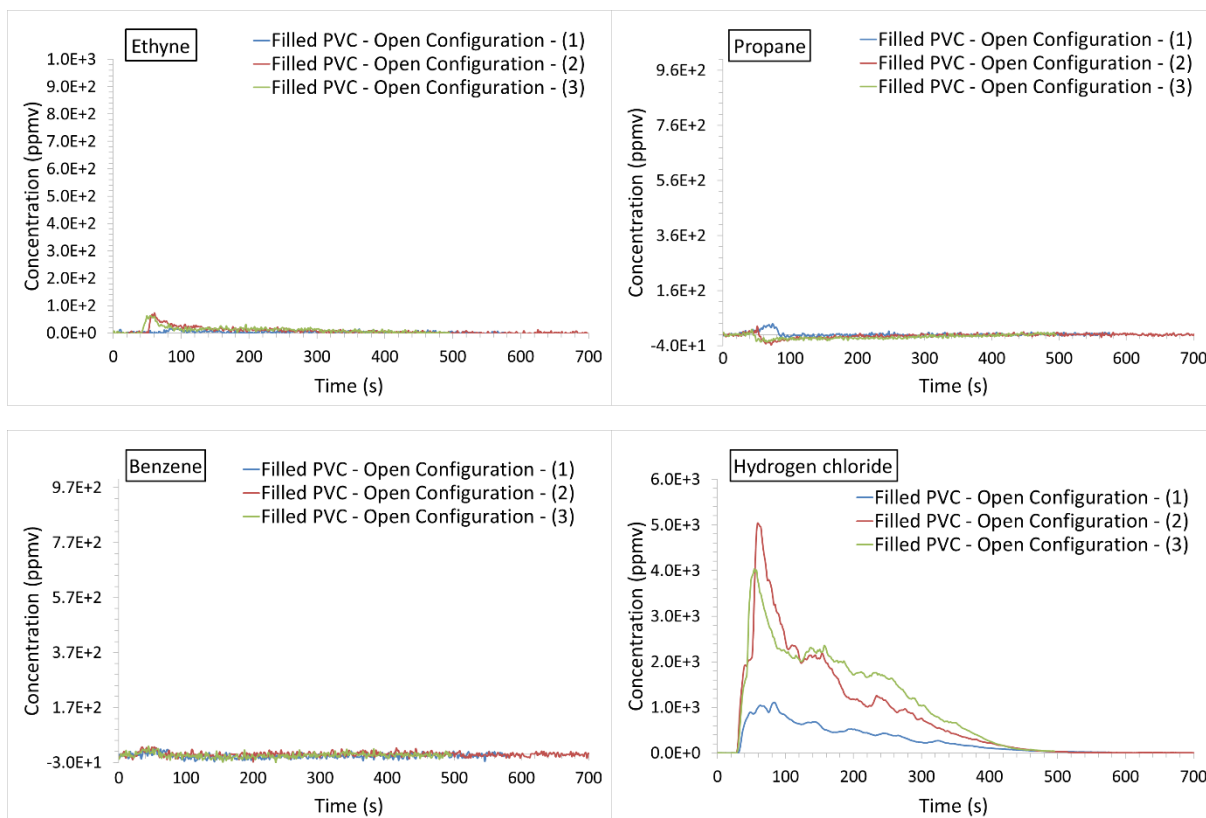
1.2.2. *Unfilled PVC*





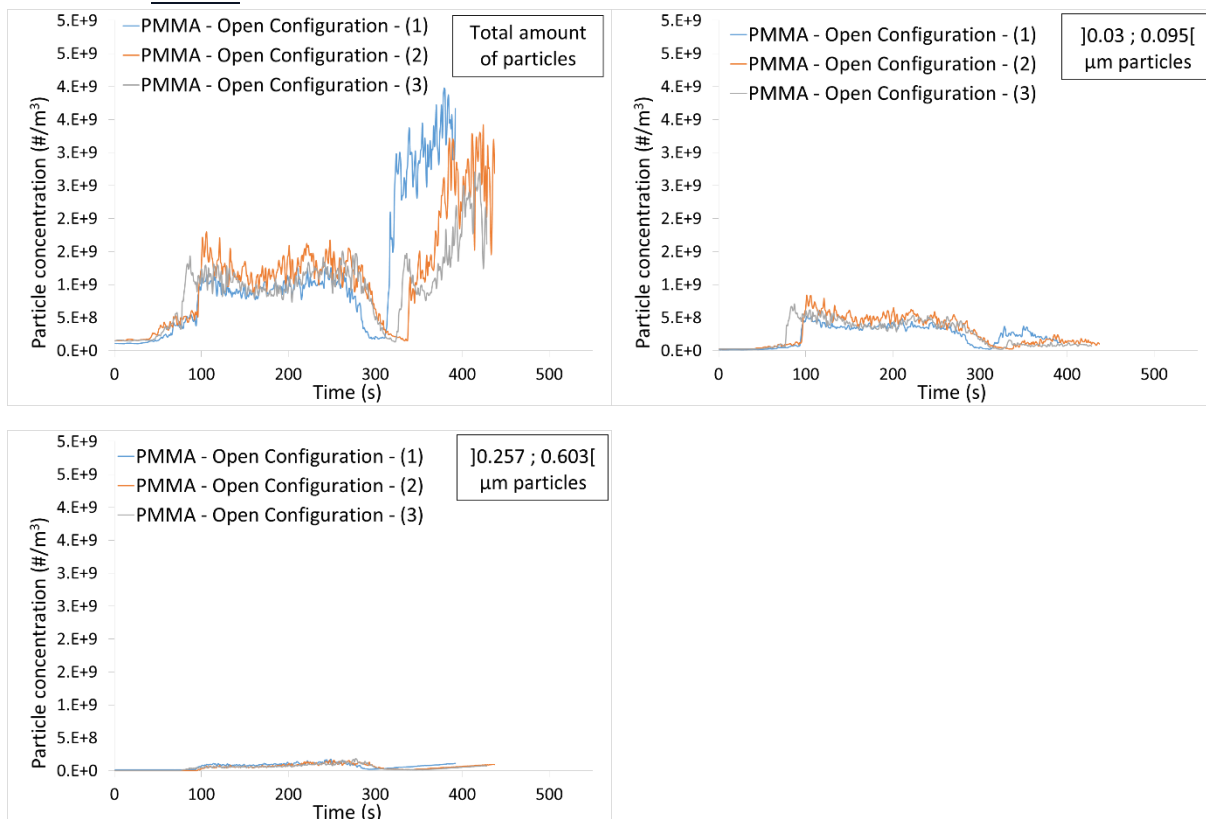
1.2.3. Filled PVC



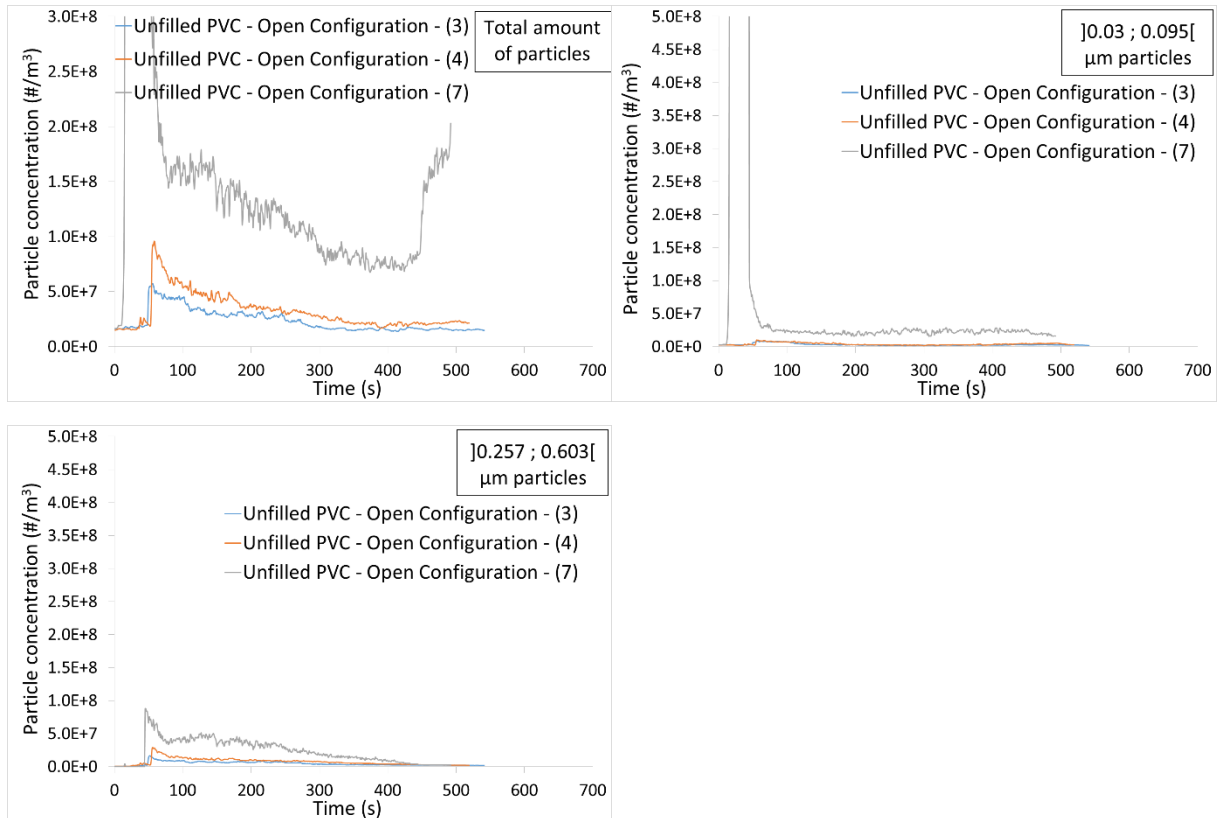


1.3. Aerosols

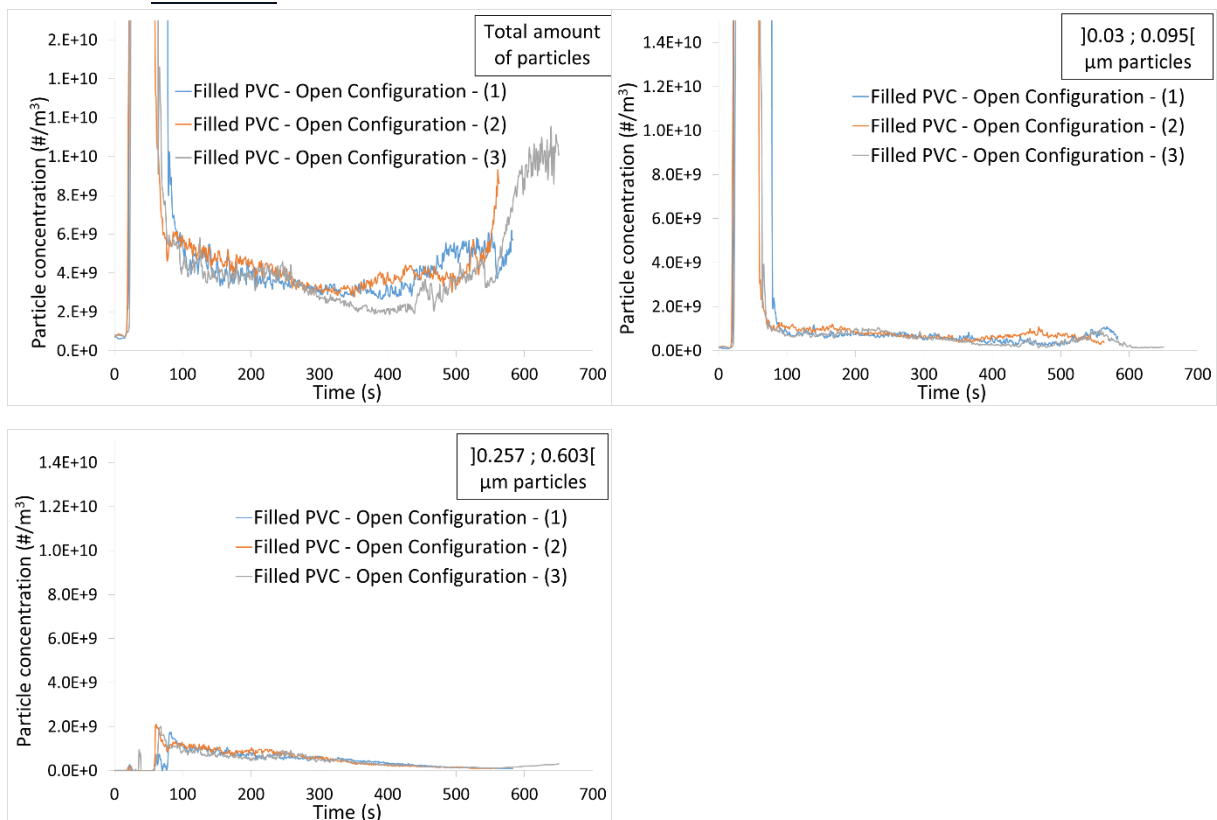
1.3.1. PMMA



1.3.2. Unfilled PVC



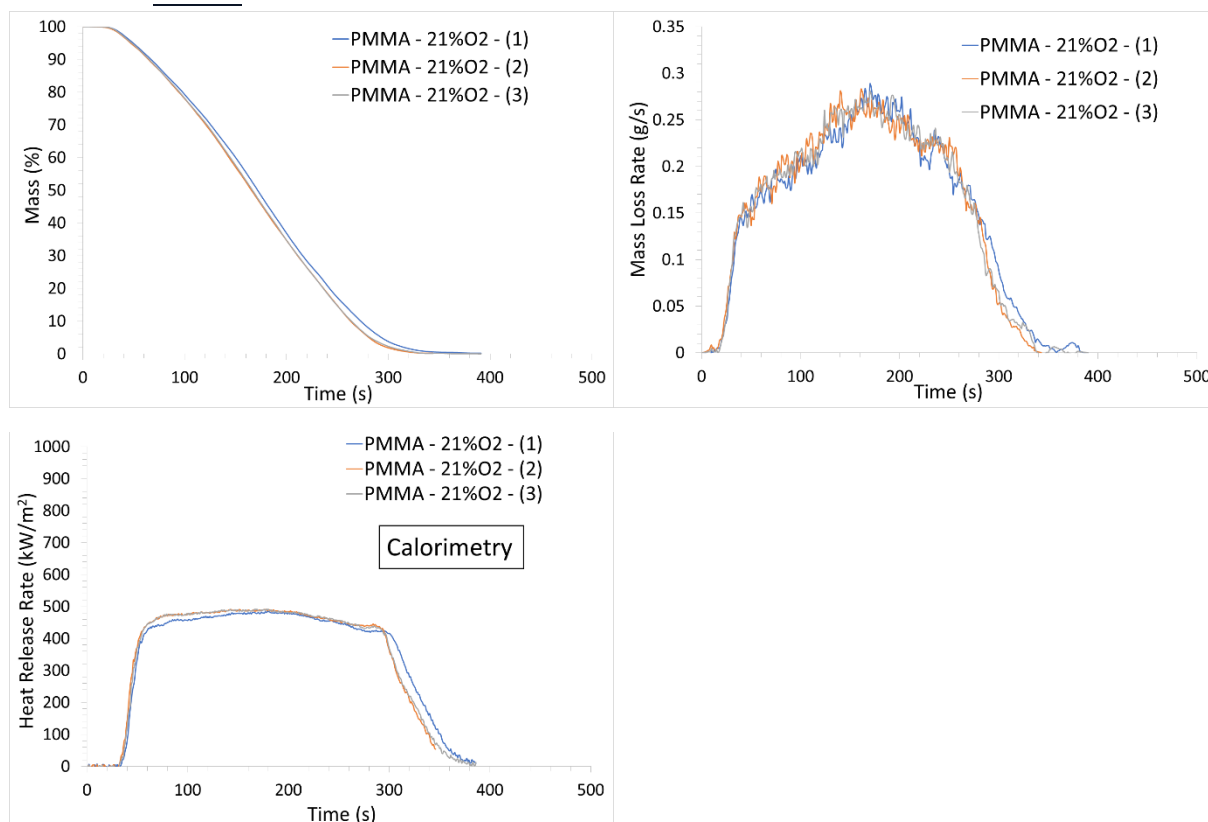
1.3.3. Filled PVC



2. Confined configuration

2.1. Mass loss and heat release rate

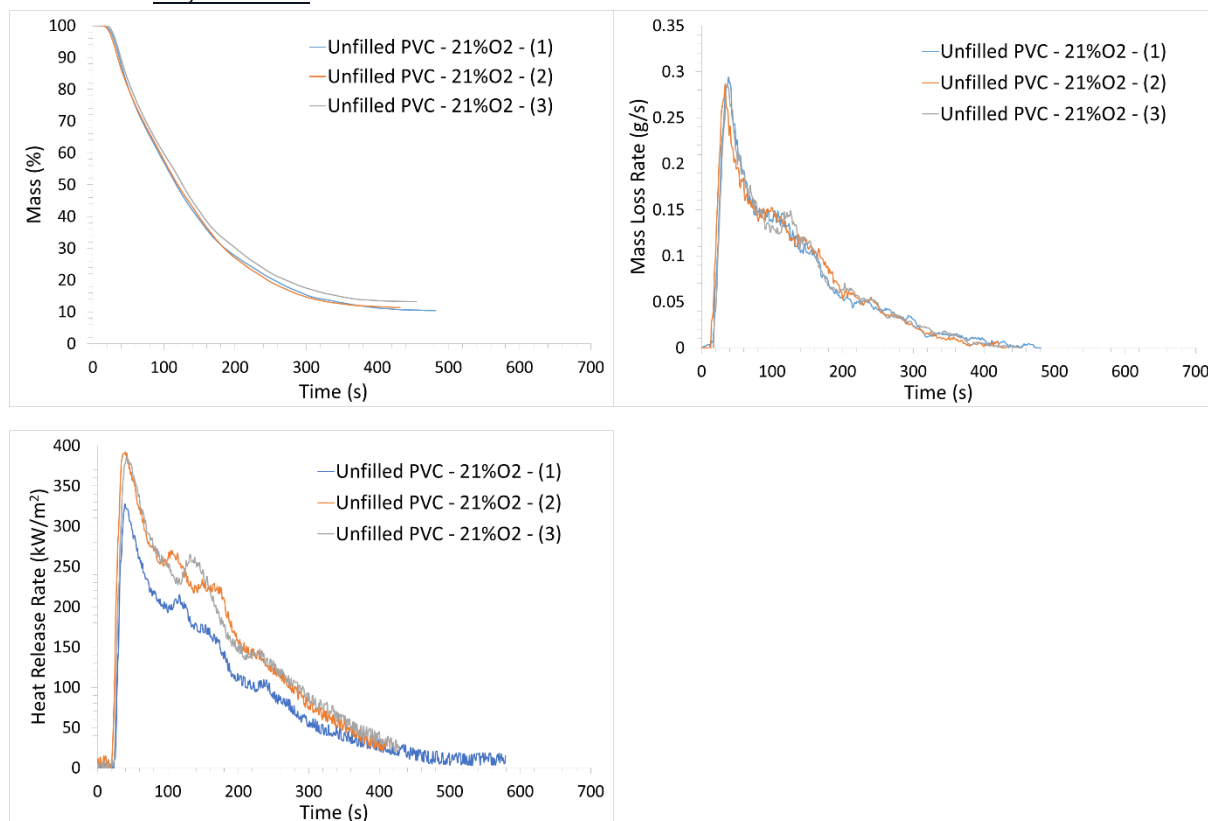
2.1.1. PMMA



Experiment	TTI (s)	TTE (s)	Residue (%)	pMLR (g/s)	pHRR (kW.m ⁻²)	THR (MJ.m ⁻²)
PMMA – 21 vol. %O ₂ – (1)	23	386	0	0.289	484.3	130.5
PMMA – 21 vol. %O ₂ – (2)	22	339	0	0.283	490.9	128.9
PMMA – 21 vol. %O ₂ – (3)*	23	375	0	0.280	491.5	130.1
Average	22.7	366.7	0	0.284	488.9	129.8
Standard deviation	0.6	24.6	0	0.005	3.9	0.8

*Experiment presented in the chapter

2.1.2. *Unfilled PVC*

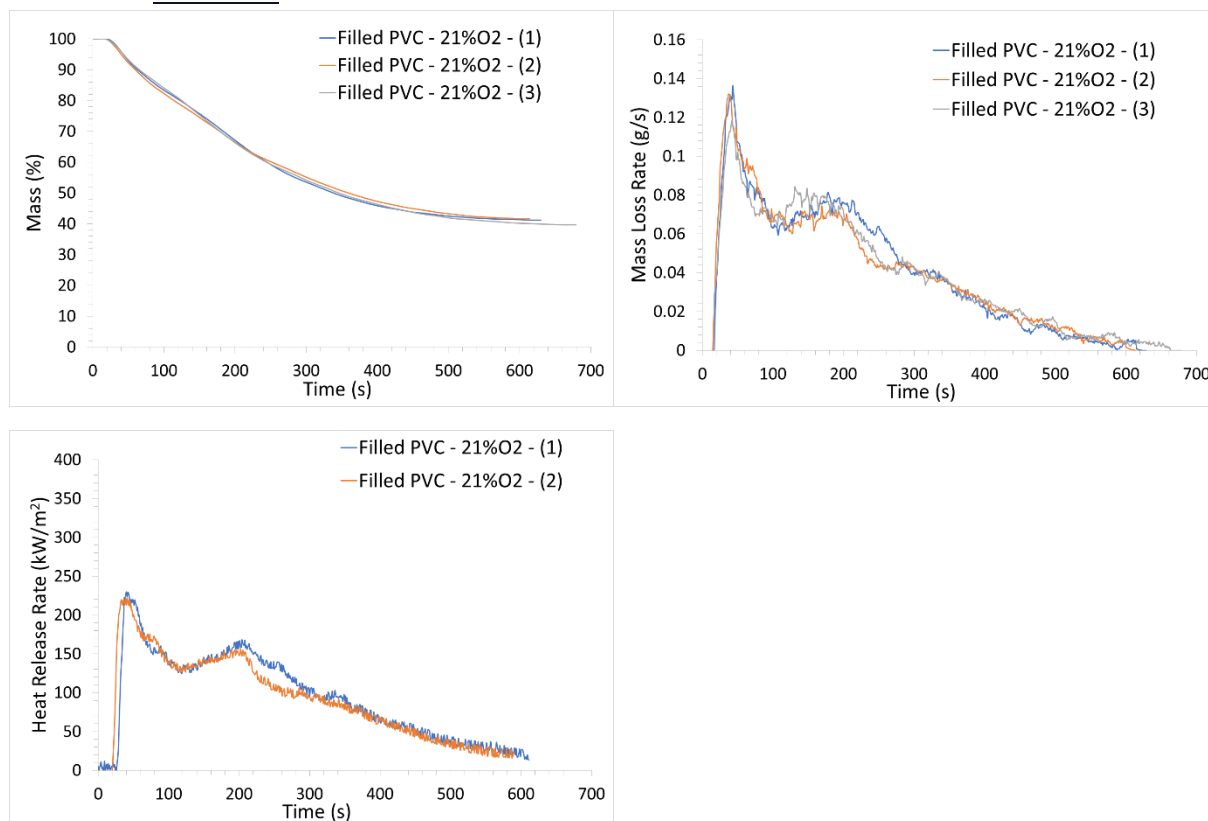


Experiment	TTI (s)	TTE (s)	Residue (%)	pMLR (g/s)	pHRR (kW.m ⁻²)	THR (MJ.m ⁻²)
Unfilled PVC – 21 vol. %O ₂ – (1)	24	464	6.9	0.271	327.7 ¹	46.5 ¹
Unfilled PVC – 21 vol. %O ₂ – (2)*	20	409	9.6	0.294	392.2	62.0
Unfilled PVC – 21 vol. %O ₂ – (3)	22	418	8.5	0.287	386.6	61.4
Average	22	430.3	8.4	0.284	389.4	61.7
Standard deviation	2	29.5	1.4	0.012	3.9	0.4

¹Values omitted from average

*Experiment presented in the chapter

2.1.3. Filled PVC

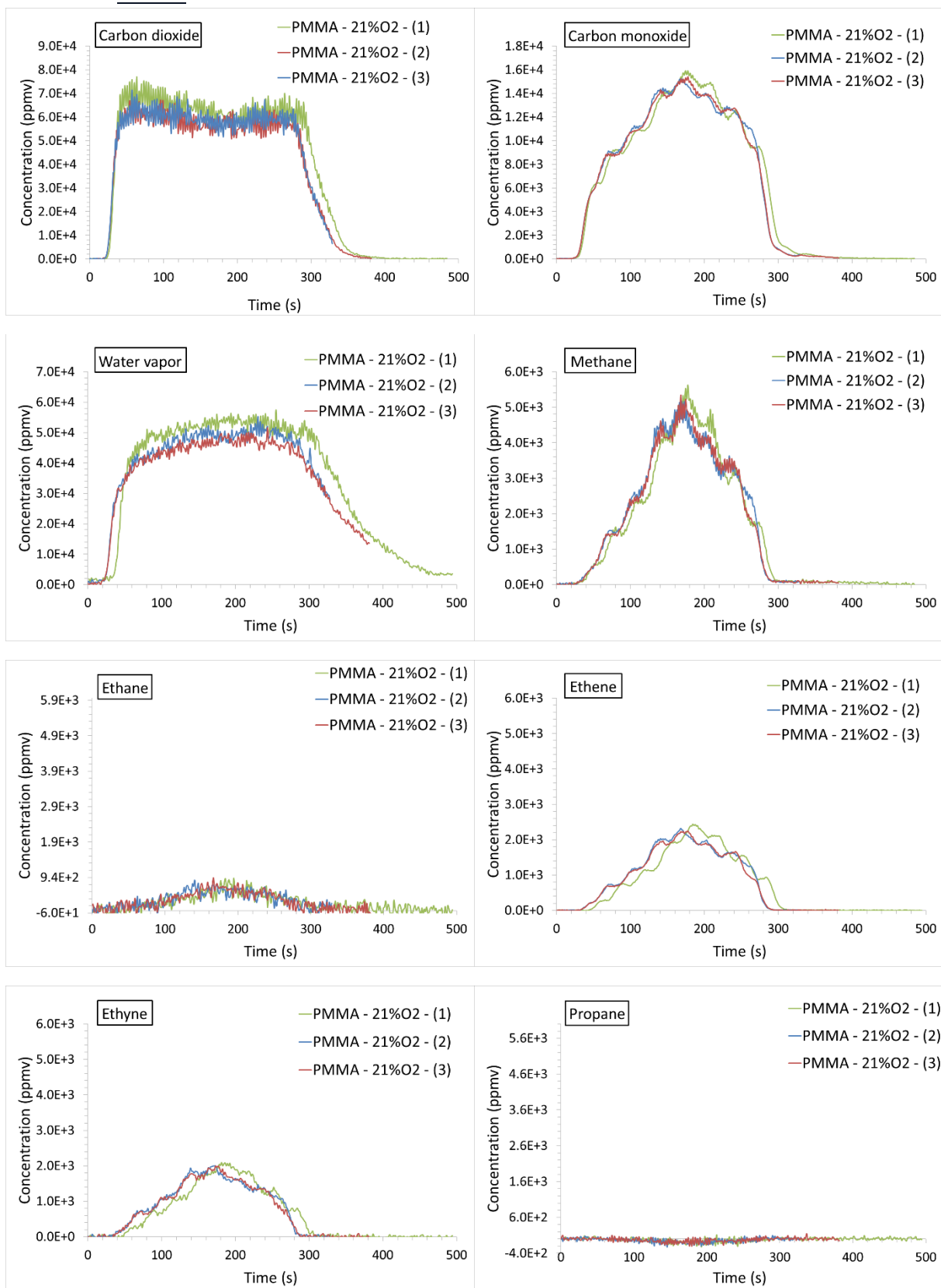


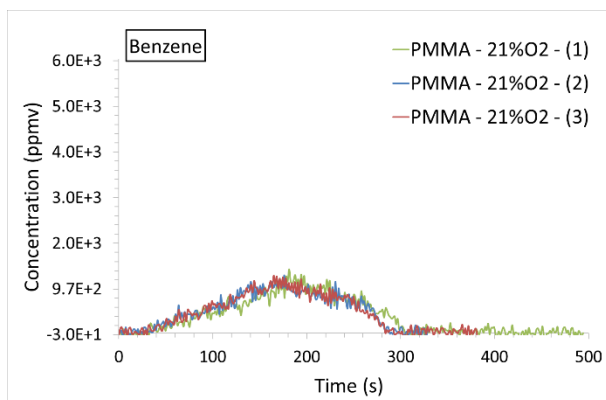
Experiment	TTI (s)	TTE (s)	Residue (%)	pMLR (g/s)	pHRR (kW.m ⁻²)	THR (MJ.m ⁻²)
Filled PVC – 21 vol. %O ₂ – (1)*	25	612	37.3	0.136	229.8	46.9
Filled PVC – 21 vol. %O ₂ – (2)	21	597	35.8	0.132	222.2	45.3
Filled PVC – 21 vol. %O ₂ – (3)	24	654	36.9	0.118	/	/
Average	23.3	621.0	36.7	0.129	226	46.1
Standard deviation	2.1	29.5	0.7	0.009	5.4	1.1

*Experiment presented in the chapter

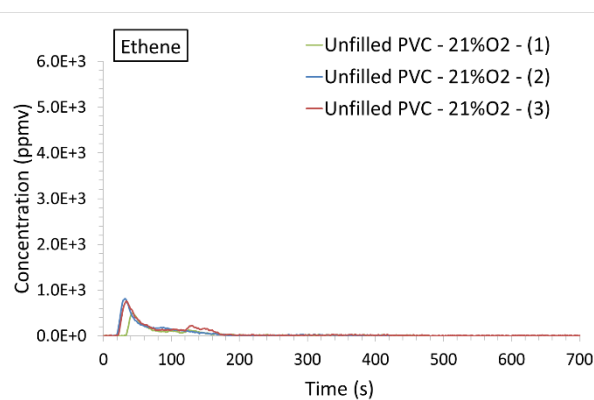
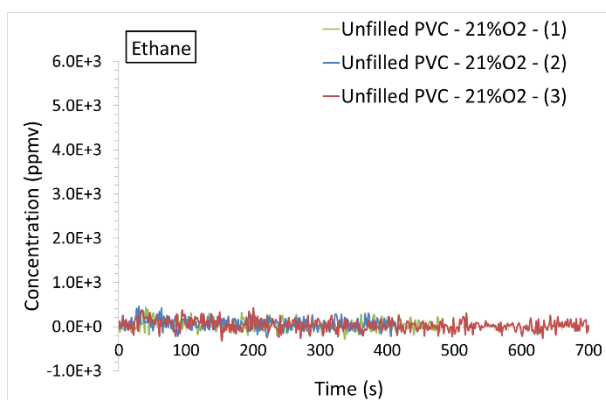
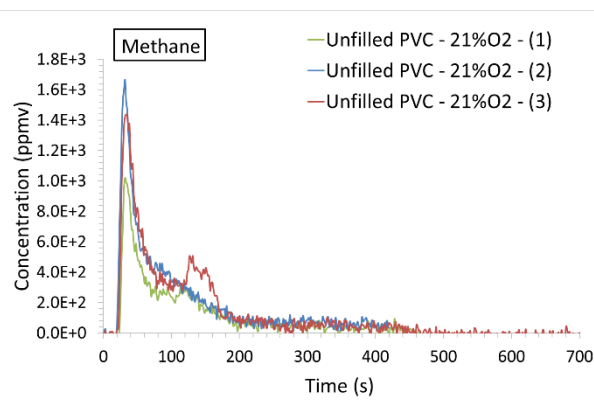
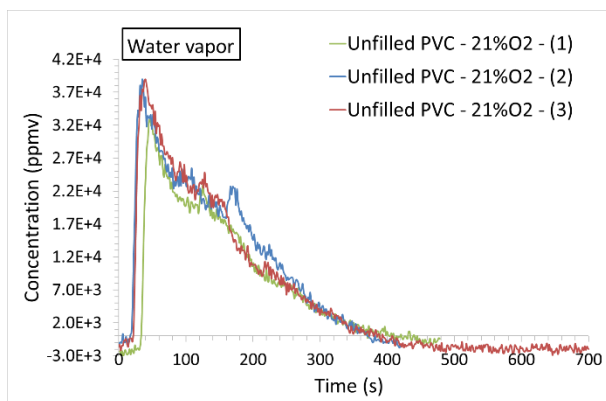
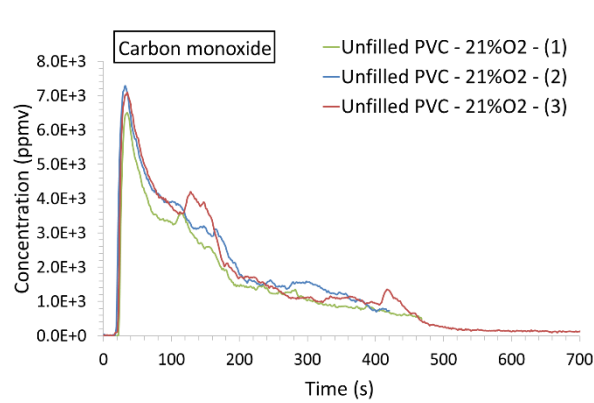
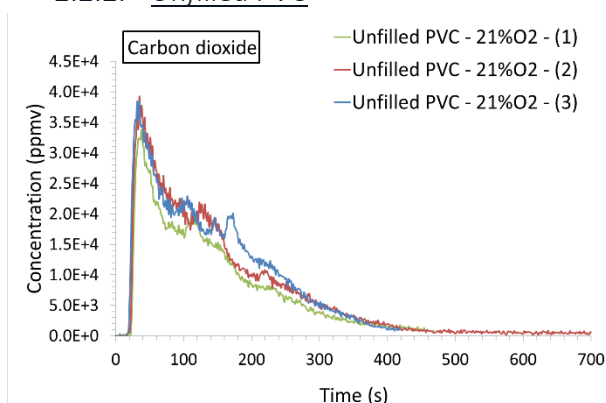
2.2. Gases

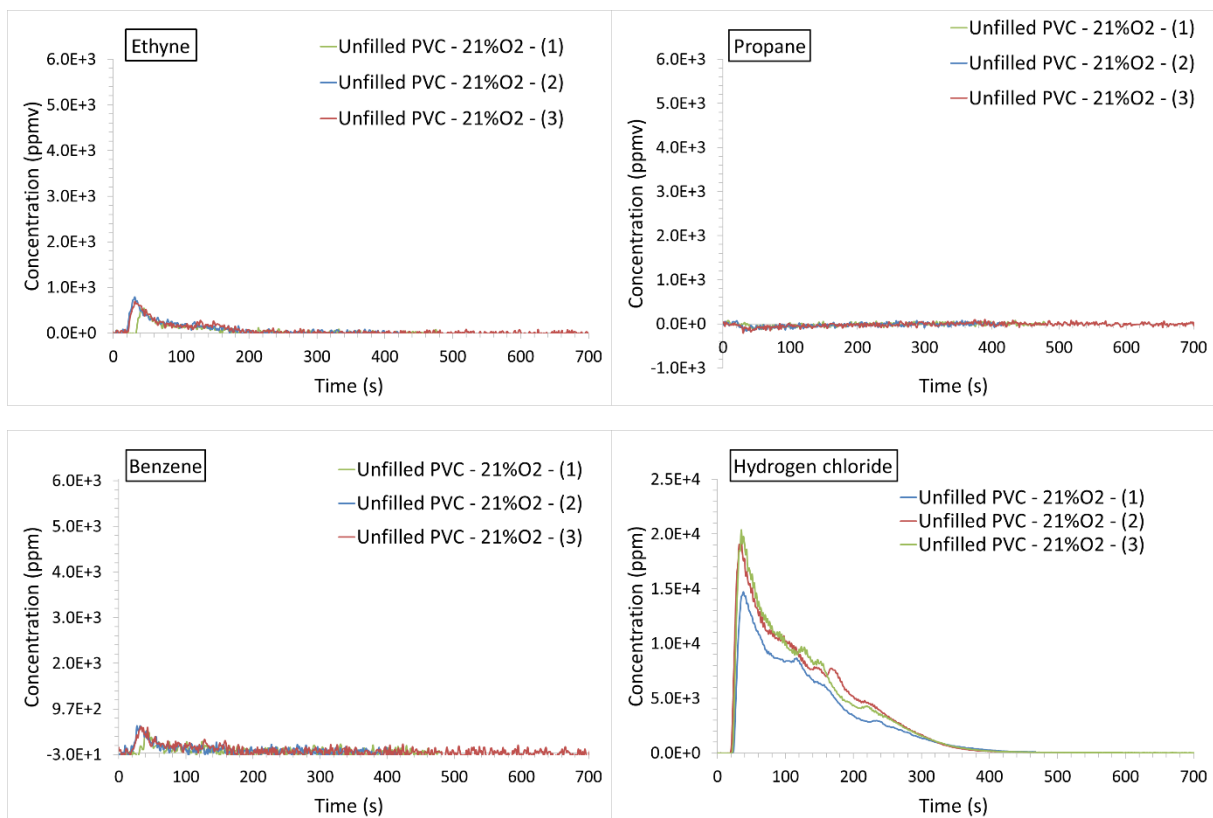
2.2.1. PMMA



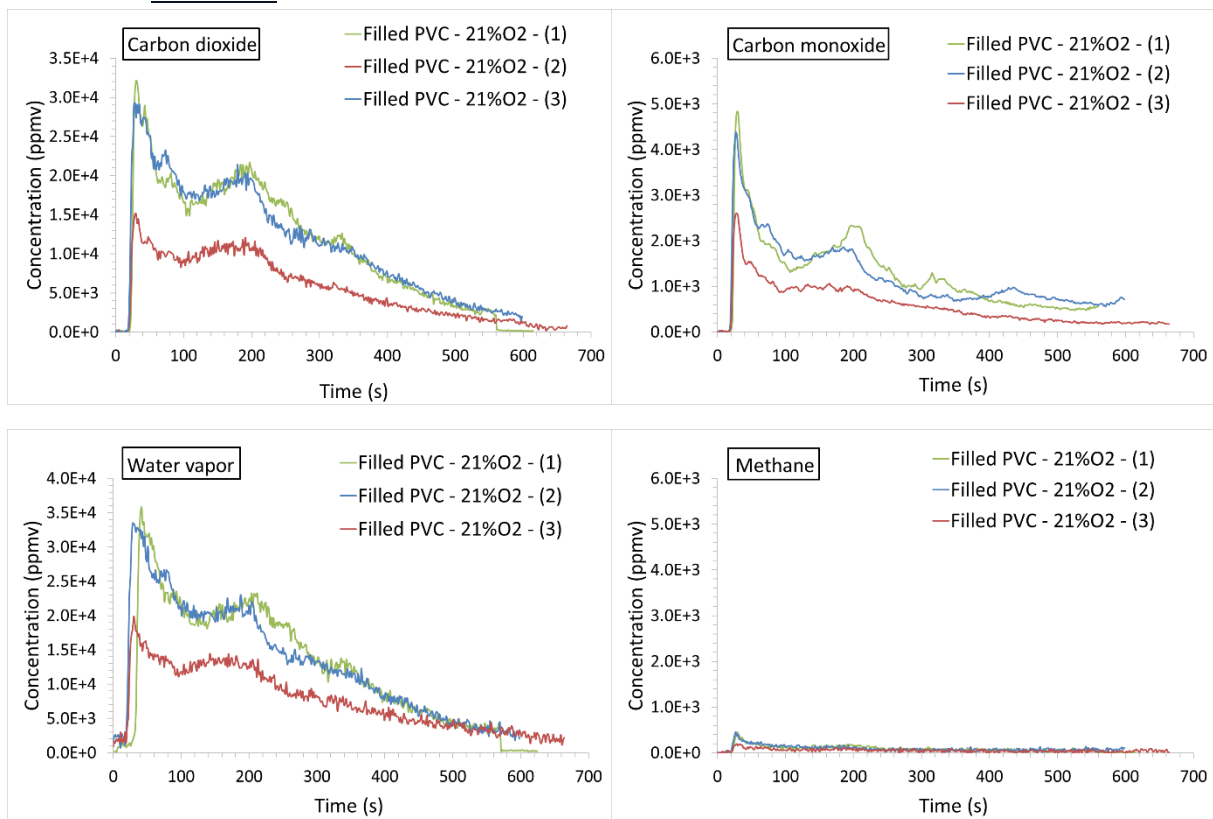


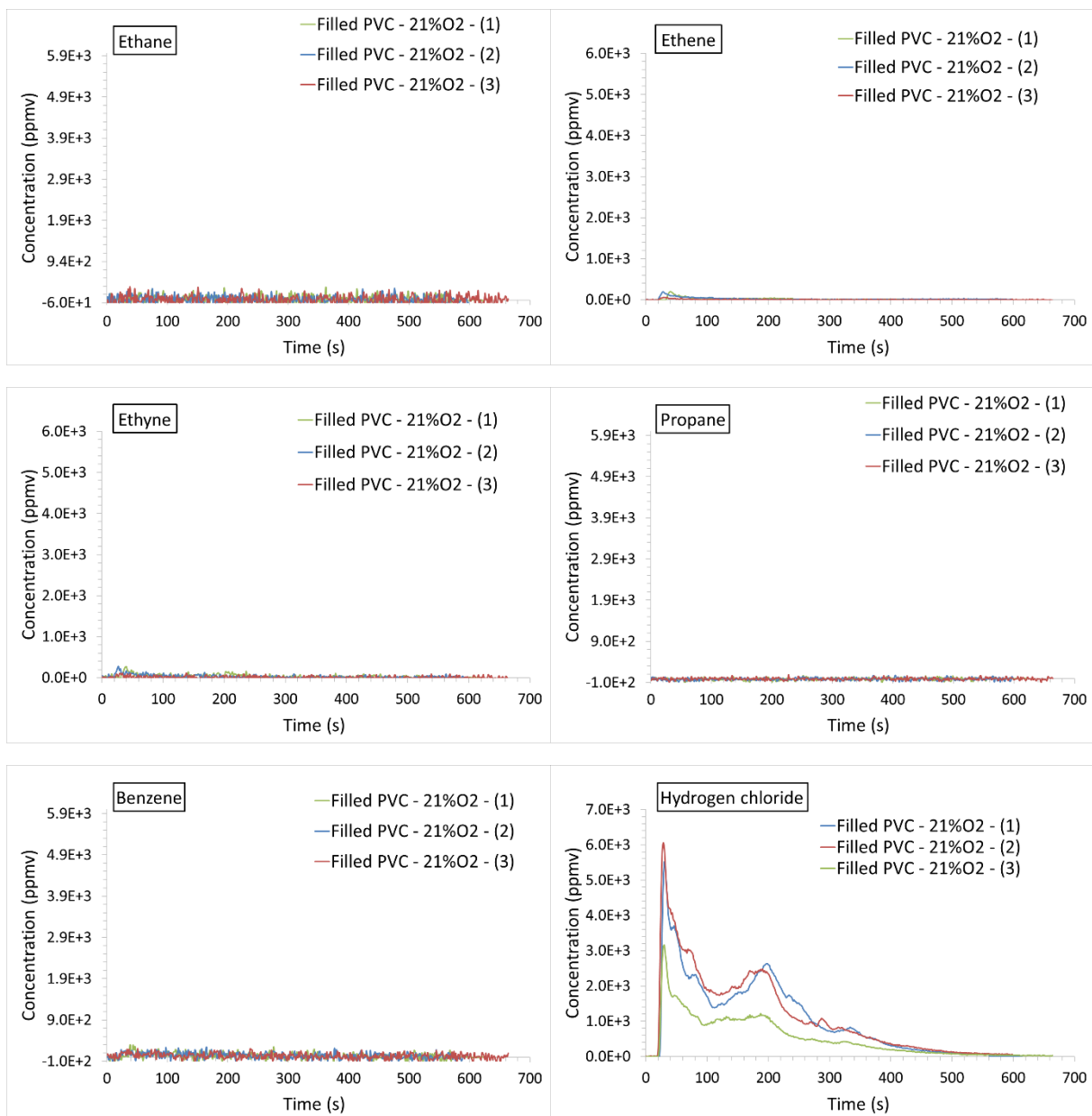
2.2.2. Unfilled PVC





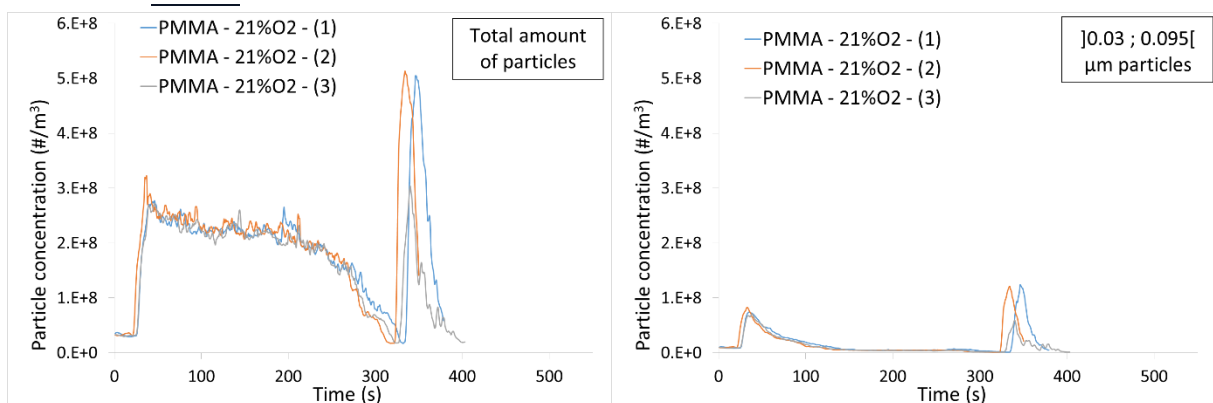
2.2.3. Filled PVC

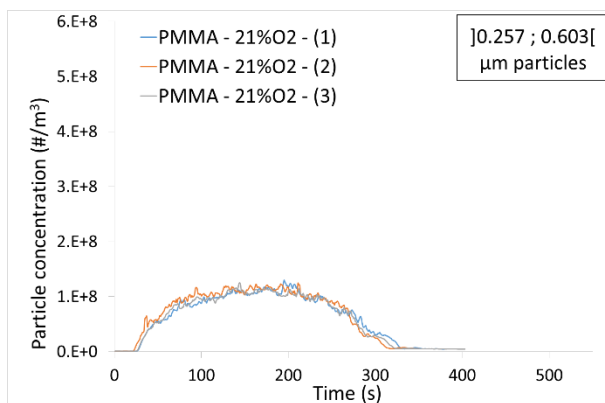




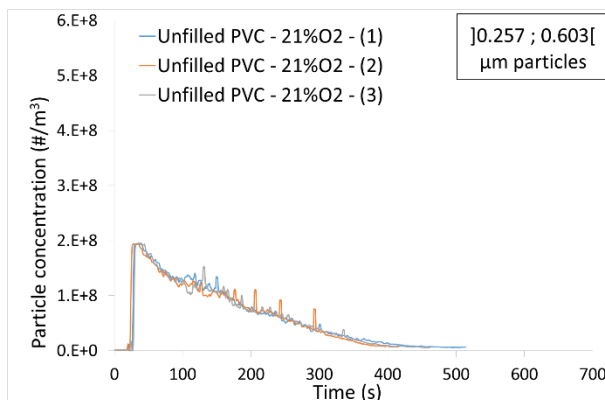
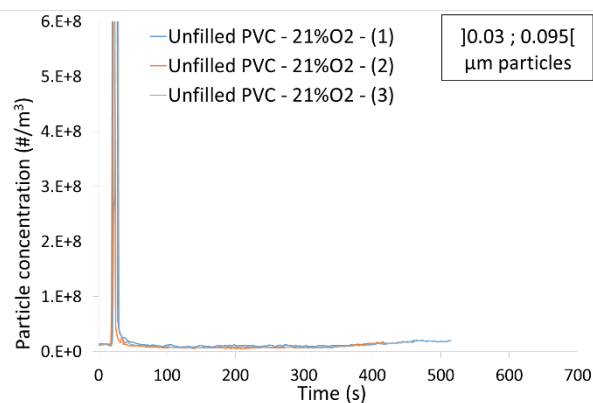
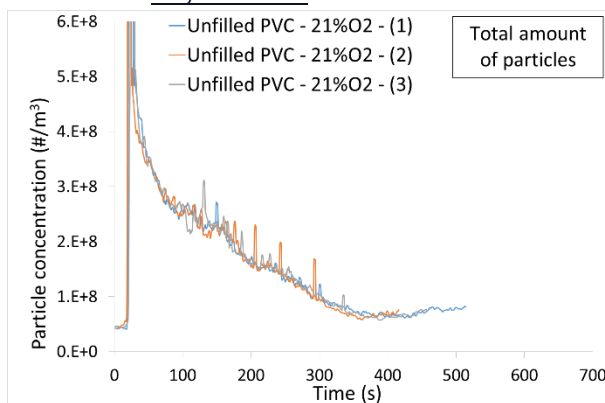
2.3. Aerosols

2.3.1. PMMA

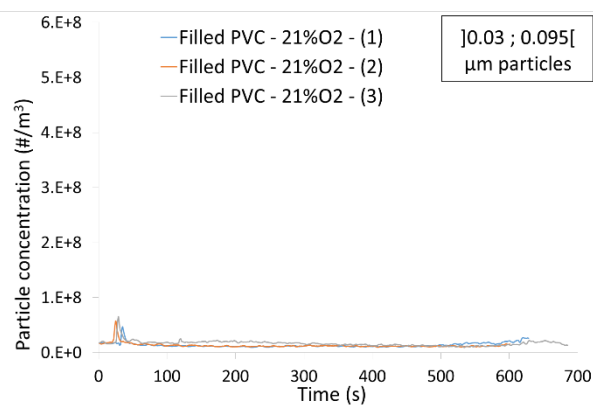
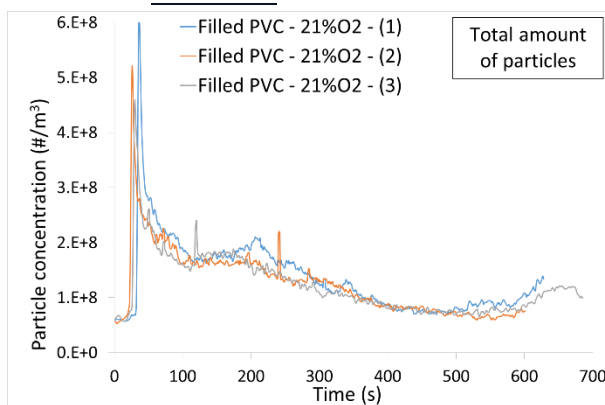


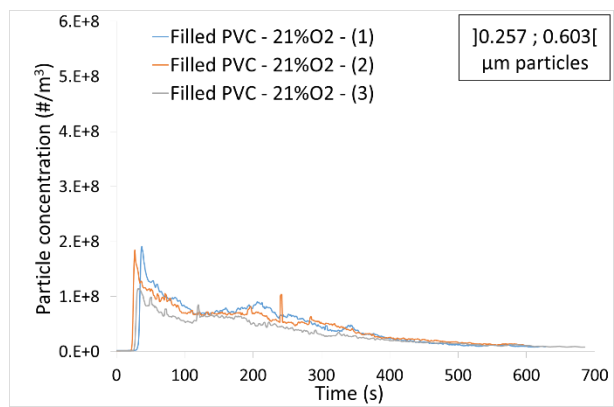


2.3.2. Unfilled PVC



2.3.3. Filled PVC





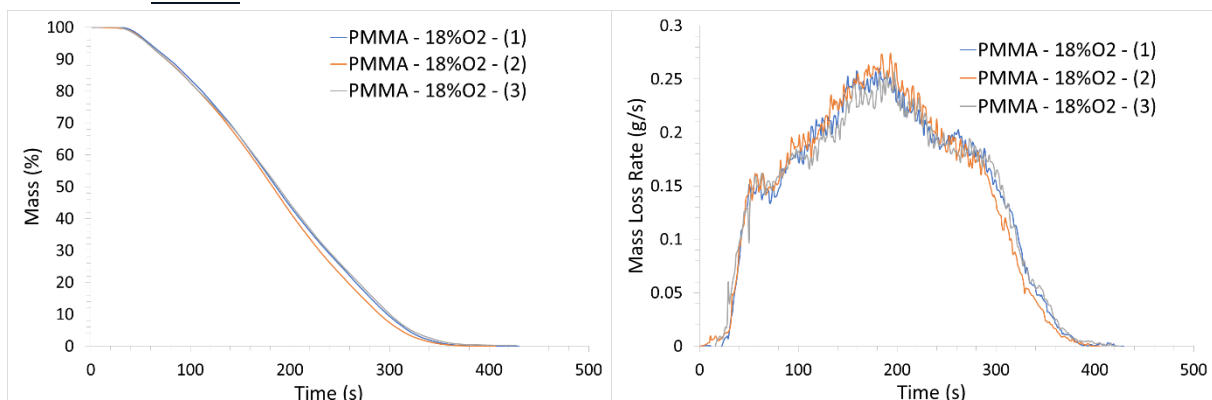
Appendix 5: Tests performed in confined configuration under various oxygen contents

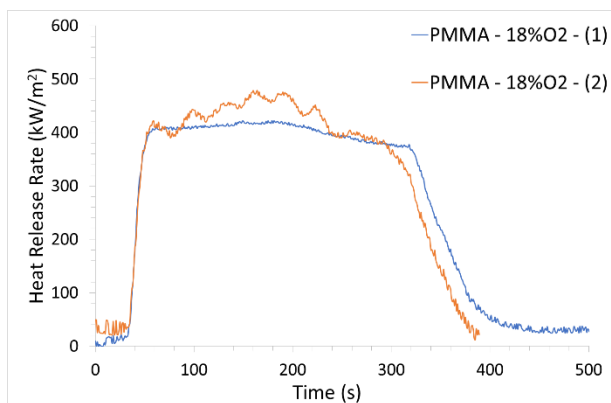
1. Mass Loss and Heat Release Rate	203
1.1. 18 vol. %O ₂	203
1.2. 16 vol. %O ₂	206
1.3. 13 vol. %O ₂	209
1.4. 9 vol. %O ₂	210
1.5. 6 vol. %O ₂	212
1.6. 2 vol. %O ₂	214
2. Gases	216
2.1. 18 vol. %O ₂	216
2.2. 16 vol. %O ₂	220
2.3. 9 vol. %O ₂	224
2.4. 6 vol. %O ₂	227
2.5. 2 vol. %O ₂	231
3. Aerosols	235
3.1. 18 vol. %O ₂	235
3.2. 16 vol. %O ₂	236

1. Mass Loss and Heat Release Rate

1.1. 18 vol. %O₂

1.1.1. PMMA

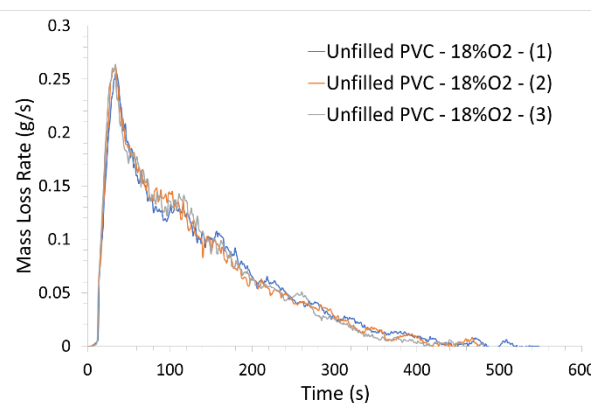
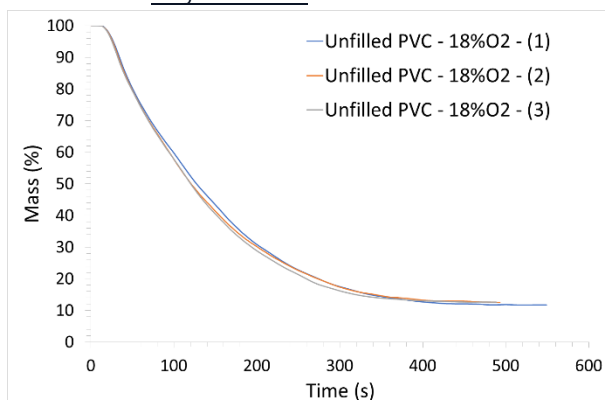


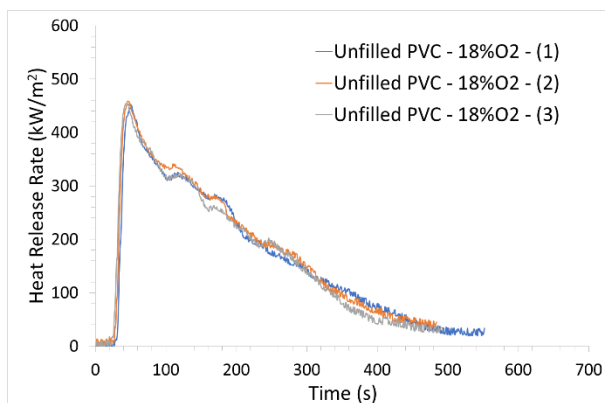


Experiment	TTI (s)	TTE (s)	Residue (%)	pMLR (g/s)	pHRR (kW.m ⁻²)	THR (MJ.m ⁻²)
PMMA – 18 vol. %O ₂ – (1)*	35	396	0	0.260	422.4	125.7
PMMA – 18 vol. %O ₂ – (2)	36	385	0	0.274	478.6	127.3
PMMA – 18 vol. %O ₂ – (3)	32	398	0	0.257	/	/
Average	34.3	393	0	0.264	450.5	126.5
Standard deviation	2.1	7	0	0.009	39.7	1.1

* Experiment presented in the chapter

1.1.2. Unfilled PVC

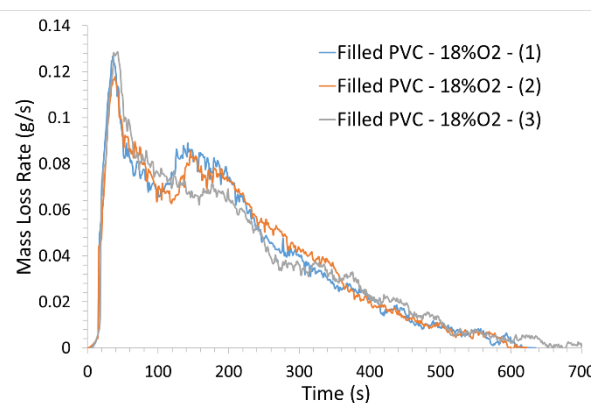
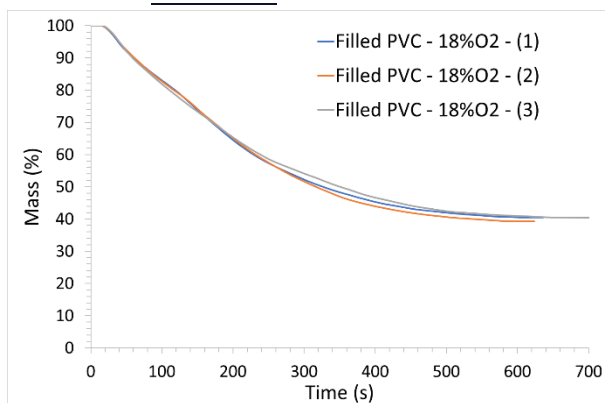


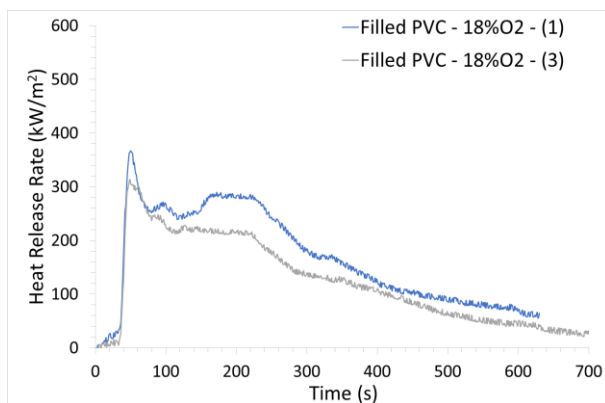


Experiment	TTI (s)	TTE (s)	Residue (%)	pMLR (g/s)	pHRR (kW.m ⁻²)	THR (MJ.m ⁻²)
Unfilled PVC – 18 vol. %O ₂ – (1)	20	544	9.7	0.256	451.3	80.9
Unfilled PVC – 18 vol. %O ₂ – (2)*	18	486	10.4	0.264	458.9	83.5
Unfilled PVC – 18 vol. %O ₂ – (3)	16	487	9.7	0.263	454.5	81.1
Average	18	505.7	9.9	0.261	454.9	81.8
Standard deviation	2.0	33.2	0.4	0.004	3.8	1.4

* Experiment presented in the chapter

1.1.3. Filled PVC



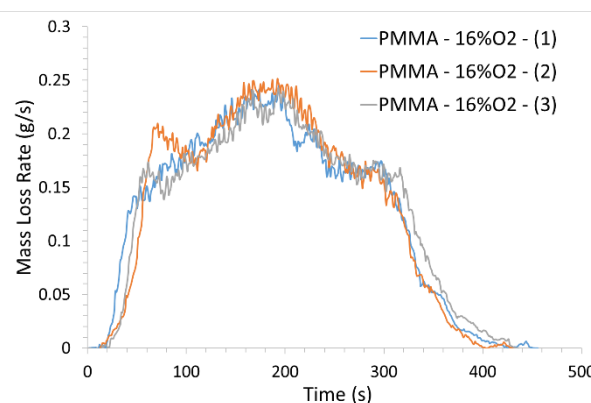
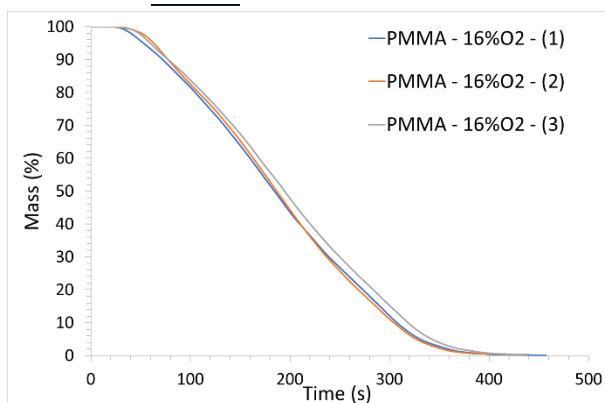


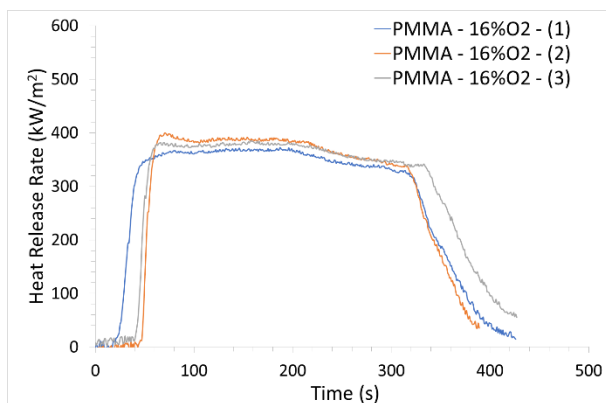
Experiment	TTI (s)	TTE (s)	Residue (%)	pMLR (g/s)	pHRR (kW.m ⁻²)	THR (MJ.m ⁻²)
Filled PVC – 18 vol. %O ₂ – (1)	22	626	/	0.127	366.9	82.5
Filled PVC – 18 vol. %O ₂ – (2)	23	621	37.1	0.118	/	/
Filled PVC – 18 vol. %O ₂ – (3)*	23	646	37	0.129	313.7	66.7
Average	22.7	631.6	37.1	0.125	340.3	74.6
Standard deviation	0.6	13.2	0.1	0.006	37.6	11.2

* Experiment presented in the chapter

1.2. 16 vol. %O₂

1.2.1. PMMA

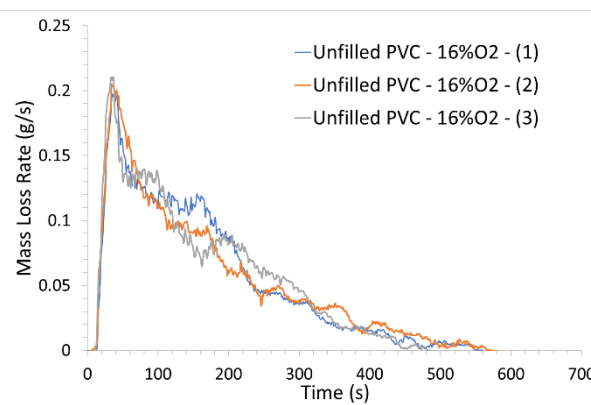
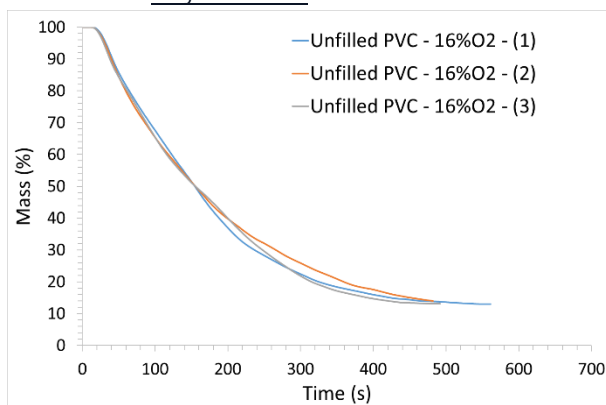


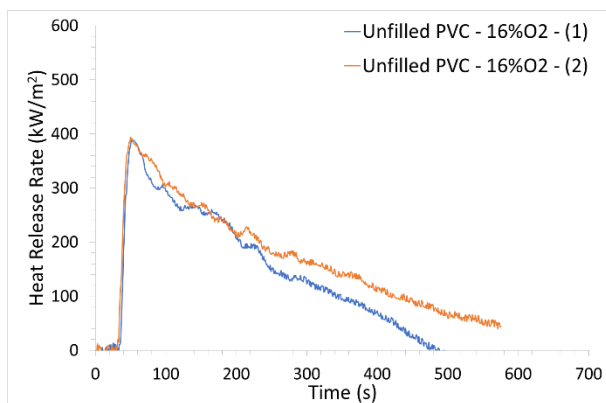


Experiment	TTI (s)	TTE (s)	Residue (%)	pMLR (g/s)	pHRR (kW.m ⁻²)	THR (MJ.m ⁻²)
PMMA – 16 vol. %O ₂ – (1)	24	439	0	0.250	372.5	113.1
PMMA – 16 vol. %O ₂ – (2)	57	405	0	0.244	399.7	110.2
PMMA – 16 vol. %O ₂ – (3)*	41	434	0	0.245	384.8	116.4
Average	40.6	426	0	0.246	385.7	113.2
Standard deviation	16.5	18.4	0	0.003	13.6	3.1

* Experiment presented in the chapter

1.2.2. Unfilled PVC

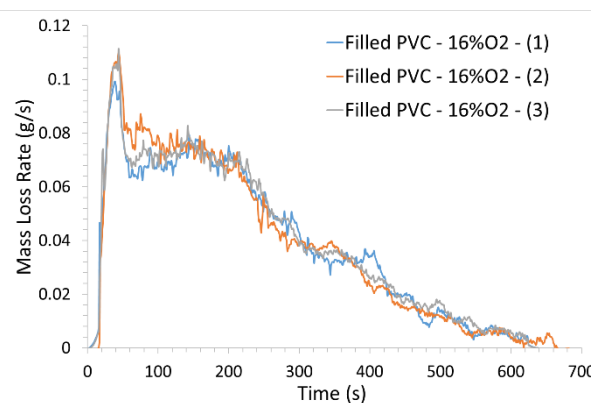
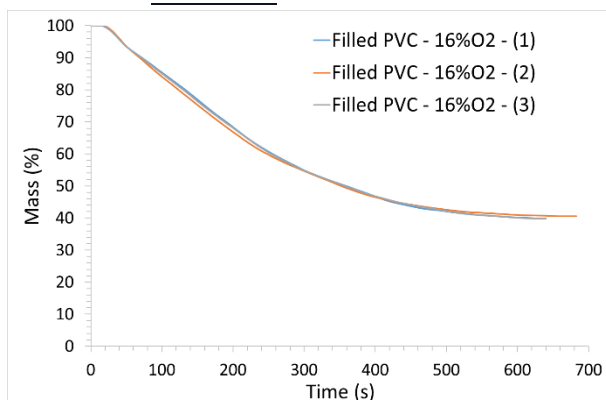


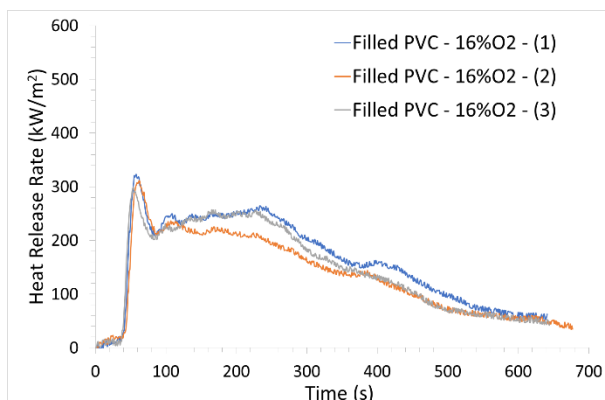


Experiment	TTI (s)	TTE (s)	Residue (%)	pMLR (g/s)	pHRR (kW.m ⁻²)	THR (MJ.m ⁻²)
Unfilled PVC – 16 vol. %O ₂ – (1)*	23	540	10.8	0.198	388.1	70.7
Unfilled PVC – 16 vol. %O ₂ – (2)	20	569	11.2	0.205	394.1	80.0
Unfilled PVC – 16 vol. %O ₂ – (3)	21	485	10.8	0.211	/	/
Average	21.3	531.3	10.9	0.205	391.1	75.4
Standard deviation	1.5	42.7	0.2	0.006	4.2	6.6

* Experiment presented in the chapter

1.2.3. Filled PVC



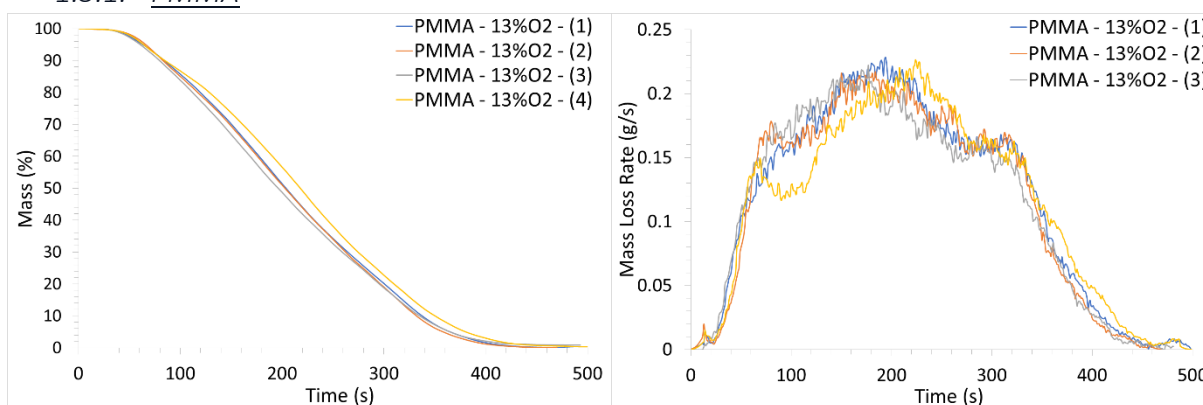


Experiment	TTI (s)	TTE (s)	Residue (%)	pMLR (g/s)	pHRR (kW.m ⁻²)	THR (MJ.m ⁻²)
Filled PVC – 16 vol. %O ₂ – (1)	23	636	36.8	0.099	323.0	77.8
Filled PVC – 16 vol. %O ₂ – (2)	25	668	37.3	0.111	311.4	67.7
Filled PVC – 16 vol. %O ₂ – (7)*	23	624	37.7	0.111	298.6	74.3
Average	23.7	642.7	37.7	0.107	311	73.3
Standard deviation	1.2	22.7	0.5	0.007	12.2	5.1

* Experiment presented in the chapter

1.3. 13 vol. %O₂

1.3.1. PMMA



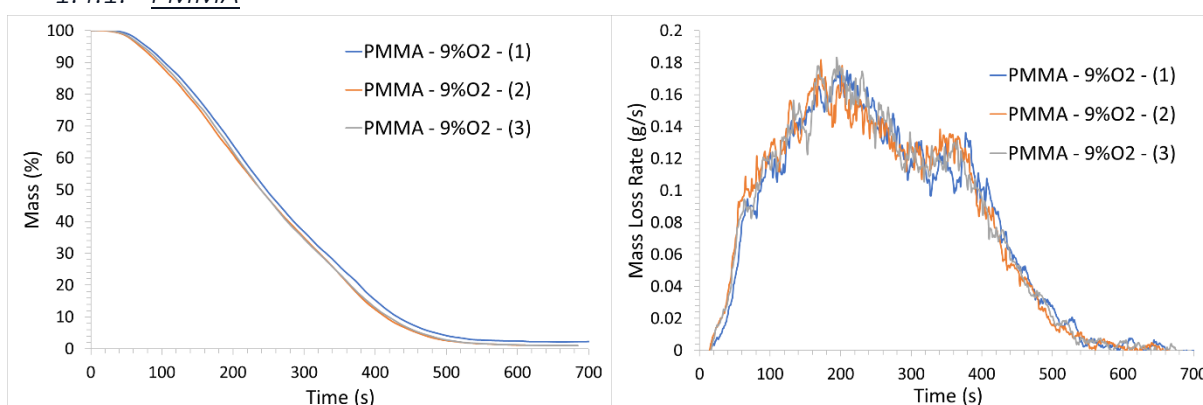
Experiment	TTI (s)	TTE (s)	Residue (%)	pMLR (g/s)
PMMA – 13 vol. %O ₂ – (1)	28	482	0	0.217
PMMA – 13 vol. %O ₂ – (2)*	66	450	0	0.222

PMMA – 13 vol. %O₂ – (3)	28	476	0	0.227
PMMA – 13 vol. %O₂ – (4)	51	494	0	0.227
Average	43.3	475.5	0	0.223
Standard deviation	18.6	18.6	0	0.005

* Experiment presented in the chapter

1.4. 9 vol. %O₂

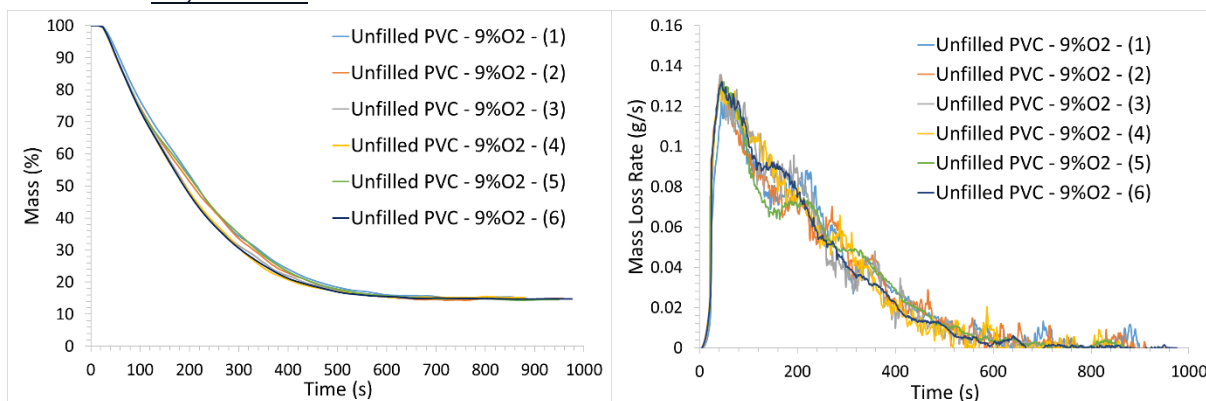
1.4.1. PMMA



Experiment	Residue (%)	pMLR (g/s)
PMMA – 9 vol. %O₂ – (1)	0	0.175
PMMA – 9 vol. %O₂ – (2)*	0	0.182
PMMA – 9 vol. %O₂ – (3)	0	0.183
Average	0	0.180
Standard deviation	0	0.004

* Experiment presented in the chapter

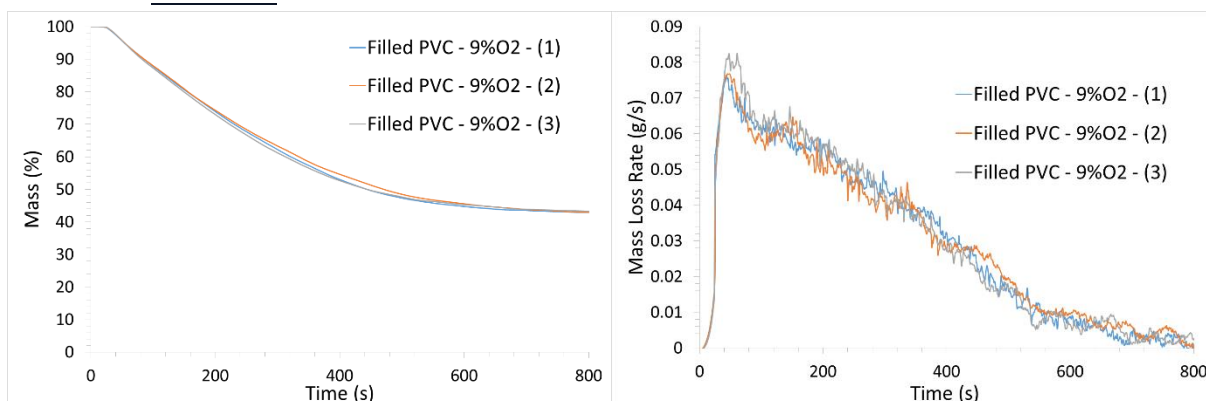
1.4.2. Unfilled PVC



Experiment	Residue (%)	pMLR (g/s)
Unfilled PVC – 9 vol. %O ₂ – (1)	12.5	0.125
Unfilled PVC – 9 vol. %O ₂ – (2)	12.2	0.135
Unfilled PVC – 9 vol. %O ₂ – (3)	12.4	0.136
Unfilled PVC – 9 vol. %O ₂ – (4)	12.1	0.128
Unfilled PVC – 9 vol. %O ₂ – (5)*	12.1	0.132
Unfilled PVC – 9 vol. %O ₂ – (6)	11.3	0.132
Average	12.1	0.131
Standard deviation	0.4	0.004

* Experiment presented in the chapter

1.4.3. Filled PVC

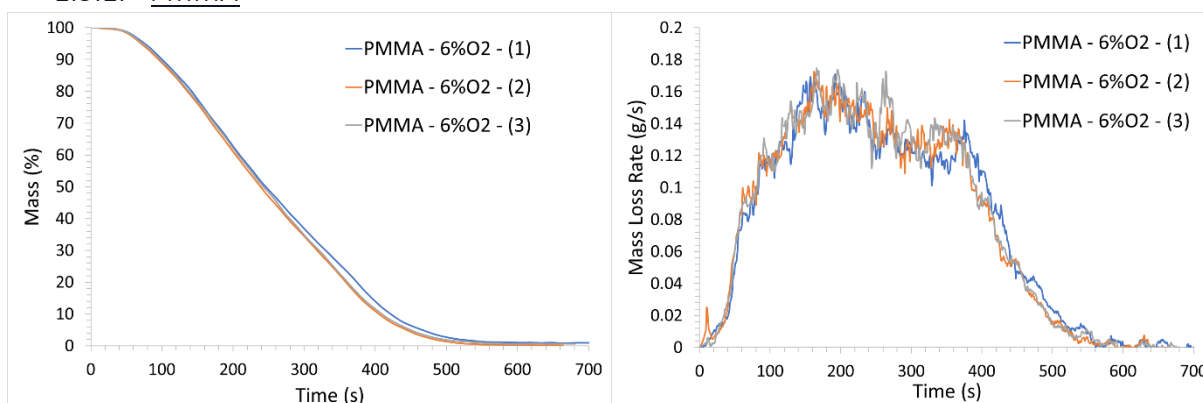


Experiment	Residue (%)	pMLR (g/s)
Filled PVC – 9 vol. %O ₂ – (1)	39.1	0.076
Filled PVC – 9 vol. %O ₂ – (2)*	38.6	0.077
Filled PVC – 9 vol. %O ₂ – (3)	38.9	0.083
Average	38.9	0.079
Standard deviation	0.3	0.004

*Experiment presented in the chapter

1.5. 6 vol. %O₂

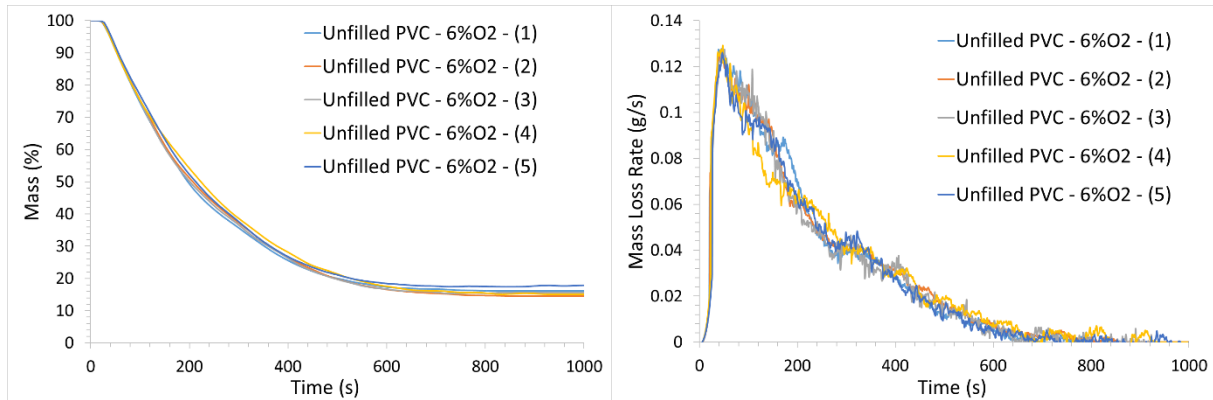
1.5.1. PMMA



Experiment	Residue (%)	pMLR (g/s)
PMMA – 6 vol. %O ₂ – (1)	0	0.171
PMMA – 6 vol. %O ₂ – (2)*	0	0.173
PMMA – 6 vol. %O ₂ – (3)	0	0.175
Average	0	0.173
Standard deviation	0	0.002

* Experiment presented in the chapter

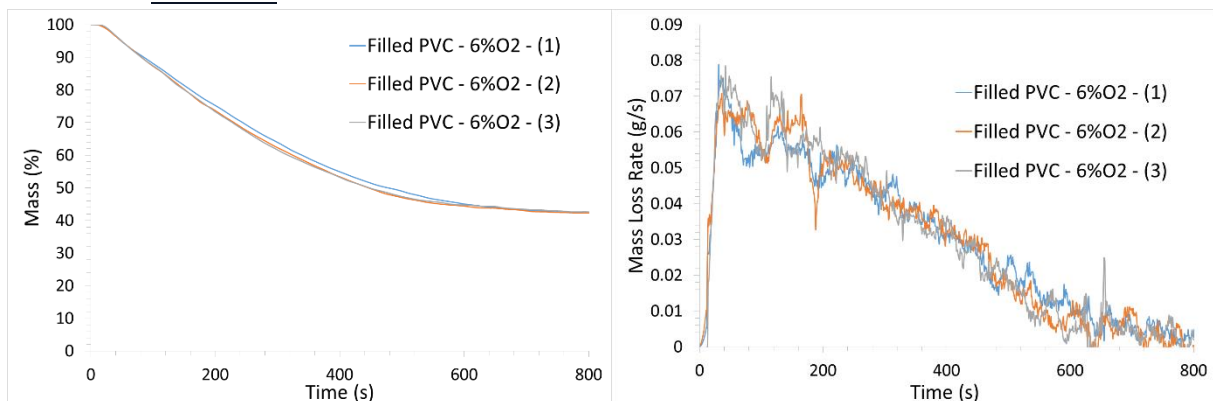
1.5.2. Unfilled PVC



Experiment	Residue (%)	pMLR (g/s)
Unfilled PVC – 6 vol. %O ₂ – (1)	13.1	0.128
Unfilled PVC – 6 vol. %O ₂ – (2)	/	0.127
Unfilled PVC – 6 vol. %O ₂ – (3)*	12.8	0.128
Unfilled PVC – 6 vol. %O ₂ – (4)	13.1	0.129
Unfilled PVC – 6 vol. %O ₂ – (5)	12.7	0.126
Average	12.9	0.128
Standard deviation	0.2	0.001

* Experiment presented in the chapter

1.5.3. Filled PVC



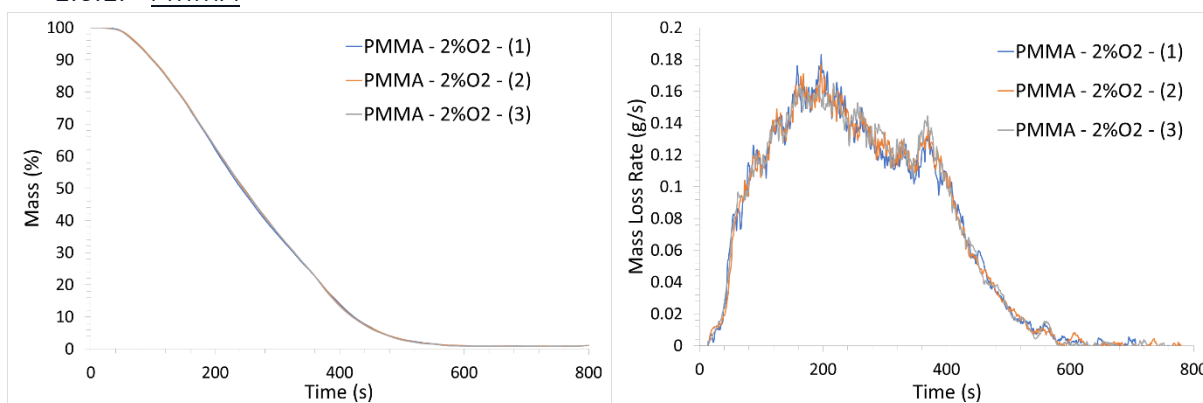
Experiment	Residue (%)	pMLR (g/s)
------------	-------------	------------

Filled PVC – 6 vol. %O₂ – (1)*	40.1	0.079
Filled PVC – 6 vol. %O₂ – (2)	40.8	0.071
Filled PVC – 6 vol. %O₂ – (3)	40.0	0.079
Average	40.3	0.076
Standard deviation	0.4	0.005

* Experiment presented in the chapter

1.6. 2 vol. %O₂

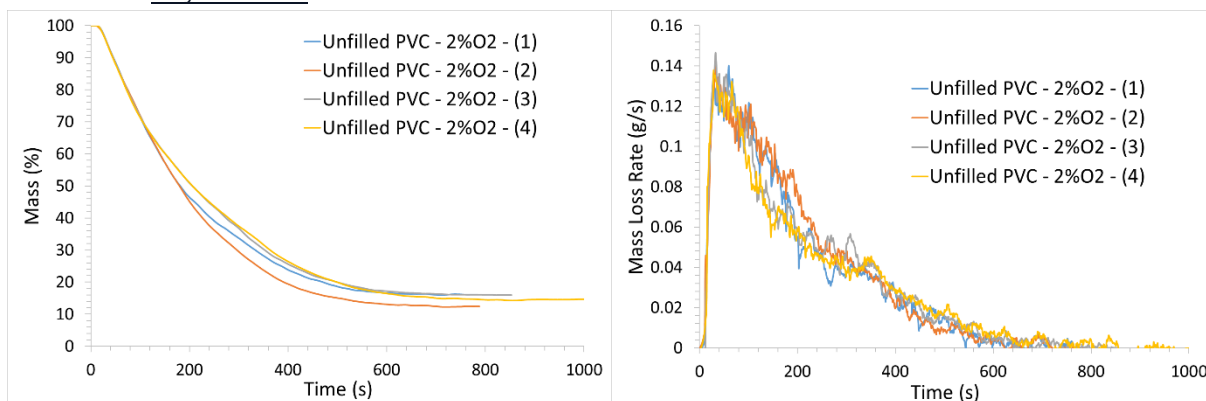
1.6.1. PMMA



Experiment	Residue (%)	pMLR (g/s)
PMMA – 2 vol. %O₂ – (1)	0	0.183
PMMA – 2 vol. %O₂ – (2)*	0	0.176
PMMA – 2 vol. %O₂ – (3)	0	0.165
Average	0	0.175
Standard deviation	0	0.009

* Experiment presented in the chapter

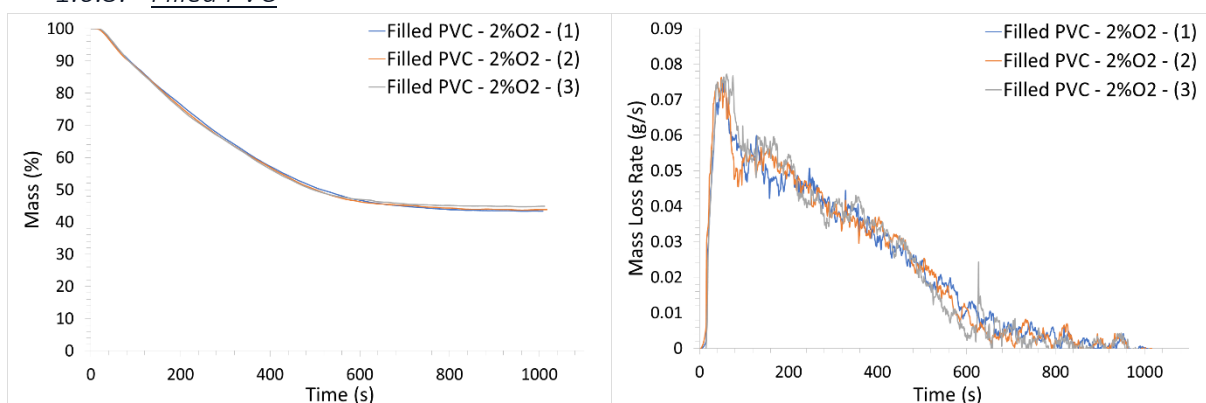
1.6.2. Unfilled PVC



Experiment	Residue (%)	pMLR (g/s)
Unfilled PVC – 2 vol. %O ₂ – (1)	13.9	0.140
Unfilled PVC – 2 vol. %O ₂ – (2)	13.0	0.149
Unfilled PVC – 2 vol. %O ₂ – (3)	12.8	0.142
Unfilled PVC – 2 vol. %O ₂ – (4)*	13.1	0.147
Average	13.2	0.145
Standard deviation	0.5	0.004

* Experiment presented in the chapter

1.6.3. Filled PVC



Experiment	Residue (%)	pMLR (g/s)
Filled PVC – 2 vol. %O ₂ – (1)	39.9	0.076

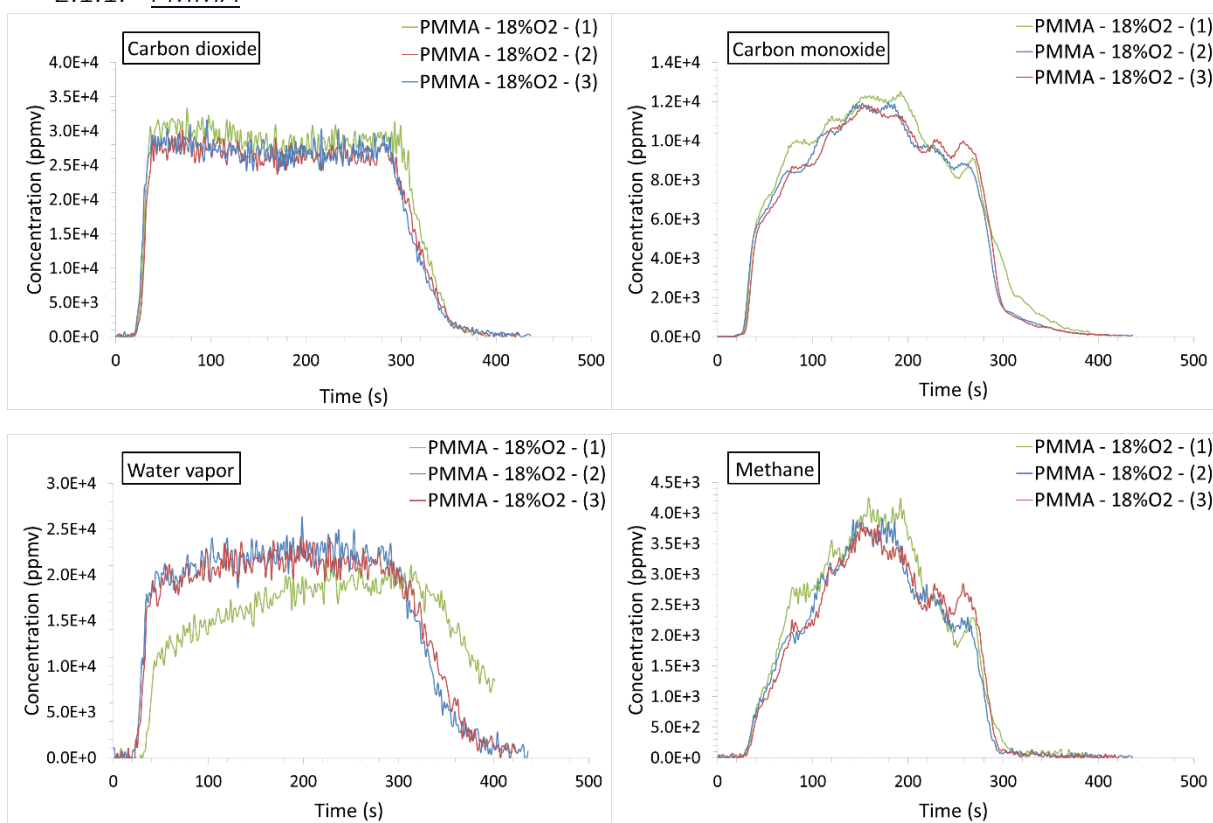
Filled PVC – 2 vol. %O₂ – (2)*	40.5	0.076
Filled PVC – 2 vol. %O₂ – (3)	40.9	0.077
Average	40.4	0.076
Standard deviation	0.5	0.001

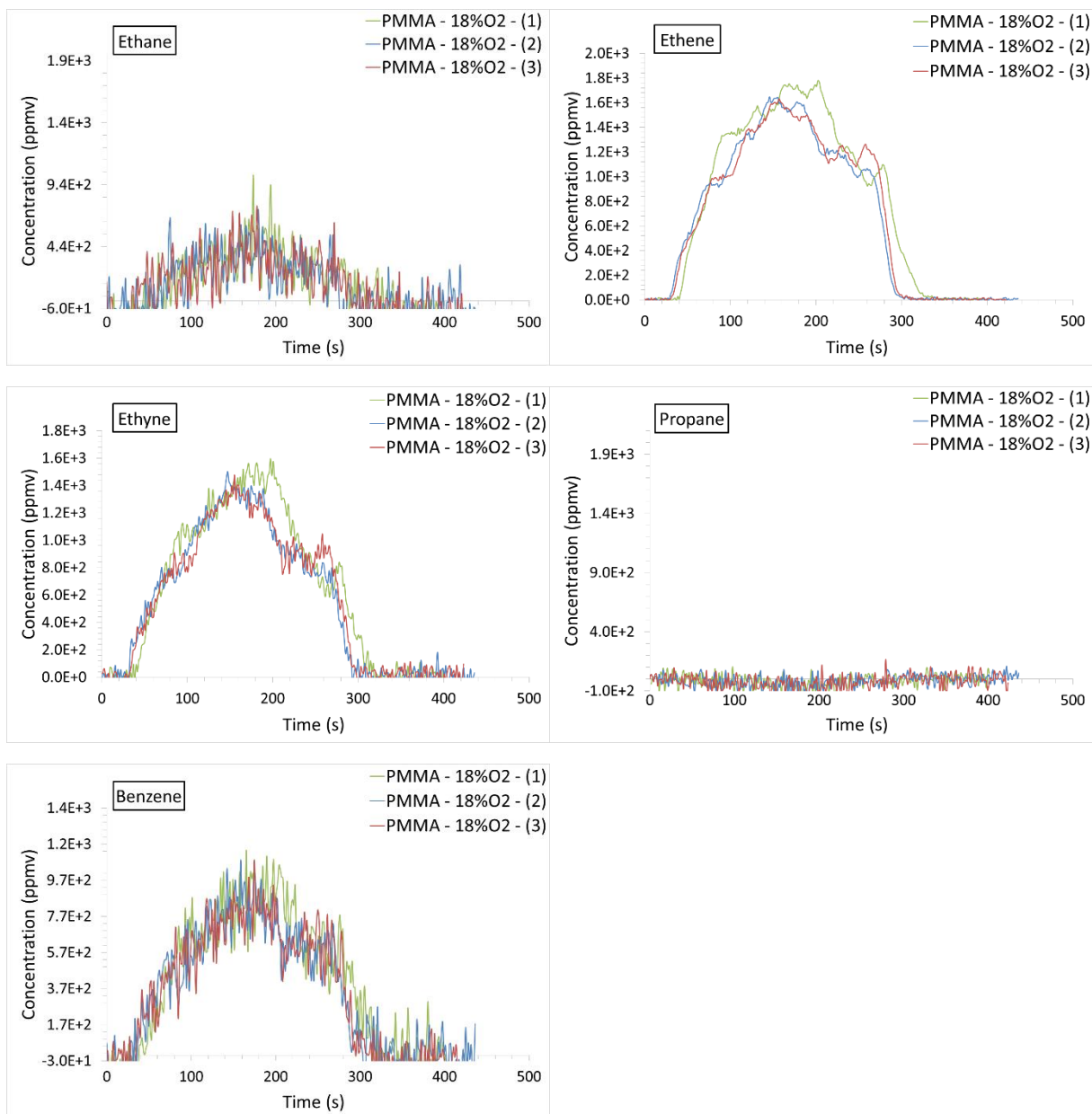
* Experiment presented in the chapter

2. Gases

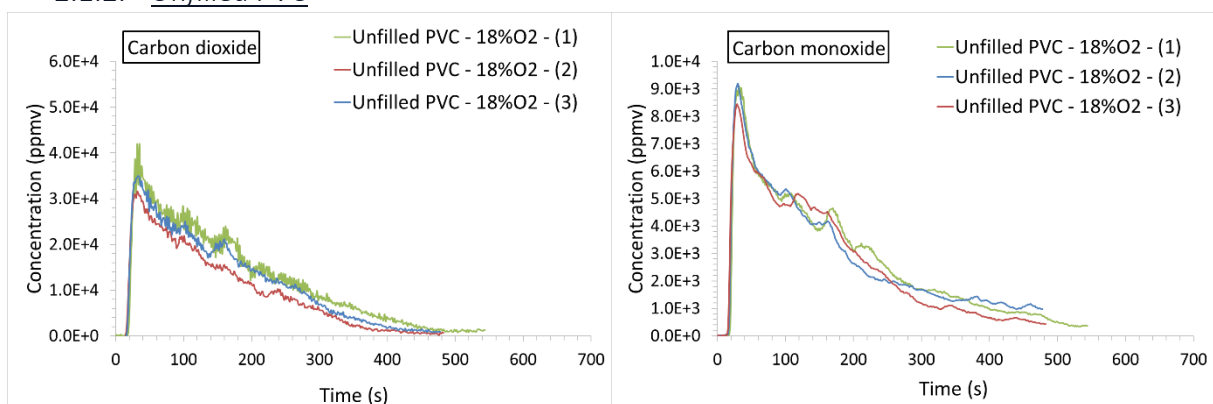
2.1. 18 vol. %O₂

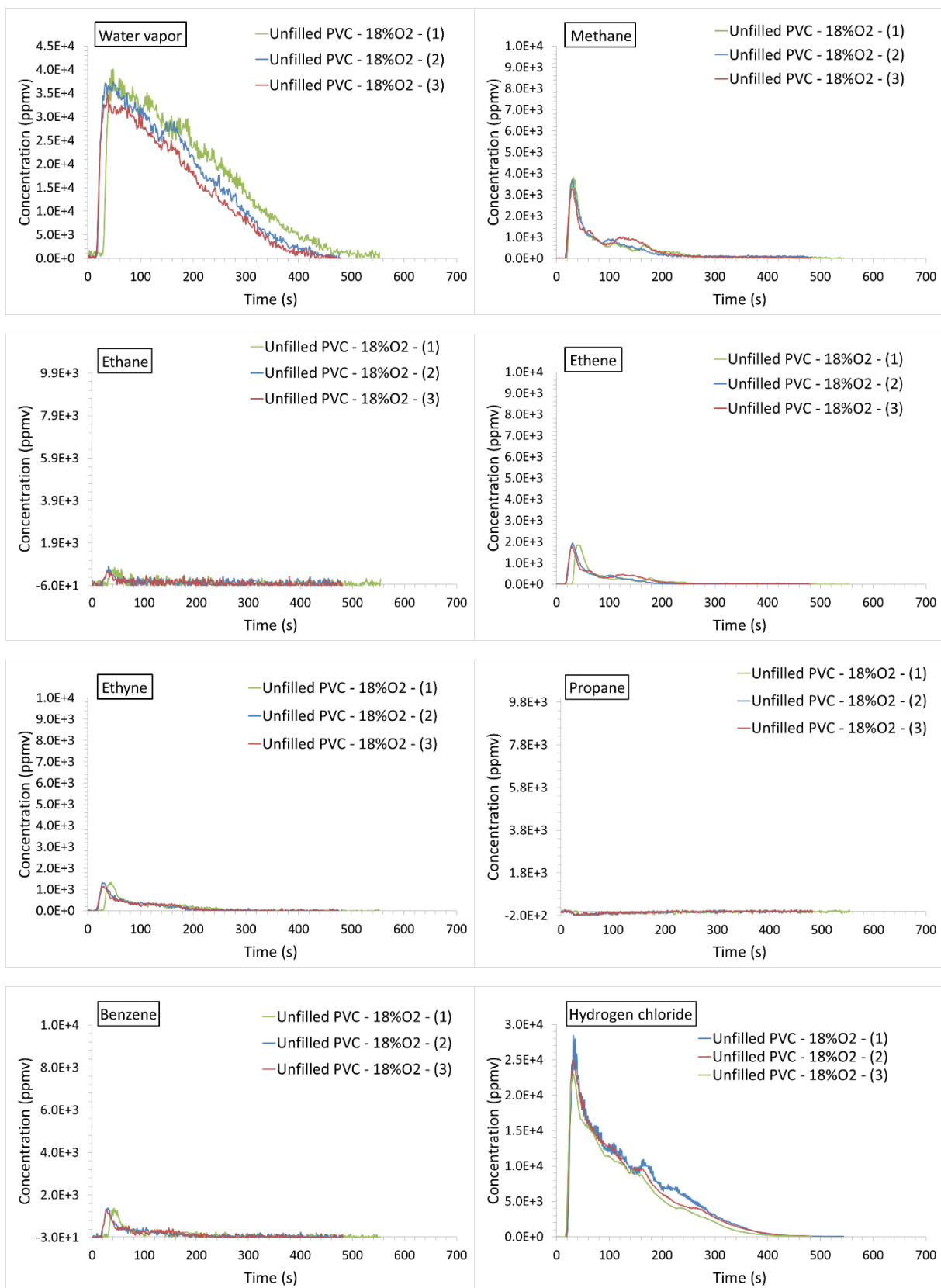
2.1.1. PMMA



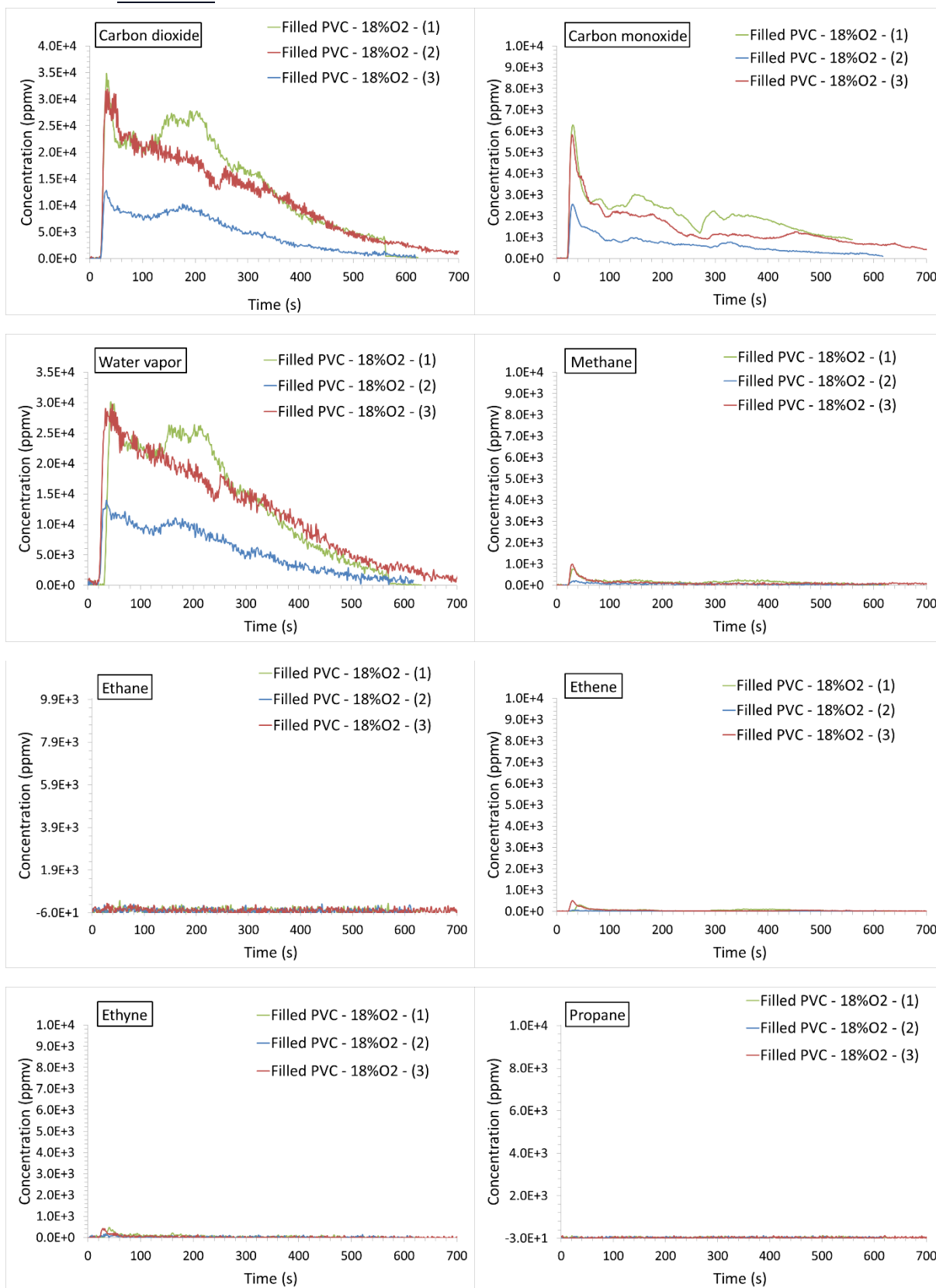


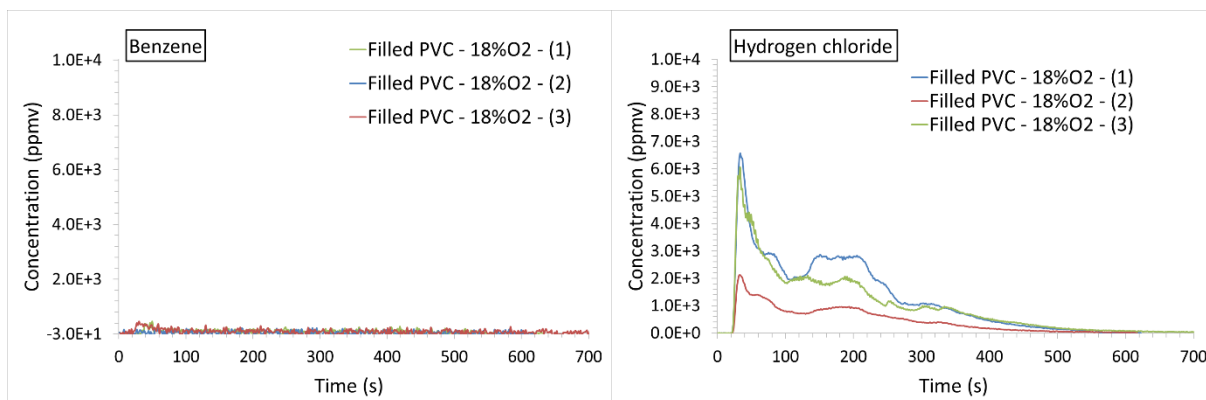
2.1.2. Unfilled PVC





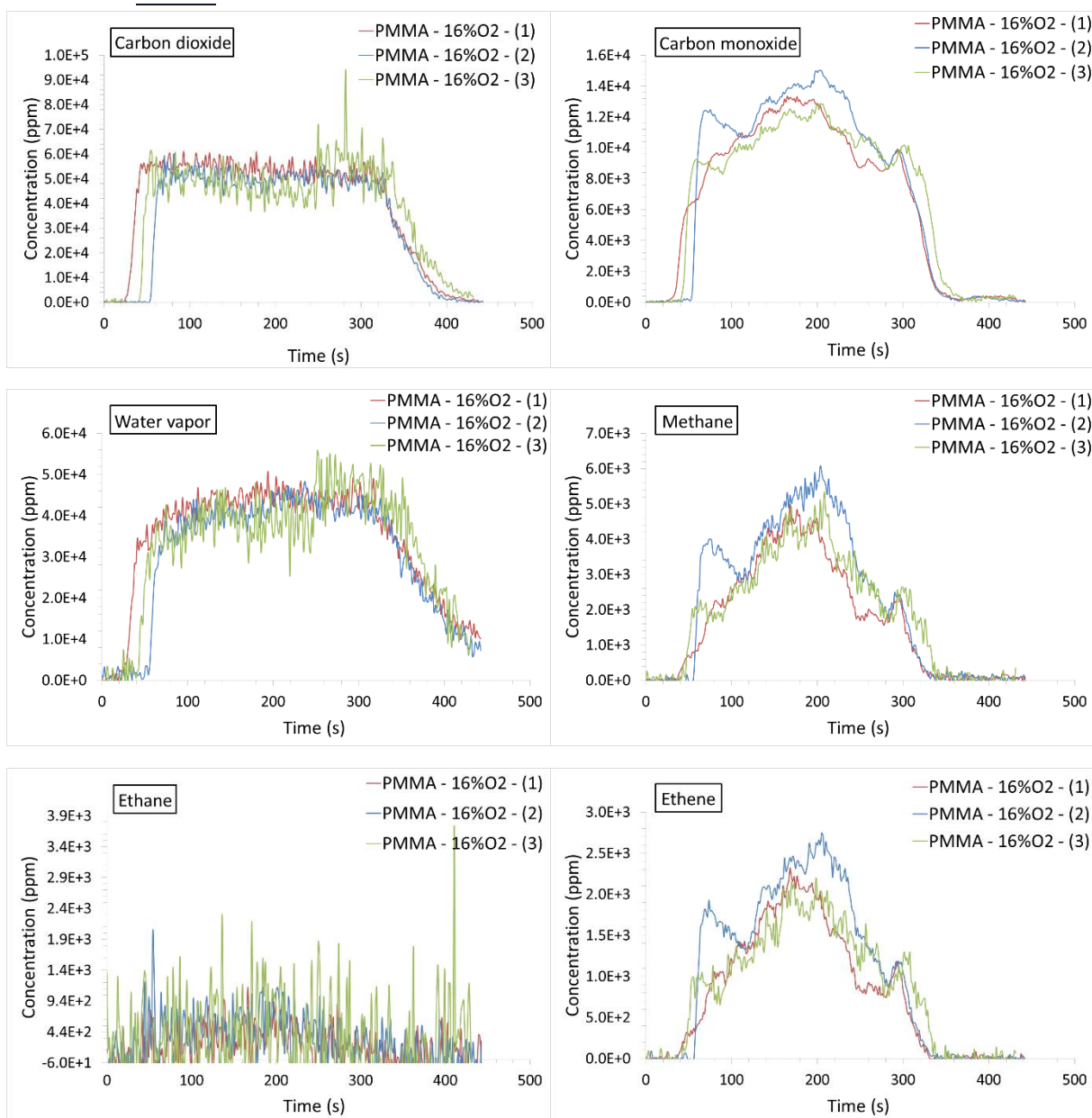
2.1.3. Filled PVC

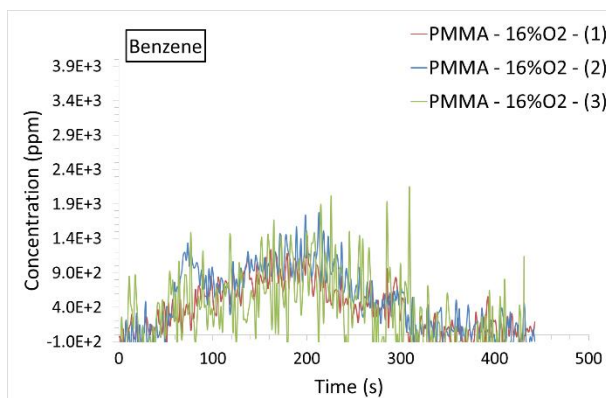
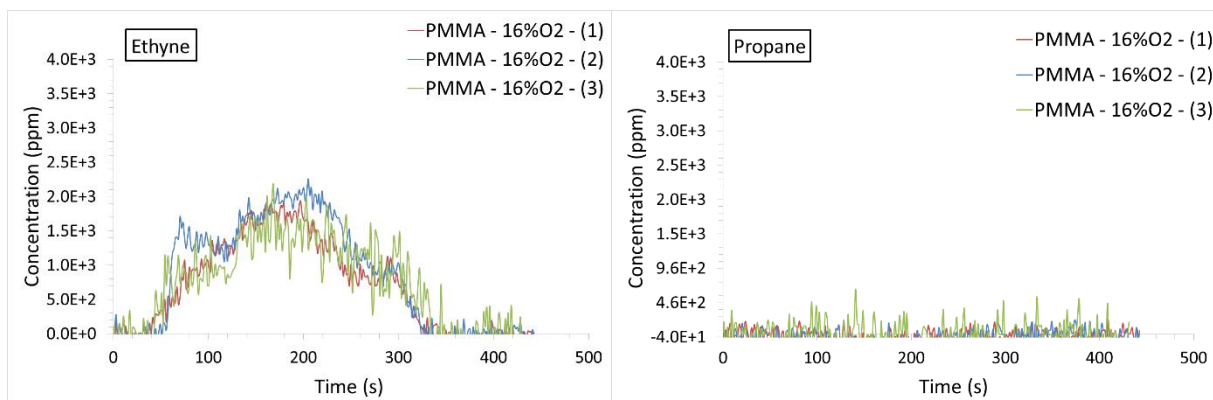




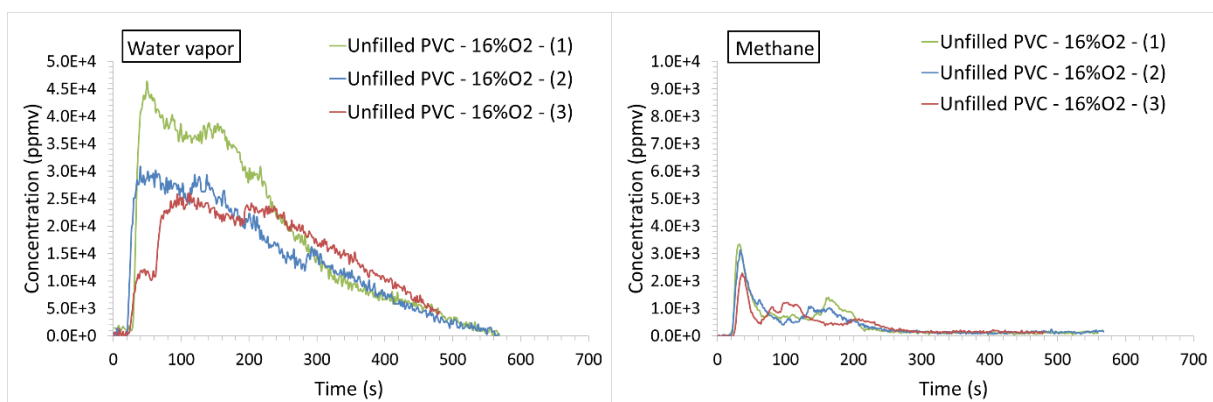
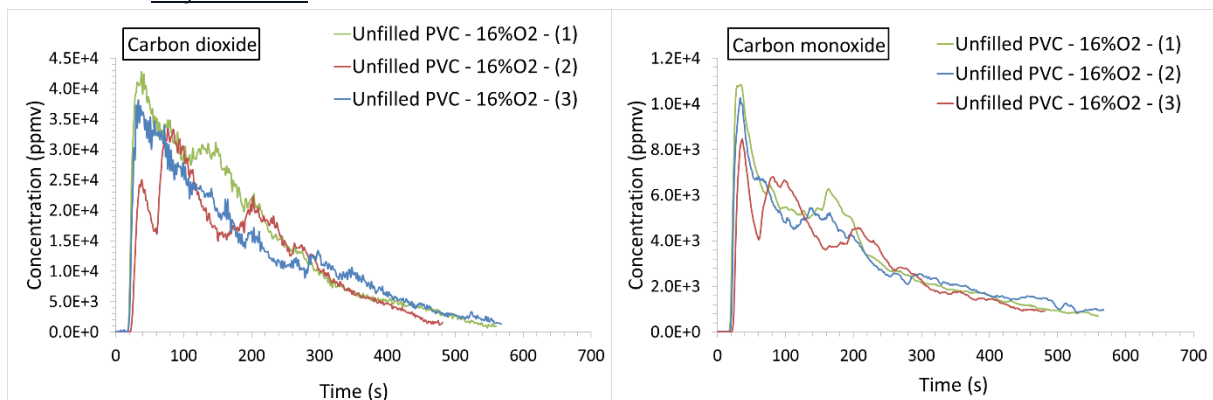
2.2. 16 vol. %O₂

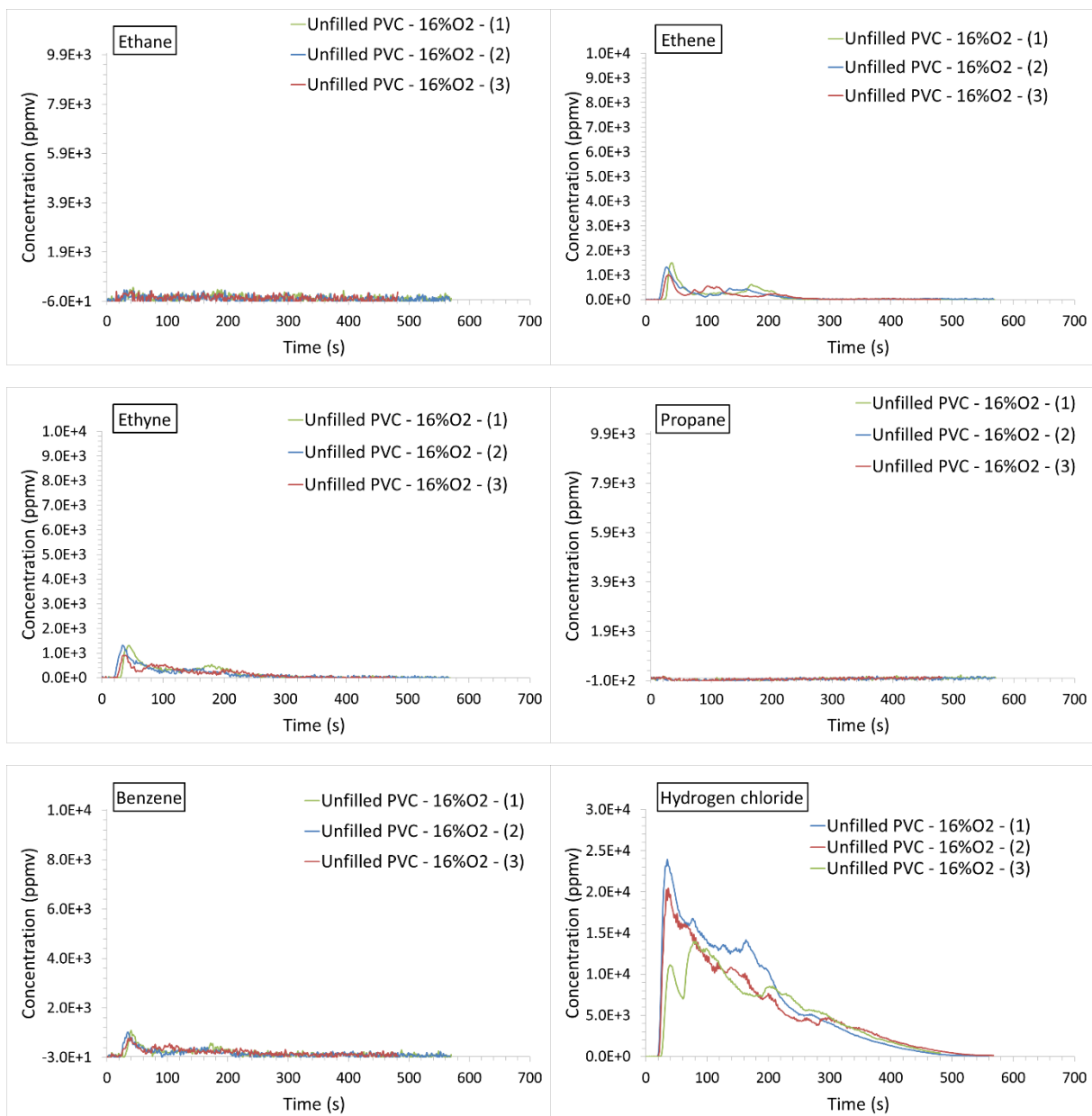
2.2.1. PMMA



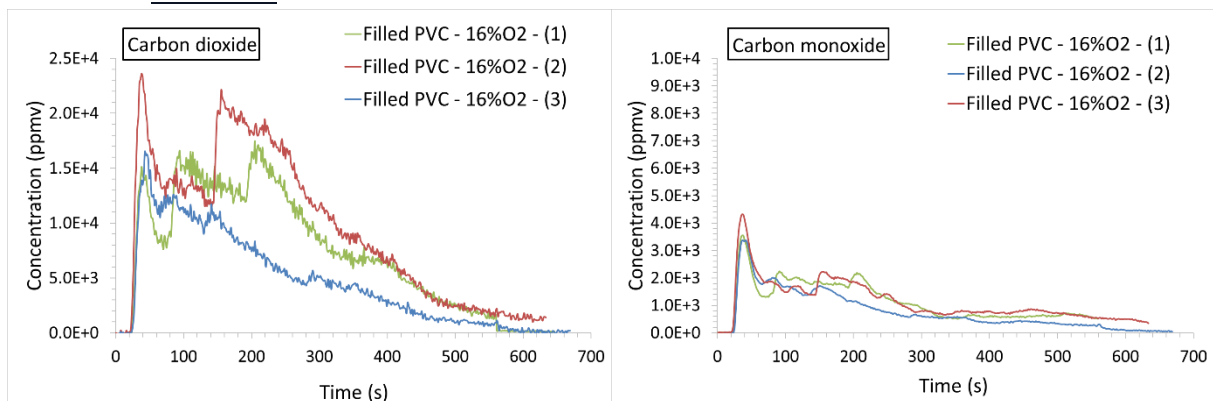


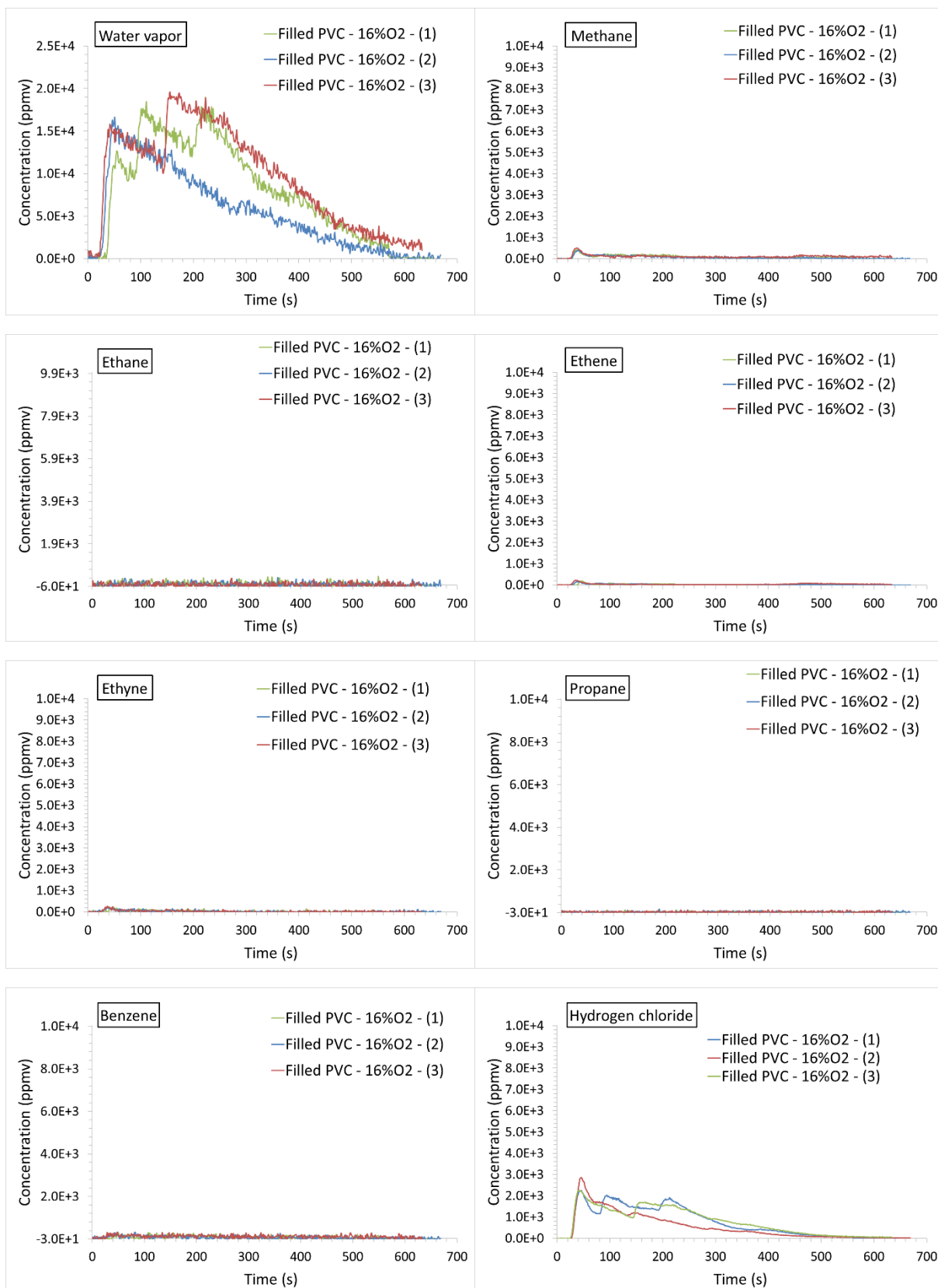
2.2.2. Unfilled PVC





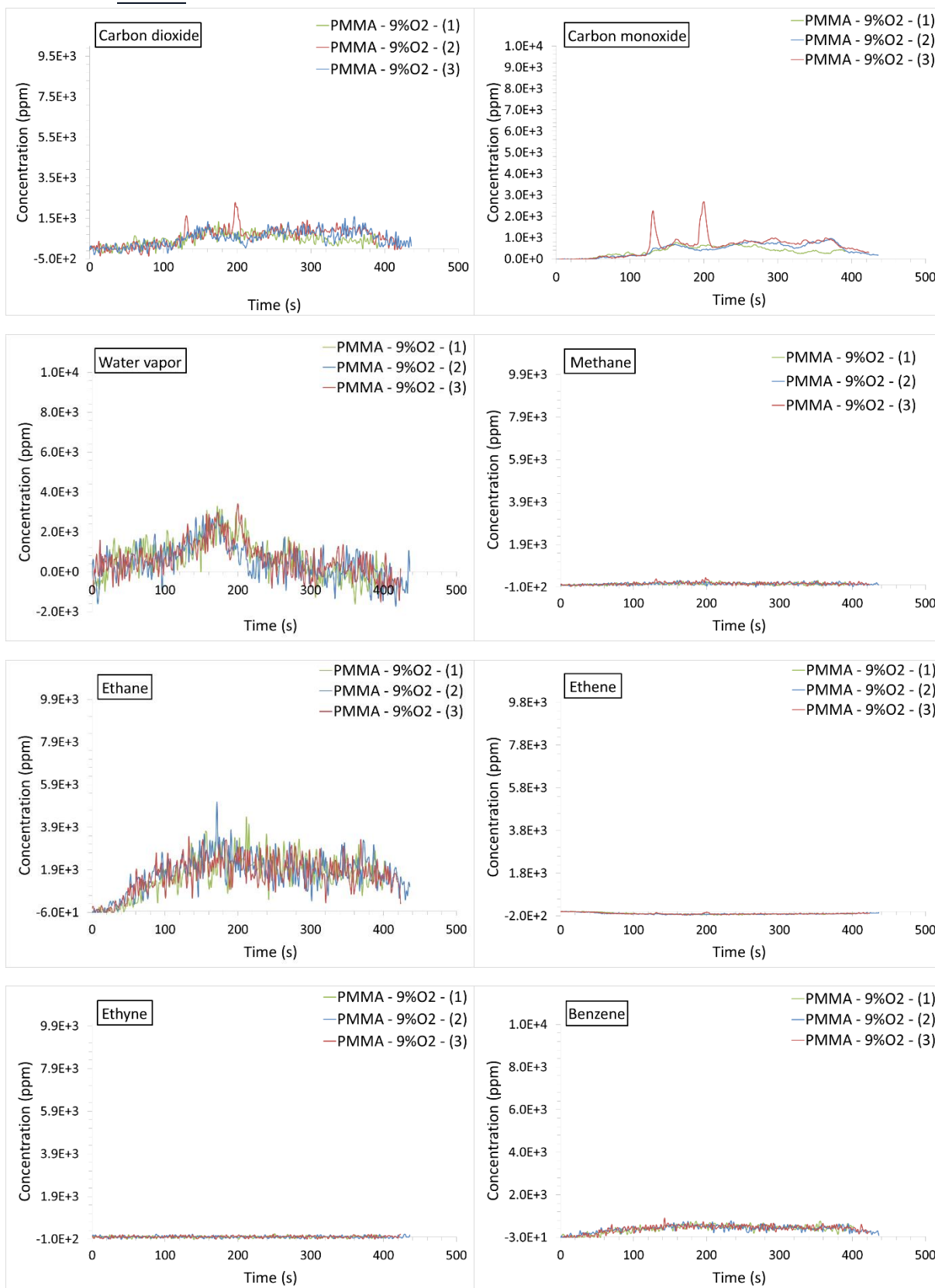
2.2.3. Filled PVC



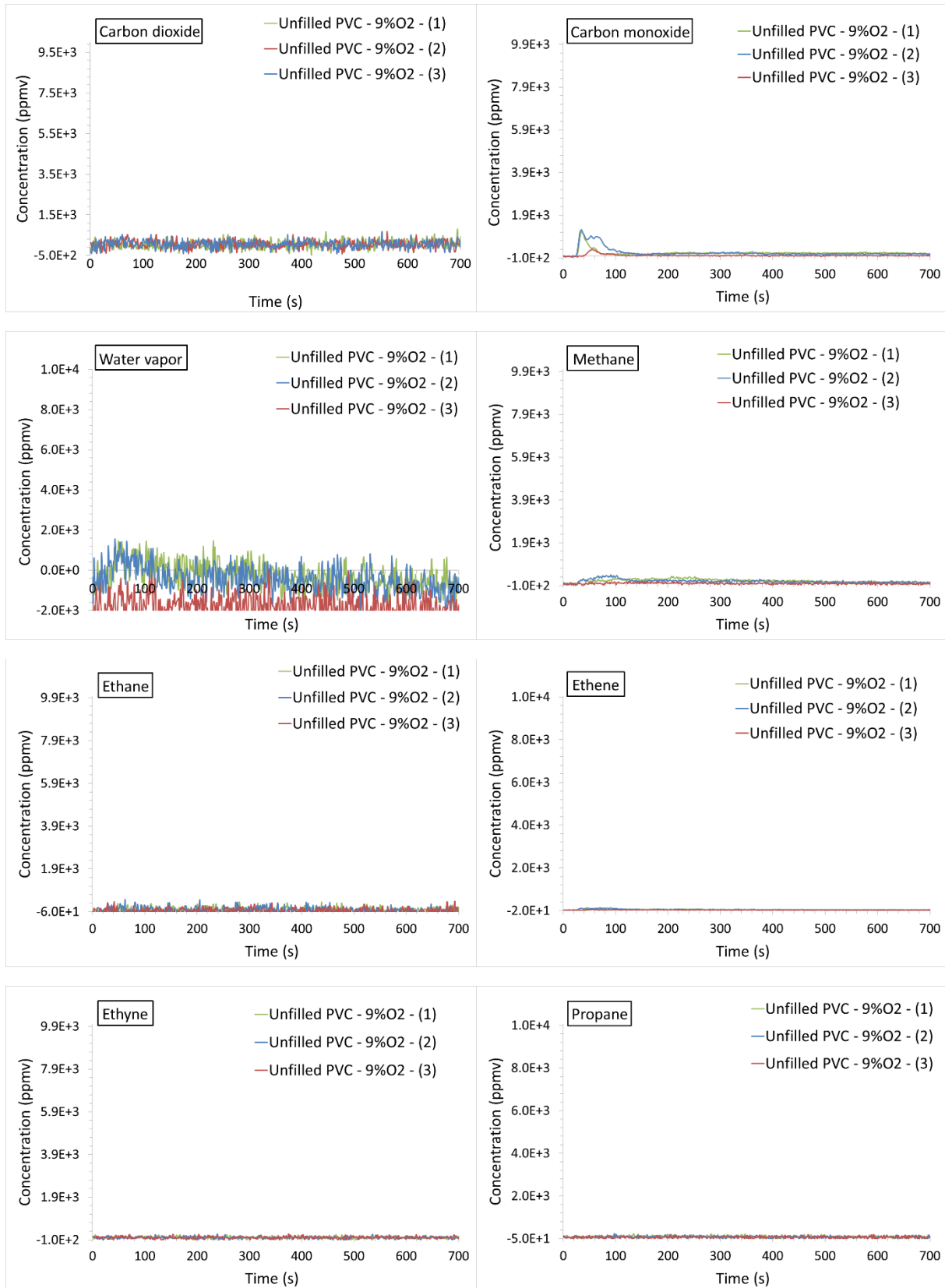


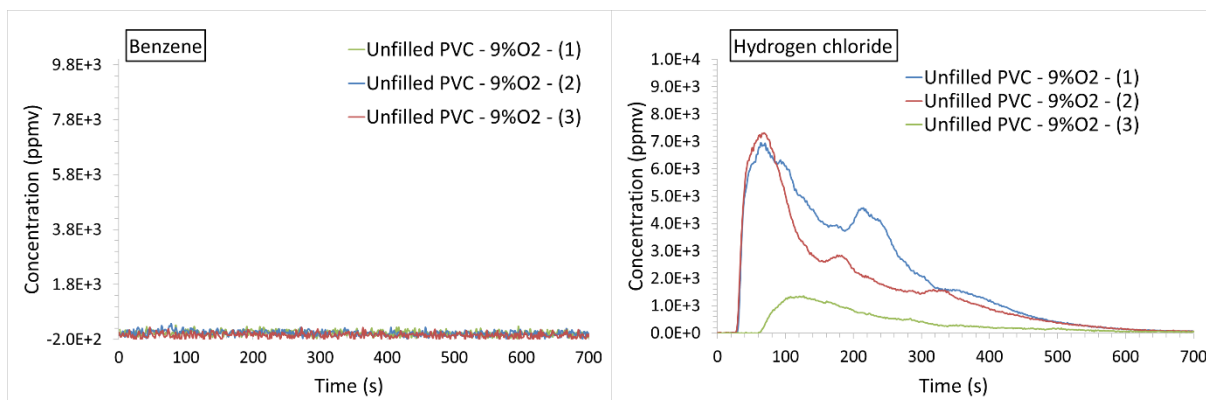
2.3. 9 vol. %O₂

2.3.1. PMMA

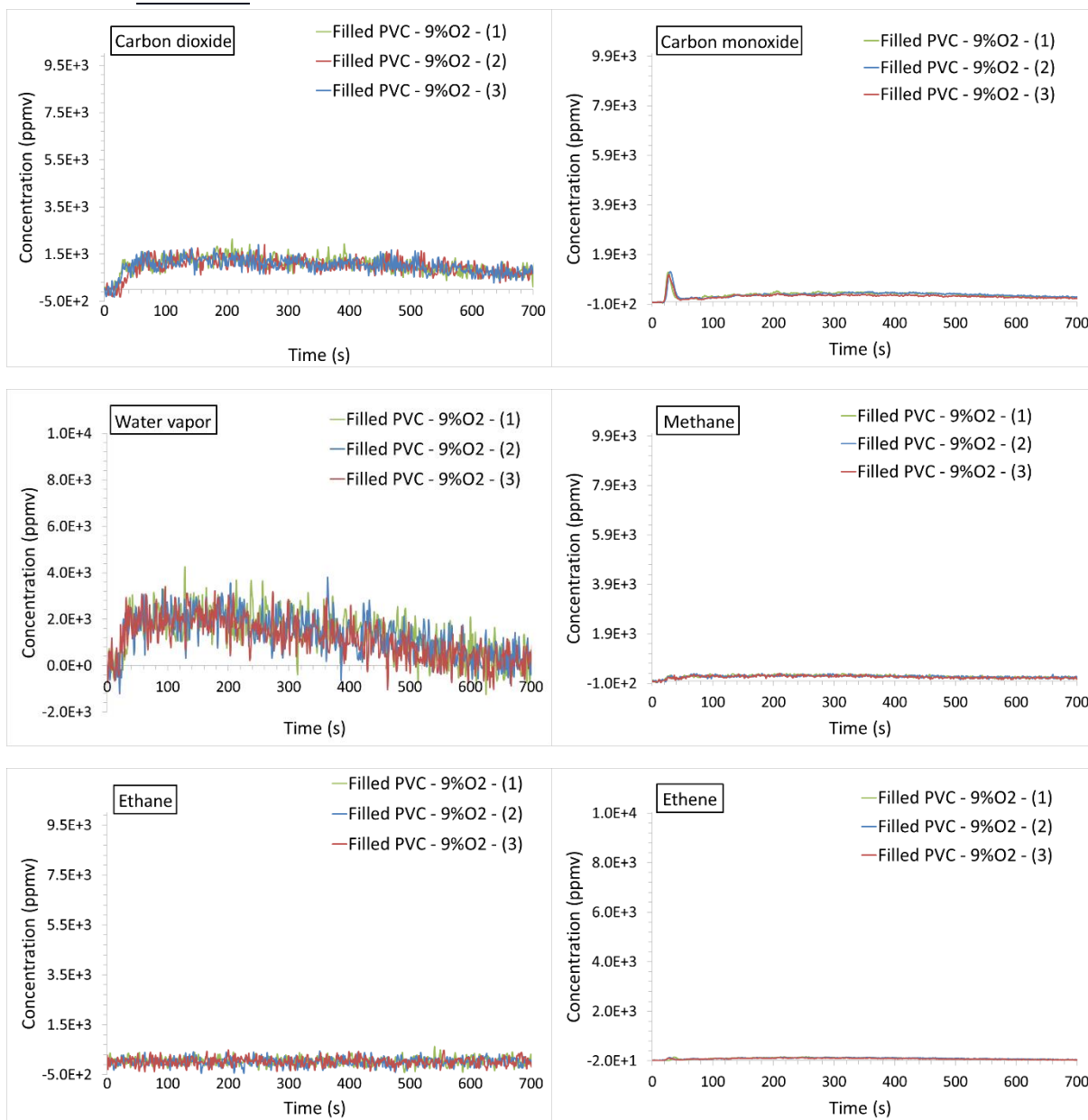


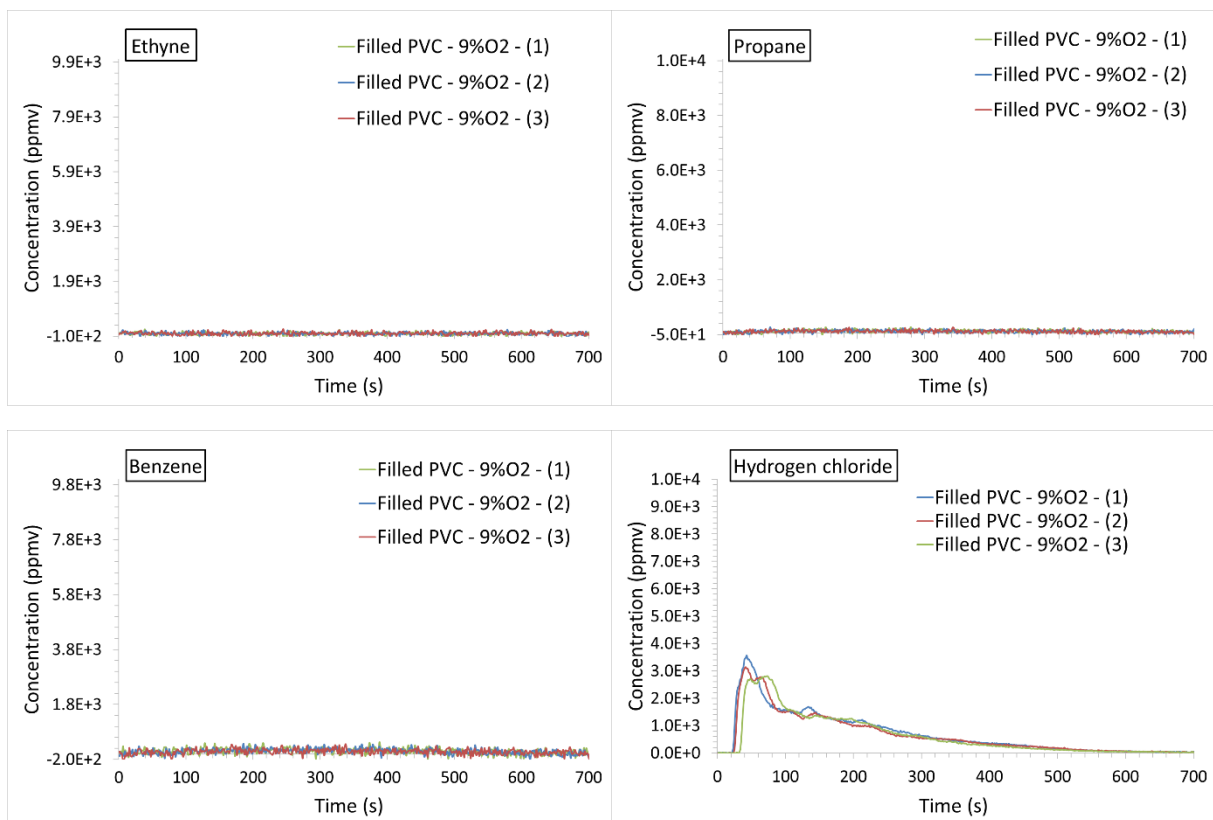
2.3.2. *Unfilled PVC*





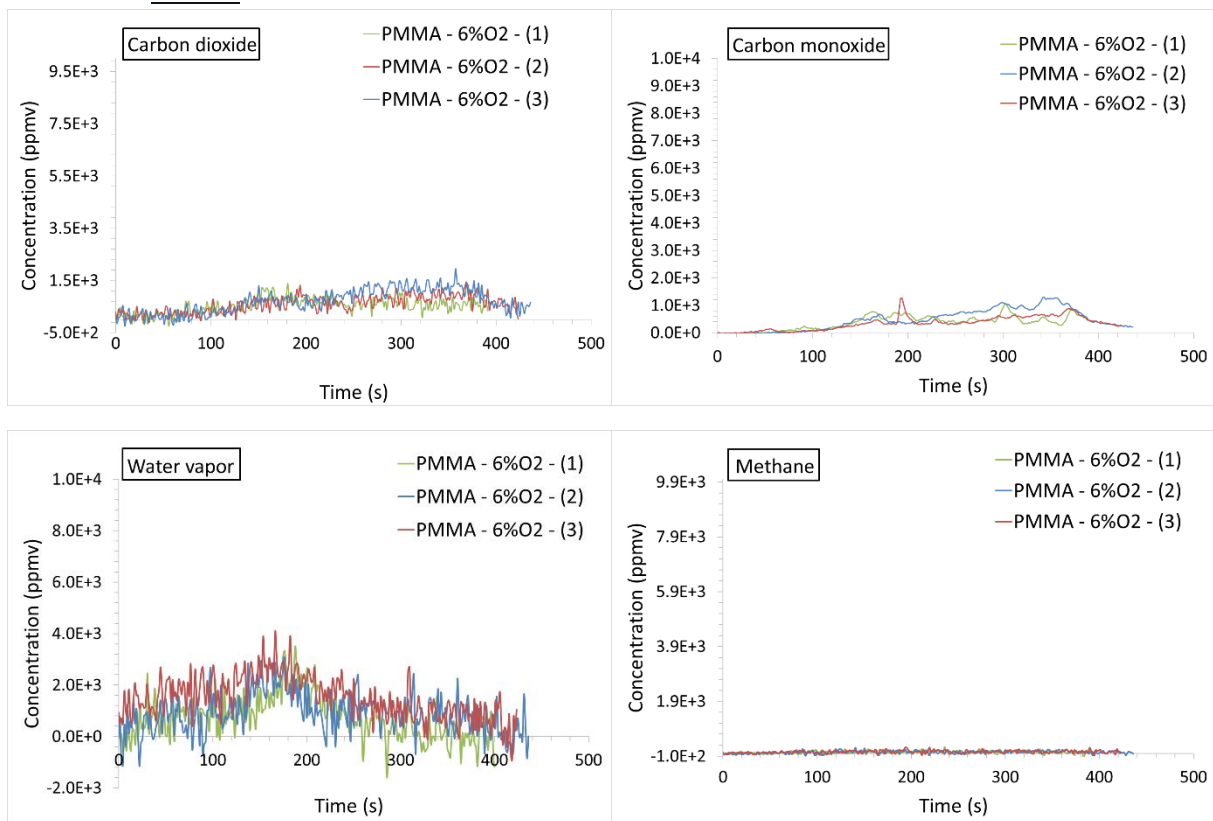
2.3.3. Filled PVC

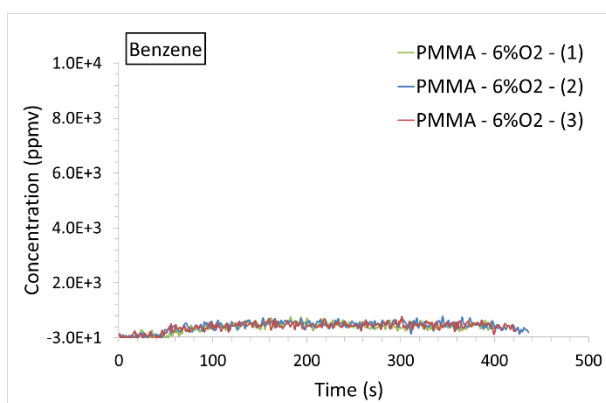
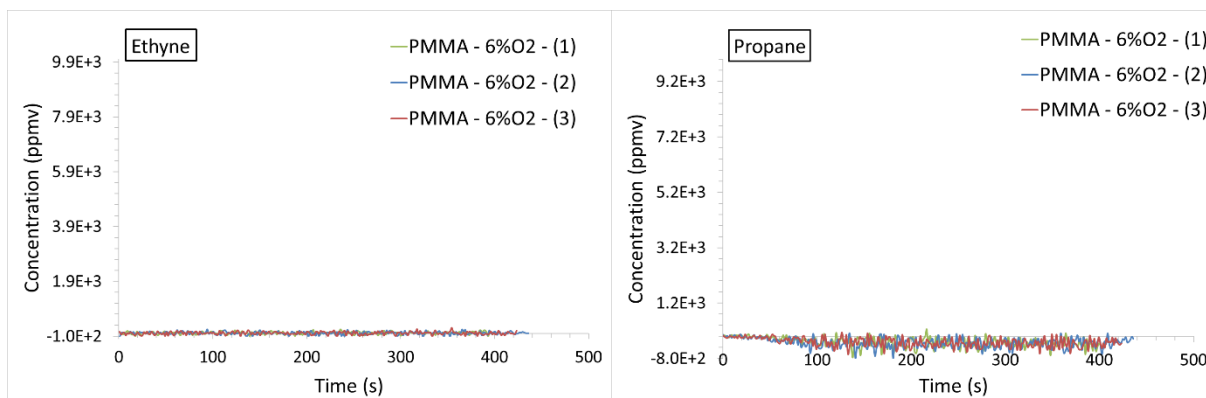
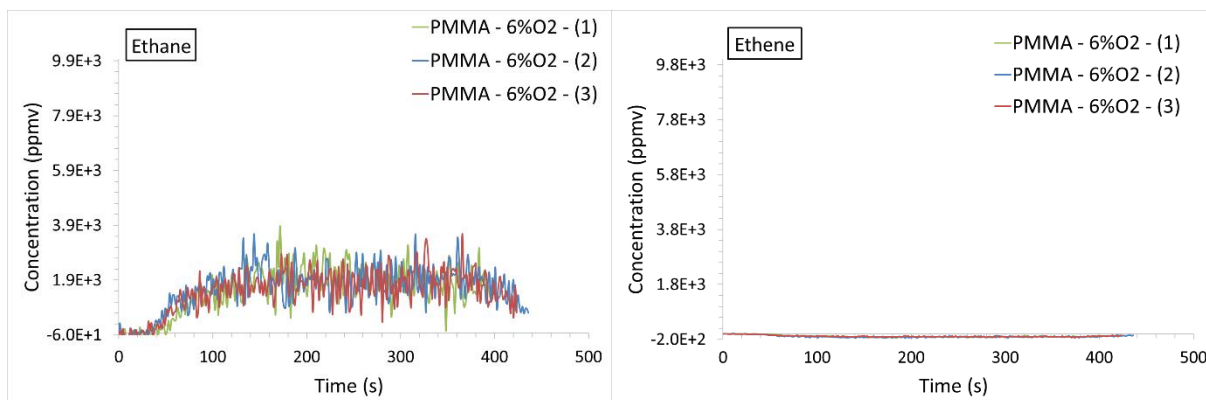




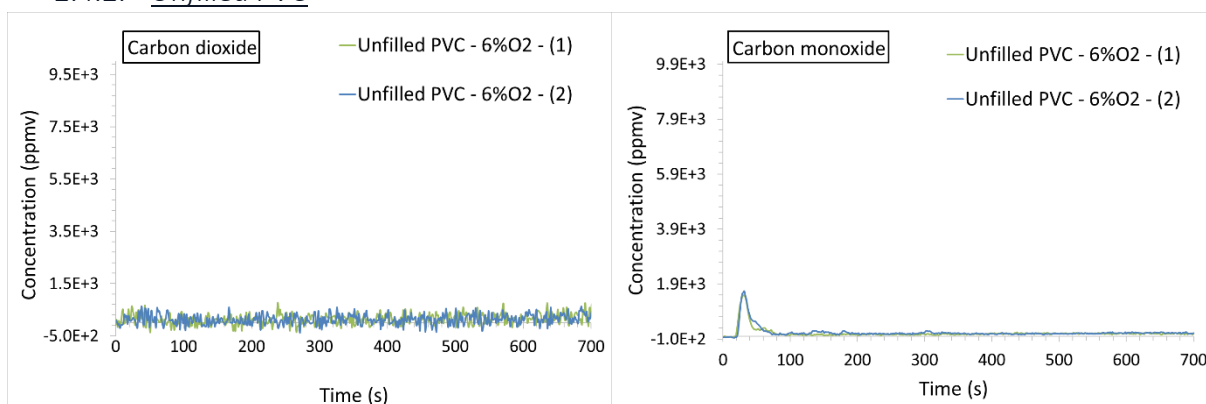
2.4. 6 vol. %O₂

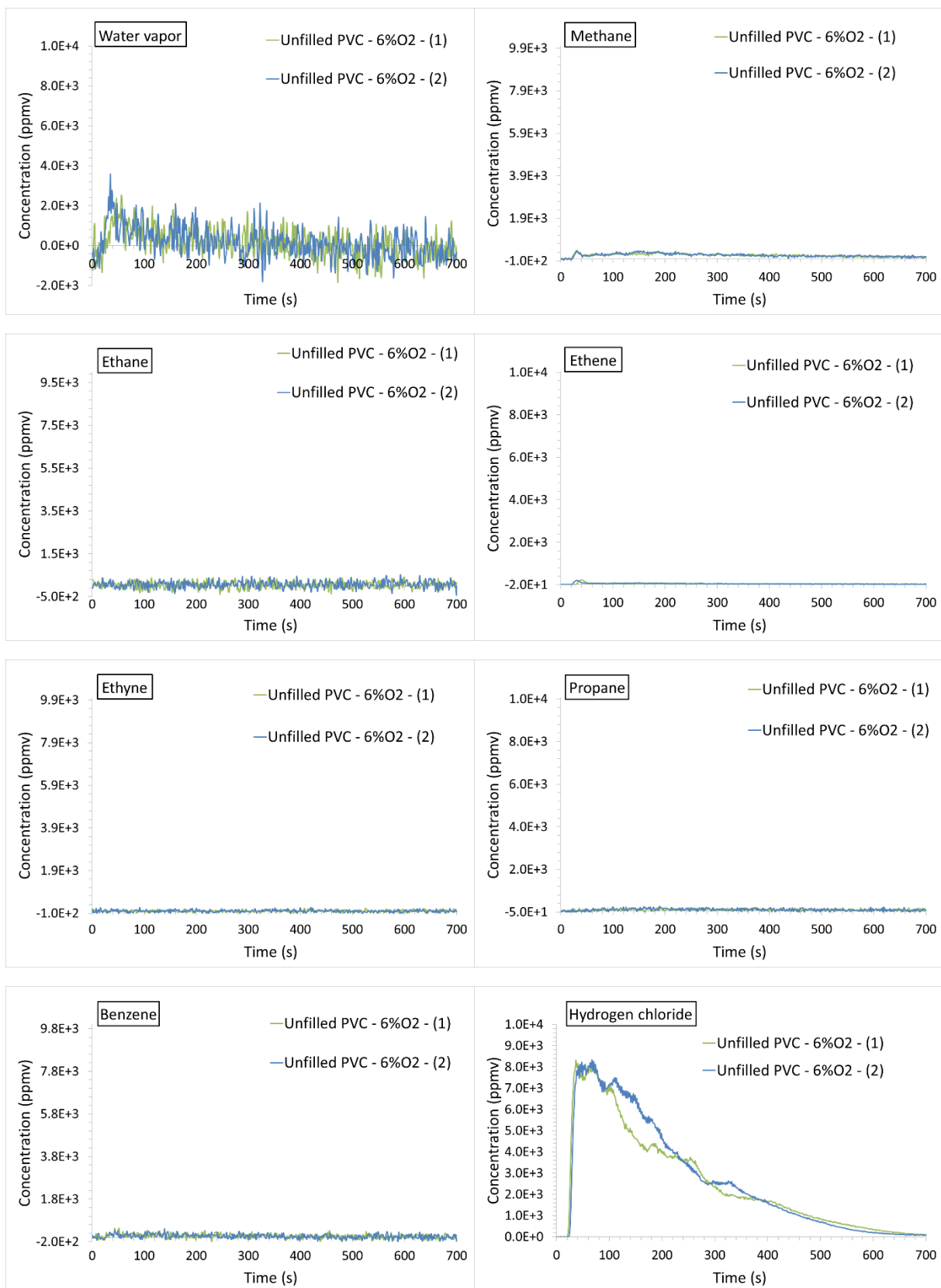
2.4.1. PMMA



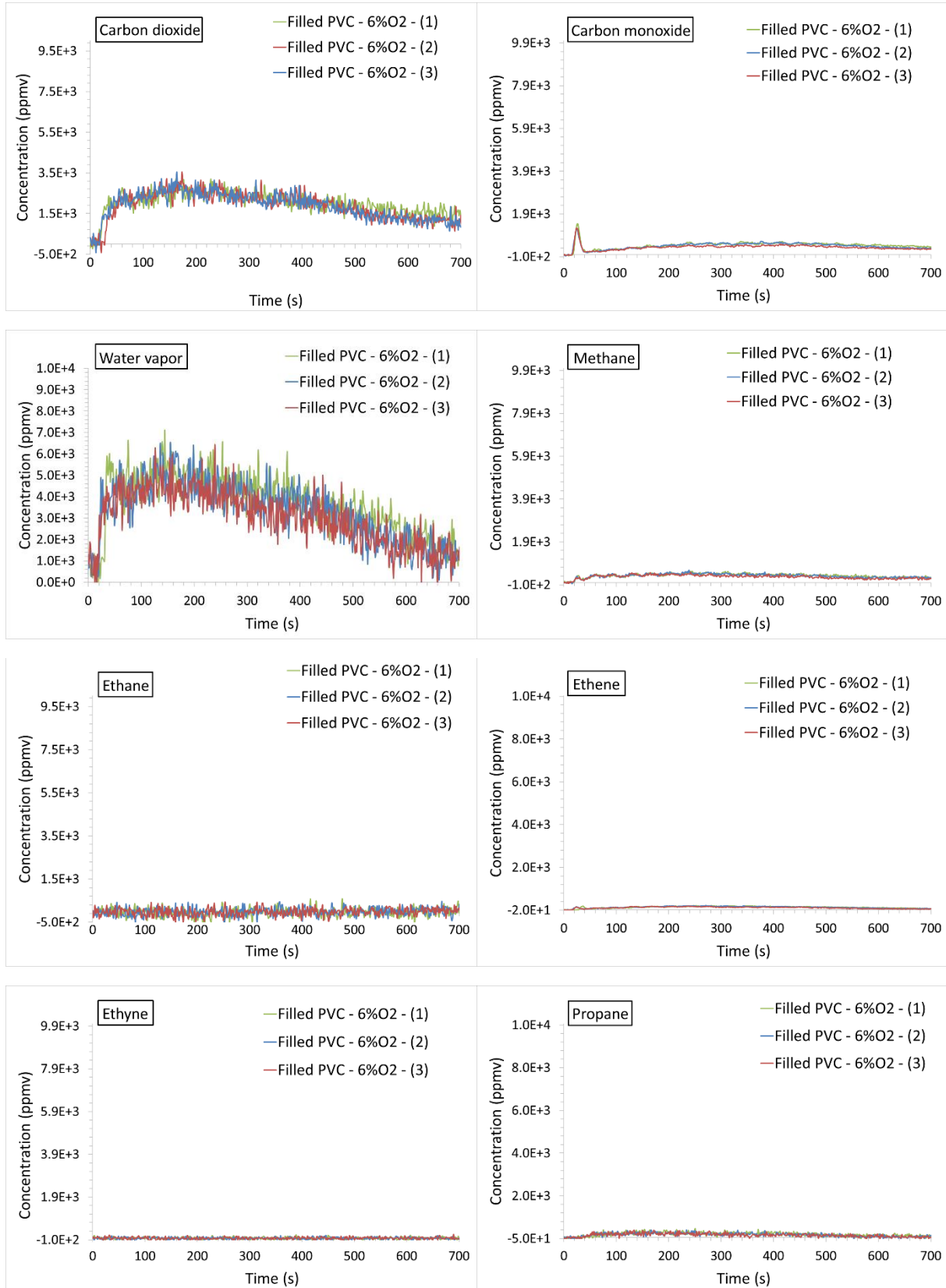


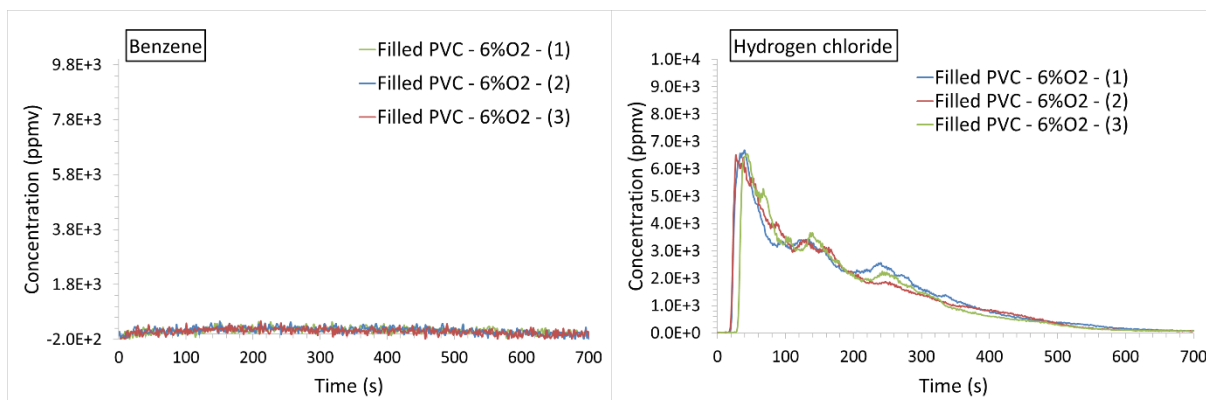
2.4.2. Unfilled PVC





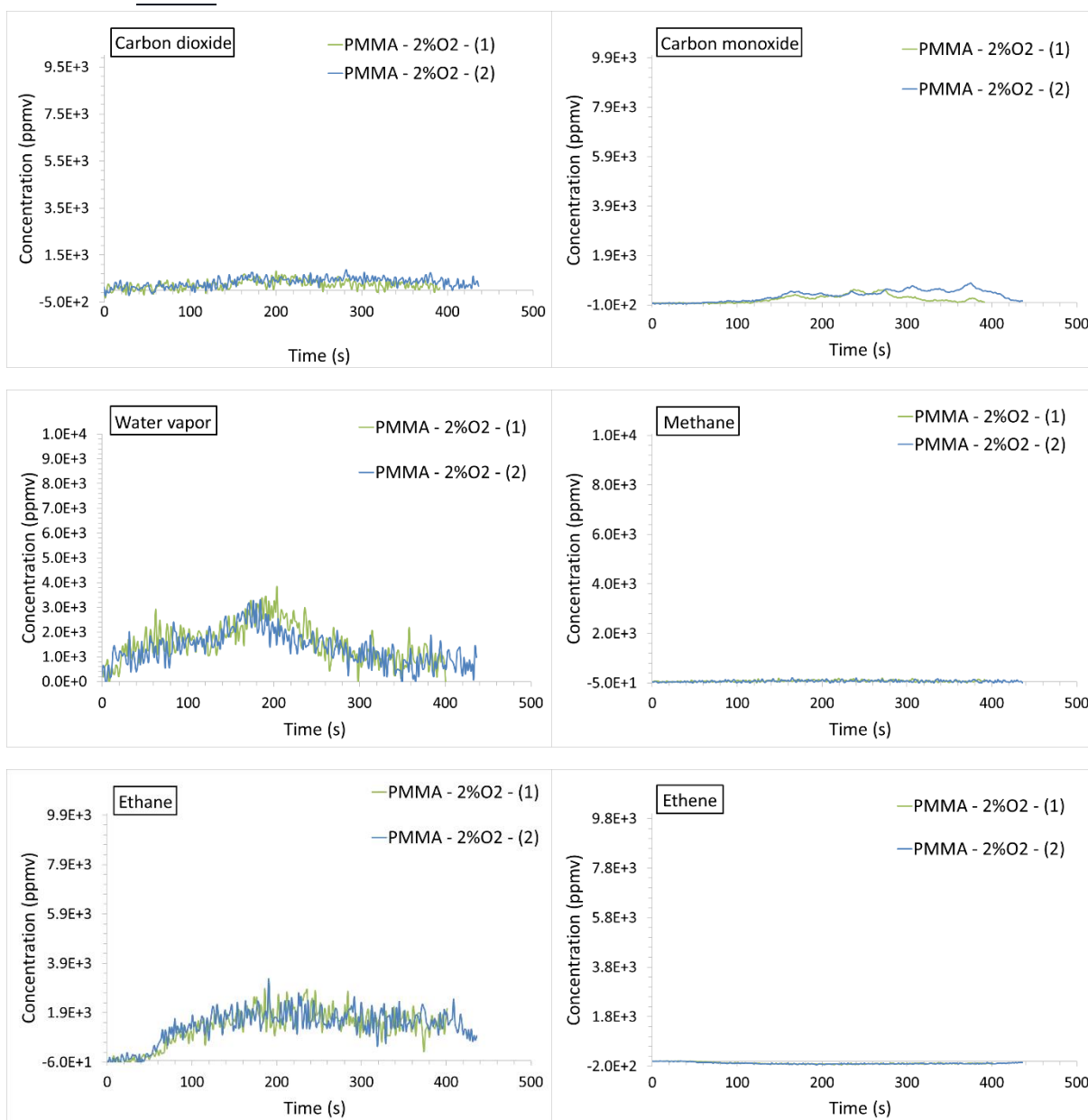
2.4.3. Filled PVC

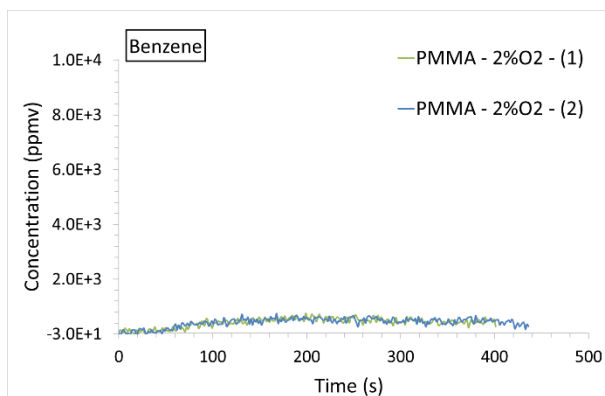
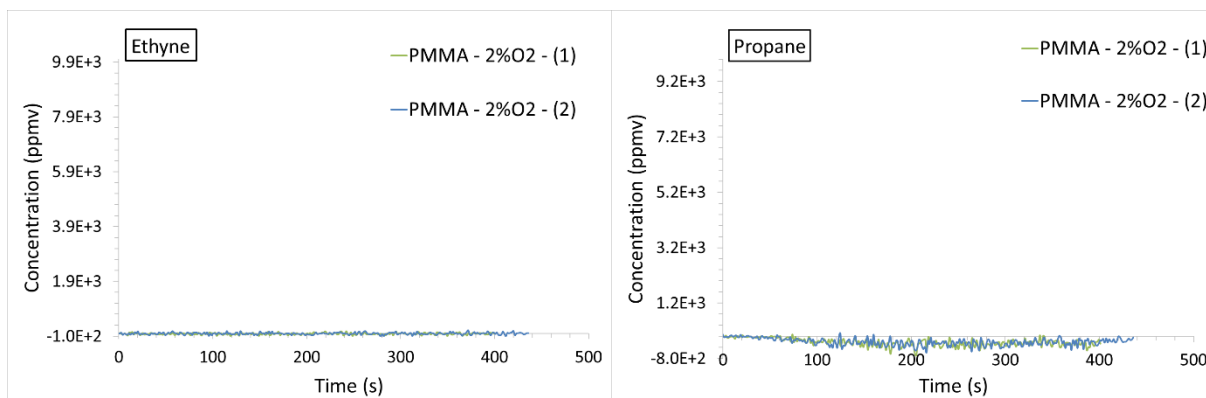




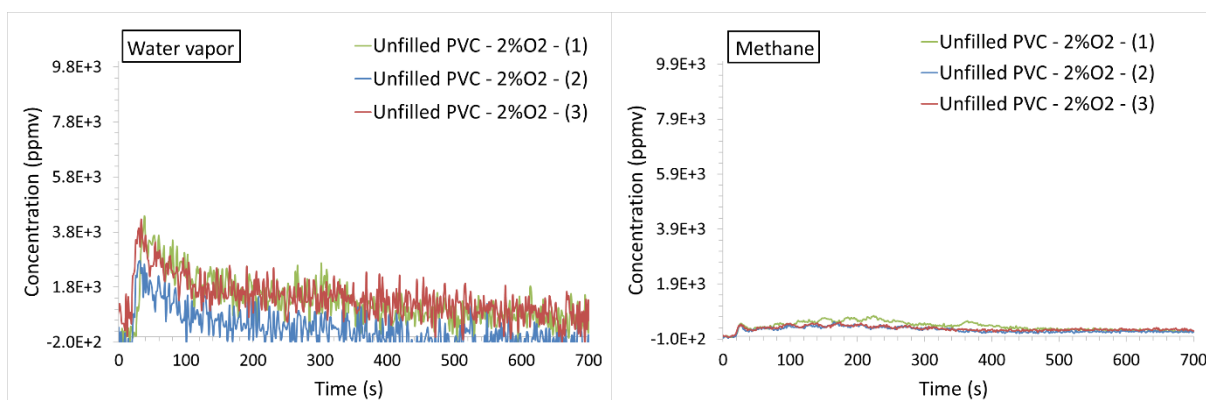
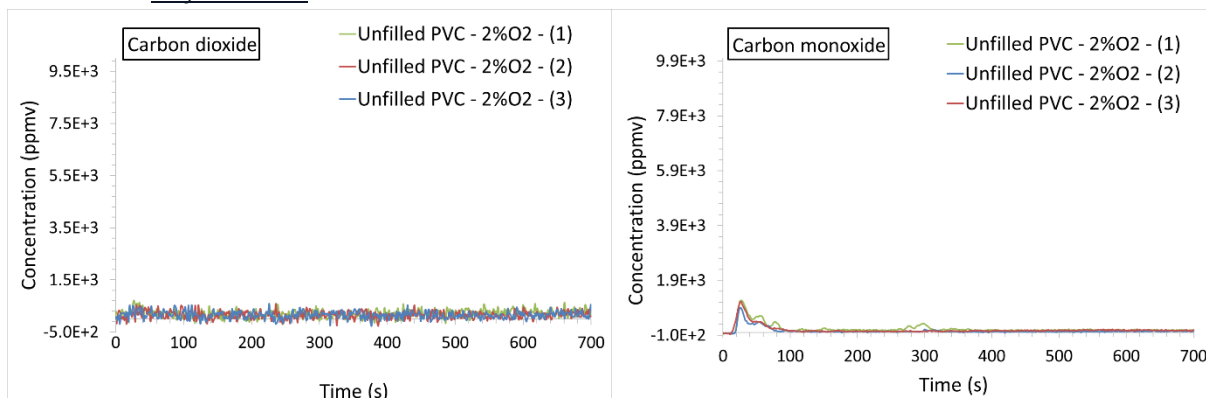
2.5. 2 vol. %O₂

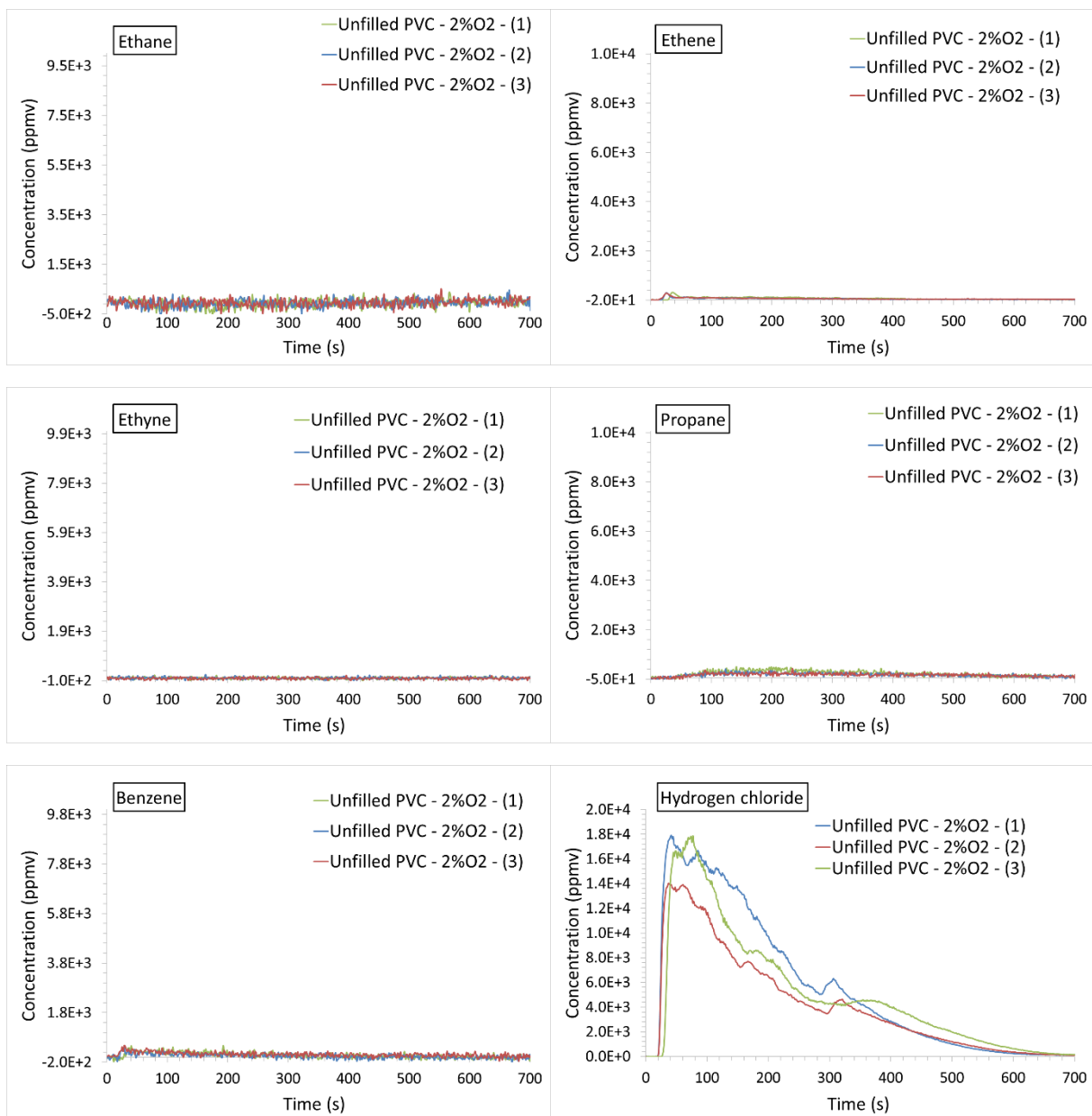
2.5.1. PMMA



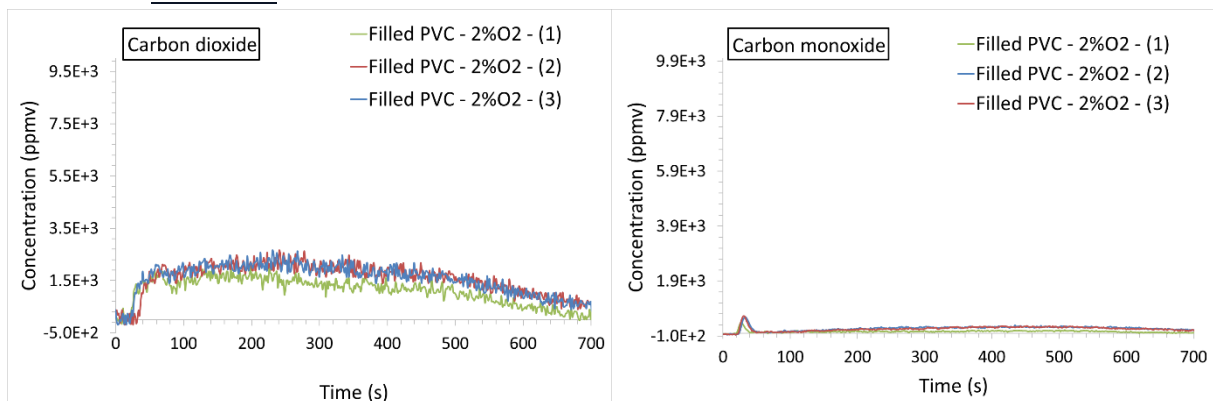


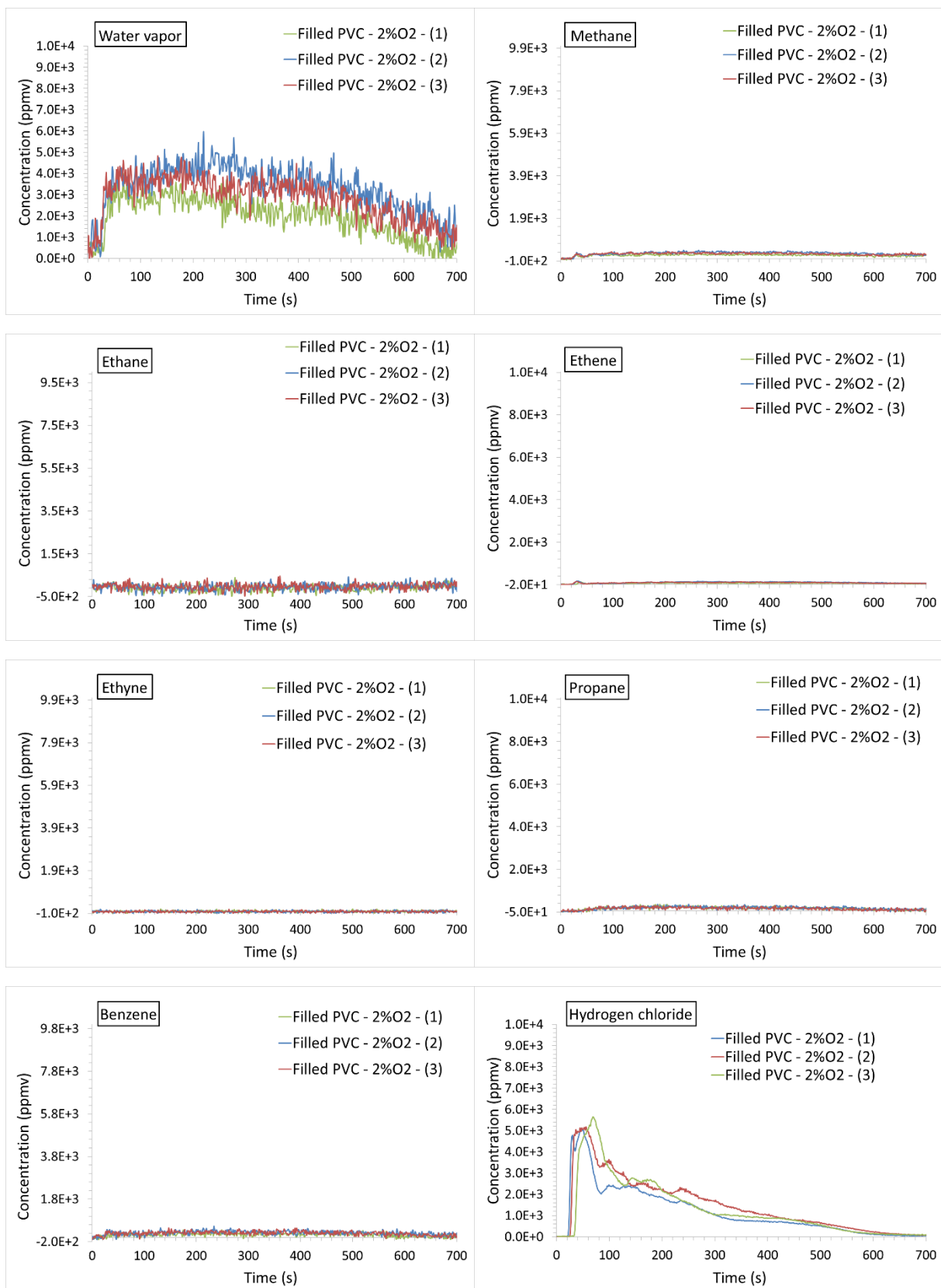
2.5.2. Unfilled PVC





2.5.3. Filled PVC

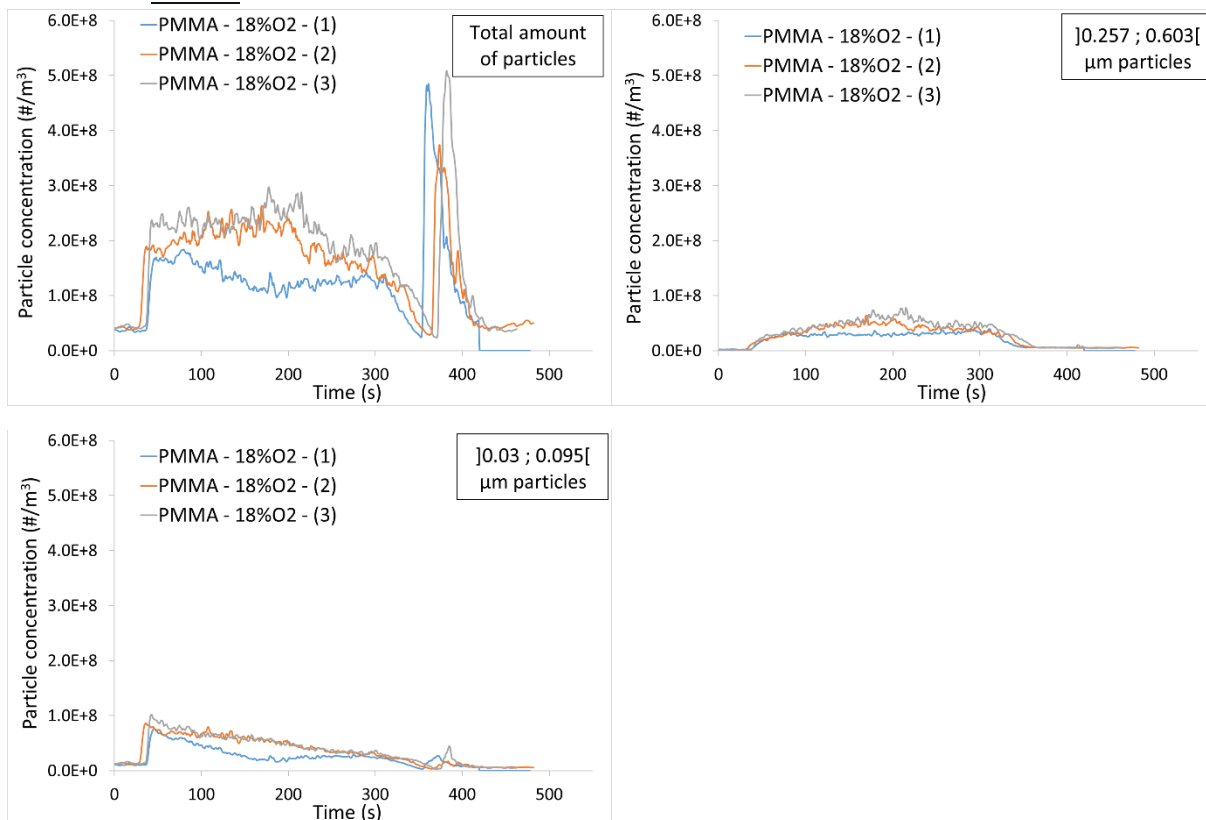




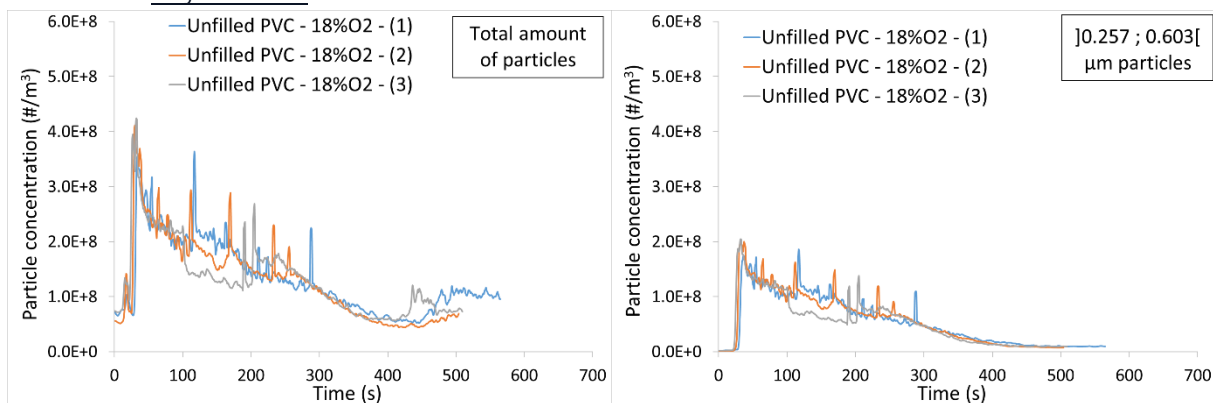
3. Aerosols

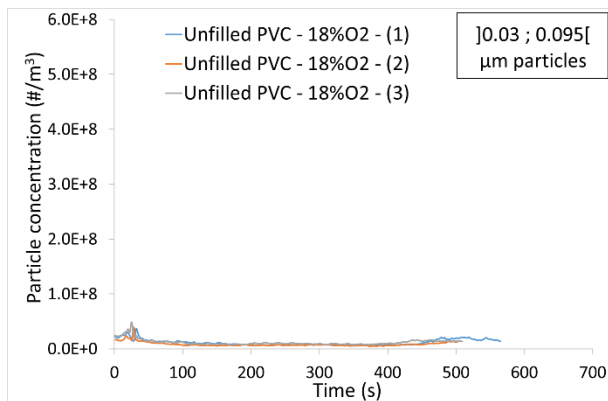
3.1. 18 vol. %O₂

3.1.1. PMMA

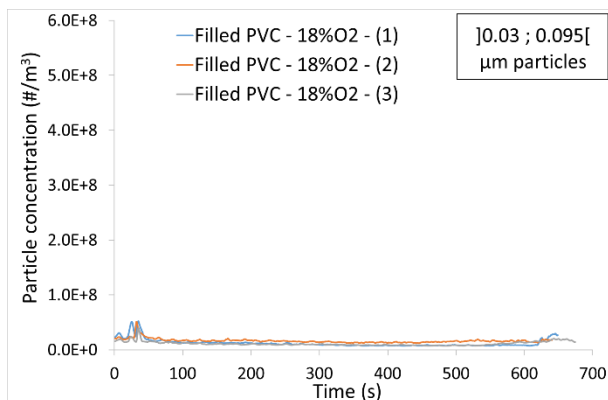
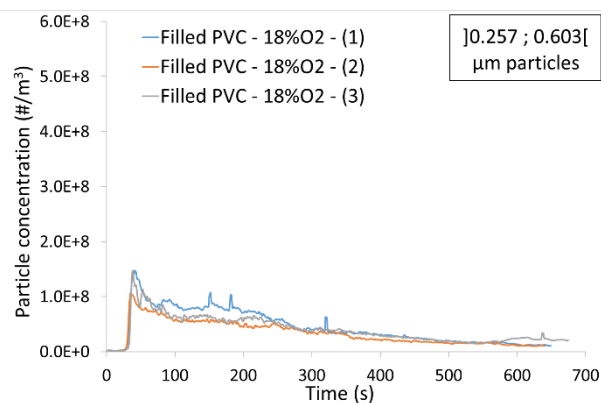
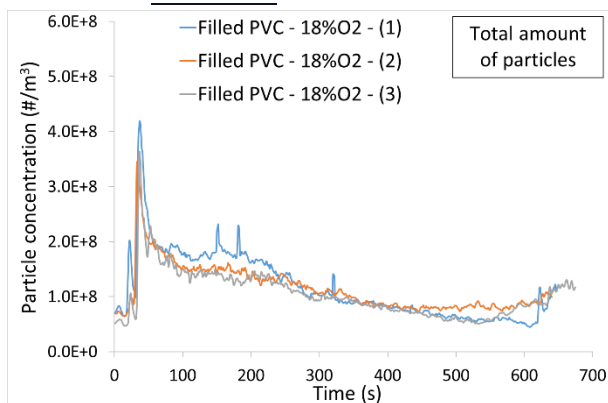


3.1.2. Unfilled PVC



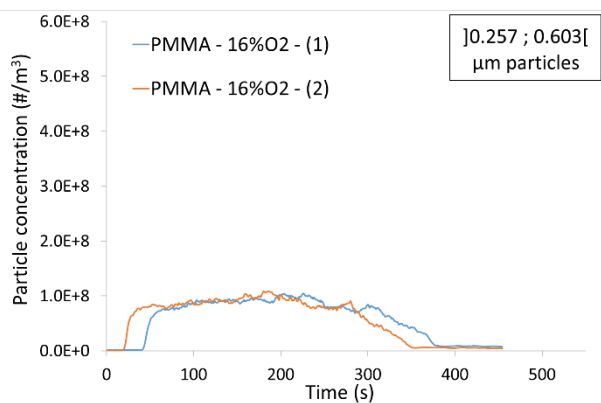
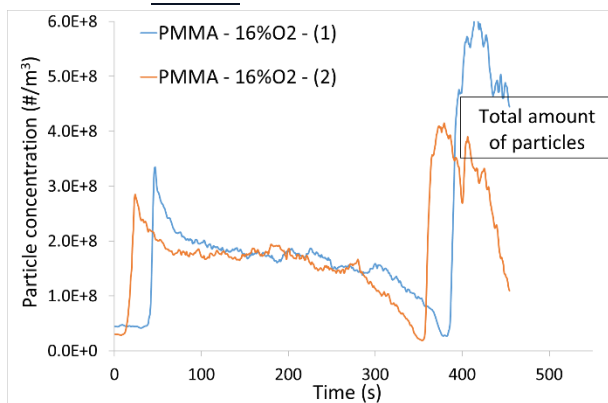


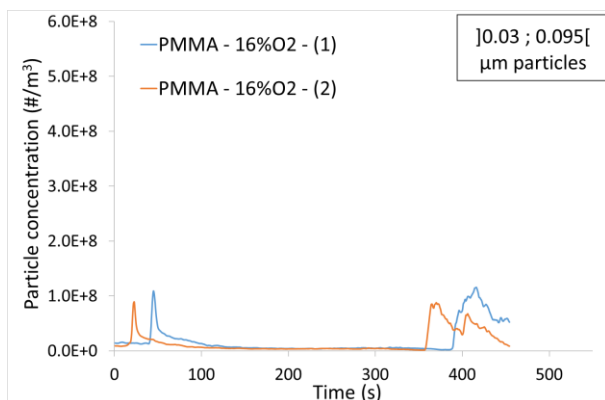
3.1.3. Filled PVC



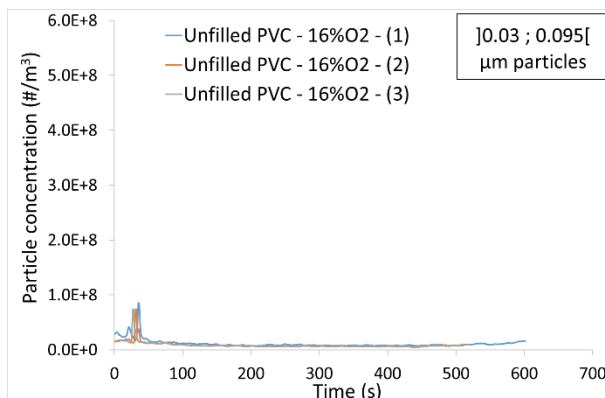
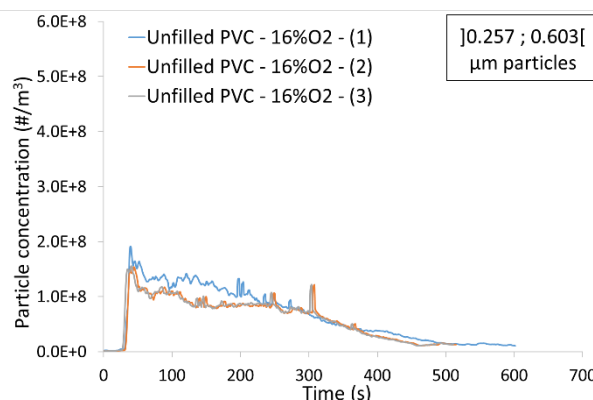
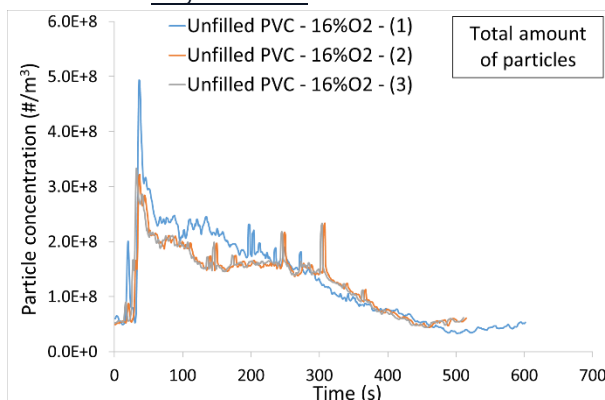
3.2. 16 vol. %O₂

3.2.1. PMMA

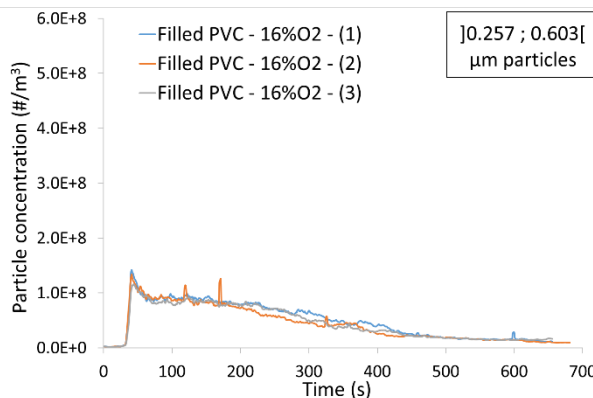
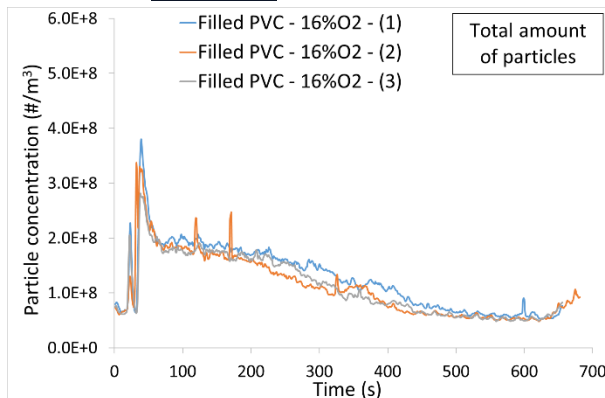


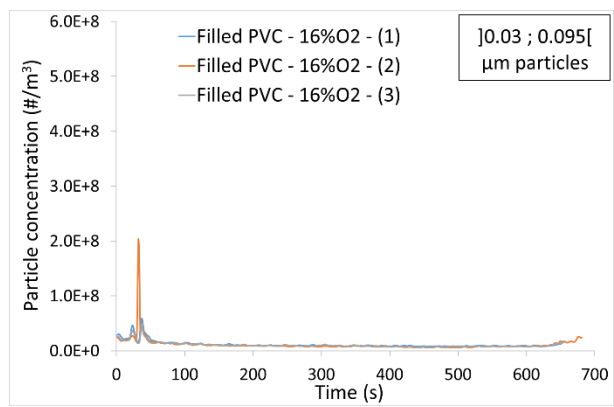


3.2.2. Unfilled PVC



3.2.3. Filled PVC





References

- [1] S. Melis and L. Audouin, "Effects of vitiation on the heat release rate in mechanically-ventilated compartment fires," *Fire Saf. Sci.*, vol. 9, pp. 931–942, 2008.
- [2] M. Subudhi, "Literature Review of Environmental Qualification of Safety-Related Electrical Cables (NUREG/CR-6384, Volume 1, Part 1)," Brookhaven National Laboratories, Upton, NY, 1996.
- [3] "Le risque incendie en milieu nucléaire," *Institut de Radioprotection et de Sûreté Nucléaire*, 2019. [Online]. Available: https://www.irsn.fr/FR/connaissances/Installations_nucleaires/incendie-risque/Pages/1-Risque-incendie-en-milieu-nucleaire.aspx#.XOWFJ4gzaUk.
- [4] F. E. Ngohang, "Combination of mass loss cone , Fourier transform infrared spectroscopy and electrical low pressure impactor to extend fire behaviour characterization of materials," PhD Thesis, Université des sciences et technologies de Lille 1, 2014.
- [5] M. R. Christy, R. V. Petrella, and Penkala J. J., "Controlled-Atmosphere Cone Calorimeter," in *Fire and Polymers II*, G. L. Nelson, Ed. 1995.
- [6] A. Witkowski, A. A. Stec, and T. R. Hull, "Thermal Decomposition of Polymeric Materials," in *SFPE Handbook of Fire Protection Engineering-5th Edition*, 2016, pp. 167–254.
- [7] R. E. Lyon, "Plastics and Rubber," in *Handbook of Building Materials for Fire Protection*, 2004, pp. 3.1-3.51.
- [8] Scharrel B. and T. R. Hull, "Development of fire retarded materials - Interpretation of cone calorimeter data," *Fire Mater.*, vol. 31, no. 5, pp. 327–354, 2007.
- [9] A. Fina and G. Camino, "Ignition mechanisms in polymers and polymer nanocomposites," *Polym. Adv. Technol.*, vol. 22, pp. 1147–1155, 2011.
- [10] R. E. Lyon and J. G. Quintiere, "Criteria for piloted ignition of combustible solids," *Combust. Flame*, vol. 151, pp. 551–559, 2007.
- [11] H. Bockhorn, A. Hornung, U. Hornung, and D. Schawaller, "Kinetic study on the thermal degradation of polypropylene and polyethylene," *J. Anal. Appl. Pyrolysis*, vol. 48, pp. 93–109, 1999.
- [12] C. Vagner, M. Cohez, H. Vahabi, and M. Ferriol, "Chimie de la combustion des polymères et ignifugation," *Techniques de l'ingénieur*. 2016.
- [13] T. Hamaide, "Polymérisation en chaîne - Mécanismes," *Techniques de l'ingénieur*. 2017.
- [14] T. Kashiwagi, A. Inaba, J. E. Brown, K. Hatada, T. Kitayama, and E. Masuda, "Effects of weak linkages on the thermal and oxidative degradation of poly(methyl methacrylates)," *Macromolecules*, vol. 8, pp. 2160–2168, 1986.
- [15] S. L. Malhotra, J. Hesse, and L.-P. Blanchard, "Thermal decomposition of polystyrene," *Polymer (Guildf.)*, vol. 16, no. 2, pp. 81–93, 1975.
- [16] C. L. Beyler and M. M. Hirschler, "Thermal decomposition of polymers," pp. 110–131.
- [17] S. Levchik and C. A. Wilkie, "Char formation," in *Fire retardancy of polymeric materials*, 2000, pp. 171–215.
- [18] D. W. Van Krevelen, "Properties of Polymers," in *Thermal Decomposition, 4th Edition*, 2009.

- [19] R. Walters and R. E. Lyon, "Calculating Polymer Flammability from Molar Group Contributions," 2001.
- [20] M. Frenklach, D. W. Clary, W. C. Gardiner, and S. E. Stein, "Detailed kinetic modeling of soot formation in shock-tube pyrolysis of acetylene," *Symp. Combust.*, vol. 20, no. 1, pp. 887–901, 1985.
- [21] J. Appel, H. Bockhorn, and M. Wulkow, "A detailed numerical study of the evolution of soot particle size distributions in laminar premixed flames," *Chemosphere*, vol. 42, no. 5–7, pp. 635–645, 2001.
- [22] A. V. Krestinin, "Polyne model of soot formation process," *Symp. Combust.*, vol. 27, no. 1, pp. 1557–1563, 1998.
- [23] J. Frenklach, M. Warnatz, "Detailed modeling of PAH profiles in a sooting low-pressure acetylene flame," *Combust. Sci. Technol.*, vol. 51, pp. 265–283, 1987.
- [24] J. a. Cole, J. D. Bittner, J. P. Longwell, and J. B. Howard, "Formation mechanisms of aromatic compounds in aliphatic flames," *Combust. Flame*, vol. 56, no. 1, pp. 51–70, 1984.
- [25] J. D. Bittner and J. B. Howard, "Composition profiles and reaction mechanisms in a near-sooting premixed benzene/oxygen/argon flame," *Symp. Combust.*, vol. 18, no. 1, pp. 1105–1116, 1981.
- [26] H. Wang and M. Frenklach, "Calculations of Rate Coefficients for the Chemically Activated Reactions of Acetylene with Vinylic and Aromatic Radicals," *J. Phys. Chem.*, vol. 98, no. 44, pp. 11465–11489, 1994.
- [27] J. a. Miller and C. F. Melius, "Kinetic and thermodynamic issues in the formation of aromatic compounds in flames of aliphatic fuels," *Combust. Flame*, vol. 91, no. 1, pp. 21–39, 1992.
- [28] W. Marinov, N. M. Castaldi, M. J. Melius, C. F. Tsang, "Aromatic and polycyclic aromatic hydrocarbon formation in a premixed propane flame," *Combust. Sci. Technol.*, vol. 128, pp. 295–342, 1997.
- [29] M. Frenklach, "Reaction mechanism of soot formation in flames," *Phys. Chem. Chem. Phys.*, vol. 4, no. 11, pp. 2028–2037, 2002.
- [30] C. F. Melius, M. E. Colvin, N. M. Marinov, W. J. Pitt, and S. M. Senkan, "Reaction mechanisms in aromatic hydrocarbon formation involving the C₅H₅ cyclopentadienyl moiety," *26th Symp. Combust.*, pp. 685–692, 1996.
- [31] M. Braun-Unkhoff, A. Chrysostomou, P. Frank, E. Gutheil, R. Lückerrath, and W. Stricker, "Experimental and numerical study on soot formation in laminar high-pressure flames," *27th Symp. Combust.*, pp. 1565–1572, 1998.
- [32] H. Frenklach, M. Wang, "Detailed modeling of soot particle nucleation and growth," *23th Symp. Combust.*, pp. 1559–1566, 1991.
- [33] J. Yon, "Caractérisation des agrégats de suie," 2010.
- [34] B. S. Haynes, H. Jander, H. Mätzing, and H. G. Wagner, "The influence of gaseous additives on the formation of soot in premixed flames," *19th Symp. Combust.*, pp. 1379–1385, 1982.
- [35] B. R. Stanmore, J. F. Brilhac, and P. Gilot, "The oxidation of soot: A review of experiments, mechanisms and models," *Carbon N. Y.*, vol. 39, no. 15, pp. 2247–2268, 2001.
- [36] I. J. Jagoda, G. Prado, and J. Lahaye, "An experimental investigation into soot formation and distribution in polymer diffusion flames," *Combust. Flame*, vol. 37, pp. 261–274, Jan. 1980.

- [37] E. Brooke and A. Yiannis, "Particulates Generated from Combustion of Polymers (Plastics)," *J. Air Waste Manage. Assoc.*, vol. 50, no. 1, pp. 94–102, 2000.
- [38] W. R. Zeng, S. F. Li, and W. K. Chow, "Review on Chemical Reactions of Burning Poly(methyl methacrylate)," *J. Fire Sci.*, vol. 20, pp. 401–433, 2002.
- [39] T. Kitayama, H. Horii, and T. Kashiwagi, "Tacticity dependence of thermal degradation of PMMAs with the same chemical structure," *Polym. Bull.*, vol. 21, no. 4, pp. 433–437, 1989.
- [40] T. Kashiwagi, A. Inaba, J. E. Brown, K. Hatada, T. Kitayama, and E. Masuda, "Effects of weak linkages on the thermal and oxidative degradation of poly(methyl methacrylate)," *Macromolecules*, vol. 19, pp. 2160–2168, 1986.
- [41] N. Grassie and G. Scott, "Polymer Degradation and Stabilization," 1985.
- [42] S. C. Moldoveanu, "Analytical Pyrolysis of Synthetic Organic Polymers," in *Techniques and Instrumentation in Analytical Chemistry, volume 25, 1st edition*, 2005.
- [43] A. Marongiu, T. Favarelli, G. Bozzano, M. Dente, and E. Ranzi, "Thermal degradation of poly(vinyl chloride)," *J. Anal. Appl. Pyrolysis*, vol. 70, pp. 519–553, 2003.
- [44] W. D. Wolley, "Decomposition Products of PVC for Studies of Fires," *Br. Polym. J.*, vol. 3, no. 4, pp. 186–193, 1971.
- [45] W. D. Wolley, "Studies of the dehydrochlorination of PVC in nitrogen and air," 1974.
- [46] F. Laoutid, L. Bonnaud, M. Alexandre, J.-M. Lopez-Cuesta, and P. Dubois, "New prospects in flame retardants polymer materials: from fundamentals to nanocomposites," *Mater. Sci. Eng.*, vol. 63, pp. 100–125, 2009.
- [47] A. Tewarson, "Generation of heat and chemical compounds in fires," in *SFPE Handbook of Fire Protection Engineering*, USA, 2002.
- [48] Association Française de Normalisation (AFNOR), *NF - ISO 19706:2011-11 : Lignes directrices pour l'évaluation des dangers du feu pour les personnes*. 2011.
- [49] A. Tewarson, "Flammability Parameters of Materials: Ignition, Combustion, and Fire Propagation," *J. Fire Sci.*, vol. 12, no. 4, pp. 329–356, 1994.
- [50] A. Tewarson, F. Jiang, and T. Morikawa, "Ventilation-controlled combustion of polymers," *Combust. Flame*, vol. 95, no. 1–2, pp. 151–169, Oct. 1993.
- [51] M. Khan, A. Tewarson, and M. Chaos, "Combustion Characteristics of Materials and Generation of Fire Products," in *SFPE Handbook of Fire Protection Engineering-5th Edition*, M. J. Hurley, Ed. 2016, pp. 1143–1232.
- [52] A. Tewarson and R. F. Pion, "Flammability of Plastics. I : Burning Intensity," *Combust. Flame*, vol. 26, pp. 85–103, 1976.
- [53] M. J. Peatross and C. L. Beyler, "Ventilation Effects On Compartment Fire Characterization," *Fire Saf. Sci.*, vol. 5, pp. 403–414, 1997.
- [54] A. Tewarson, J. L. Lee, and R. F. Pion, "The influence of oxygen concentration on fuel parameters for fire modeling," *Eighteenth Symp. Combust.*, vol. 18, no. 1, pp. 563–570, 1981.
- [55] G. Santo and F. Tamanini, "Influence of oxygen depletion on the radiative properties of PMMA flames," in *Eighteenth symposium (International) on Combustion*, 1981.
- [56] G. Mulholland, W. Twilley, V. Babrauskas, M. Janssens, and S. Yusa, "The Effect of Oxygen

- Concentration on CO and Smoke Produced by Flames,” in *Proceeding of the Third International Symposium of Fire Safety Science*, 1991, pp. 585–594.
- [57] A. Tewarson, Jiang F.H., and T. Morikawa, “Ventilation-controlled combustion of polymers,” *Combust. Flame*, vol. 95, pp. 151–159, 1993.
 - [58] J. Hietaniemi, R. Kallonen, and E. Mikkola, “Burning Characteristics of Selected Substances : Production of Heat, Smoke and Chemical Species,” *Fire Mater.*, vol. 185, pp. 171–185, 1999.
 - [59] S. Brohez, G. Marlair, and C. Delvosalle, “The effect of oxygen concentration on CO and soot yields in fires,” *Fire Mater.*, vol. 32, pp. 141–158, 2008.
 - [60] D. M. Marquis, E. Guillaume, and A. Camillo, “Effects of oxygen availability on the combustion behaviour of materials in a controlled atmosphere cone calorimeter,” *Fire Saf. Sci. - Proc. 11th Int. Symp.*, 2014.
 - [61] D. Alibert, “Effet de la sous-oxygénation sur les paramètres de combustion,” Aix-Marseille Université, 2017.
 - [62] C. Fourneau, C. Delvosalle, H. Breulet, and S. Brohez, “Study of Under-Ventilated Burning Characteristics of Materials with the Cone Calorimeter,” *Chem. Eng. Trans.*, vol. 31, pp. 871–876, 2013.
 - [63] D. Marquis, E. Guillaume, and A. Camillo, “Effects of oxygen availability on the combustion behaviour of materials in a controlled atmosphere cone calorimeter,” in *Fire Safety Science - Proceedings of the 11th international symposium*, 2014, pp. 138–151.
 - [64] R. Hull, “Bench-scale generation of fire effluents,” in *Fire Toxicity*, A. A. Stec and R. Hull, Eds. Woodhead Publishing in Materials, 2010, pp. 424–460.
 - [65] R. E. Lyon and R. N. Walters, “Pyrolysis Combustion Flow Calorimetry,” *J. Anal. Appl. Pyrolysis*, vol. 71, pp. 27–46, 2004.
 - [66] “ASTM E2257-17, Standard Test Method for Room Fire Test of Wall and Ceiling Materials and Assemblies.” ASTM International, West Conshohocken, PA, 2017.
 - [67] L. Audouin, L. Rigollet, H. Prétrel, W. Le Saux, and M. Röwekamp, “OECD PRISME project : Fires in confined and ventilated nuclear-type multi-compartments - Overview and main experimental results,” *Fire Saf. J.*, vol. 62, pp. 80–101, 2013.
 - [68] G. Marlair and C. Cwiklinski, “Large scale testing in the INERIS fire gallery : a major fires involving chemicals,” in *Workshop CEE*, 1993, pp. 301–309.
 - [69] M. Janssens, “Calorimetry,” in *SFPE Handbook of Fire Protection Engineering-5th Edition*, M. J. Hurley, Ed. Springer, 2016, pp. 905–951.
 - [70] “ISO 12136:2011(E), Reaction to fire tests — Measurement of material properties using a fire propagation apparatus.” International Standard, 2011.
 - [71] ASTM International, “ASTM E2058-13a, Standard Test Methods for Measurement of Material Flammability Using a Fire Propagation Apparatus (FPA).” West Conshohocken, PA, 2013.
 - [72] ASTM International, “ASTM E1354-17, Standard Test Method for Heat and Visible Smoke Release Rates for Materials and Products Using an Oxygen Consumption Calorimeter.” West Conshohocken, PA, 2017.
 - [73] “NF P92-190-1, NF ISO 5660-1, Reaction-to-fire tests - Heat release, smoke production and mass loss rate - Part 1: Heat release rate (cone calorimeter method) and smoke production rate (dynamic measurement).” National Standards, 2015.

- [74] D. Marquis, E. Guillaume, and D. Lesenechal, "Accuracy (trueness and precision) of cone calorimeter tests with and without a vitiated air enclosure," *Procedia Eng.*, vol. 62, pp. 103–119, 2013.
- [75] V. Babrauskas, W. Twilley, M. Janssens, and S. Yusa, "A Cone Calorimeter for Controlled Atmosphere Studies," *Fire Mater.*, vol. 16, p. 37, 1992.
- [76] N. F. Bal, H. Biteau, G. Rein, and P. Girods, "Comparison of Pyrolysis Behavior Results between the Cone Calorimeter and the Fire Propagation Apparatus Heat Sources," in *10th International Symposium on Fire Safety Science*, 2011, pp. 889–901.
- [77] "ISO 13927, Plastics - Simple heat release test using a conical radiant heater and a thermopile detector." European Standard, 2015.
- [78] M. Dietenberger, "HRR upgrade to mass loss calorimeter and modified Schlyter test for FR wood," in *Proceedings of the Fire and Materials 2013 Conference*, 2013.
- [79] E. E. Smith, "Heat Release Rate Calorimetry," in *Fire Technology*, vol.32, 1996, pp. 333–347.
- [80] W. M. Thornton, "The relation of oxygen to the heat of combustion of organic compounds," *Philos. Mag. J. Sci.*, vol. 33, pp. 196–203, 1917.
- [81] W. J. Parker, "An investigation of the Fire Environment in the ASTM E 84 Tunnel Test," in *National Bureau of Standards*, Washington DC, 1977.
- [82] C. Huggett, "Estimation of Rate of Heat Release by Means of Oxygen Consumption Measurements," *Fire Mater*, vol. 4, pp. 61–65, 1980.
- [83] P. W.J., "Calculations of the heat release rate by oxygen consumption for various applications," NBSIR 81-2427-1, 1982.
- [84] M. L. Janssens, "Measuring rate of heat release by oxygen consumption," *Fire Technol.*, vol. 27, no. 3, pp. 234–249, 1991.
- [85] I. Caré, "Mesures locales de la vitesse d'un fluide," *Techniques de l'ingénieur*, 2013.
- [86] F. E. Ngohang, G. Fontaine, L. Gay, and S. Bourbigot, "Smoke composition using MLC/FTIR/ELPI: Application to flame retarded ethylene vinyl acetate," *Polym. Degrad. Stab.*, vol. 115, pp. 89–109, May 2015.
- [87] F.-X. Ouf, "Caractérisation des aérosols émis lors d'un incendie," Faculté des Sciences et Techniques de Rouen, 2006.
- [88] Dekati Ltd., "Dekati Diluter User Manual," Tampere, Finland, 2010.
- [89] Dekati Ltd., "Dekati FPS Manual," Kangasala, Finland, 2015.
- [90] F. Hewitt, A. Witkowski, B. Girardin, and F. Michael, "Development of an anaerobic pyrolysis model for fire retardant cable sheathing materials," *Polym. Degrad. Stab.*, vol. 113, pp. 208–217, 2015.
- [91] J.-L. Vignes, "Polychlorure de vinyle," *Société Chimique de France*, 2017. .
- [92] C. Strelt, P. Wobrauschek, and P. Kregasmer, "X-ray Fluorescence Spectroscopy, Applications," *ENcyclopedia of Spectroscopy and Spectrometry*. pp. 2478–2487, 1999.
- [93] J. R. Opfermann, "Kinetic Analysis Using Multivariate Non-linear Regression. I: Basic Concepts," *J. Therm. Anal. Calorim.*, vol. 60, pp. 641–658, 2000.
- [94] E. D. Weil, S. Levchik, and P. Moy, "Flame and Smoke Retardants in Vinyl Chloride Polymers –

- Commercial Usage and Current Developments," *J. Fire Sci.*, vol. 24, pp. 211–236, 2006.
- [95] Chemceed, "Formulation 101: Wire and Cable Insulation and Jacket PVC Compounds," 2017. .
 - [96] Z. Hruska, P. Guesnet, C. Salin, and J.-J. Couchoud, "Poly(chlorure de vinyle) ou PVC," *Techniques de l'ingénieur*. Ref: am3325, 2007.
 - [97] K. Cavalier, "Carbonate de calcium, additif multifonctionnel," *Techniques de l'ingénieur*. Ref: am3222, 2007.
 - [98] A. Chabrol and S. Girois, "Stabilisation du PVC," *Techniques de l'ingénieur*. Ref: am3233, 2013.
 - [99] N. Denis, "Comportement au feu des nappes de cables électriques en centrale en cas d'incendie," Internal Report, Moret sur Loing, France, 1995.
 - [100] P. Ševěček and V. Stůžka, "Study of solid char residues after thermal degradation of polystyrene, PVC and polyamide—Part II," *Fire Mater.*, vol. 11, no. 2, pp. 89–93, 1987.
 - [101] G. Matthews and G. S. Plemper, "Effects of calcium carbonate fillers on the behaviour of PVC in fires," *Br. Polym. J.*, 1981.
 - [102] T. Karayildirim, J. Yanik, M. Yuksel, and M. Saglam, "The effect of some fillers on PVC degradation," *J. Anal. Appl. Pyrolysis*, vol. 75, pp. 112–119, 2006.
 - [103] K. Saido, H. Taguchi, and S. Yada, "Thermal Decomposition Products of Phthalates with Poly(vinyl chloride) and Their Mutagenicity," *Macromol. Res.*, vol. 11, no. 3, pp. 178–182, 2003.
 - [104] A. H. Frye and R. W. Horst, "The mechanism of poly(vinyl chloride) stabilization by barium, cadmium, and zinc carboxylates. I. Infrared studies," *J. Polym. Sci.*, vol. 40, no. 137, pp. 419–431, 1959.
 - [105] L. Murer, S. Chatenet, G. Fontaine, S. Bourbigot, and O. Authier, "Influence of model assumptions on charring polymer decomposition in the cone calorimeter," *J. Fire Sci.*, vol. 36, no. 3, pp. 181–201, 2018.
 - [106] S. I. Stoliarov, S. Crowley, R. N. Walters, and R. E. Lyon, "Prediction of the burning rates of charring polymers," *Combust. Flame*, vol. 157, pp. 2024–2034, 2010.
 - [107] T. Kashiwagi and T. J. Ohlemiller, "A study of oxygen effects on non flaming transient gasification of PMMA and PE during thermal irradiation," in *Proceedings of the Symposium (international) on Combustion 19*, 1982, pp. 815–823.
 - [108] T. Kashiwagi, "Polymer combustion and flammability - Role of the condensed phase," in *Proceedings of the Symposium (international) on Combustion 25*, 1994, pp. 1423–1437.
 - [109] G. Impallomeni, G. Montaudo, C. Puglisi, E. Scamporrino, and D. Vitalini, "The Role of Intumescence on the Flammability of Vinyl and Vinylidene Polymers," *J. Appl. Polym. Sci.*, vol. 31, pp. 1269–1274, 1986.
 - [110] S. I. Stoliarov, S. Crowley, R. E. Lyon, and G. T. Linteris, "Prediction of the burning rates of non-charring polymers," *Combust. Flame*, vol. 156, no. 5, pp. 1068–1083, 2008.
 - [111] J. Luche, T. Rogaume, F. Richard, and E. Guillaume, "Characterization of thermal properties and analysis of combustion behavior of PMMA in a cone calorimeter," *Fire Saf. J.*, vol. 46, pp. 451–461, 2011.
 - [112] B. T. Rhodes and J. G. Quintiere, "Burning rate and flame heat flux for PMMA in a cone calorimeter," *Fire Saf. J.*, vol. 26, pp. 221–240, 1996.

- [113] R. Filipczak, S. Crowley, and R. E. Lyon, "Heat release rate measurements of thin samples in the OSU apparatus and the cone calorimeter," *Fire Saf. J.*, vol. 40, pp. 628–645, 2005.
- [114] J. G. Quintiere and A. S. Rangwala, "A theory for flame extinction based on flame temperature," *Fire Mater.*, vol. 28, no. 5, pp. 387–402, 2004.
- [115] P. Patel, T. Hull, and A. Stec, "Influence of physical properties on polymer flammability in the cone calorimeter," *Polym. Adv. Technol.*, vol. 22, pp. 1100–1107, 2011.
- [116] A. Tewarson, J. L. Lee, and R. F. Pion, "The influence of oxygen concentration on fuel parameters for fire modelling," in *Proceedings of the Symposium (international) on Combustion 18*, 1980, pp. 563–570.
- [117] A. Renoux and D. Boulaud., "Les aérosols : Physique & métrologie," *Recherche*, vol. 67, p. 2, 1998.
- [118] P. F. DeCarlo, J. G. Slowik, D. R. Worsnop, P. Davidovits, and J. L. Jimenez, "Particle Morphology and Density Characterization by Combined Mobility and Aerodynamic Diameter Measurements. Part 1: Theory," *Aerosol Sci. Technol.*, vol. 38, no. 12, pp. 1185–1205, 2004.
- [119] B. Hervé-Bazin, "Généralités sur les particules ultra-fines," in *Les nanoparticules, un enjeu majeur pour la santé au travail*, INRS, 2007, p. 51.
- [120] M. Wentzel, H. Gorzawski, K.-H. Naumann, H. Saathoff, and S. Weinbruch, "Transmission electron microscopical and aerosol dynamical characterization of soot aerosols," *J. Aerosol Sci.*, vol. 34, no. 10, pp. 1347–1370, 2003.
- [121] Ü. Ö. Köylü and G. M. Faeth, "Structure of overfire soot in buoyant turbulent diffusion flames at long residence times," *Combust. Flame*, vol. 89, no. 2, pp. 140–156, 1992.
- [122] Mathieu MAUGENDRE, "Etude des particules de suie dans les flammes de kerosene et de diester," Institut national des sciences et techniques nucléaires (CEN Saclay), 2009.
- [123] M. Yvan, "Les fractales." [Online]. Available: <http://www.maths-et-tiques.fr/index.php/detentes/les-fractales>. [Accessed: 01-Jan-2015].
- [124] S. R. Forrest and T. A. Witten, "Long-range correlations in smoke-particle aggregates," *J. Phys. A. Math. Gen.*, vol. 12, pp. L109–L117, 1979.
- [125] R. Samson, G. Mulholland, and J. Gentry, "Structural analysis of soot agglomerates," *Langmuir*, vol. 3, pp. 272–281, 1987.
- [126] J. Cai and C. Sorensen, "Diffusion of fractal aggregates in the free molecular regime," *Phys. Rev. E Stat. Nonlinear Soft Matter Phys.*, vol. 50, pp. 3397–3400, 1994.
- [127] H. Burtscher, "Charaterization of ultra fine particle emissions from combustion systems," *Soc. Automot. Eng. Tech. Pap. Ser.*, 2000.
- [128] A. Schmidt-Ott, "In situ measurement of the fractal dimensionality of ultrafine aerosol particles," *Appl. Phys. Lett.*, vol. 52, pp. 954–956, 1988.
- [129] M. WU and S. Friedlander, "Enhanced power law agglomerate growth in the free-molecular regime," *J. Aerosol Sci.*, vol. 24, pp. 273–282, 1993.
- [130] Ü. Ö. Köylü, G. M. Faeth, T. L. Farias, and M. G. Carvalho, "Fractal and projected structure properties of soot aggregates," *Combust. Flame*, vol. 100, no. 4, pp. 621–633, 1995.
- [131] C. Sorensen and G. Roberts, "The prefactor of Fractal Aggregates," *J. Colloid Interface Sci.*, vol. 186, no. 2, pp. 447–452, 1997.

- [132] F.-X. Ouf, J. Vendel, A. Coppalle, M. Weill, and J. Yon, "Characterization of soot particle in the plume of over-ventilated diffusion flames," *Combust. Sci. Technol.*, vol. 180, no. 4, pp. 674–698, 2008.
- [133] W. Hinds, "Aerosol Technology: Properties, Behavior, and Measurement of Airborne Particles," 1999.
- [134] P. Baron and K. Willeke, "Gas and Particle Motion," *Aerosol Meas. Princ. Tech. Appl.*, pp. 61–97, 2001.
- [135] L. Katsikas, M. Avramovic, R. Cortes, and M. Milovanovic, "The thermal stability of poly(methyl methacrylate) prepared by RAFT polymerisation," *J. Serbian Chem. Soc.*, vol. 73, pp. 915–921, 2008.

Les câbles électriques constituent la charge calorifique la plus abondante dans les centrales nucléaires et l'incendie est la source d'agression interne ayant la plus grande occurrence (un départ de feu par tranche et par an en France). Le risque incendie est caractérisé par deux vecteurs : la chaleur dégagée, qui peut conduire à la propagation de l'incendie, et la fumée produite, composée de gaz et d'aérosols, qui peuvent être toxiques et corrosifs et interagir avec les composants présents dans le local. À un stade avancé, un incendie confiné devient sous-ventilé et vicié car la combustion consomme l'oxygène disponible. La production d'imbrûlés augmente donc considérablement, ce qui a pour effet de rendre l'incendie possiblement plus agressif. Pour se protéger des risques d'un incendie confiné, il est donc important de quantifier la chaleur libérée, les gaz et les aérosols produits lors de la combustion de câbles électriques dans des conditions de déplétion d'oxygène. Pour ce faire, un banc expérimental à l'échelle intermédiaire, connu sous le nom de cône calorimètre à atmosphère contrôlée (CCAC), a été développé. Ce banc d'essai a été caractérisé préalablement à l'aide de plaques de PMMA. Des matériaux modèles représentatifs de gaines de câbles électriques à base de PVC ont été formulés puis manufacturés sous forme de plaques échantillons. Ces matériaux ont été caractérisés simultanément en termes de paramètres liés à l'incendie (taux de dégagement de chaleur, perte de masse), de gaz produits et d'aérosols émis, en conditions de sous-ventilation et de viciation à l'aide du couplage CCAC/FTIR/ELPI. La viciation a pour effet de diminuer le débit calorifique et le débit de pyrolyse de façon linéaire, alors que la sous-ventilation favorise la production d'imbrûlés et d'aérosols.

¹ Spectromètre infrarouge à transformée de Fourier

² Granulomètre d'impaction électrique à basse pression

***Mots-clés :** incendie, cône calorimètre, câble électrique, sous-ventilation, viciation, polychlorure de vinyle, polyméthacrylate de méthyle.*

Electrical cable sheaths are the most abundant fire load in nuclear power plants and fire is the most frequent internal aggression (one fire outbreak per year and per nuclear unit in France). A fire is threatening by two means: the heat it releases that may drive a fire growth and the smoke it yields, composed of gases and aerosols, that may be toxic and corrosive and interact with components in the area. At advanced stages, confined fires become oxygen depleted and the combustion regime shifts towards under-ventilated and vitiated combustion with the production of unburnt species leading to a higher threat. To assess the potential hazard of a confined fire, it is then of high importance to quantify the heat release, the gases and the aerosols produced by electrical cable sheaths fires in oxygen depleted conditions. To do so, a bench scale apparatus known as the controlled-atmosphere cone calorimeter (CACC) has been developed. The apparatus has been primarily qualified with PMMA plaques. Representative materials of PVC based electrical cable sheath have been formulated and manufactured in the shape of plaque samples. These materials have been characterized in terms of fire parameters (heat release rate, mass loss rate), evolved gases and evolved aerosols under different oxygen concentrations in under-ventilated conditions thanks to the CACC/FTIR/ELPI coupling. Vitiating lowers the heat release rate and decreases the fuel mass loss rate while under-ventilation increases unburnt species and aerosols production.

¹ Fourier Transformed Infrared spectrometer

² Electrical Low-Pressure Impactor

***Key-words:** fire, cone calorimeter, electrical cable, under-ventilation, vitiation, polyvinyl chloride, polymethylmethacrylate.*